THÈSE

Pour obtenir le grade de

DOCTEUR DE L'UNIVERSITÉ GRENOBLE ALPES

Spécialité : Sciences de la Terre et de l'Univers et de l'Environnement

Arrêté ministériel : 25 mai 2016

Présentée par

Zhanar ZHAKIYEVA

Thèse dirigée par **Alejandro FERNANDEZ-MARTINEZ**,chercheur, Université Grenoble Alpes
et codirigée par **Alexander VAN DRIESSCHE**,chercheur, Université Grenoble Alpes
et **Gabriel CUELLO**,ILL

préparée au sein du **Laboratoire Institut des Sciences de la Terre**
dans **l'École Doctorale Sciences de la Terre de lEnvironnement et des Planètes**

Structure et dynamique de leau dans le ciment Portland et dans de ciments a bas CO2

Structure and dynamics of water in ordinary Portland and low CO2 cements.

Thèse soutenue publiquement le **30 novembre 2021**,
devant le jury composé de :

Monsieur Alejandro FERNANDEZ-MARTINEZ
DOCTEUR EN SCIENCES, Institut des Sciences de la Terre (ISTerre), Université Grenoble Alpes , Directeur de thèse
Monsieur Andrey G. Kalinichev
DIRECTEUR DE RECHERCHE, Laboratoire SUBATECH Radiochimie, Institut Mines-Télécom Atlantique , Rapporteur
Madame Claire White
PROFESSEUR, The Department of Civil and Environmental Engineering, Princeton University, Rapporteure
Monsieur Laurent Charlet
PROFESSEUR EMERITE, Institut des Sciences de la Terre (ISTerre), Université Grenoble Alpes , Examinateur
Monsieur Miguel Angel García Aranda
PROFESSEUR, University of Malaga, Inorganic Chemistry Department, Examinateur
Monsieur Alexander E.S. Van Driessche
DOCTEUR EN SCIENCES, Institut des Sciences de la Terre (ISTerre), Université Grenoble Alpes , Co-directeur de thèse
Monsieur Gabriel Cuello
DOCTEUR EN SCIENCES, Institut Laue-Langevin, Co-directeur de thèse

Abstract

Cement is the single most used material in the world. Despite many centuries of intensive usage and an ever-increasing worldwide demand, many fundamental physico-chemical questions regarding its structure at the nanoscale level remain elusive. During the process of cement setting, different hydrates nucleate and grow, of which calcium silicate hydrate (C-S-H) is the most important binding phase. C-S-H is indeed the key compound controlling the final cement properties, such as strength and durability. Although a large deal of research effort has been devoted to the study of C-S-H, its poorly crystalline character has made it inherently difficult to characterize its structural and dynamical properties, and the properties of water adsorbed at its interfaces. Moreover, the presence of aluminate phases both in ordinary Portland cement and in new low-CO_2 emissions cement formulations results in C-A-S-H, an Al-bearing C-S-H. Understanding water organization in the C-S-H phase is not only important for the setting behavior, but also because water plays a key role in the dissolution-recrystallization and carbonation processes which are the main causes of the loss of cement strength. Moreover, water diffusion in C-S-H nanopores is important to understand the exchange of ions in pollutant removal or in the context of nuclear waste storage.

In this Ph.D. project, the structure and dynamics of water in the different pores of C-(A)-S-H were studied using a combination of neutron and X-ray scattering techniques with laboratory-based methods such as water sorption isotherms (WSI), infrared spectroscopy and thermogravimetric analyses. The results of the scattering techniques were analyzed with molecular dynamics (MD) simulations.

In particular, the structure of water was studied using neutron diffraction with isotopic substitution (NDIS), a method that allowed probing the local ordering of water molecules adsorbed at C-(A)-S-H / water interfaces. The NDIS results coupled with MD simulations showed that the main mechanism for water adsorption is the coordination of water by hydrophilic calcium ions, which induce a strong hydrogen-bond network with other water molecules and with surface oxygen atoms. The C-S-H surface combines wet and dry regions, with wet areas that were dominated by the presence of hydrophilic calcium ions with strong hydration shells, whereas dry areas exposed only silica chains and silanol hydroxyls. The results of the X-ray scattering and MD simulations revealed that water exerts an influence on the ordering of C-S-H, with the more hydrated C-S-H structure showing a larger degree of mesoscale ordering.

The dynamics of water were studied using inelastic incoherent neutron scattering (IINS), a method that probes inter- and intra-molecular vibrations of matter, yielding a vibrational density of states of water in the C-(A)-S-H phase. The experimental data were interpreted with the help of the calculated power spectra from the MD models. The multilayer surface adsorbed water showed a characteristic intensity in the 300-550 cm-1 region, which turned into ice-like features upon capillary condensation at higher RH values. The so-called “fingerprint” of confined water was observed at lower energies for drier C-(A)-S-H samples. In good accordance with the WSI results, water in C-(A)-S-H samples at higher Ca/Si ratios was found to be more structured and less bulk-water like, due to an increased number of hydrophilic cites created by calcium ions.

The results from this thesis will contribute to the understanding of the properties of interfacial water at C-(A)-S-H, a key phase to understand cement mechanical properties and durability.

Résumé

Le ciment est le matériau anthropogénique le plus utilisé au monde. Au cours du processus de prise du ciment, différents hydrates sont formés, parmi lesquels l'hydrate de silicate de calcium (C-S-H) est la phase liante la plus importante. Le C-S-H est en effet le composé clé qui contrôle les propriétés finales du ciment, telles que sa résistance et la durabilité. Bien que de nombreux efforts de recherche aient été consacrés à l'étude de cette phase, son caractère cryptocristallin rend difficile la caractérisation de ses propriétés structurelles et dynamiques, ainsi que les propriétés de l'eau adsorbée aux interfaces avec la solution. De plus, la présence de phases aluminates à la fois dans le ciment Portland ordinaire et dans les nouvelles formulations de ciment à faibles émissions de CO_2 donne lieu à la formation de C-A-S-H, du C-S-H avec de l'Al structurale. La compréhension de l'organisation de l'eau dans la phase C-(A)-S-H est clé : l'eau joue un rôle clé dans les processus de dissolution-recristallisation et de carbonatation qui sont la cause principale de la perte de résistance du ciment. De plus, la diffusion de l'eau dans les nanopores du C-S-H est importante pour comprendre les échanges d'ions dans le piégeage des polluants ou dans le contexte du stockage des déchets nucléaires.

Dans cette thèse, la structure et la dynamique de l'eau dans les différents pores de C-(A)-S-H ont été étudiées en combinant des techniques de diffusion des neutrons et des rayons X avec des méthodes de laboratoire telles que les isothermes de sorption d'eau (WSI), la spectroscopie infrarouge et les analyses thermogravimétriques. Les résultats des techniques de diffusion ont été analysés par des simulations de dynamique moléculaire (MD).

En particulier, la structure de l'eau a été étudiée en utilisant la diffraction des neutrons avec substitution isotopique (NDIS), une méthode qui a permis de sonder l'ordre local des molécules d'eau adsorbées aux interfaces C-(A)-S-H / eau. Les résultats de la NDIS couplés aux simulations MD ont montré que le principal mécanisme d'adsorption de l'eau est la coordination par des ions calcium hydrophiles, qui induisent un fort réseau de liaisons hydrogène avec d'autres molécules d'eau et avec les atomes d'oxygène de surface. La surface du C-S-H combine des régions humides et sèches, les zones humides étant dominées par la présence d'ions calcium avec de fortes sphères d'hydratation, tandis que les zones sèches n'exposent que des chaînes de silice et des groupements silanol. Les résultats de la diffusion des rayons X et des simulations MD ont révélé que l'eau exerce une influence sur la cristallinité du C-S-H, la structure la plus hydratée présentant un plus grand degré d'ordre a la meso-échelle.

La dynamique de l'eau a été étudiée à l'aide de la diffusion inélastique incohérente des neutrons (IINS), une méthode qui sonde les vibrations inter- et intra-moléculaires de la matière, ce qui a permis d'obtenir une densité des états vibrationnelle de l'eau dans la phase C-(A)-S-H. Les données expérimentales ont été interprétées à l'aide des spectres calculés à partir des modèles MD. Des pics caractéristiques de multicouches d'eau adsorbée ont été identifiés dans la région 300-550 cm^{-1} des spectres ; des spectres similaires à ceux de la glace à structure hexagonale sont identifiés lors de la condensation capillaire de l'eau. L'empreinte de l'eau confinée a été observée à des énergies plus faibles pour les échantillons C-(A)-S-H plus secs. En accord avec les résultats du WSI, l'eau dans les échantillons C-(A)-S-H à des rapports Ca/Si plus élevés s'est avérée plus structurée et moins semblable à de l'eau 'bulk', en raison d'un nombre accru de sites d'adsorption hydrophiles créés par les ions calcium.

Les résultats de cette thèse contribuent à la compréhension des propriétés de l'eau interfaciale du C-(A)-S-H, une phase clé pour comprendre les propriétés mécaniques et la durabilité du ciment.

Acknowledgements

I would like to thank my supervisors for their endless support, enthusiasm, and their inexhaustible belief in me and this thesis. I want to express my deep gratitude to our collaborators at BRGM, Princeton University and ILL, engineers at ISTerre, the beamline scientists at ILL, ISIS, ESRF, and APS for sharing their time and expertise, and their help to finalize this work.

I am grateful to my colleagues at ISTerre and ILL for their support and care during these four years.

Finally, I am deeply grateful to my husband, my son, and to my big Kazakh-Italian family for helping and supporting me over this incredible journey.

This thesis would not have been possible without all of you, thank you.

Menin’ atama (1938-2021)

Table of contents

List of Figures

List of Tables

Chapter 1 General introduction and motivation

1.1. Cement

Concrete is the most used material in the world, and second most individually consumed substance in the world after water. Cement is a precursor of concrete, with a worldwide annual production of 4 billion tonnes that is increasing every year. Production of cement involves chemical and thermal combustion processes that result in nearly 10% of global CO_2 emissions. It is expected that the growing population worldwide, and especially in developing countries, will boost the cement production immensely. At the same time cement industry is under pressure to create new 'greener' formulations leading to reduced amount of CO_2 emissions (Lehne and Preston, 2018; van Deventer, White and Myers, 2021).

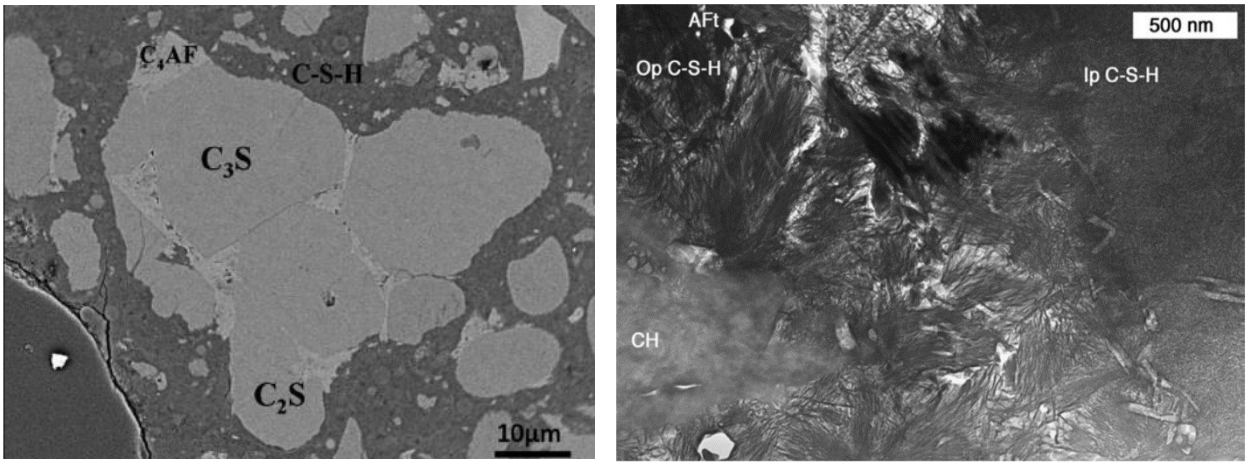

*Figure 1.1.1. (left) A scanning electron microscopy (SEM)image of a hydrated cement paste: light grey areas show alite, belite, and ferrite phases, darker grey zones show C-S-H. (right) A transmission electron miscroscopy (TEM) image from a 4-year old hydrated cement paste. The outer product (Op) C-S-H has fine fibrillar morphology and the inner product (Ip) has a fine homogeneous morphology. (Images taken from Cement Chemistry and Sustainable Cementitious Materials cou*rse (Scrivener, 2017) *and* (Richardson, 2008)*).*

Cement is a powdered material that generally contains clinker, gypsum, supplementary cementitious materials (SCM) and fillers. The most widespread type of cement is ordinary Portland cement (OPC) which in many cases is interchangeable with cement. Cement clinker consists of granules produced by heating a mix of clay, limestone and sand in a rotary kiln at 1450°C. This process leads to the decomposition of limestone (calcium carbonate) into calcium oxide and carbon dioxide, and constitutes around 60% of CO_2 emissions coming from cement production. The rest of carbon dioxide comes from burning fossil fuels to heat the kiln, and transportation emissions. The SCM are the materials that decrease the overall volume of the clinker in a final cement mix by physically replacing a part of the clinker.

Most abundant phases in cement clinker are alite, belite, aluminate, and aluminoferrite phases (Figure 1.1.1). Alite makes up the majority of the clinker (40-70% in OPC) with a formula Ca_3SiO_5 or C_3S (in cement notation the chemical formula of oxides are shortened for convenience: C is CaO, S is SiO_2, H is H_2O, A is Al_2O_3, F is Fe_2O_3 etc.). It reacts fast with water, thus controlling the setting time, and forms calcium-silicate-hydrate (C-S-H) and calcium hydroxide (CH). Belite (C_2S), constitutes about 15% of

cement and it reacts much slower with water, and also forms C-S-H and CH at the later phases of cement formation. Other phases include aluminate (C_3A) ~8-15%, and ferrite (C_4AF) ~7%. C_3A reacts the fastest with water, releasing heat and leading to a rapid setting of cement. Gypsum ($CaSO_4 \cdot 2H_2O$) is added to slow down this reaction by forming ettringite ($3CaO \cdot Al_2O_3 \cdot 3CaSO_4 \cdot 32H_2O$) and sulfoaluminates AFm ($CaO \cdot Al_2O_3 \cdot CaSO_4 \cdot 12H_2O$). C_4AF forms metastable hydrate phases with C_3A that stabilize over time (Taylor, 1997).

The mechanism of hydration is generally described by four stages:

- *Pre-induction period (first minutes):* starts immediately when water is added to cement, with a rapid dissolution of ionic species into the liquid phase and formation of hydrate phases. The alkali sulfates dissolve immediately, calcium sulfate dissolves until saturation, therefore providing K^+, Na^+, SO_4^{2-} , and Ca^{2+}, SO_4^{2-} ions, respectively. The aluminate and ferrite phases dissolve and react with Ca^{2+} and SO_4^{2-} to form ettringite (Aft). A saturated calcium hydroxide solution is formed. The early fast hydration reaction is slowed down by a thin layer of hydration products formed on the cement grain surfaces, thus causing an increase in the concentration of dissolved ions in the liquid phase.

-*Induction or dormant period (first few hours):* the hydration of all clinker minerals proceeds very slowly. The concentration of calcium hydroxide in the liquid phase reaches its maximum, and the concentration of SO_4^{2-} remains constant, as the fraction consumed in the formation of the Aft phase is replaced by a continuous dissolution of $CaSO_4$.

- *Acceleration stage (3-12 h after mixing):* the hydration accelerates again, and second stage C-S-H starts to form. Calcium hydroxide precipitates from the liquid phase into crystals, thus lowering the Ca^{2+} concentration. The $CaSO_4$ dissolves completely, and SO_4^{2-} concentration decreases due to the formation of Aft phase and the adsorption of sulfate ions on the C-S-H surface.

- *Post-acceleration period:* the hydration rate slows down gradually, and the rate of hydration process is diffusion-controlled. The C-S-H phase continues to be formed by a gradual dissolution of alite and belite. The Aft phase formed at the earlier stages of hydration starts to react with additional C_3A and $C_2(A,F)$ to form a monosulfate. At a high initial water/cement ratios the hydration goes on until all initial cement is consumed. However, even after the hydration process has been completed, the ageing of the material takes place, i.e. the average SiO_4 chain length may increase in the C-S-H phase formed (Beaudoin and Odler, 2019).

1.2. Calcium silicate hydrate

C-S-H is the main binding phase of cement with variable Ca/Si and water content and a general formula $CaO_x \cdot SiO_2 \cdot H_2O_y$, where x varies from 0.6 to 1.54 for synthetic C-S-H, and from 1.7 to 2 for hydrated cement pastes (Richardson, 2008), and y varies considerably depending on the amount of Ca ions, the hydration state or drying method (Feldman and Sereda, 1970; H. Taylor, 1997; Richardson, 2008; Lothenbach and Nonat, 2015).

1.2.1. C-S-H structure

On the microstructural level, two types of C-S-H can be discriminated. A denser C-S-H forms inside the cement grain, thus called an inner product, and less dense C-S-H formed outside is called an outer product (Figure 1.1.1.). At the nanoscale, the C-S-H is a partially disordered phase, with an atomic structure that is still a subject of debate. According to Taylor, the C-S-H phase formed by C_3S hydration consists from a mixture of highly distorted tobermorite-like and jennite-like layers (Taylor, 1986b). The model by Richardson and Groves, also encompasses the distribution of tobermorite (T) and jennite (J) units (Richardson and Groves, 1992) (more in Chapter 4 introduction). The low Ca/Si ratio C-S-H is generally described using tobermorite models, and higher Ca/Si ratios by applying jennite models.

In this thesis an atomistic model of C-S-H with Ca/Si=1 was created. Its atomic structure was based on the crystal structure of tobermorite. Some of its structural characteristics include: layers of calcium oxide sandwiched between the 'dreierketten' chains (3-chain) of silicon oxides, with an interlayer filled with water and Ca^{2+} ions (Figure 1.2.1.1, left). Each of the oxygens of Ca is shared with SiO_4 tetrahedra. In each SiO_4 'dreierkette', the two SiO_4 that share their oxygens with CaO_2 are called 'paired' tetrahedra. The SiO_4 that connect them are called 'bridging' tetrahedra. The interlayer Ca^{2+} ions balance out the negatively charged C-S-H layers (Figure 1.2.1.1)(Richardson, 2008; Beaudoin and Odler, 2019).

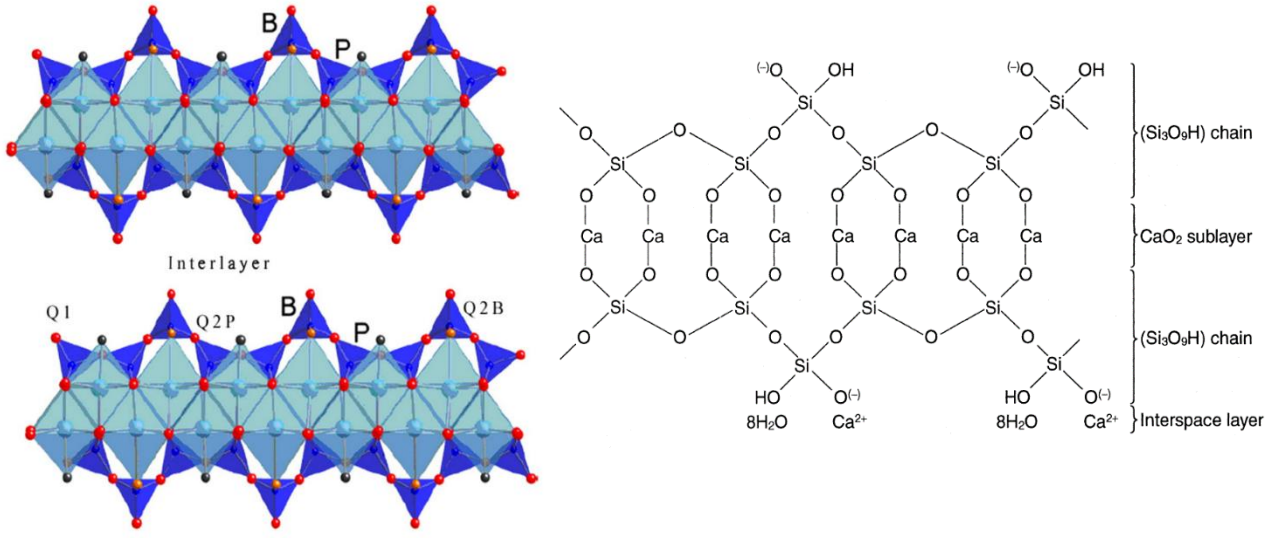

Figure 1.2.1.1. (left) Atomic structure of tobermorite showing 3-unit silica chains, with B signifying bridging silica tetrahedra, P pairing silica tetrahedra. Image was adapted by Lothenbach (Lothenbach and Nonat, 2015) *from Richardson* (Richardson, 2008)*(right) A schematic structure of 14 Å tobermorite. Image taken from Lea's Chemistry of Cement and Concrete* (Beaudoin and Odler, 2019).

The structure of C-S-H differs from tobermorite in several ways:

- An increased Ca/Si ratio, which changes from 0.83 in tobermorite, up to 2 in the real cement. The extra Ca is accommodated in the structure by creating defects, i.e. removing bridging silica tetrahedra, and introducing additional interlayer Ca^{2+} ions (Taylor and Howison, 1956; Richardson, 2008).
- The finite size of C-S-H, which is reported to be about 3-5 nm. According to a 'colloid' model by Jennings, the stacked distorted C-S-H layers form platelets (or globules) that assemble

together, with water present everywhere (Jennings, 2008). In a model by Feldman and Sereda, the C-S-H layers are connected forming distorted sheets (Feldman and Sereda, 1970). The common feature in both models is that different types of water are present ubiquitously in the C-S-H phase.

- The disorder in stacking of C-S-H layers. X-ray diffraction analysis indicates that the layers are characterized by turbostratic disorder (Grangeon, Claret, Lerouge, *et al.*, 2013), which include random translations parallel to the layers and/or rotations, and interstratification of low Ca/Si layers with high Ca/Si layers (Grangeon, Claret, Linard, *et al.*, 2013).

Existing atomistic models of C-(A)-S-H of different Ca/Si ratios (Abdolhosseini Qomi *et al.*, 2014; Androniuk, 2017; Hou, 2020), hydration levels (Manzano *et al.*, 2012; Zhou *et al.*, 2019), and created using various computational methods (Youssef, Pellenq and Yildiz, 2011; Kunhi Mohamed *et al.*, 2020) are described in Chapter 4.

1.2.2. Water in C-S-H

Water is present everywhere in the hydrated cement, thus affecting its mechanical properties, such as drying shrinkage (Ferraris and Wittmann, 1987; Thomas and Jennings, 2006; Rougelot, Skoczylas and Burlion, 2009) and creep (Wittmann, 1973; Thomas and Jennings, 2006), and acts as a medium for ion transportation (Androniuk, 2017). The early classification of water by Powers and Brownyard distinguished between 'evaporable' and 'non-evaporable' water (Powers, T. C.; Brownyard, 1946). Taylor later discussed problems defining bound (non-evaporable) water in the cement paste (Taylor, 1986a). Allen et al. provided a more detailed classification of water based on a colloidal model by Jennings (Jennings, 2008), which included water inside and on the surfaces of the globules (stacked C-S-H layers of ~5 nm size), as well as water in the nanopores in between randomly stacked globules (Allen, Thomas and Jennings, 2007).

The challenge with water classification, besides the structural complexity of the hydrated cement phase, and different sensitivities of the experimental techniques, lies in the changing porosity of the hydrated cement dependent on drying conditions (Thomas, Jennings and Allen, 1999; Roosz *et al.*, 2016; Gaboreau *et al.*, 2020), exposure to humidity (Muller *et al.*, 2013), equilibration time (duration of exposure) (Badmann, Stockhausen and Setzer, 1981; Odler, 2003), and an ever-going exchange of different types of water between each other (Muller *et al.*, 2013; Wyrzykowski *et al.*, 2017).

In order to narrow down the variables, this thesis focuses on the distribution, structure, and dynamics of water in a synthetic C-(A)-S-H phase. Certainly, all above-mentioned factors influence the porosity, and thus the distribution of water in the synthetic C-(A)-S-H as discussed very recently (Roosz *et al.*, 2016; Gaboreau *et al.*, 2020; Abdolhosseini Qomi *et al.*, 2021). Therefore, to observe some of the effects, the C-(A)-S-H samples studied here vary in Ca/Si ratios and humidity values, thus containing, in different proportions, interlayer, interfacial, and bulk-pore water.

1.3. Research questions

The objectives of this thesis stem from the long debated questions on the distribution, structure and dynamics of water in the main binding phase of cement, the C-(A)-S-H phase. As it was discussed earlier, and will be discussed later in the introductions to each chapter, plenty is known about the structure of C-(A)-S-H, and the distribution, structure and dynamics of different types of water. However, each of these topics is highly debated. This thesis offers a direct insight into long debated issues by applying state-of-the-art neutron and X-ray scattering, and molecular dynamics methods.

The research questions can be formulated as:

- What is the effect of Ca/Si ratios on the overall stoichiometry and water distribution in C-(A)-S-H?
- How does the structure of water on the C-(A)-S-H interfaces and interlayers differ from the one of bulk water? Is the structure of water for C-(A)-S-H dependent on Ca/Si ratios?
- What is the effect of increased hydration level both on the local structure and long-range structure?
- What is the wetting mechanism of the C-(A)-S-H surfaces?
- What is the influence of Ca/Si ratios and different hydration states on the dynamics of water?
- What is the effect of different Ca/Si ratios on the dynamics of water in C-(A)-S-H?

This thesis is organized as following:

- Chapter 2 will discuss the theory behind the neutron scattering and molecular dynamics methods, and brief reviews of the instrumentation and data treatment.
- Chapter 3 will focus on the characterization of the amount and distribution of water in C-(A)-S-H samples of varying Ca/Si ratios and hydration levels.
- Chapter 4 will examine the structure of water in the C-(A)-S-H phase for varying hydration levels (55% and 98% RH) and Ca/Si ratios (0.9, 1, 1.1, 1.27).
- Chapter 5 will be focused on the vibrational and diffusional dynamics of interfacial and interlayer water distinct from the dynamics of bulk water in C-(A)-S-H samples of different Ca/Si ratios and hydration levels (fully hydrated, oven-dried, 55RH, 98RH, desiccator dried).

In conclusion, the primary goal of this thesis is to examine the distinct properties, i.e. structure and dynamics, of interfacial and interlayer water in C-(A)-S-H samples.

Chapter 2 Experimental and theoretical methods

2.1. Neutron Diffraction with Isotopic Substitution (NDIS)

The result of a diffraction experiment on a liquid or an amorphous system (water in a disordered nanocrystalline C-S-H phase in our case) is a diffraction pattern or diffractogram, which is a sum of all scattered intensity from all coherence volumes in the sample. The measured intensity (I) is a function of the scattering vector (Q), which is the difference between the scattered and incident wave-vectors, and whose norm, Q, is a function of the wavelength λ and scattering angle 2θ:

$$Q = \frac{4\pi sin\theta}{\lambda} \qquad Eq.\,(2.1.1)$$

Therefore, a diffractogram can be obtained by varying λ or 2θ, or both. In the case of a reactor source of neutrons (D4c, ILL) a monochromatic beam is used and 2θ is varied, whereas in time-of-flight pulsed sources (SANDALS, ISIS) both λ and 2θ are varied (Henry E. Fischer, Barnes and Salmon, 2006).

To obtain the sample intensity, the intensities contributed by the empty container and the instrument background are measured and subtracted. The data are corrected for attenuation (from absorption and scattering) and multiple scattering (from within the sample and sample environment). A vanadium standard is measured as well to normalize the sample scattering data to absolute units of scattering cross section. The effect relies on a property of vanadium to scatter neutrons almost incoherently, therefore resulting in a structureless flat background (Cuello, 2008).

The data are presented in units of barn per steradian per atom (where barn is a cross section unit, 1 barn = 100 fm^2) as a function of the scattering vector. The corrected intensity is given within the so-called static approximation (in which the energy exchanged between the incident neutron and the sample is minimal compared to the incident neutron energy) as:

$$I(Q) = \sum_{\alpha} c_\alpha \overline{b_\alpha^2} + F(Q) \qquad Eq.\,(2.1.2)$$

where c_α is the atomic fraction of species α and $\overline{b_\alpha^2}$ is its mean square scattering length (is an intrinsic measure of the tendency of nuclei to scatter neutrons). The first component in equation 2 is known as the self-scattering term and gives a downward slope to $I(Q)$ with increasing Q due to the recoil effect by the light nuclei (H and D). The second component $F(Q)$ contains the structural information as:

$$F(Q) = \sum_{\alpha}\sum_{\beta} c_\alpha c_\beta \; b_\alpha b_\beta \; [S_{\alpha\beta}(Q) - 1] \qquad Eq.\,(2.1.3)$$

where b_α and b_β are the mean coherent scattering lengths of species α and β and $S_{\alpha\beta}(Q)$ are their partial structure factors. The Fourier transformation of the partial structure factors yields the real space partial pair distribution function (PDF) $g_{\alpha\beta}(r)$. This last function defines the probability of finding an atom β at a distance r from an atom α (and equally β from α) as (for an isotropic system):

$$g_{\alpha\beta}(r) = 1 + \frac{1}{2\pi^2\rho_n}\int_0^\infty [S_{\alpha\beta}(Q) - 1]Q^2 \frac{\sin Qr}{Qr} dQ \qquad Eq.\,(2.1.4)$$

where ρ_n is the atomic number density (number of atoms per unit of volume, $Å^{-3}$). In Eq. 2.1.4 an integral is taken over the whole Q-space, from zero to infinity. In a real diffraction experiment the Q-range is finite, and the integral is taken from zero to Q_{max} leading to broader peaks and non-physical oscillations in $g(r)$. To reduce this problem, the $S(Q)$ can be convoluted with a window function, $M(Q)$, which has the property of going to zero as Q_{max} is approached, thus modifying Eq. 2.1.4 to:

$$g_{\alpha\beta}(r) = 1 + \frac{1}{2\pi^2\rho_n}\int_0^\infty [S_{\alpha\beta}(Q) - 1]Q^2 \frac{\sin Qr}{Qr} M(Q) dQ \qquad Eq.\,(2.1.5)$$

In our case, we used the Lorch function defined as:

$$L(Q, \Delta_0) = \frac{sinQ\Delta_0}{Q\Delta_0} \qquad Eq.\,(2.1.6)$$

where $\Delta_0 = \frac{2\pi}{Q_{max}}$ defines the resolution of the radial distribution function (Lorch, 1969). In a diffraction experiment, all partial structure factors and their corresponding PDFs are summed up in a single diffractogram. In order to obtain information about the partials separately, it is necessary to modulate either c_α or b_α without modifying the system structure. Modulating c_α requires a change in sample composition, which is not possible without modifying the structure. Modulating b_α, on the other hand, is possible because of the tendency of different isotopes of the same element to scatter neutrons differently. However, not all isotopes are suitable for the implementation of this neutron diffraction with isotopic substitution (NDIS) method, as it requires a sufficient contrast between the scattering lengths of the two isotopes of the same element. In our case, we use the high contrast between the b_α values of different isotopes of hydrogen, ^{1}H and ^{2}H (D), to perform NDIS experiments (Pitteloud *et al.*, 2003).

The *first-order difference* of the total structure factor of samples with ^{1}H and samples with D leads to a partial structure factor where all contributions not involving H are cancelled out, given as:

$$\Delta_H(Q) = c_H\left(\overline{b}_H^2 - \overline{b}_D^2\right) + c_H^2\left(\overline{b}_H^2 - \overline{b}_D^2\right)[S_{HH}(Q) - 1] + \sum_{\alpha\neq H} 2c_H c_\alpha (b_H - b_D) b_\alpha [S_{H\alpha}(Q) - 1] \qquad Eq.\,(2.1.7)$$

Finally, the real-space pair correlation function $G_H(r)$ is then a weighted sum of the partial PDFs centered on H atom (Powell, Fischer and Skipper, 1998; Henry E. Fischer, Barnes and Salmon, 2006; Cuello, 2008):

$$G_H(r) = \frac{1}{2\pi^2\rho_n}\int_0^\infty \left[\Delta_H(Q) - c_H^2(b_H^2 - b_D^2)\right] Q^2 \frac{\sin Qr}{Qr} dQ \qquad Eq.\,(2.1.8)$$

$$= c_H^2(b_H^2 - b_D^2)[g_{HH}(r) - 1] + \sum_{\alpha\neq H}^{n} 2c_H c_\alpha (b_H - b_D) b_\alpha [g_{H\alpha}(r) - 1]$$

2.1.1. The D4c diffractometer and data treatment

D4c is a two-axis high-precision disordered materials diffractometer, which uses short-wavelength neutrons from the ILL's hot source to measure diffraction patterns over a large Q-range. D4c combines high counting-rate stability with very low background counts, and can be applied to study short and intermediate range order in liquid, amorphous and nano-structured materials: the neutron diffraction with isotopic substitution method can be used to obtain partial structure factors; Pair-Distribution Function (PDF) analysis of powder diffraction patterns can be utilized; and magnetic structure studies on very absorbent systems, such as those containing Gd, Eu can be used as well (Fischer *et al.*, 2002).

Instrument description: D4c shares the beam tube H8 with the IN1 Triple-Axis spectrometer, and Lagrange secondary spectrometer (described in section 2.2.1.) at ILL. The monochromator take-off angle is variable with $2\theta_M \approx 20 - 40°$. Three available monochromators are all horizontally and vertically focusing: Cu (220) for λ = 0.7 Å, Cu (220) for λ = 0.5 Å, Cu (331) for λ = 0.35 Å, with faces of 20 cm high and 23 cm wide. A high-transmission monitor located between monochromator and beam-defining slits are used for normalization to incident beam intensity. The samples are usually loaded in vanadium containers. After loading the samples are mounted in a cylindrical bell jar (Ø = 46 cm, 55 cm height) under vacuum, with a vertical and horizontal slits defining a maximum illuminated cross-section of 5 cm in vertical and 2 cm in horizontal directions (Figure 2.1.1.1).

The instrument has nine ^{3}He-gas 1D position-sensitive detectors, each containing 64 cells covering 8° in 2θ . A combination of at least two angular positions of detectors is required for a complete diffractogram, with a combination of 5-6 angular positions normally used to obtain good counting statistics. Generally, a counting statistics of 0.1% per 0.125° can be obtained in about 3 hours for a sample of average dimensions and scattering cross-section (Fischer *et al.*, 2002).

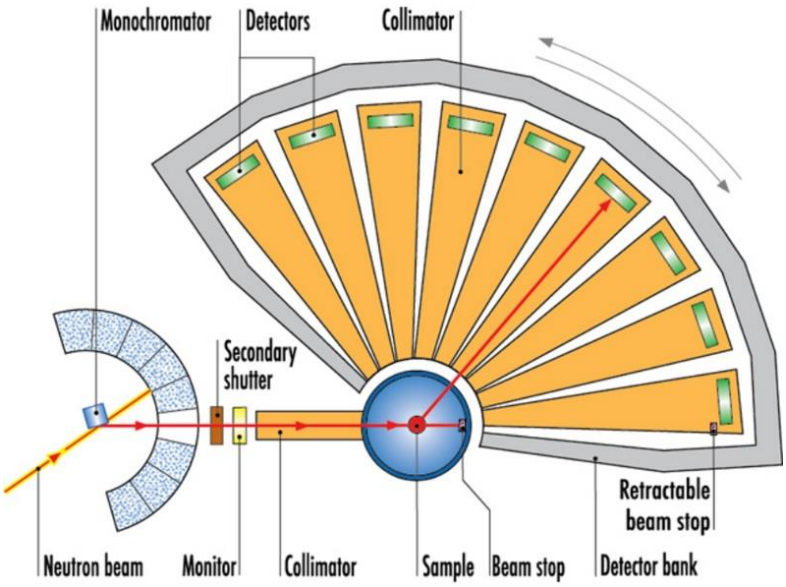

Figure 2.1.1.1. A schematic diagram of D4c instrument. Image taken from D4 description at www.ill.eu (Fischer *et al.*, 2002).

Data treatment: There are two types of corrections that are performed on the experimental data: one type of corrections is coming from the experimental conditions, and the other from the theoretical assumptions made to obtain structure factors (Cuello, 2008).

Here, we will briefly list the data treatment steps and programs used. Detailed descriptions of the data treatment protocol can be found in the primary sources (Howe, McGreevy and Zetterstrom, 1998; Cuello, 2008), and thesis by Rovira-Esteva (Rovira-Esteva, 2014).

1. The primary data treatment steps use d4creg software specifically written for D4c instrument:
- The data are corrected for *detector deadtime* (the minimum amount of time that separates two neutrons arriving at detectors so that they are recorded as distinct events);
- Then data are normalized to *monitor counts* (to correct small neutron flux fluctuations);
- A numor (NUMber Of Run) is the results of one recording with a single angular position. A single numor is an incomplete diffractogram, which needs to be grouped with others to cover the complete angular range. This is done by the program d4creg. In the case of volatile samples, or samples containing evaporable water (as C-S-H) the numors and pressure in the evacuated belljar are constantly checked to ensure accuracy of the measurement.
- The *errors* are calculated accounting for isotropic nature of liquid and amorphous materials. The concentric rings at the diffractogram affect the resolution of the measurement as a function of scattering angle.
2. Next steps aim at producing the comparable scattering functions in *absolute units*. Specially written software CORRECT (Howe, McGreevy and Zetterstrom, 1998) is used in following steps:

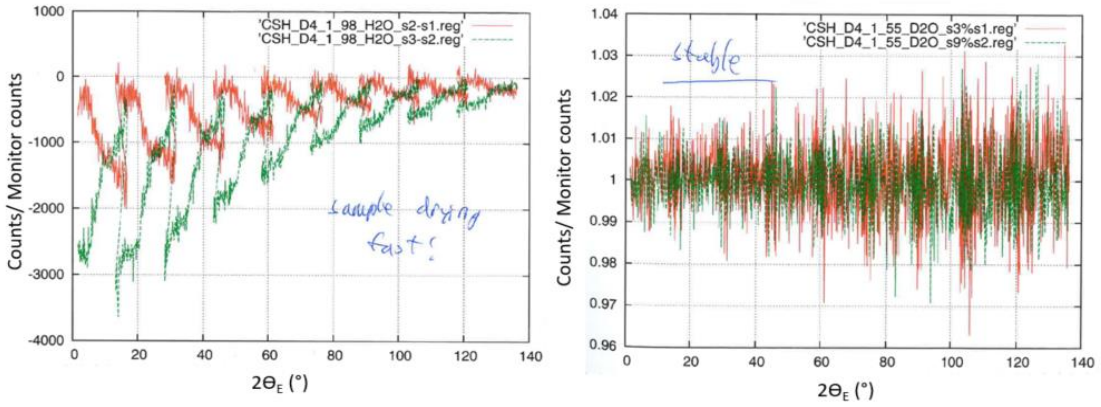

Figure 2.1.1.2. D4c experiment journal extracts of deuterated and hydrogenated C-S-H measurements.(left) An example from the experiment: The water from the sample was evaporating as seen by comparing numors of several runs due to bad sealing of the sample cell. The run had to be stopped, and the sample had to be re-loaded and sealed properly. The faulty numors were ignored, and only accurate numors were grouped for the final diffractogram (right) An example of a stable sample with no water evaporating (comments by H. Fischer).

- *Non-sample contributions* such as empty sample holder, empty instrument are removed from the total signal.
- *Attenuation and multiple scattering* are evaluated and subtracted from the experimental data. These effects come from the sample size being large enough for neutrons to be scattered or absorbed after the initial scatter of the sample.
- The correction for *instrumental resolution* are performed using vanadium rod, which has an isotropic and nearly completely incoherent cross section with few Bragg peaks, and should result in a flat diffractogram. In fact, the diffractogram is not flat due to the instrumental resolution. The ratio of the sample diffractogram over vanadium one results in the resolution corrected data. Then by using the cross-section of vanadium, the *normalization of the sample to absolute* values is done.
- *Scattering lengths* are corrected. The tabulated scattering lengths (Sears, 1992) refer to thermal neutrons, and D4c uses hot neutrons with slightly different values that are adjusted by CORRECT. The tabulated values offer bound scattering lengths for nuclei that are fixed and have no recoil effect. In reality the nuclei are never rigidly fixed and there is always some recoil effect taking place. Another variation is a free scattering length for free and rigid molecules. In our case, the scattering cross sections values for H and D were modified to account for 0.4963 Å (experimental neutron wavelength) neutrons and for the adsorbed and bulk pore water, which lie outside of neutron's coherence volume.
- Fullness of the cell is taken into an account by calculating *packing fraction* of the sample. Then, the normalization is done taking only proportional part of the measurement, and sample density.

3. Next steps require inelasticity corrections that come from breaking the static approximation. It works when the initial energy of neutron is much larger than the exchange energy between the scattered neutron and the nucleus. The approximation fails at higher scattering angles, where the energy and momentum exchange are much larger and samples with light atoms (i.e. H-containing) experience larger recoil effect.
   - *Placzek correction* (Placzek, 1952), named after George Placzek, relies on the assumption that the static approximation is the best fit. Therefore, the inelastic correction of the self term is performed by fitting a polynomial or Pseudo-Voigt function (in our case), and subtracting it from the corrected diffractogram. The resulting scattering function should not decrease at high Q values and should oscillate around $\frac{\bar{\sigma}_{scat}}{4\pi}$. It is possible to use Yarnell formula built in CORRECT, however in our case fitting a Pseudo-Voigt function worked the best. We should note that there are other ways of correcting inelasticity effects by assuming that the free nucleus is the best approximation, and can be looked up elsewhere (Powles, 1973).

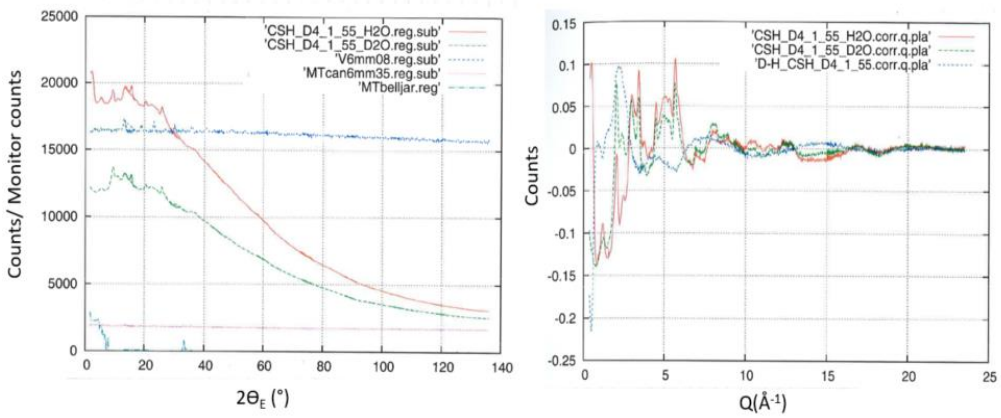

Figure 2.1.1.3. D4c experiment journal extract. (left) Resulting diffractograms after grouping the numors. For the NDIS experiment on powder, typically these measurements are done (starting from the top of the legend): deuterated sample, hydrogenated sample, vanadium rod, empty sample holder, empty instrument (belljar); (right) Scattering functions of deuterated and hydrogenated samples in Q after Placzek correction, and their corresponding difference.

4. Finally, after all corrections and normalizations are completed, the distinct part of the diffractogram should undergo *Fourier transformation (FT)*. We have used a custom-built Python script to obtain density function $G(r)$, an equivalent of pair-distribution function (PDF).

- To perform Fourier transform (Eq. 2.1.5) the scattering function must be integrated to infinity, meaning that the experimental Q values should reach infinity. This is impossible, as the maximum experimentally attainable Q value is related to incoming wavelength as $q_{max} = 4\pi/\lambda sin(\Theta_{\max})$. The experimental truncation of the scattering function leads to peak broadening in real space reducing the resolution, and it leads to spurious oscillations in $G(r)$ that interfere with real information about intramolecular distances. Therefore, the q_{max} values should be as high as possible, without however increasing noise, which also leads to false oscillations in the real space data.
- One way to minimize the false ripples coming from the finite q_{max} values is to apply a window step function, such as Lorch function shown in Eq. 2.1.6 (Lorch, 1969).

2.1.2. The SANDALS diffractometer

SANDALS (**S**mall **A**ngle **N**eutron **D**iffractometer for **A**morphous and **L**iquid **S**amples) is a time-of-flight diffractometer at ISIS Neutron and Muon Source. The instrument was designed to study the structure and bond distances in hydrogen containing materials.

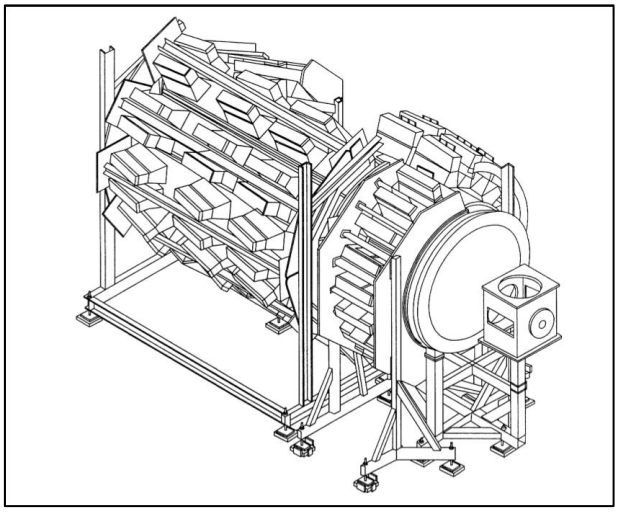

Figure 2.1.2.1. A schematic diagram of SANDALS instrument. Image taken from SANDALS instrument description page on www.isis.stfc.ac.uk

Instrument description: the instrument consists of 660 zinc sulphide scintillator detectors covering the angular range from 3° to 38° (Figure 2.1.2.1). The raw data is recorded as number of counts, where one count is equal to one neutron captured by the detectors. To minimize the background noise coming from the air, the beam collimation and the sample space are evacuated during data collection. The wavelength of the incident neutrons ranges from 0.05 to 4.95 Å, which gives access to a Q-range from 0.13 to 50 $Å^{-1}$. The resolution can reach up to 2% of $\Delta Q/Q$, which coupled with detector stability allows to perfrom isotopic substitution experiments reliably. Average measurement time for hydrogen containing samples is about 6-8 hours, slightly less for deuterated samples. The sample holders represent flat plate containers made of a 'null scattering' alloy of Ti and Zr (35 mm x 35 mm x 2 mm) (Soper, 2009).

Data treatment: The overall logic is similar to the treatment of D4c data, such as removing data from faulty detectors, correcting for attenuation and multiple scattering, and bringing the data to absolute units. The data are treated using Gudrun package (Soper, 2012), and the process is briefly reviewed here:

- The data from *faulty detectors* is removed automatically by using a 'purge' routine. The data by detectors are grouped and their standard deviation is calculated. The values that are too high or too low from the mean are deleted.
- Next the experimental data is corrected for *attenuation, multiple scattering, inelastic scattering, and absorption effects*. The cross-sections of hydrogen containing compounds have *wavelength dependence*, which is calculated using sample thickness (i.e. thickness of the TiZr cell), and an approximate density of the sample.

- The data are normalized to remove the effect of *incident flux fluctuations*.
- Then the data is converted to an *absolute scale* by using a vanadium standard.
- Finally, the *Fourier transform* of obtained $S(Q)$ to $G(r)$ function (Eq. 2.1.5) is done automatically by Gudrun. The method follows top hat evolution described by Soper (Soper, 2009). The idea is that the Q dependence of the background is corrected before the FT. The background is generated by a convolution of the data with the top hat function. All of these complex mathematical manipulations are calculated by automatically Gudrun. However, the user needs to choose the width of the top hat function, which can be tricky. Nowadays, it is possible to subtract the average value over specified Q-range, which in effect would be the same as setting top hat function width to infinity (Soper, 2012).

2.2. Inelastic Incoherent Neutron Scattering (IINS)

The neutron wavelength λ (Å) is described by the de Broglie relation:

$$\lambda = \frac{h}{mv} \qquad Eq.\,(2.2.1)$$

where h is Planck's constant and v is the neutron velocity, and k (Å^{-1}) is defined as:

$$k = \frac{2\pi}{\lambda} \qquad Eq.\,(2.2.2)$$

Therefore, the neutron momentum becomes $p = mv = \hbar k$, and the energy of neutron:

$$E = \tilde{\nu}\, hc = \frac{1}{2}mv^2 = \frac{\hbar^2 k^2}{2m} \qquad Eq.\,(2.2.3)$$

The key difference of neutron spectroscopy from infrared and Raman spectroscopies. The first one is related to the fact that the neutrons have mass. This makes that an inelastic neutron scattering is characterized by both the transfer of momentum $\boldsymbol{Q}$ (Å^{-1}) and energy E_T (cm^{-1}), which are defined as:

$$E_T = \hbar\omega = E_i - E_f \qquad Eq.\,(2.2.4)$$

$$\boldsymbol{Q} = \boldsymbol{k_i} - \boldsymbol{k_f} \qquad Eq.\,(2.2.5)$$

where i signifies the incident, and f signifies the final values.

The second key difference is the nature of the interaction. Unlike photons, which interact via electromagnetic coupling with the sample electrons, neutrons interact with the sample nuclei via strong interaction. The nature of this interaction makes that, unlike IR and Raman spectroscopies, INS technically has no selection rules.

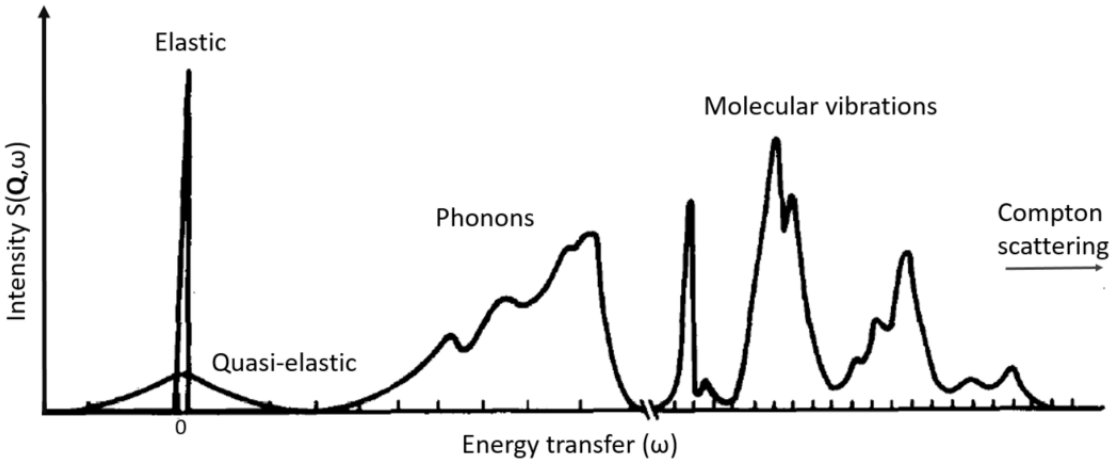

Figure 2.2.1. An example of generalized incoherent inelastic neutron scattering spectrum for a molecular crystal. Elastic scattering is a sharp peak at ω=0; quasielastic broad signal is centered at ω=0; phonons with rising intensity come from the external modes of the molecular crystal; the molecular vibrations come from the internal vibrational modes (adapted from (Eckert, 1992)*).*

Another advantage of INS method is that the intensity of the scattered signal, $S(\boldsymbol{Q}, \omega)$ an be computed given an accurate model (Sivia, 2011). Finally, the INS technique can access the energy ranges as in IR spectroscopy, with much finer detail in lower energies, and giving information about the dispersion of the modes (Mitchell *et al.*, 2005).

The interaction of neutron with nuclei can be considered a weak perturbation (Born approximation), to allow the use of Fermi's Golden Rule, which examines the transitions per unit of time. It states that the transition rate from the initial to the final state is proportional to the strength of the coupling between the initial and the final states of the system and to the number of ways the transition can happen, the density of final states. The number of transitions per second $W_{i\to f}$ is given as:

$$W_{i\to f} = \left(\frac{2\pi}{\hbar}\right)|\langle final\ states|V(r)|initial\ states\rangle|^2\rho_f \qquad Eq.\ (2.2.6)$$

Where ρ_f is the density of the final states. A more detailed description of the Fermi's Golden Rule applied for interaction of neutron with nuclei can be found elsewhere (Mitchell *et al.*, 2005).

In INS experiment, the measured intensity is proportional to the double differential cross-section, which is a number of scattered neutrons within energy range $d\omega$, and into a solid angle $d\Omega$. The expression for double differential cross section can be written in terms of the weak perturbation:

$$\frac{d^2\sigma}{dE_f d\Omega} = \frac{\sigma\, k_f 1}{4\pi\ k_i\ 2\pi\hbar}\sum_{jj'}\int_{-\infty}^{\infty} e^{i\boldsymbol{Q}.(R_j(t)-R_{j'}(0))}\, e^{-i\omega t}dt \qquad Eq.\ (2.2.7)$$

This way of describing double differential cross section is specific for the case of vibrational spectroscopy of hydrogenous molecular systems. Another useful way of expressing the double differential cross section is by introducing the scattering function (or dynamic structure factor) $S(\boldsymbol{Q}, \omega)$:

$$\frac{d^2\sigma}{dE_f d\Omega} = \frac{\sigma}{4\pi}\frac{k_f}{k_i}S(\boldsymbol{Q}, \omega) \qquad Eq.\ (2.2.8)$$

This relationship connects the observable experimental data (double differential cross section) to the dynamics of individual atoms in the sample (scattering function). The scattering function $S(\boldsymbol{Q}, \omega)$ is expressed in scaled units (y-axis) and only relative intensities are measured, due to the difficulties of obtaining absolute values in hydrogen signal dominant spectra (Mitchell *et al.*, 2005).

The actual scattering system is composed of different nuclei that scatter in different ways, i.e. possess different scattering lengths b (m). The inherent property of each nuclei b defines the strength of the interaction of nuclei with neutrons, and is related to the cross section as:

$$\sigma = 4\pi b^2 \qquad Eq.\ (2.2.9)$$

Depending on the nature of the scattering, the nuclei have coherent and incoherent cross-sections, which are expressed as:

$$\sigma_{coh} = 4\pi\langle b\rangle^2 \qquad Eq.(2.2.10)$$

$$\sigma_{inc} = 4\pi\langle b_{inc}\rangle^2 = 4\pi(\langle b^2\rangle - \langle b\rangle^2) \qquad Eq.(2.2.11)$$

The coherent scattering occurs when there is an interference between the scattered neutron waves from different nuclei. The incoherent scattering arises when the interference of scattered waves is disturbed by the natural isotope or spin mixture, and is expressed as a mean-square deviation from the mean potential.

$$\left(\frac{d^2\sigma}{d\Omega d\omega}\right)_{coh} = \frac{k_f}{k_i} b_{coh}^2 S_{coh}(\boldsymbol{Q},\omega) \qquad Eq.(2.2.12)$$

$$\left(\frac{d^2\sigma}{d\Omega d\omega}\right)_{inc} = \frac{k_f}{k_i} b_{inc}^2 S_{inc}(\boldsymbol{Q},\omega) \qquad Eq.(2.2.13)$$

The coherent scattering function is related to the G_d distinct-correlation between different atoms, and thus describes the collective excitations as:

$$S_{coh}(\boldsymbol{Q},\omega) = \frac{1}{2\pi\hbar}\iint G_d(\boldsymbol{R},t) e^{\{i(\boldsymbol{Q}.\boldsymbol{R}-\omega t\}} d\boldsymbol{R}dt \qquad Eq.(2.2.14)$$

The incoherent dynamical structure factor is related to the G_s time-dependent spatial correlation of an atom with itself, and describes the excitations of single atoms:

$$S_{inc}(\boldsymbol{Q},\omega) = \frac{1}{2\pi\hbar}\iint G_s(\boldsymbol{R},t) e^{\{i(\boldsymbol{Q}.\boldsymbol{R}-\omega t\}} d\boldsymbol{R}dt \qquad Eq.(2.2.15)$$

Finally, the generalized density of states (GDOS) can be expressed in a simplified form as:

$$GDOS \cong S_{inc}(Q,\omega)\frac{\boldsymbol{k}_f}{\boldsymbol{k}_i}\frac{\omega}{Q^2}\left\{1 - e^{\frac{-\hbar\omega}{k_bT}}\right\} \qquad Eq.(2.2.16)$$

where k_b is the Boltzmann constant and T is the temperature (Russo *et al.*, 2011). Since our spectra are dominated by the motion of hydrogen atoms, the equation (Berg *et al.*, 2017) can be written as:

$$GDOS \cong \frac{m}{k_bT}\left(\frac{\hbar\omega}{Q}\right) e^{\frac{-\hbar\omega^2}{k_BT}} S_H(Q,\omega) \qquad Eq.(2.2.17)$$

where m is is the mass of water molecule or of the individual H atom –depending on the nature of the vibration-, and $S_H(Q,\omega)$ is an experimental incoherent scattering function dominated by the motion of water molecules and hydroxyl groups.

2.2.1. IN1-Lagrange spectrometer

In inelastic neutron scattering both initial and final neutron energy have to be defined to calculate the energy transfer to the sample $\hbar\omega = E_i - E_f$, which is done differently for continuous and pulsed sources.

The **IN1-LAGRANGE** (**L**Arge **G**Raphite **AN**alyser for **G**enuine **E**xcitations) secondary spectrometer is a universal instrument that can study the molecular and lattice excitations in complex materials with energy resolution $\Delta E/E$ ~2-3%. It is located on a hot neutron beamtube H8 at ILL and shares the beam with D4c diffractometer (described in Section 2.1.1), and Triple-Axis spectrometer IN1.

The instrument works by space focusing of neutrons scattered over a very large solid angle, which are detected by small single ^{3}He gas detectors. The increased solid angle does not enhance the counting volume or the corresponding background. IN1-Lagrange is applied to studies of phonon dispersions in single crystals, and vibrational density of states in polycrystalline samples. The samples range from biological materials, to nanocrystalline powders, to complex molecular compounds, and especially hydrogen containing compounds.

Instrument description: The focusing reflecting surface of ~1 m^2 is built around the vertical sample-detector axis from pyrolytic graphite (PG) crystals that have a fixed energy of 4.5 meV (~36.4 cm^{-1}) (Figure 2.2.1.1). There are 612 crystal holders in total that are mounted on the solid mechanical structure so that the individual flat crystals are set tangentially to the calculated ellipsoid of rotation. The monochromators are shared between D4c, and the accessible energy ranges vary from roughly 5.5 meV to about 500 meV (44.4-4,040 cm^{-1}). In our case, we used three reflecting planes: Cu(220) with incident energies of around 27-500 meV (218.16-4,040 cm^{-1}), Si(311) reflection with incident energies in the range 16.5-200 meV (129-1,617 cm^{-1}), and Si(111) with energies around 5.5-20 meV (44.4-161.6 cm^{-1}) (Jiménez-Ruiz, Ivanov and Fuard, 2014).

The beryllium filter is installed immediately after the sample in order to remove higher-order harmonics in the analyzer reflections. Absorber containing boron is located in the sample-detector axis to remove the intense elastic scattering coming from the sample. The whole instrument is built similarly to triple-axis spectrometer, with a significant modification of having the fixed energy analyzer. The incident energies change step-by-step, similarly to triple-axis instruments, but the energy transfer is calculated by subtracting the 4.5 meV from the energy of incident monochromatic neutrons (Ivanov, Jimenéz-Ruiz and Kulda, 2014).

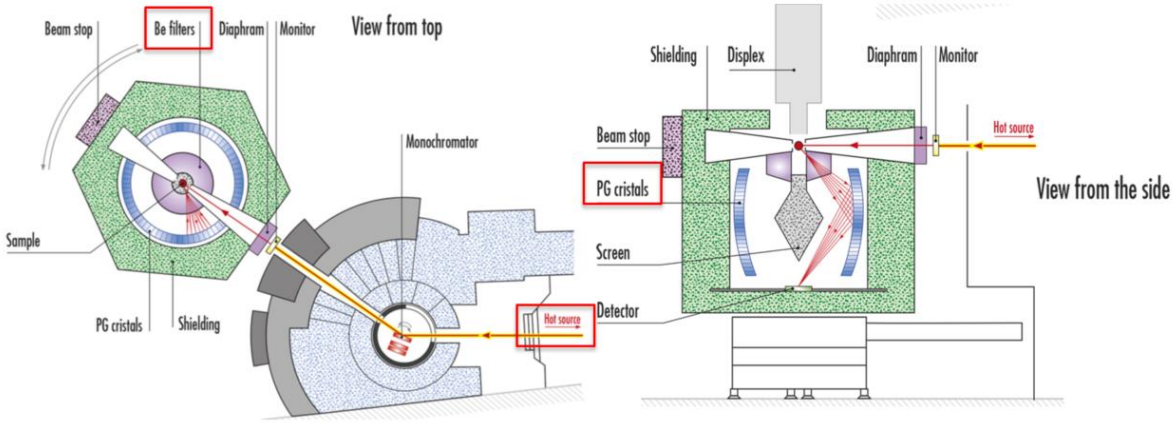

Figure 2.2.1.1. A schematic diagram of IN1-Lagrange spectrometer at ILL.

Data treatment involves several steps, which are done using LAMP (Large Array Manipulation Program) software (Richard, Ferrand and Kearley, 1996):

- The obtained spectra are normalized for monitor counts and corrected for monitor efficiency.
- The contributions coming from the sample holder (usually made from Al) and instrument are subtracted from the total signal.
- The intensity of collected spectra are corrected by water standard.

2.2.2. TOSCA spectrometer

In a pulsed source either initial or final energy have to be determined, usually by Bragg reflection from crystals or by chopping the beam in short time pulses close to the sample. There are two types of spectrometer geometries: direct and indirect (Lefmann, 2019). The measured intensity in the detector expresses the time dependence of the incoming spectrum. In vibrational spectroscopy large energy transfers with high resolution are necessary, which makes the indirect geometry spectrometers especially advantageous (Mitchell *et al.*, 2005).

TOSCA is an indirect geometry time-of-flight spectrometer located at the N8 beamline on ISIS pulsed spallation neutron source at the Rutherford Appleton Laboratory (Figure 2.2.2.1). An indirect geometry spectrometer, meaning that the sample is hit by a 'white' beam. Only neutrons with a particular energy are scattered by analyzer crystals to the detector. Therefore, the E_f is fixed and time-of-flight is used to determine the value of E_i (Lefmann, 2019). The spectrometer is 17 m away from the room temperature water moderator, and is illuminated by a pulsed polychromatic beam of neutrons. The advantages of TOSCA are the energy transfers reaching up to 8000 cm^{-1}, a very good resolution (especially up to 1500 cm^{-1}), and simplicity in handling, which makes it ideal for hydrogenous materials (Mitchell *et al.*, 2005).

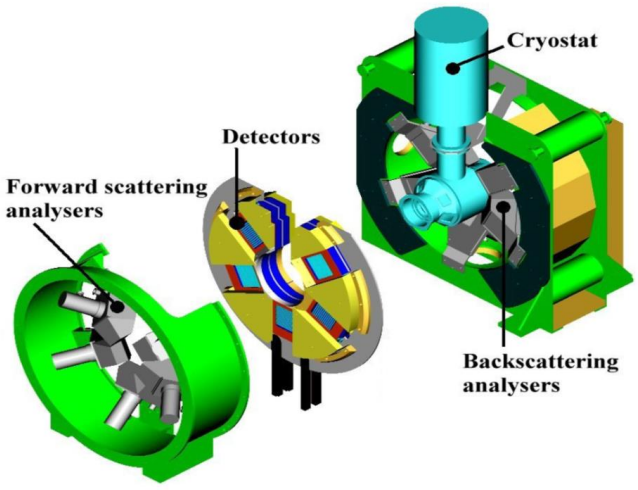

Figure 2.2.2.1. A schematic diagram of TOSCA spectrometer at ISIS. Image adapted from TOSCA manual (Ramirez-Cuesta, Parker and Tomkinson, no date).

Instrument description: The Scattered neutrons are Bragg reflected from a pyrolytic graphite analyzer (Figure 2.2.2.1). The final energy of 32 cm^{-1} (3.98 meV) is defined by cooled beryllium filter that also removes the higher order reflections beyond (002). This fixed final energy results in a direct

relationship between energy transfer (E_T, cm^{-1}) and momentum transfer (Q, Å^{-1}) such that $E_T \approx 16Q^2$. The detector array consists of ten banks with thirteen ^{3}He tubes with areas of 30 × 1 cm^2. Five banks are located in forward scattering (scattering angle 45°) and five in backscattering (135°). A disc chopper is positioned at 8 m from the moderator to prevent frame overlap. The spectral resolution is ~1.25% E_T coming from: the narrow bandpass of the PG002/Be analyser, tight moderator pulse widths (~10 μs/Å), a long incident flight path and a time- and energy-focused detector geometry (Parker *et al.*, 2014).

Data treatment: the raw data are converted to the energy transfer spectrum by the *ISISindirectEnergyTransfer* algorithm in Mantid software. Here is the brief description of steps, full version can be found on a website of Mantid (STFC, 2017), and thesis by (Pinna *et al.*, 2018).

- The data are loaded into the workspace, which produces a workspace per loaded run. The data in each workspace are chopped into single frames, this produces 4 workspaces containing all raw data, and 4 workspaces containing monitor values. Then 'chopped' runs are merged into one with an average signal.
- The noisy detectors' data is excluded from the data analysis. The data are corrected for monitor efficiency and scaled by a scaling factor defined in the parameter file.
- The artefacts arising from the peculiar shape of the incident spectrum are eliminated, and the normalized detector workspaces are converted to ΔE. Then the energy transfer data are corrected for final energy E_f.
- Finally, the resulting different workspaces are merged, averaged, and converted to ΔE in cm^{-1}.

2.3. Molecular dynamics simulations

Molecular dynamics (MD) is a simulation method in which the evolution of the movement of a group of particles is calculated over a certain period of time. The goal is to study the macroscopic properties of a system by understanding the structure and microscopic interactions within assemblies of atoms and/or molecules. This is done by applying the second law of classical Newton's equations of motions $\boldsymbol{F} = m\boldsymbol{a}$, where $\boldsymbol{F}$ is the force exerted on a particle, m is the mass of the particle, and $\boldsymbol{a}$ is the acceleration of the particle. Force is the second derivative of the position x with respect to time t, where velocity $\boldsymbol{v}$ is the first derivative of x with respect to time, which makes force equal to a first derivative of momentum $\boldsymbol{p}$ with respect to time.

$$\boldsymbol{F} = m\boldsymbol{a} = m\frac{d^2(x)}{dt^2} = \frac{d}{dt}\left(m\frac{d(x)}{dt}\right) = \frac{d}{dt}(m\boldsymbol{v}) = \frac{d\boldsymbol{p}}{dt} \qquad Eq.\,(2.3.1)$$

On the other hand, force is a negative first derivative of the potential energy U with respect to position x.

$$\boldsymbol{F} = -\frac{dU(x)}{dx} \qquad Eq.\,(2.3.2)$$

Combining Eq. 2.3.1 and 2.3.2 results in Eq. 2.3.3:

$$\frac{d\boldsymbol{p}_{x_i}}{dt} = -\frac{dU}{dx_i} \qquad Eq.\,(2.3.3)$$

where the rate of change of the momentum is equal to the negative rate of change of a potential energy. This equation is possible to solve analytically when it is applied for a one-dimensional system, however in the systems of N atoms (particles) with x, y and z coordinates, there are $3N$ coordinates with Eq. 2.3.3 for each coordinate. Therefore, it is impossible to solve it analytically, but it is possible to do so *numerically*. The steps that should be take are following:

1) The initial coordinates and velocities (i.e. momentum) should be assigned at $t = 0$. The initial coordinates for our model were taken from the X-ray structure of 14 Å tobermorite by Bonaccorsi (Bonaccorsi, Merlino and Kampf, 2005) with some defects introduced to derive the C-S-H structure. The positions of atoms determine the potential energy of the system.

The kinetic energy of the system is determined by the velocities of these atoms. Since the system is 3N dimensional, it should have 3N velocities: v_x, v_y, and v_z for every single atom. The initial velocities are assigned based on the direct proportionality between the kinetic energy $K = \sum_{i=1}^{N} m_i(v_{xi}^2 + v_{yi}^2 + v_{zi}^2)$ and temperature T of the system:

$$Nk_bT = \frac{N}{2}\left(\frac{1}{N}\sum_{i=1}^{N} m_i(v_{xi}^2 + v_{yi}^2 + v_{zi}^2)\right) = \frac{N}{2}\langle mv^2\rangle \qquad Eq.\,(2.3.4)$$

where k_b is a Boltzmann constant and m_i is the mass of the particle. Since $\langle mv_x^2\rangle = \langle mv_y^2\rangle = \langle mv_z^2\rangle = 3\langle mv^2\rangle$, Eq. 2.3.4 becomes:

$$|\bar{v}_{xi}| \approx \sqrt{\frac{2k_bT}{3m_i}} \qquad Eq.\,(2.3.5)$$

Random velocities are selected from Gaussian distribution centered at zero with sigma according to Maxwell-Boltzmann distribution. Then the velocities are rescaled to match a desired temperature of the system.

2) The potential energy and the gradient of the potential energy should be calculated. The potential energy is composed of non-bonded potentials, that are characterized using Lennard-Jones (first term in Eq. 2.3.6) and Coulomb potentials (second term in Eq. 2.3.6), and bonded potentials (Eq. 2.3.7):

$$U_{non-bonded} = 4\varepsilon\left[\left(\frac{\sigma}{r}\right)^{12} - \left(\frac{\sigma}{r}\right)^{6}\right] + \frac{Q_1Q_2}{4\pi\epsilon_0 r} \qquad Eq.\,(2.3.6)$$

where r is the distance between two interacting atoms, ε is a depth of the potential well, σ finite distance at which the inter-particle potential is zero, Q_1 and Q_2 are the charges, and ϵ_0 is the permittivity of free space. The Lennard-Jones function represents the short-range repulsion with an increase in energy as two atoms come closer, and the attraction at long-range interactions (Figure 2.3.1).

$$U_{bonded} = \frac{1}{2}\sum_{bonds} k_{ij}^{r}\left(r_{ij} - r_{eq}\right)^2 + \frac{1}{2}\sum_{\substack{bend\\angles}} k_{ijk}^{\theta}\left(\theta_{ijk} - \theta_{eq}\right)^2 + \frac{1}{2}\sum_{\substack{torsion\\angles}}\sum_{m} k_{ijkl}^{\phi,m}\left(1 + \cos(m\phi_{ijkl} - \gamma_m\right)^2 \qquad Eq.\,(2.3.7)$$

where the bonds are described by a harmonic term with $r_{ij} = |r_i - r_j|$ representing the separation between pairs of atoms in a molecule, r_{eq} is the equilibrium bond length, and k_{ij}^{r} is the bond force constant; the angle bend term is also described by a simple harmonic term, with θ_{ijk} representing the bond angle between two r_{ij} and r_{jk} bonds, and θ_{eq} is an equilibrium bond angle; the torsion angles term is represented by three connected bonds r_{ij}, r_{jk}, and r_{kl} (Allen, 2004).

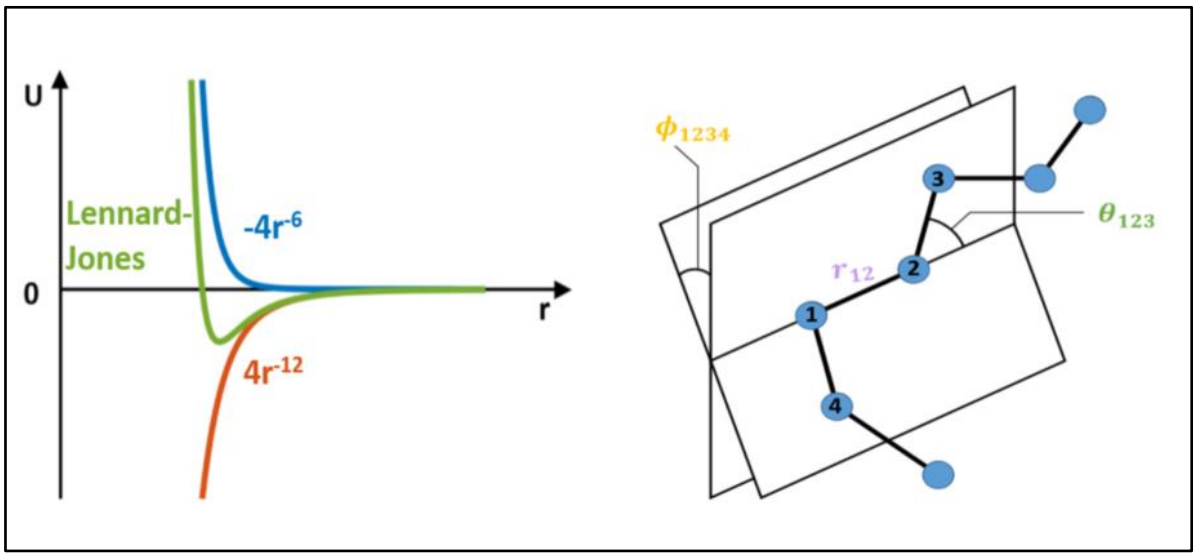

Figure 2.3.1. (left) Lennard-Jones pair potential with repulsive r-12 and attractive r-6 contributions; (right) Simple chain molecule showing the interatomic distance r_12, bend angle θ_123 , and torsion ϕ _1234. Images were adapted from (Allen, 2004) by Tutueanu Ana (for ILL seminar).

3) *The coordinates and the momentum* should be updated by the changed values for new time $t = t + dt$. To optimize these calculations some numerical integration algorithms are used. Verlet algorithm, based on Taylor expansion series, is one of the most used methods. The idea behind is that it is possible to calculate the change in the positions by using the 'past' time $t - dt$, instead of using the velocity. The positions and the velocities of the particles at a time $t + dt$ can be written as Eq. 2.3.8 and Eq. 2.3.9:

$$\vec{v}_i(t + dt) = \vec{v}_i(t) + \frac{d\vec{v}_i}{dt}dt + \cdots \qquad Eq.\,(2.3.8)$$

$$\vec{r}_i(t + dt) = \vec{r}_i(t) + \frac{d\vec{r}_i}{dt}dt + \cdots \qquad Eq.\,(2.3.9)$$

where the first derivative of the velocity is acceleration $\vec{a}_i(t)$, and the first derivative of the position is the velocity $\vec{v}_i(t)$. If Eq. 2.3.9 is written for 'future' time $t + dt$ and 'past' time $t - dt$, the summation of the two equations leads to the velocity terms being cancelled out:

$$\vec{r}_i(t + dt) = \vec{r}_i(t) + \cancel{\vec{v}_i(t)dt} + \frac{\vec{a}_i(t)dt^2}{2} \qquad Eq.\,(2.3.10)$$

$$\vec{r}_i(t - dt) = \vec{r}_i(t) - \cancel{\vec{v}_i(t)dt} + \frac{\vec{a}_i(t)dt^2}{2}$$

The resulting Eq. 2.3.11 allows to obtain the new positions of the particles at time $t + dt$ using only positions and accelerations at time t and $t - dt$:

$$\vec{r}_i(t + dt) = 2\vec{r}(t) - \vec{r}_i(t - dt) + \vec{a}_i(t)dt^2 \qquad Eq.\,(2.3.11)$$

The velocities can be calculated using new positions at time $t + dt$ from Eq. 2.3.11:

$$\vec{v}_i(t) = \frac{1}{2dt}[\vec{r}_i(t + dt) - \vec{r}_i(t - dt)] \qquad Eq.\,(2.3.12)$$

4) These steps *are repeated in a loop until the t approaches the final time* t_f, then the desired properties of the system can be computed (Frenkel, Daan, 2001). The dt is the timestep is constrained by the fastest movements in the system, typically, the vibrations of an H-containing atoms which occur in the range of 10 fs ($10x10^{-15}$ s). The simulation duration depends on the goals of the simulation: the vibrations occur in the range of 10 to 1,000 fs (in our case to compare to IINS data); the diffusion in the range of ns to μs (in our case the diffusion of water in ns scale).

A thermodynamic state of a macroscopic system is defined by number of particles N, temperature T, and pressure P, e.g. NPT. A microscopic state is determined by the atomic positions, and momenta, which are coordinates in 6N-dimensional phase space containing N atoms. One point in a phase space is denoted **Γ**. Since following a time evolution for large number of molecules is complex, instead an *ensemble* average, i.e. a collection of points **Γ** in phase space is used. The points are spread according to the probability density $\rho(\mathbf{\Gamma})$, which are defined by the macroscopic parameters NPT, NVT , NVE etc. (Allen and Tildesley, 1991).

- In *isothermal-isobaric ensemble* (NPT) the N, P, and T are fixed. It corresponds to a closed system that exchanges energy and volume with a large reservoir at a given T and P.
- In *canonical ensemble* (NVT) the N, V, and T are fixed. It corresponds to a closed system that exchanges energy with a large reservoir with a given T (thermal bath).
- In *microcanonical ensemble* (NVE) the N, V, and E are fixed. It corresponds to completely closed system with no exchange of energy or particles with the outside environment.

A computer simulation gives information at the microscopic scale, which is converted to a macroscopic scale using statistical mechanics. On a practical level, the MD simulations calculate time averages, and experimental observables are the ensemble averages. These two concepts are made equal in statistical

mechanics by using *ergodic hypothesis*, i.e. ensemble average $\langle A \rangle_{ens}$ equals time average $\langle A \rangle_{time}$. The meaning is that the system will pass through all possible states if the time is long enough or the number of microscopic configurations are sufficiently big (Allen and Tildesley, 1991).

The limitations of the MD simulations include:

- *Computational cost*: the MD simulations are time consuming, and the most computationally intensive part is the evaluation of potential energy and interatomic forces. In a N-atoms system the number of non-bonded interactions is proportional to N^2. The energy of interaction of two atoms that are far away from each other is not necessary, as at long distances the energy of interaction is close to zero as seen from the Lennard-Jones potential well (Figure 2.3.1). Define a cut-off distance, distance at which their potential energy of interaction is so small, that it can be neglected (usually about 3-5 times of interatomic diameter). However, this still leaves the problem of needing to calculate distances for all atom pairs in $x, y,$ and z dimensions $\frac{N(N-1)}{2}$ times. One of the ways to overcome this problem is to use *neighbors list algorithm*. The assumption is made that if the atoms are initially very far from each other, then probably they will remain this way for some time, so there is no need to waste the computational time on calculating the distances between them repeatedly. Instead, a list of potential neighbors is made for atom i by adding to r_c and 'skin' distance r_s. When the list of real neighbors is needed, then this list of potential neighbors is retrieved, rather than looping over all the atoms in the system (Rapaport, 2004).
- *Surface effects*: An average size of a MD simulated system studying C-S-H is ~1000-4000 atoms (3236 atoms in our CSH_1_55RH model) with a 2 to 5 nm cell sizes. The surface effects play a major role for such systems, since a significant amount of atoms will be on the surface. To prevent the surface effects a *periodic boundary condition* is used, when the atoms within a distance of a boundary interact with atoms in an adjacent copy of the system. If an atom leaves the simulation region from a particular side, it immediately reenters the simulation region through the opposite side.

Chapter 3 Water distribution in calcium silicate hydrates

3.1. Introduction

Total amount of water varying with Ca/Si

The water content in C-S-H and the variation of H_2O/Si as a function of the Ca/Si ratio have been a subject of discussion for years. The most reliable data were first compiled by Richardson (2014), and more recently by Qomi et al. (2020), among others (Cong and Kirkpatrick, 1995; Lothenbach and Nonat, 2015; Rodriguez *et al.*, 2015; Roosz *et al.*, 2016) (Figure 3.1.1). Most of these authors used TGA to determine the water content, with a few authors using ^{1}H NMR, SANS and/or WSI methods to probe the water distribution within the C-S-H pores. TGA is a most widespread method, as it is the simplest way to determine the total water content in a sample by monitoring its weight loss upon heating.

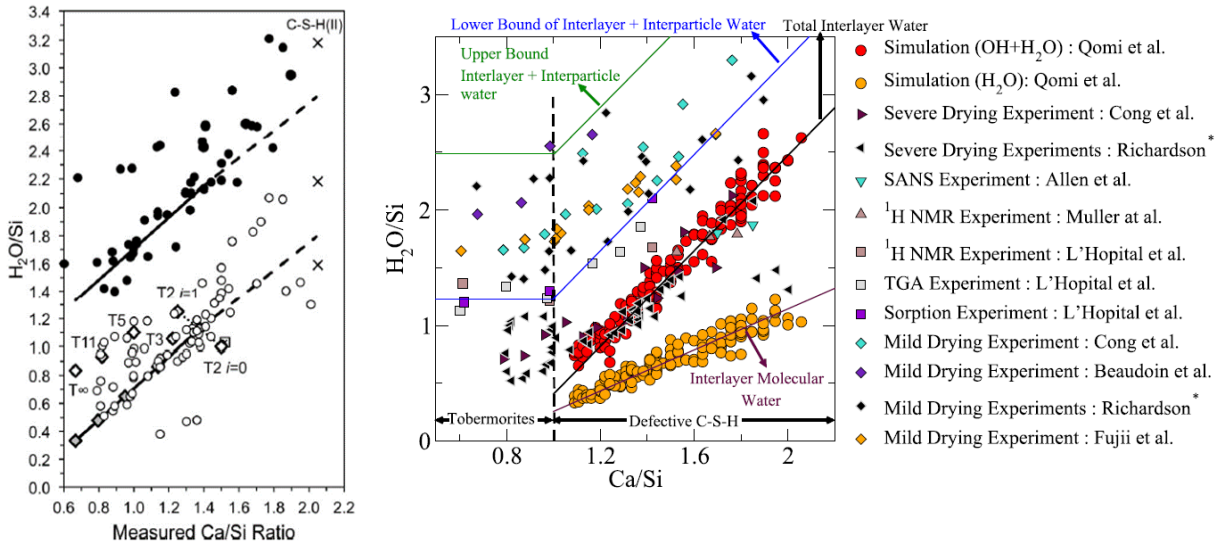

Figure 3.1.1. (left) Compilation by Richardson (2014) and (right) Qomi et al. (2020) showing the effect of calcium-to-silicon ratio on C-S-H's H_2O/Si.

The general trend observed in these experiments reflects an increase of the H_2O/Si with increasing Ca/Si ratio. Richardson referred to the samples at the upper boundaries as 'lightly dried', and lower boundaries as 'harshly dried' C-(A)-S-H samples. As it is clear from Figure 3.1.1 (left) the scatter along y axis is very large, with 'harshly dried' samples ranging from 0.3-2 H_2O/Si, and 'lightly dried' samples from 1.4-3.3 H_2O/Si. The average difference between the two boundaries is about 1 H_2O/Si. If we look at the results of computer simulations by Qomi et al. (2020), the difference becomes even larger (right panel, Figure 3.1.1). These discrepancies point towards the need of a careful use of these datasets, which may be referring to different types of water within the samples. In Table 3.1.1 the different synthesis routes, stirring or reaction times, drying methods, drying temperatures, and different temperature ranges used when determining water contents are summarized.

Table 3.1.1. The water content in C-S-H samples and the drying methods taken from the literature, and plotted in Figure 3.3.1.1.

Source	Actual Ca/Si	H_2O/ Si	TGA temp. range (°C)	Composition	Synthesis method	Drying method	Type of water
Renaudin et al. (2009)	0.82 0.98 1.08 1.24 1.4 1.59	1 1.7 1.7 1.7 2.1 1.9	r.t.-1100°C	$C_{0.8}SH_{1.0}$ $C_{1.0}SH_{1.7}$ $C_{1.1}SH_{1.7}$ $C_{1.2}SH_{1.7}$ $C_{1.4}SH_{2.1}$ $C_{1.4}SH_{1.9}$	20°C, 3 weeks, under N_2, washed with acetone upon filtration (time not indicated)	In a dessicator, under slight vacuum, over silica gel at r.t.	Non-evaporable water for H/S 1.3-1.5, evaporable for H/S ~2
L'Hopital et al. (2016)	>0.67 0.8 1 1.2 1.4 1.6	1.1 1.3 1.2 1.5 1.6 1.8	30-550°C	$C_{0.67}SH_{1.1}$ $C_{0.8}SH_{1.3}$ $C_1SH_{1.2}$ $C_{1.2}SH_{1.5}$ $C_{1.4}SH_{1.6}$ $C_{1.6}SH_{1.8}$	20°C, up to 1 year, under N_2, washed with 50%–50% water–ethanol, then with ethanol	Freeze-drying for 7 days, re-equilibrated to 30% RH in a desiccator until analysis	Total bound water
Cong et al. (1996)			r.t.-1000		Bottles shaken at water bath for 2 months at r.t., then at 40°C for 4 months under N_2 Hydration of β-C_2S	Dried under flowing N_2 at r.t.	Total water Water at 110°C
Fuji et al. (1981)	1.7 1.6 1.5 1 0.6	2.6 2.4 2.2 1.6 1.25	50-60 w%	$nCaO*SiO_2*(n+0.8)H_2O$, where $0.8 < n < 1.8$	Double decomposition of Na_2SiO_3 and $Ca(NO_3)_2$, stirred for 1 month at 20 or 50°C	Put in a filter press to squeeze out excess water.	
Beaudoin et al. (1990)	0.68 0.87 0.99 1.17 1.49 1.26	1.91 2.01 2.49 2.58 5.53 6.69			$Ca(OH)_2$ with Na_2SiO_3 at r.t. (stirring time not indicated); washed with acetone and ether.	Flushed with N_2 (for 4 days), and dried at 40°C for 24 hours.	
Allen et al. (2007)	1.7	1.8	SANS, SAXS	$(CaO)_{1.7}(SiO_2)(H_2O)_{1.8}$	0.4 w/c mass ratio, hydrated for 28 d in H_2O at 20 ◦C and sliced into thin coupons and submerged in the appropriate H_2O/D_2O fluid mixture for 24 h before measurement	-	All water physically bound within the internal structure of the particles, but no adsorbed or liquid water outside the particle boundaries.

Muller et al. (2012)	1.6	2	^{1}H NMR	Caz = 1.53(Si_y = 0.96, $Al_{(1\_y)}$=0.04)$O_{(z+y/2+3/2)}$ = 3.51(H_2O)x = 1.92	28-day-old paste cured underwater.		Excludes water on the outer surface of locally aggregated C–S–H sheets since "never dried" this water is in fast exchange with the gel pore water
Muller et al. (2012)			^{1}H NMR		Samples were stored in temperature - controlled room at 20 °C during hydration.	At 10 days the hydration was stopped by isopropanol exchange and freeze-drying. At 28 days, only isopropanol exchange was used	
Nemes et al. (2011)			QENS, INS	$C_{1.7}SH_y$ y =3.9 ± 0.6 at RH 100% and y = 2.5 ± 0.4 at RH 11%	The C_3S was cured at 20 °C for 28 days	The cured cement paste was crushed to powder and dried at RH ranging from 6% to 100% for 3 weeks. drying at 105 °C under N_2 for 3 weeks, vacuum drying, D-drying treatment, and immersing in deuterated isopropanol (IPA)	Different distribution of water depending on the RH of the sample

The data from Beaudoin et al. (1990) were obtained from C-S-H samples dried at mild conditions, under N_2 flow and then at 40°C for 24 hours. Therefore, their samples contain higher amounts of water per Si and fall in the uppermost boundaries of the Figure 3.1.1. It should be noted that the values for the two Ca/Si of 1.49 and 1.26 contain much larger amounts of water, 5.53 and 6.69, respectively, and are not shown on Figure 3.1.1 for visualization purposes. These two outliers demonstrate that the C-S-H can adsorb much higher amounts of water, than generally reported. Overall, the lower Ca/Si=0.7 contains between 0.7 to 1.9 H_2O/Si, with high Ca/Si≥1.7 containing from 1.46 to 3.2 H_2O/Si. It was noted by many authors that lower Ca/Si ratio C-S-H contains amorphous silica, while higher Ca/Si have some portlandite inclusions, both of which affect the Ca/Si.

In case of Cong and Kirkpatrick (1996), the samples were 'lightly' dried by N_2 flow at room temperature (r.t.). The authors report the amount of water at 110°C, and the total amount of water. Thus, their data falls in two ranges: total water for 'lightly' dried samples, which falls in the upper boundaries in Figure 3.1.1, and >110°C for 'harshly' dried samples, which is at the bottom of the graphs. The so-called 'harshly dried' C-S-H samples mainly contain interlayer water, and make up the lower boundaries of the plots.

The data by Allen et al. (2007) and Muller et al. (2012) report the water content of a fully hydrated interlayer obtained with SANS and ^{1}H NMR methods, respectively. The use of SANS allowed determining the water content of C-S-H nanoparticles excluding any exterior water, and the use of ^{1}H NMR probed the water content of the fully hydrated interlayer of the C-S-H sample. The data that fall in between the driest and the wettest samples were gently dried, as in the case of Renaudin et al. (2009) who dried the samples in a dessicator at room temperature; or as in the case of L'Hôpital et al (2016), who freeze dried and then conditioned at 30% RH. We should also note that the TGA temperature ranges reported are different for each case. Usually, the total water content is reported for the weight loss from ~r.t. to ~1000°C (Cong and Kirkpatrick, 1995; Renaudin *et al.*, 2009; Roosz *et al.*, 2016). Sometimes, the maximum temperature is 550°C (L'Hôpital *et al.*, 2016) or not reported at all (Fujii and Kondo, 1981; Beaudoin, Ramachandran and Feldman, 1990).

Richardson explained the observed increase in H_2O/Si with increasing Ca/Si ratio by the presence of tetrahedral sites, a reduced number of hydroxyl groups and the introduction of interlayer Ca^{2+}(Richardson, 2014). L'Hôpital et al. (2016) explain in a similar way the increase of the H_2O/Si at high Ca/Si ratio by the presence of calcium hydroxide. They report the decrease of H_2O/Ca with increasing Ca/Si, and a constant water content of 18±1 wt.% in their samples (L'Hôpital *et al.*, 2016), which is very similar to our 'dry' C-(A)-S-H samples (Section 3.3).

In overall, the total amount of H_2O per Si in relatively dry C-(A)-S-H samples is known to increase with rising Ca/Si ratios. Some authors showed the decrease of H_2O per Ca with increasing Ca/Si ratios(L'Hôpital *et al.*, 2016), and a constant weight fraction of total water regardless of Ca/Si ratios (Beaudoin, Ramachandran and Feldman, 1990; Cong and Kirkpatrick, 1995; L'Hôpital *et al.*, 2016). Our results agree with these conclusions, as it will be shown in Section 3.3. In addition, we note that in the samples conditioned at high RH levels (>95%), the equilibration time becomes a major factor of total water amount (Badmann, Stockhausen and Setzer, 1981; Odler, 2003).

Classification and distribution of water

According to the International Union of Pure and Applied Chemistry (IUPAC) classification of pore sizes, the range of the micropores falls in sizes smaller than 2 nm (20 Å), mesopores range from 2 to 50 nm, and macropores have sizes larger than 50 nm (Thommes *et al.*, 2015). It is a consensus that the pore volume in cement paste exceeds the water volume. Water is easily removed from the pores, with larger pores being the easiest to escape from, and is easily adsorbed depending on the RH levels (Bordallo, Aldridge and Desmedt, 2006). Various techniques have been used to estimate pore sizes and distribution, such as N_2 and H_2O sorption isotherms (Pinson *et al.*, 2015; Maruyama *et al.*, 2018, 2019), ^{1}H NMR(Muller *et al.*, 2013; Wenzel *et al.*, 2017), and SANS (Allen, Thomas and Jennings, 2007) methods.

The water sorption isotherm method from Pinson et al. (2015) allows differentiating between: 1) interlayer spaces of ≲1 nm size; 2) gel pores of about 1 to 10 nm size; 3) capillary pores > 10 nm size, which are empty at RH 85% and lower. The pores between 10-100 nm can fill only at RH close to 100%, and are represented by a thin shell of adsorbed water (Pinson *et al.*, 2015). The ^{1}H NMR experiment can distinguish three pore sizes: interlayer pores of about 1 nm width; gel pores of about 2-5 nm width, and interhydrate pores of roughly 10 nm (most probably not part of C-S-H) (Valori, McDonald and Scrivener, 2013). Thus, the overall distribution of pores in cement and C-(A)-S-H can be summarized as following: 1) interlayer pores of about 1 nm size, mostly found in the C-(A)-S-H phase; 2) gel pores ranging from 2 nm to 5-8 nm, found between the C-(A)-S-H platelets (globules); 3) capillary pores ranging from 8-10 nm to few μm sizes, where water is in a bulk liquid-like state and capillary effects take place. In the C-(A)-S-H phase probably the majority of the capillary pores is less than 10 nm width pores.

Many authors classified different types of water in C-(A)-S-H based on the pore size distributions. One of the earlier classifications was proposed by Taylor (Taylor, 1986a). This author classified different types of water in the cement phase by assuming that structural hydroxyl groups are a part of total water content. The author applied the Feldman-Sereda model (Feldman and Sereda, 1970) of joining stacked C-S-H to differentiate between five types of water: 1) water in intercrystallite pores, which are formed by merging interlayer spaces into micropores. Taylor does not give the size of these pores, but from the schematic drawing in the manuscript it looks like the gel pore water is located in between the stacked C-S-H nanoparticles/platelets; 2) water in the gel, found in the layers and/or in the interlayers. By 'gel' here Taylor most probably implied a nanoparticle/platelet of C-S-H, thus referring to intra- and interlayer waters; 3) adsorbed or monolayer water found on the surfaces of micropores; 4) water in micropores, and 5) water in larger pores. The first three are classified as bound water, i.e. water that at r.t. and 10% to 90% RH do not form part of the pore solution (Taylor, 1986a).

A more recent classification by Pinson et al. (2015) based on water sorption isotherms provide a more detailed view. The authors include:

- The *interlayer water,* all the water in the interlayer spaces with width ≲1 nm, specifically water in contact with with atomistically rough surfaces built from silicate tetrahedra with nonhydroxylated dangling oxygen atoms. The authors report the RH value of 20% below which it is possible to remove interlayer water, and they suggest that mechanical disjoining effect is dependent on shrinkage and swelling of the interlayer space.
- *Gel pore water* found in pores of 1-10 nm range.
- *Capillary pore water* in pores larger than 10 nm, where capillary condensation leads to a hysteresis behavior.
- *Surface adsorbed water* in empty pores present as a thin layer on the pore walls. The authors suggest that this water determines shrinkage because it affects the surface energy of the solid-pore interface.

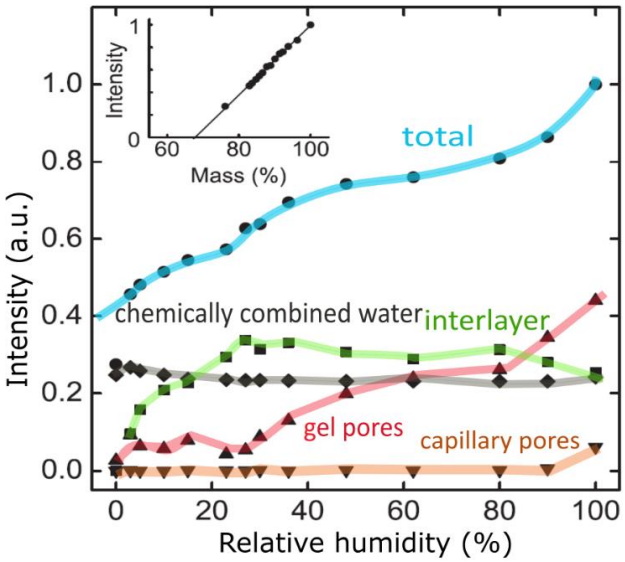

Figure 3.1.2. Pore-size resolved desorption isotherm in white cement paste (cured underwater for 28 days, w/c=0.46) calculated from NMR analysis over progressive drying. Reprinted and adapted from Muller et al.(Muller *et al.*, 2013)

The same way as for pore classification, water in the cement / C-S-H pores can be classified in many ways. There are several points of debate about the sizes of gel pores and therefore the nature of gel water; about the adsorbed interfacial water having properties different from the confined water and from the bulk water; about interlayer water including 'structural' water and/or structural hydroxyls etc. A difficulty with these classifications lies also in the constant exchange and interdependence of different types of water between each other. A clear example of a dependence of total water content and constituting water types was provided through ^{1}H NMR experiments (Muller et al., 2013). The authors followed the evolutions of T_2 relaxation signals for a sample with decreasing RH levels and noted that the total water diminished steadily as RH decreased.

The capillary pore water started emptying from 90% RH and lower. The gel pore water decreased in the same manner as the total water, emptying up nearly completely at 25% RH. The authors suggested that surface water in a full gel pore rapidly exchanged with the pore water, thus resulting in the same signal (longer T_2). Close to 25% RH the gel pore was nearly empty, but the monolayer of immobile surface water was still present, which had the same signal (shorter T_2) as interlayer water. Hence, a slight increase of interlayer water intensity over the same RH range was observed. As RH was below 25%, the interlayer water signal declined with an acceleration at around 10% RH (Muller *et al.*, 2013). ^{1}H NMR experiments showed that capillary water in gel pores interchanges with interlayer water. Upon evaporation of adsorbed interfacial water, a monolayer of interfacial adsorbed water has the same signal as interlayer water.

All these previous results put in evidence some ambiguities when it comes to distinguish different water types in the cement paste and C-S-H. In this thesis, we have decided to apply the model described by Bourg and Steefel, in which the pore size can be used to determine the type of and distribution of water (Bourg and Steefel, 2012).

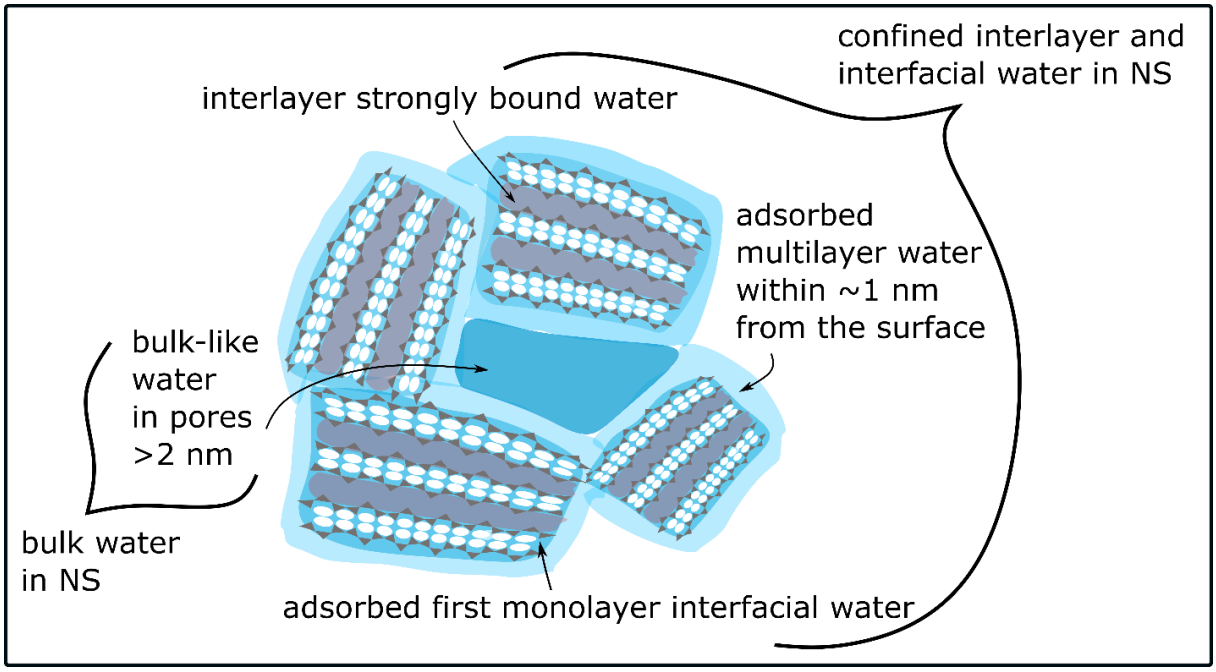

Figure 3.1.3. A schematic representation of different water types present in the C-(A)-S-H phase based on Bourg and Steefel model (Bourg and Steefel, 2012)*, and the types of water probed by Neutron Scattering (NS).*

These authors showed that water in the center of pores of sizes 2-20 nm in diameter behaves as bulk liquid-like water, unlike water from ~ first 3 monolayers of interfacial water, which behaves differently. In pores smaller than 2 nm, the bulk-liquid core is absent due to the strong electrostatic interactions with both interfaces (Bourg and Steefel, 2012). The same conclusions were reported by Badmann et al. (Badmann, Stockhausen and Setzer, 1981) based on WSI results and chemical potential calculations. The authors found that 2 nm sized pores are the limiting pore size at which the wall effects become too strong, and capillary condensation cannot take place. The results of ^{1}H NMR experiments by Muller et al. showed that the signal of strongly bound monolayer water is indistinguishable from the signals of interlayer water (Muller *et al.*, 2013).

The structural and dynamical characteristics of water were probed using a combination of neutron scattering techniques, complemented with molecular dynamics simulations. These techniques, in particular the inelastic incoherent neutron scattering (IINS) technique, probe the vibrational dynamics of water, offering a new, complementary perspective to that offered by ^{1}H NMR and other characterization methods that have been used in the literature. In particular, the IINS technique allows recognizing collective properties of water, such as lattice modes, which are characteristic of water in its liquid state, where it adopts a nearly-tetrahedral coordination. These modes are attenuated when water is coordinated close the interfaces, and the vibrational modes adopt a different, characteristic spectrum.

The schematic drawing of water in C-(A)-S-H is shown in Figure 3.1.3, where the types of water are grouped according to sensitivity of the IINS technique. In the following sections, a characterization of the water distribution in C-(A)-S-H samples with increasing RH levels and Ca/Si ratios is provided. The of this chapter is to determine the water content in C-(A)-S-H samples used for the NDIS (Chapter 4) and IINS (Chapter 5) experiments, and its distribution in the different pores.

3.2. Materials and methods

3.2.1. Sample preparation

Figure 3.2.1.1. A wet glove-box used for synthesis, conditioning, and storing C-S-H samples at the geochemistry laboratory, ISTerre.

C-S-H samples of varying Ca/Si ratios (Table 3.A.1, Appendix) were synthesized by reacting calcium oxide and fumed silica in water inside a N_2 wet glove-box. Calcium oxide was obtained by calcination of $CaCO_3$ (Sigma-Aldrich, Fluka, Bioultra) at 1000 °C for 18 h and stored in a vacuum desiccator until usage. Fumed silica SiO_2 (Sigma-Aldrich, Aerosil 200) was placed in an oven at 40°C for ~24 h to remove physisorbed water prior to each experiment. Deionized water was boiled and degassed with N_2 gas to remove all dissolved CO_2. The quantities of calcium oxide and fumed silica required to prepare C-S-H of predetermined stoichiometry were calculated using the method reported by Haas and Nonat (Haas and Nonat, 2015).

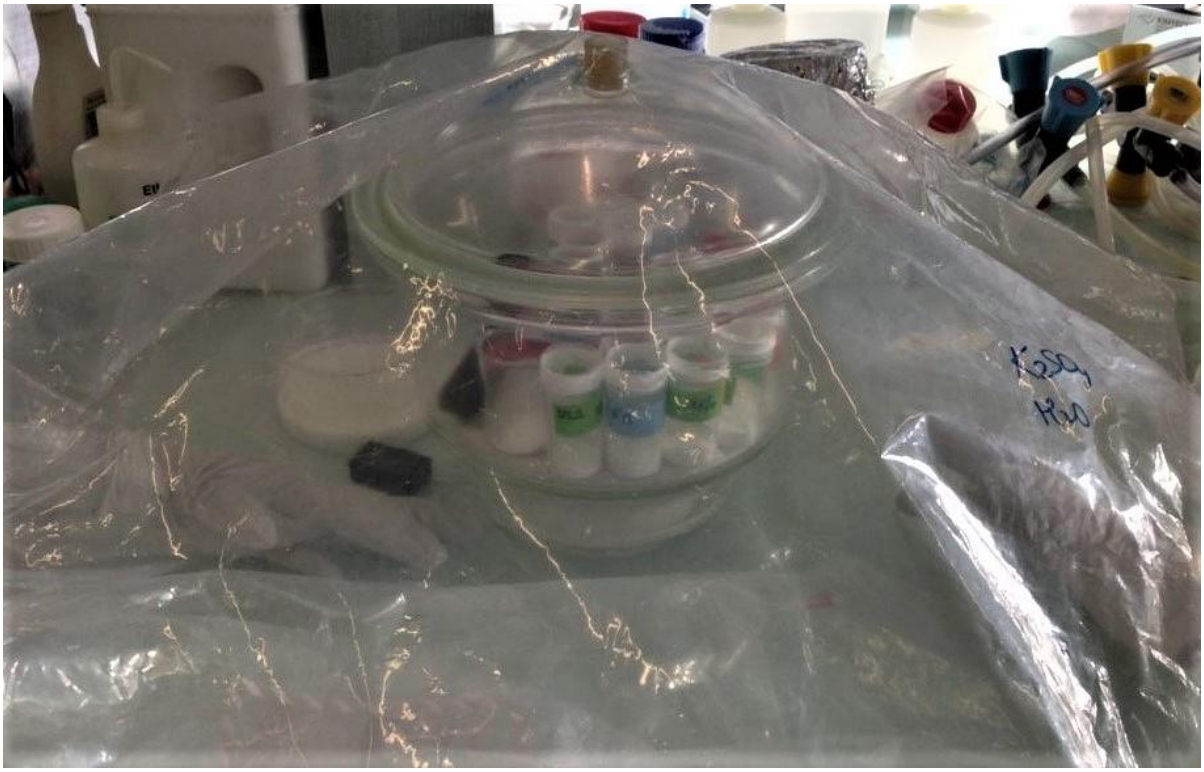

Figure 3.2.1.2. An example of C-(A)-S-H samples conditioned under certain RH atmosphere. The desiccator with a salt solution was put in the glove-bag with a salt solution. The hygrometers were kept inside the desiccators and the glove-bags to check the RH values.

Samples were reacted under stirring conditions for ~1 month in High Density Polyethylene (HDPE) bottles inside a wet N_2 glove-box, then filtered using Millipore® filter paper (0.22 μm, GSW1 UM), and wet C-S-H residue was left to dry inside the glove-box for ~12 h. A part of these C-S-H samples was put aside to have a 'fully-hydrated' C-S-H. The remaining C-S-H was oven-dried at 40 °C in a vacuum oven for ~24 h. A part of these samples was put aside to have 'oven-dried' C-S-H. After drying, samples were conditioned at controlled RH of 55%RH (CSH with Ca/Si 1, 1.2, 1.27, 1.33, and CASH with Ca/Si 0.9, 1.1) for ~ 1 week for C-S-H samples, and ~ 1 month for C-A-S-H samples using saturated salt solutions of $Mg(NO_3)_2{\cdot}6H_2O$.

The rest of the samples were conditioned under 98% RH using saturated salt solutions of K_2SO_4 for ~1 month for CASH samples, and ~ 1 week for CSH samples (schematically drawn on Figure 3.2.1.3). Then samples conditioned at 98%RH were stored inside the vacuum desiccators containing silica beads, to remove any adsorbed and bulk water. We refer to these samples as 'desiccator-dried' samples. As samples are sensitive to atmospheric CO_2, all synthesis and conditioning processes were performed under an inert gas atmosphere of N_2. The C-A-S-H samples with Ca/Si=0.9, and Al/Si=0.1, were synthesized following the protocol that can be found elsewhere (Roosz *et al.*, 2018). We note that any future experiments involving water adsorption in C-(A)-S-H should be done in the same timeframe to eliminate the equilibration time effect.

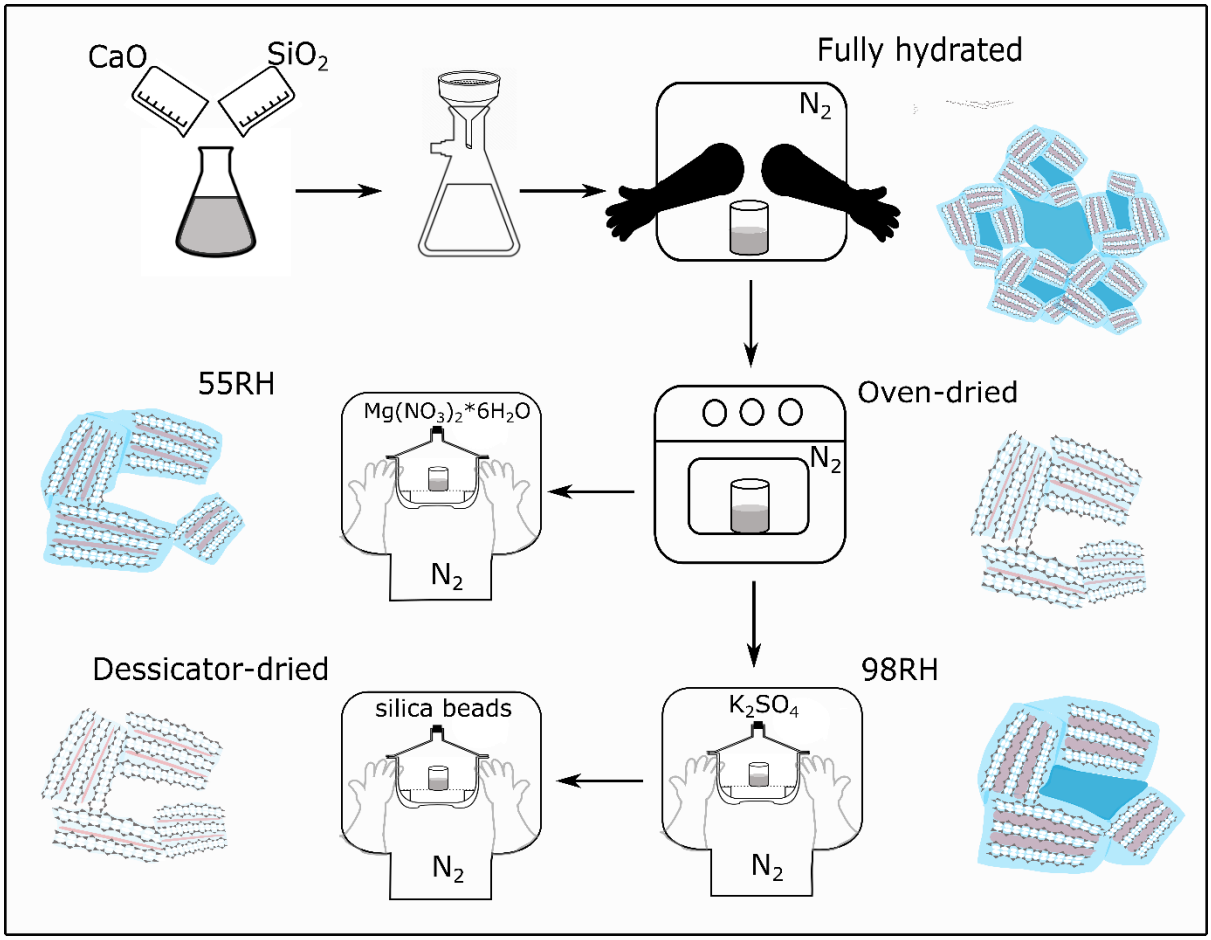

Figure 3.2.1.3. Schematic drawing of a synthesis protocol and a schematic representation of C-(A)-S-H samples of varying water content. Light blue is interfacial adsorbed water, red is interlayer water, and dark blue is bulk water.

Following these conditioning protocols, we obtained C-S-H samples labeled CSH_Ca/Si_%RH, where %RH is the relative humidity value at which they were conditioned. The C-A-S-H samples were labeled CASH_Ca/Si_%RH. In the text we refer to 'wet' and 'dry' C-(A)-S-H samples. The 'wet' include fully-hydrated and 98% RH samples; 'dry' refer to 55% RH, dessicator-dried, and oven-dried samples.

3.2.2. Inductively coupled plasma - atomic emission spectrometer (ICP-AES).

Ca/Si ratios were determined using ICP-AES (Varian 720ES Agilent). The C-S-H particles (5-10 mg) were dissolved by adding concentrated 14M HNO_3 (distilled) and 28M HF (47-51%, Trace Metal™, for Trace Metal Analysis, Fisher Chemical) acids, followed by heating the solution for ~24h at ~80°C. The final step involved diluting with boric acid and ultrapure water prior to the measurement.

3.2.3. Water adsorption volumetry

Water adsorption isotherms were obtained at 25 °C using a Belsorp-Max instrument by BEL JAPAN Inc.III. A long acquisition time of at least 2 weeks was required due to the slow equilibrium kinetics. Prior to the measurements, all samples were outgassed at 50 °C for 24 h under a residual pressure of

4.652×10^{-5} Pa. The classical Brunauer–Emmett–Teller (BET) theory was used to analyze the isotherms and derive the specific surface area (SSA) (Brunauer, Emmett and Teller, 1938).

3.2.4. Thermogravimetric analysis

Thermogravimetric analysis (TGA, Mettler-Toledo TGA-DSC3+) was used to examine the thermal decomposition and the water content of the C-S-H and C-A-S-H samples. The samples were analyzed at a heating rate of 10°C/min up to 600°C in a N_2 environment with a flow rate of 20 mL/min. The final temperature was dictated by the melting point of Al crucibles, which is however sufficient to evaporate all water and portlandite from the samples (portlandite dehydroxylation occurs around 450°C (Jansen *et al.*, 2018). Thus, the total water included all evaporated mass from 25-600°C.

Figure 3.2.4.1. (left) Sealing press for Al crucibles for thermogravimetric analysis with Al cell and a cap (right) after the crucible was sealed.

The samples were loaded in aluminum crucibles and were hermetically sealed with aluminum caps (Figure 3.2.4.1) inside a glove-box or a glove-bag, filled with N_2 equilibrated at the same RH used to condition the sample. The sample mass used for TGA analyses varied between 8 and 30 mg.

3.2.5. X-Ray diffraction

Synchrotron X-Ray diffraction

Synchrotron XRD measurements for the C-S-H samples were performed at the ID31 beamline of the European Synchrotron Radiation Facility (ESRF) in Grenoble, France. Prior to analysis, C-(A)-S-H samples were loaded into 1.5 mm (ID31) polyimide capillaries (Figure 3.2.5.1, left), inside the glove-bags or wet glove-box at the same RH values. The capillaries were closed on both ends using a two-parts epoxy adhesive.

At the ID31 beamline, a monochromatic X-ray beam of 78 keV (λ = 0.159 Å) was used to obtain scattering patterns of C-S-H samples. The data sets were collected by using a Pilatus 2M CdTe detector placed at a sample-to-detector distance of d_1 = 1.226 m to obtain scattering patterns with a Q range of 0.1-6.2 $Å^{-1}$, allowing the measurement of the Bragg peak corresponding to the interlayer distance of C-S-H. Data were automatically corrected for internal dark current. Two-dimensional images of the scattered intensity were azimuthally integrated using the pyFAI software package (Kieffer and Wright, 2013). The pattern from the empty capillary was subtracted as a background.

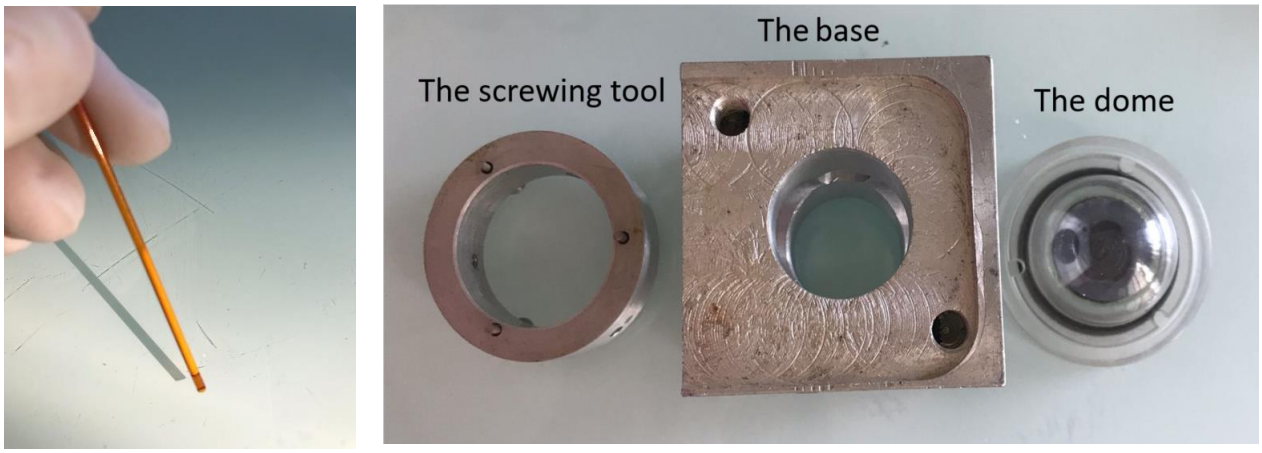

Figure 3.2.5.1. (left) An example of the polyimide tube filled with C-(A)-S-H sample used for synchrotron XRD measurements; (right) Laboratory X-ray diffraction tools and dome sample holder used to prevent CO_2 from carbonating the C-(A)-S-H during the measurement.

The C-A-S-H samples were measured at the 11-ID-B beamline at the Advanced Photon Source, Argonne National Laboratory. The samples were analyzed with a monochromatic X-ray beam of 58.6 keV (λ = 0.2115 Å). The data were collected with a Perkin Elmer XRD 1621 N ES detector and sample-to-detector distance of d = 0.799 m to access a Q range of 0.2-10.4 $Å^{-1}$. Data were automatically corrected for internal dark current. Two-dimensional images of the scattered intensity were azimuthally integrated using the GSAS II software package (Toby and Dreele, 2013).

Laboratory X-Ray diffraction

The XRD patterns of some C-S-H samples (CSH_1.2, 1.26) were recorded with a Bruker D8 powder diffractometer at ISTerre Geochemistry Laboratory. The diffractometer is equipped with a SolXE Si(Li) solid state detector from Baltic Scientific Instruments using CuKα radiation. Intensities were recorded at 0.026° 2-theta step intervals from 5 to 90° (10 s counting time per step). The average measurement time was about 16 hours. A special custom-made dome sample holder was used inside the glove-box or glove-bags to prevent carbon dioxide reacting with the C-(A)-S-H powders (Figure 3.2.5.1, right). Eva Bruker software associated with ICCD pdf database was used to determine the modal composition of powder.

3.3. Results and discussion

3.3.1. Variation of water content with Ca/Si

Total water amount as a function of Ca/Si

Here we present water content and distribution in samples with varying Ca/Si ratios and containing five different water amounts and distributions. The relative amount of water per Si is presented in Figure 3.3.1.1. Nominally, we distinguish between 'dry' C-S-H and 'wet' C-S-H samples by their water content. The 98RH and fully hydrated samples are the 'wet', while 55RH, desiccator-dried and oven-dried samples are referred to as 'dry' samples. In a good accordance with literature, the H_2O/Si rises with increasing Ca/Si ratios for increasing RH levels. The difference between the 'driest' samples, desiccator-dried, and the 'wettest' -fully hydrated-, is about 1.2 water per silicon, close to ~ 1 H_2O/Si reported in the literature (Richardson, 2008; L'Hôpital *et al.*, 2016; Gaboreau *et al.*, 2020).

Fully-hydrated C-(A)-S-H samples

We start by describing the fully-hydrated samples, following the sample conditioning protocol shown in Figure 3.2.1.3. The fully hydrated C-(A)-S-H samples were left overnight in the glove-box after the filtration. Therefore, these samples contain the largest amount of water, with bulk liquid-like water being the major phase as seen from the IINS spectra in Section 5.3. The water content in fully-hydrated samples is in a good accordance with the upper boundary of H_2O/Si vs Ca/Si plot from the literature (Figure 3.3.1.1, black dots), with H_2O/Si rising from 2.06 for Ca/Si=0.66 to H_2O/Si=3.37 for Ca/Si=1.46.

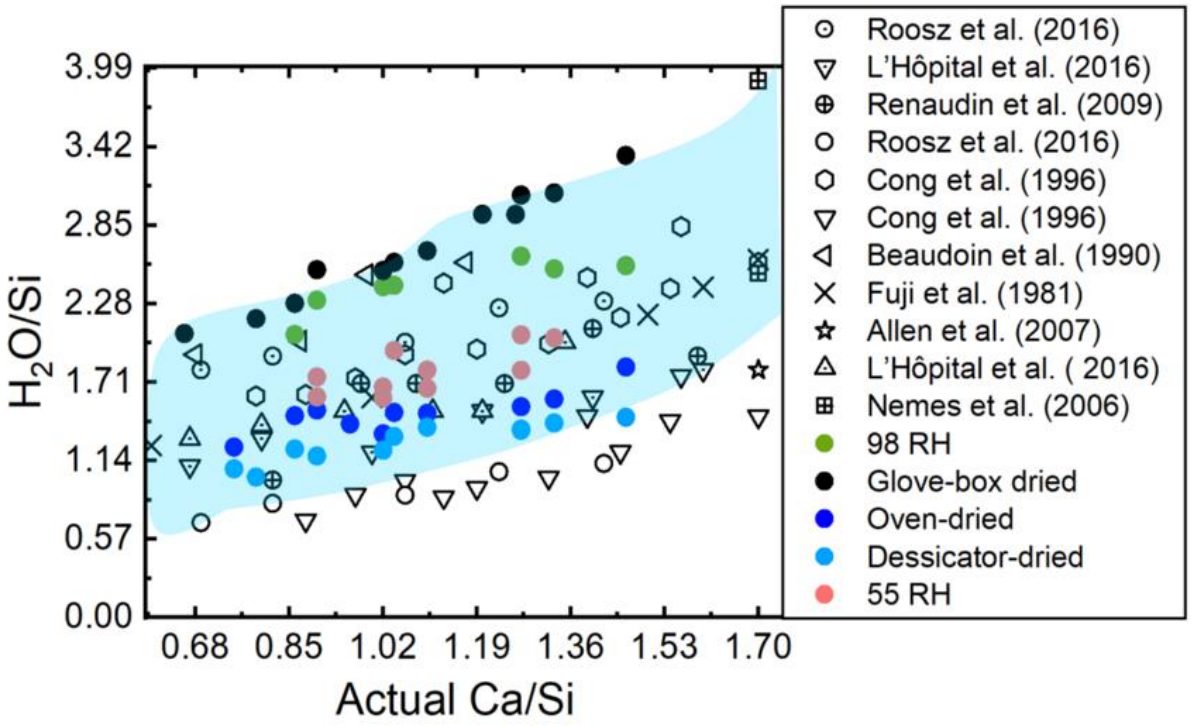

Figure 3.3.1.1. The H_2O/Si changing with Ca/Si ratios and varying hydration levels for C-(A)-S-H samples from the literature (hollow signs), and this work (colored signs).

Oven-dried C-(A)-S-H samples

Part of the 'fully-hydrated' samples were dried in a vacuum oven at 40°C. It is known from other authors (Gaboreau *et al.*, 2020), and from our own experience, that this temperature is not sufficient to remove highly-bound water, even under conditions of dynamic vacuum. The oven-dried samples are not the driest C-(A)-S-H samples (blue dots in Figure 3.3.1.1), with the desiccator-dried samples containing the lowest amount of water. Indeed, TGA experiments for desiccator-dried samples were performed after months of exposure to a very dry atmosphere, which is a very effective method to remove water (Feldman and Sereda, 1970).

The XRD data collected for the same set of samples prior to the TGA experiments, show that the d_{001} reflection for the oven-dried samples is lower by about 0.6 Å on average (Figure 3.3.2.2). Still, the results of both TGA and XRD experiments for the oven-dried and desiccator-dried samples are quite close in values. The difference between the two samples is evident from the results of IINS spectra (Chapter 5), where the oven-dried samples show an extra peak at ~249 cm^{-1} that is not present in other C-(A)-S-H samples. As it is shown in Chapter 5, most probably this peak signifies a thin monolayer of adsorbed interfacial water, which stems from the wetting mechanism of the C-(A)-S-H surfaces as evidenced by our MD simulations.

The adsorption of water onto C-(A)-S-H surfaces is characterized by the coordination of water molecules around calcium ions and strong H-bonding to the surface oxygens (Chapter 4). According to IUPAC, the adsorption of water on C-(A)-S-H surfaces is an intermediate case between physisorption and chemisorption (Everett, 1972). The adsorption of water layers beyond the first monolayer can be considered as physisorption, as the H-bonding between water molecules is weaker than between the water molecules and the surface. As it is discussed in Chapter 4, the average distance between water hydrogens and the deprotonated surface oxygens is about 1.73 Å, whereas the intermolecular distance between water hydrogens and oxygens is roughly 1.99 Å. Therefore, removing the first monolayer of water and the interlayer water requires much higher temperatures, which however lead to a collapse of layers and the damage of the C-(A)-S-H structure (shown in XRD drying tests in Annex 1).

In comparison to the literature values, the oven-dried samples contain about 0.75 H_2O/Si more than the driest samples (Figure 3.3.1.1). This could also be explained by the relatively mild drying conditions, as compared to the more harshly-dried samples constituting the lowest boundary of the Figure 3.3.1.1. The average quantity of total water for the oven-dried samples was about 18 wt.%, regardless of Ca/Si value, and in accordance with the literature (L'Hôpital *et al.*, 2016).

C-(A)-S-H samples conditioned at 98RH

Next, the oven-dried samples were split into two batches. The first portion was exposed to 98RH atmosphere (green dots in Figure 3.3.1.1), and resulted in varying amounts of H_2O/Si with increasing Ca/Si ratios. Water adsorption isotherms were used to calculate the specific surface areas accessible to water of the samples. According to the IUPAC classification (Gregg, Sing and Salzberg, 1967), the water sorption isotherms belong to the type II with a H3 hysteresis type formed throughout the whole RH range (Figure 3.3.1.2).

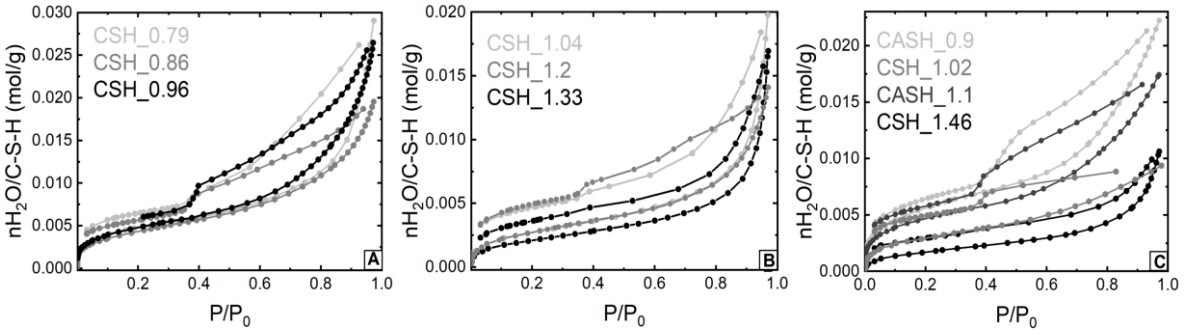

Figure 3.3.1.2. Water sorption isotherms for varying Ca/Si ratios. A characteristic hysteresis between adsorption and desorption branches, and a sudden drop at the adsorbed amount at RH ~35% can be observed for nearly all samples.

The results show a clear decrease in SSA of C-(A)-S-H at increasing Ca/Si ratios (Figure 3.3.1.4, left). The values for surface areas of cement pastes and pure C-S-H vary widely depending on the adsorbate used, the drying technique and the temperature of the sample, etc. Mikhail et al. reported values around 170 m^2/g from water adsorption methods (Mikhail, Kamel and Abo-El-Enein, 1969). Thomas et al. commented that depending on the methods used (SANS, SAXS, NMR) the range of the SSA for hydrated cement paste varies from 80 to 280 m^2/g (Thomas, Jennings and Allen, 1999).

The origin of the hysteresis is generally explained by the presence of 'ink bottle pores' that have narrow entrances to the pore, which are considerably smaller than the actual pore diameter. These pores tend to fill completely through capillary condensation, but upon emptying water molecules need to overcome an energetic barrier caused by the narrow entrance. This results in a characteristic hysteresis in the adsorption/desorption cycle (Thomas, Jennings and Allen, 1999). Another typical feature observed in the water sorption isotherms of the C-(A)-S-H, is the sudden drop in the amount of water on the desorption branch occurring at RH about 35% at 20°C.

Maruyama et al. performed extensive tests at different temperatures and samples of varying water/cement ratios, coupled with length change isotherm tests and concluded that the origin of this drop is a cavitation phenomenon. This is due to the instability of the ink-bottle pore system, causing a sudden release of water from the pore at the relative humidity value of about 0.35, and increasing with elevated temperature of the water adsorption tests.

Another noteworthy feature of the adsorption isotherms is that the amount of the adsorbed water at higher RH levels depends on the equilibration times. Badmann et al. (1981) noted that the sorption measurements of type II isotherms are not very reliable for RH levels exceeding 95%, due to capillary condensation being superimposed with adsorption (Badmann, Stockhausen and Setzer, 1981). The comparison of our WSI data with the data from Roosz et al. (Roosz *et al.*, 2016) show that long exposure to RH > 95% leads to higher amounts of water being adsorbed on the C-(A)-S-H surfaces, followed by a capillary condensation in pores (Figure 3.3.1.3).

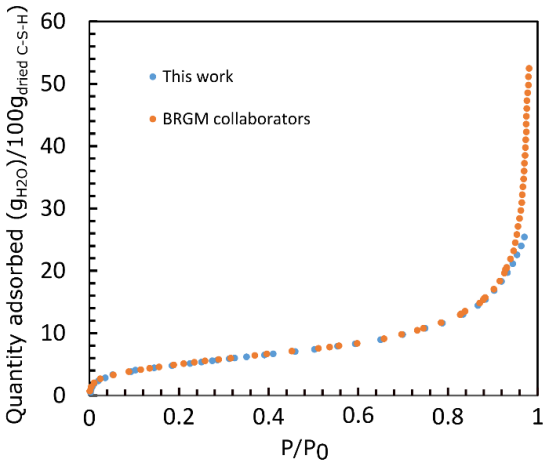

Figure 3.3.1.3. WSI data (adsorption branch) from this work compared to the results of Roosz et al. for CSH_1.2 (Roosz et al., 2016)

The BET method (Brunauer, Emmett and Teller, 1938) allows to calculate the specific surface area (SSA) from the adsorption branch at relative pressure levels from 0.05 to 0.3, where the WSI adsorption branches from this thesis coincide with the ones of Roosz et al. (2016) (Figure 3.3.1.3). Therefore, the results of this work are directly comparable to the ones by Roosz et al. (Roosz *et al.*, 2016). The SSA decreases with increasing Ca/Si ratios as evidenced from Figure 3.3.1.4 (left). As we go from Ca/Si of 0.75 to 1.45, the SSA decreases by nearly 200 m²/g, from 300 m²/g for the lowest Ca/Si, and to 100 m²/g for the higher ratios. The amounts of adsorbed water at 55RH and 98RH deduced from WSI follow similar trends, albeit the decrease is much steeper for 98RH samples (Figure 3.3.1.4, right).

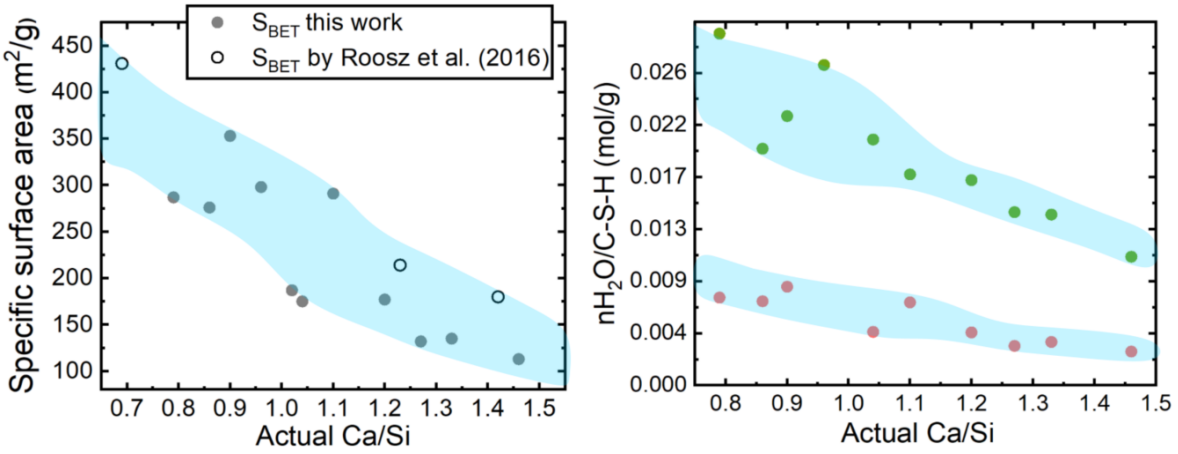

Figure 3.3.1.4. (left) Specific surface area and (right) the amount of adsorbed water varying with Ca/Si ratio at 98% RH (green dots) and 55% RH (red dots).

The amount of water adsorbed at 98RH lowers from 0.03 mol/g C-S-H with Ca/Si=0.75, to 0.012 mol/g for C-S-H with Ca/Si=1.46. However, at these humidity values the results are very sensitive to the equilibration time of the C-(A)-S-H. Most of the samples were equilibrated during equal amounts of time, with exceptions for some C-(A)-S-H samples that were equilibrated separately as they were used for neutron scattering experiments. This results in diverse amounts of total H_2O/Si for 98RH samples shown in Figure 3.3.1.1.

C-(A)-S-H samples conditioned at 55RH

The second batch of the oven-dried C-(A)-S-H samples were exposed to 55RH conditions, and resulted in an intermediate amount of total water (red dots on Figure 3.3.1.1). The H_2O/Si rise less steep than in fully-hydrated samples, from 1.6 for Ca/Si=0.9 to 2.03 for Ca/Si=1.46.

The results of WSI show a decrease in the amount of adsorbed water with rising Ca/Si ratios. The 55RH samples were chosen as the most reliable samples to compare directly the data from the TGA and WSI measurements. The oven-dried or desiccator-dried samples are more difficult to compare since the exact RH levels are not known. The 98RH samples lie on the other extreme, and the amount of adsorbed water strongly depends on the equilibration time as was explained earlier. Therefore, we have chosen a middle value for RH at 55% RH. The WSI give the amount of adsorbed water only in one gram of C-S-H. Prior to the experiment the C-(A)-S-H samples were degassed at 50°C in vacuum. This process removes the majority of water, but not the strongly bound water. Therefore, the WSI results provide the amount of water adsorbed on C-(A)-S-H, added to already present interlayer and interfacial water. By subtracting WSI adsorbed water from the total TGA water it is possible to obtain information about the interlayer water.

The WSI adsorbed water was converted from the initial moles per 1 g of C-S-H to weight percent (wt.%) of adsorbed water. Then, the wt.% of adsorbed water was subtracted from the total wt.% obtained by TGA. Thus, the two trends emerged: first, with increasing Ca/Si ratio the amount of total interlayer water increases, second, the amount of adsorbed water decreases (Figure 3.3.1.5).

Generally, an increasing amount of interlayer water can be explained by an increased number of calcium ions at higher Ca/Si ratios. These Ca^{2+} act as water binding sites, and thus lead to an increased amount of water in the interlayers and at the interfaces.

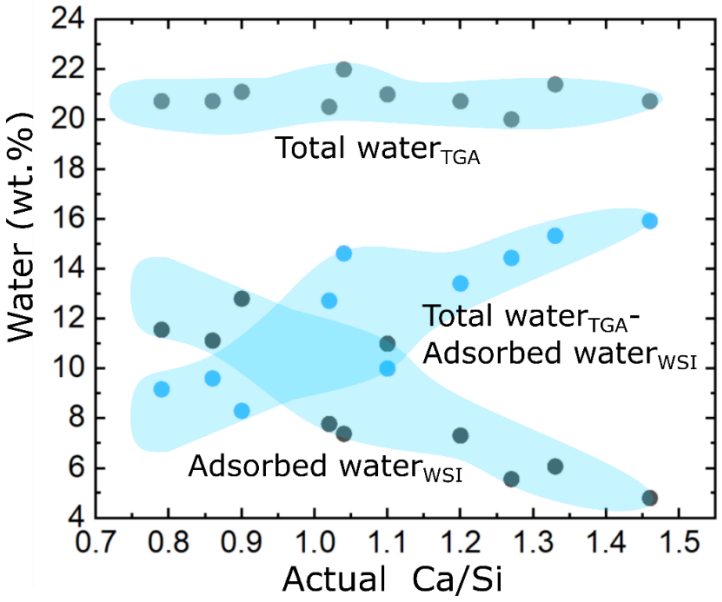

Figure 3.3.1.5. The total water wt.% changing with increasing Ca/Si ratios. The wt.% for 55RH TGA data are missing for Ca/Si=0.76, 0.86, and 1.46, therefore an average value of 20.75 wt.% was considered.

At the same time the amount of adsorbed interfacial water decreases with increasing Ca/Si as evidenced from WSI data, which is related to an increased stacking of the C-S-H layers, thus larger crystallite sizes. Overall, the weight percent of total water in C-(A)-S-H samples is constant over rising Ca/Si at low RH values. In the case of 55RH samples it is about 21 wt.%.

Desiccator-dried C-(A)-S-H samples

A half of the 98RH samples after the equilibration were put in the desiccators filled with silica gel (that was renewed when saturated with water) over a span of several months, which allowed samples to dry significantly.

The desiccator-dried samples contain about 0.5 H_2O/Si more than the harshly dried samples corresponding to the lower boundaries in Figure 3.3.1.1 (light-blue dots). The highest Ca/Si sample with a stoichiometric formula $(CaO)_{1.46}(SiO_2)(H_2O)_{3.38}$ for a fully-hydrated sample, loses about 1.9 H_2O/Si for a desiccator-dried sample. This is in a good accordance with the value from Allen et al. (2007) for saturated C-S-H with $(CaO)_{1.7}(SiO_2)(H_2O)_4$ losing about 1.9 H_2O/Si upon equilibration to 11% RH. The authors showed that equilibration to 11% RH still leaves some fraction of adsorbed water on the surface (0.3 H_2O/Si), which is not part of the solid structure (Allen, Thomas and Jennings, 2007). The average amount of total water was about 16 wt.%.

Looking at these data it is straightforward to deduce that the total amount of water increases with increasing Ca/Si ratio. However, Lothenbach and Nonat note in their review that H_2O/Si includes not only water molecules, but also Si-OH and Ca-OH if present (Lothenbach and Nonat, 2015). The average amount of the total water for the C-(A)-S-H at RH levels lower than 90-95% is constant (within ±2%). In pores larger than 2 nm in diameter (gel pores and capillary pores), and at RH levels >95% the capillary condensation becomes important, and the total water content depends on the equilibration time.

3.3.2. Variation of d_{001} reflection with varying Ca/Si

Interlayer water content change with Ca/Si ratios

As shown in Figure 3.3.2.2, a general trend is observed by which d_{001} decreases with increasing Ca/Si ratios. This trend is maintained until about Ca/Si=1.3, after which it becomes constant. This is in agreement with the structural C-S-H model by which Ca is accommodated in the structure via the formation of defects, up to Ca/Si ~ 1.3-1.4, value from which the formation of portlandite is observed (Grangeon *et al.*, 2017). At the same time, and as shown above, the amount of interlayer water increases with increasing Ca/Si ratios, which sounds counterintuitive if one assumes the direct relationship between the d_{001} value and the interlayer distance.

This fact can be explained by the opposition between two effects: on the one side, the presence of more Ca^{2+} ions in the interlayer leads to an increase of the hydrophilicity of the material, as these are hydrated ions. On the other hand, the presence of Ca^{2+} leads to an enhancement of the electrostatic interactions between adjacent layers, leading to their collapse.

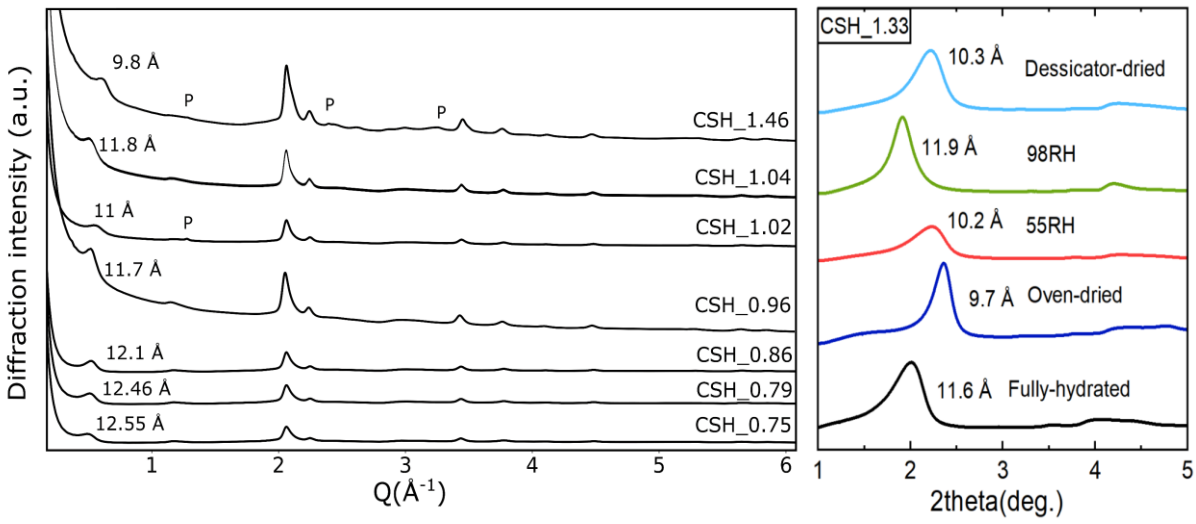

Figure 3.3.2.1. X-ray diffraction of some C-S-H samples showing changes in the d_{001} values with: (left) increasing Ca/Si ratios (an example for oven-dried samples); (right) with changing RH levels (an example of CSH_1.33).

A set of data for the d_{001} reflection at different RH values is shown in Figure 3.3.2.1. The methodology used to synthesize and condition the C-S-H at the different humidity values consisted in taking over-dried samples and exposing them to the different wet atmospheres, similarly to the methodology followed to prepare samples for the neutron scattering experiments. The rewetting (at 98% RH) of our oven-dried samples proceeds through water populating the interfaces and the interlayer (Feldman and Sereda, 1970). When these rewetted samples (C(A)SH_98RH) are subjected to a very dry atmosphere in a desiccator filled with silica beads, with an RH value inside the desiccator being <11% RH, a major drying takes place, including the interlayer. As noted earlier by Feldman and Sereda, the drying of interlayer water starts under 11% RH at ambient temperature (Feldman and Sereda, 1970). The WSI studies by Pinson et al. (Pinson *et al.*, 2015; Roosz *et al.*, 2016) note that the water does not leave the interlayer spacing until lower than 20% RH.

This dataset complements previous existing data, following the swelling of C-S-H for given Ca/Si ratios. It is worth pointing out here that these data do not take into account possible effects of layer interstratification, as discussed by Gaboreau et al. (Gaboreau *et al.*, 2020). In the context of increasing Ca/Si ratios, we need to remember that the effect of coherent domain size, turbostratism and interstratification can be affecting the real value of interlayer spacing as discussed by Claret et al. (Claret *et al.*, 2004).

The XRD fitting using a mathematical model by Drifts and Tchoubar performed by Grangeon et al. for C-S-H of varying Ca/Si ratios, show that the real values d_{001} can be shifted sometimes by ~1 Å (Grangeon, Claret, Linard, *et al.*, 2013). However, although the values cannot be considered as absolute values in the absence of this advanced treatment of the diffraction data, relative variations of these values within the dataset can be considered as more reliable.

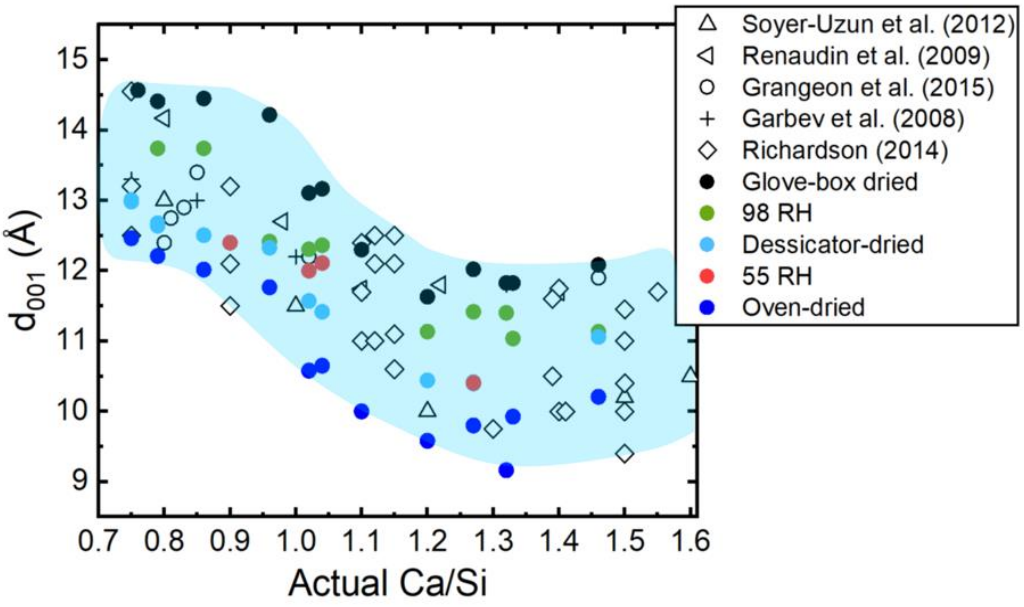

Figure 3.3.2.2. The evolution of d_{001} reflection changing over Ca/Si ratios (colored symbols) compared to literature values (hollow symbols) with varying RH levels.

A comparison of our values to the literature shows that the extent of C-(A)-S-H interlayer space swelling is about 2.5 Å from 'dry' to 'wet' samples. This is in a good accordance with other authors, the latest being data from Gaboreau et al. stating the range of about 3 Å (Gaboreau *et al.*, 2020). This value is roughly the size of a water molecule, which is complementary to the TGA data showing a difference of about 1 H_2O/Si between the 'dry' and 'wet' C-(A)-S-H samples.

Overall, these experiments show that different drying and rewetting methods lead to different values of the interlayer distance, and that a hysteretic behavior is present in the samples after exposure to 98RH, with none of them reaching the value obtained for samples dried in the glove-box after sample filtering (a method that yields very humid samples).

3.4. Conclusions

This Chapter 3 focuses on determining the amount and distribution of water in C-(A)-S-H samples of varying Ca/Si ratios, with the main goal being the characterization of C-(A)-S-H samples used for neutrons scattering experiments. The samples were characterized using a combination of TGA, WSI and XRD analysis. The results of TGA allowed quantifying the total amount of water, with H_2O/Si rising with increasing Ca/Si ratios in a good accordance with literature. The H_2O/Si increases also with increasing RH levels in C-(A)-S-H samples. However, in weight fraction, the total amount of water is relatively constant for 'drier' C-(A)-S-H samples, i.e. oven-dried, desiccator-dried and 55RH samples. In the case of 'wetter' C-(A)-S-H samples, 98RH and fully hydrated, the amount of adsorbed water is strongly dependent on the equilibration time. This is apparent from the overall trend of H_2O/Si, where the amount of water per silicon varies depending on the duration of the equilibration time.

The expected behavior from the water sorption isotherms is that the amount of adsorbed water should decrease with increasing Ca/Si ratios. However, as noted earlier, at the RH levels exceeding 95% the capillary condensation effects start overlapping with water adsorption on C-(A)-S-H interfaces. Thus, for 'wet' C-(A)-S-H samples the amount of adsorbed water does not follow strict H_2O/Si trends. The results of the XRD experiment show two trends as well: The d_{001} reflection value decreases with increasing Ca/Si ratios up to ~1.27, after which the d_{001} value is rather constant. The amount of the interlayer water is known to increase, despite the d_{001} reflection value decreasing. This can be explained by the electrostatic interactions becoming stronger as the amount of calcium ions increase, i.e., by a stronger electrostatic attractions between the layers and a decrease of the interlayer distance. At the same time, the d_{001} reflection increases with rising RH levels in the C-(A)-S-H samples, indicating the shrinking and swelling behavior of the interlayer region.

Overall, the increased number of calcium ions in the C-(A)-S-H influence the amount and distribution of water in samples with increasing Ca/Si ratios. In case of 'wet' samples containing adsorbed water, the equilibration times become more important than the effect due to Ca/Si ratios.

Appendix

Table 3.A.1. Amounts of reagents used for the synthesis of C-(A)-S-H samples. Other Ca/Si ratios can be found in Chapter 4 and 5.

	Ca/Si nominal ratio	Actual Ca/Si ratio	Moles (mmol)	Volume (mL)	Concentration (mmol/mL)	Mass actual (g)
CaO	0.76	0.75	52.5	350	0.15	2.94
SiO_2			70.0	350	0.20	4.21
CaO	0.80	0.79	57.5	350	0.16	3.23
SiO_2			72.5	350	0.21	4.36
CaO	0.84	0.84	55.0	350	0.16	3.08
SiO_2			65.4	350	0.19	3.93
CaO	0.90	0.92	40.6	350	0.12	2.28
SiO_2			44.2	350	0.13	2.66
CaO	1.51	1.66	76.7	350	0.22	4.30
SiO_2			46.3	350	0.13	2.78
CaO	1.10	1.19	71.5	388	0.18	4.01
SiO_2			60.2	388	0.16	3.62
CaO	1.10	1.19	20.5	111	0.18	1.15
SiO_2			17.2	111	0.16	1.04
CaO	0.76	0.75	135.0	900	0.15	7.57
SiO_2			180.0	900	0.20	10.81

Table 3.A.2. The stoichiometry in C-(A)-S-H samples deduced from the TGA experiment and XRD d_{001} reflections.

RH level	Actual Ca/Si	CaO	SiO_2	H_2O (total)	d_{001} reflection
Oven-dried	0.75	0.75	1	1.24	12.55
Oven-dried	0.79	0.79	1	-	12.46
Oven-dried	0.86	0.86	1	1.47	12.1
Oven-dried	0.9	0.90	1	1.51	12.02
Oven-dried	0.96	0.96	1	1.41	11.7
Oven-dried	1.02	1.02	1	1.34	11
Oven-dried	1.04	1.04	1	1.49	10.6
Oven-dried	1.1	1.10	1	1.48	10.65
Oven-dried	1.2	1.20	1	-	-
Oven-dried	1.26	1.26	1	-	-
Oven-dried	1.27	1.27	1	1.53	-
Oven-dried	1.33	1.33	1	1.60	9.8
Oven-dried	1.46	1.46	1	1.62	-
Dess.dried	0.75	0.75	1	1.08	-
Dess.dried	0.79	0.79	1	1.02	12.98
Dess.dried	0.86	0.86	1	1.22	12.68
Dess.dried	0.9	0.90	1	1.18	12.51
Dess.dried	0.96	0.96	1	-	-

Dess.dried	1.02	1.02	1	1.21	-
Dess.dried	1.04	1.04	1	1.32	11.57
Dess.dried	1.1	1.10	1	1.38	11.42
Dess.dried	1.2	1.20	1	-	10.6
Dess.dried	1.26	1.26	1	-	-
Dess.dried	1.27	1.27	1	1.37	-
Dess.dried	1.33	1.33	1	1.43	10.40
Dess.dried	1.46	1.46	1	1.47	-
55RH	0.75	0.75	1	Not cond.	Not cond.
55RH	0.79	0.79	1	Not cond.	Not cond.
55RH	0.86	0.86	1	Not cond.	Not cond.
55RH	0.9	0.90	1	1.68	12.4
55RH	0.96	0.96	1	Not.cond	Not cond.
55RH	1.02	1.02	1	1.63	11.6
55RH	1.04	1.04	1	1.95	12.1
55RH	1.1	1.10	1	1.73	12.4
55RH	1.2	1.20	1	Not.cond	Not.cond
55RH	1.26	1.26	1	Not.cond	Not.cond
55RH	1.27	1.27	1	1.92	10.3
55RH	1.33	1.33	1	2.00	Not.cond
55RH	1.46	1.46	1	Not.cond	Not.cond
98RH	0.75	0.75	1	-	14.5
98RH	0.79	0.79	1	-	Not.det
98RH	0.86	0.86	1	2.06	Not.det
98RH	0.9	0.90	1	2.31	13.74
98RH	0.96	0.96	1	-	12.52
98RH	1.02	1.02	1	2.41	12.31
98RH	1.04	1.04	1	2.42	12
98RH	1.1	1.10	1	-	12.36
98RH	1.2	1.20	1	-	12.4
98RH	1.26	1.26	1	-	-
98RH	1.27	1.27	1	2.62	11.5
98RH	1.33	1.33	1	2.45	11.9
98RH	1.46	1.46	1	2.57	11.2
Full.hydrated	0.75	0.75	1	-	Not vis.
Full.hydrated	0.79	0.79	1	2.17	Not vis.
Full.hydrated	0.86	0.86	1	2.28	14.41
Full.hydrated	0.9	0.90	1	2.53	14.45
Full.hydrated	0.96	0.96	1	-	14.2
Full.hydrated	1.02	1.02	1	2.52	13.17
Full.hydrated	1.04	1.04	1	2.58	13.11
Full.hydrated	1.1	1.10	1	2.66	12
Full.hydrated	1.2	1.20	1	2.94	11.75
Full.hydrated	1.26	1.26	1	2.94	11.63
Full.hydrated	1.27	1.27	1	3.06	10.3
Full.hydrated	1.33	1.33	1	3.05	11.5
Full.hydrated	1.46	1.46	1	3.38	12.1

Chapter 4 Structure of water in C-(A)-S-H

(Manuscript under review – ACS publications – Journal of Physical Chemistry C)

Structure of water adsorbed on nanocrystalline calcium silicate hydrate determined from neutron scattering and molecular dynamics simulations

Zhanar Zhakiyeva[1,2,*], Gabriel J. Cuello[2,*], Henry E. Fischer[2], Daniel T. Bowron[3], Catherine Dejoie[4], Valerie Magnin[1], Sylvain Campillo[1], Sarah Bureau[1], Agnieszka Poulain[1], Rogier Besselink[1], Stephane Gaboreau[5], Sylvain Grangeon[5], Francis Claret[5], Ian C. Bourg[6,*], Alexander E. S. Van Driessche[1], Alejandro Fernandez-Martinez[1,*]

[1] *University of Grenoble Alpes, University of Savoie Mont Blanc, CNRS, IRD, IFSTTAR, ISTerre, 38000 Grenoble, France.*

[2] *Institut Laue–Langevin, 71 Avenue des Martyrs, CS 20 156, 38042 Grenoble Cedex 9, France.*

[3] *ISIS, Science and Technology Facilities Council Rutherford Appleton Laboratory, Harwell Oxford, Didcot, UK.*

[4] *ESRF, The European Synchrotron, 71 Avenue des Martyrs, CS40220, 38043 Grenoble Cedex 9, France*

[5] *BRGM, 3 Avenue Guillemin, Orléans Cedex 2 45060, France.*

[6] *Department of Civil and Environmental Engineering and High Meadows Environmental Institute, Princeton University, Princeton, New Jersey 08544, United States.*

***Corresponding Authors**

Zhanar Zhakiyeva - ISTerre, 1381 rue de la Piscine, 38400 St Martin d'Heres, France. Phone: +33(0)82713094; Email: zhanar.zhakiyeva@univ-grenoble-alpes.fr

Gabriel J. Cuello - Institut Laue–Langevin, DS, 71 Avenue des Martyrs, CS 20 156, 38042 Grenoble Cedex 9, France. Phone: +33(0)476207697; Email: cuello@ill.eu

Ian C. Bourg - Department of Civil and Environmental Engineering and High Meadows Environmental Institute, Princeton University, Princeton, New Jersey 08544, United States. Phone: +1 609-258-4541. Email: bourg@princeton.edu

Alejandro Fernandez-Martinez - ISTerre, 1381 rue de la Piscine, 38400 St Martin d'Heres, France. Phone: +33(0)635197; Email: Alex.Fernandez-Martinez@univ-grenoble-alpes.fr

1 Introduction

Portland cement is one of the most important synthetic materials known to humans. In particular, it plays a critical role in infrastructure and contributes a significant portion of anthropogenic CO_2 emissions (Fischedick *et al.*, 2014; Van Ruijven *et al.*, 2016; Lehne and Preston, 2018; CEMBUREAU, 2020). Although its formulation has remained remarkably constant for decades, the development of alternative formulations (low CO_2, CO_2 resistant, fire resistant, resistant to sulfate attack, etc.) has emerged in recent years as an important research goal (Scrivener and Kirkpatrick, 2008; Lothenbach and Nonat, 2015; Lehne and Preston, 2018; Van Damme, 2018; van Deventer, White and Myers, 2021). This new focus has generated a strong need for detailed insight into the fundamental origins of the structural, mechanical, and chemical properties of Portland cement. The task is challenging, however, largely because the structural complexity of the hydrated Portland cement phase remains incompletely understood.

The atomistic structure of C-S-H

Calcium-silicate-hydrate (C-S-H), the main binding phase in Portland cement, is a nanocrystalline, partially disordered, hydrated phase with water being present in C-S-H pores of all sizes, from micro- to meso- and macropores (Skalny and Odler, 1972; Lothenbach and Nonat, 2015; Papatzani, Paine and Calabria-Holley, 2015; Wenzel *et al.*, 2017). In addition to its structural disorder C-S-H is also a complex material due to its significant chemical versatility, in particular by its variable Ca/Si ratio (Chen *et al.*, 2004; Lothenbach and Nonat, 2015; Grangeon *et al.*, 2017). Since Taylor established in 1950 the presence of two distinct phases with lower or higher Ca/Si ratios (C-S-H(I) and C-S-H(II), respectively), there have been decades of debate about the structures of these phases.(Taylor, 1950) It is now generally accepted that the structure of C-S-H(I) resembles a defective tobermorite, and that C-S-H(II) contains (nano)portlandite crystallites. Though questions remain regarding the spatial localization of the portlandite, a relatively unified view has emerged with many atomistic models available (Richardson and Groves, 1992; Richardson, 2014; Grangeon *et al.*, 2017; Kunhi Mohamed *et al.*, 2018; Roosz *et al.*, 2018). These different C-S-H models are consistently based on the structure of tobermorite, which consists of layers of calcium oxide sandwiched between silica chains formed by groups of three tetrahedra (dreierketten), with an interlayer space filled with water and ions (Richardson, 2014). These models differ primarily in their assumptions about the types of defects that exist in the tobermorite structure, with some common points regarding the substitution of Ca^{2+} ions by two hydroxyl groups and the presence of silica defects mainly in the 'bridging' tetrahedra of the 'dreierketten' silica chains.

In the last decade, a significant advance towards a more comprehensive understanding of C-S-H structure has been the application of atomistic simulation techniques to link C-S-H structural models to measured physical properties (Faucon *et al.*, 1997). A milestone in C-S-H atomistic modeling was reached by Pellenq and coworkers with their development of a first C-S-H structural model with Ca/Si = 1.65, generated by creating defects in a tobermorite structure and then populating it with water molecules, using a Grand Canonical Monte Carlo (GCMC) approach (R. J. M. Pellenq *et al.*, 2009). Overall, the model reproduced several mechanical properties of C-S-H, such as stiffness, strength, and hydrolytic shear response, while deviating from measurements of certain structural features such as coordination numbers (Richardson, 2013). Qomi et al. later refined this model by

using a “reactive” interatomic potential model (ReaxFF) to generate more chemically realistic structures and by creating a statistical ensemble of 150 atomic structures of C-S-H with varying Ca/Si ratios (Abdolhosseini Qomi *et al.*, 2014). A similar approach was used by Kovačević et al. (2015) who also used a statistical approach to generate a large number of C-S-H structures with Ca/Si = 1.67 and with random numbers of silica oligomers for each model using both geometry optimizations and Molecular Dynamics (MD) simulations carried out with the ReaxFF force field. They showed that from an energetic point of view the model with Ca/Si = 1.67, achieved by randomly removing bridging silica tetrahedra and adding calcium ions charge-balanced by hydroxide ions, was the most stable structure. This also involved the breaking of silica chains into dimers and pentamers (Kovačević *et al.*, 2015, 2016).

More recently, an atomistic model that included a careful description and classification of different types of defects within the C-S-H structure was developed by Kunhi-Mohamed et al. (2018) The authors created building blocks with varying defects to capture the disordered structure of C-S-H using a combination of Density Functional Theory (DFT) and MD simulations. Their model reproduced the Mean Chain Length (MCL) of C-S-H (based on experimental ^{29}Si NMR data) and its mass density. However, the authors reported that the predicted water content was significantly lower than expected and the interlayer spacing was quite large (~2.5 Å higher than the expected value) for Ca/Si = 1.67 (Kunhi Mohamed *et al.*, 2018).

Finally, another recent atomistic model was proposed by Androniuk et al. (2017) based on the structure of tobermorite, where defects were introduced only at the surfaces, keeping the tobermorite bulk structure unchanged (Androniuk *et al.*, 2017). This model was used to study gluconate and U(VI) adsorption on C-S-H. (Androniuk and Kalinichev, 2020) Deprotonated surface oxygens (which were assigned a more negative charge than structural oxygen atoms) were found to be the most favorable adsorption sites on the C-S-H surface, with a strong affinity for both Ca^{2+} and uranyl cations (Androniuk and Kalinichev, 2020), in agreement with their previous observation that the structural defects act as potential sorption sites for interfacial species (Androniuk *et al.*, 2017).

A key challenge in testing the validity of the structural models outlined above is that the X-ray diffraction pattern of C-S-H is composed of both Bragg peaks and diffuse scattering. This is indicative of a nanostructure containing some periodicity and a high degree of disorder. The presence of diffuse scattering makes the comparisons between experiments and calculations particularly challenging, albeit not impossible (Grangeon, Claret, Linard, *et al.*, 2013). In recent years, experimental studies using Pair Distribution Function (PDF) analyses of high-energy X-ray scattering data have allowed a direct comparison of experimental and calculated PDFs. Unlike Bragg analysis (i.e., ‘conventional’ XRD analysis (Aranda, 2016)), the PDF approach allows the analysis of both short and long-range order. To date, few studies have directly compared the predicted PDF of C-S-H to the experimental one. Qomi (Abdolhosseini Qomi *et al.*, 2014) and Bauchy et al.(Bauchy *et al.*, 2014) calculated the X-ray PDF from their simulation predictions, comparing it to previously reported experimental PDFs of synthetic C-S-H (Meral, Benmore and Monteiro, 2011; Soyer-Uzun *et al.*, 2012; White *et al.*, 2015). The results showed good agreement with regard to the major peaks up to 5 Å, though some peak shifts or broadenings were observed. The most recent direct comparison was done by Cuesta et al. (Cuesta *et al.*, 2021), who compared

their experimental data with calculated PDFs based on the model of Kunhi-Mohamed et al. (Kunhi Mohamed *et al.*, 2020), showing an overall good agreement with some discrepancies in the middle-range order (Kunhi Mohamed *et al.*, 2020; Cuesta *et al.*, 2021).

Water in C-S-H

The models described above have contributed significantly to the advancement of our understanding of the defective structure of C-S-H and to the development of structure-properties relationships at the molecular scale. However, few of these models have addressed the structural properties of water films present at the C-S-H surface. It is well known that thin films of water adsorbed on metal oxides exert a strong control on many physico-chemical properties of the adsorbent phase, such as wettability, rheology, mechanical strength, and chemical reactivity (e.g., reactivity towards ions present within the interfacial liquid phase) (Wittmann, 1973; Schneider *et al.*, 2017; Sinko, Bažant and Keten, 2018; Sun and Bourg, 2020). Studies of these interfacial liquid layers are thus of upmost importance to e.g. cement chemistry and engineering. Indeed, these water films have been shown to strongly influence carbonation reactions (Zhang, Ghouleh and Shao, 2017), cohesion (Jönsson *et al.*, 2005; Bonnaud *et al.*, 2012), shear strength (Manzano *et al.*, 2012), and the shrinkage (Ferraris and Wittmann, 1987), and creep behavior(Vandamme and Ulm, 2009) of cementitious materials.

Since the early studies by Powers and Brownyard in 1948, who identified the so-called evaporable and non-evaporable water in the cement phase (Powers, T. C.; Brownyard, 1946), extensive effort has focused on characterizing the different types of water in cement paste, and more specifically in the C-S-H phase. Different experimental techniques, including neutron scattering, have been used to probe the water component of C-S-H. In particular, Allen et al. (Allen, Thomas and Jennings, 2007) used small angle X-ray and neutron scattering to study the mesoscale arrangement of C-S-H nanoparticles. They concluded that C-S-H consisted of ~5 nm-wide platelets composed of stacked C-S-H layers with an interlayer space filled with water, and they distinguished between adsorbed water located on the surface of the platelets and a bulk-liquid-like water component located in the pores between these platelets (Allen, Thomas and Jennings, 2007), Pinson et al. (2015) proposed a similar classification of water based on the results of water sorption isotherms (WSI): they identified water confined in the interlayer space (≤ 1 nm), strongly bound to the C-S-H surfaces and removed only at relative humidities (RH) ≤ 11%; a "gel pore water" component in 1-10 nm wide pores; and capillary water in pores larger than 10 nm. Finally, they reported the presence of a surface layer of adsorbed water, which remained present in gel and capillary pores after the pores had been emptied of bulk-liquid-like water (Pinson *et al.*, 2015) Nuclear Magnetic Resonance (NMR), and in particular ^{1}H relaxometry experiments, have also provided detailed information on water dynamics in C-S-H and cement (Maruyama *et al.*, 2019). In particular, ^{1}H NMR relaxometry experiments by McDonald et al. (2010) allowed differentiating between the mobile intra-C-S-H sheet water and inter-C-S-H gel pore water (McDonald, Rodin and Valori, 2010). A few years later, Muller et al.(Muller *et al.*, 2013) and Valori et al. (Valori, McDonald and Scrivener, 2013) showed the potential of ^{1}H NMR relaxometry to distinguish between the dynamic characteristics of water in interlayer pores (< ~1 nm), gel pores (2-5 nm), interhydrate pores (~10 nm), and capillary pores (~1000 nm). This subdivision of water in different pores and surfaces of C-S-H was subsequently studied by Roosz et al. (Roosz *et al.*, 2016), who showed how an initially dry synthetic C-S-

H sample behaves when exposed to increasing humidity. The authors proposed a two-step process, with water being adsorbed on the surfaces when humidity increases from 0 to 75% RH, and subsequent filling of mesopores and of interlayer space as RH increases up to 95% (Roosz *et al.*, 2016). These authors also showed that the process is not reversible, with interlayer water being released at much lower RH during water desorption.

Molecular mechanisms controlling C-S-H wettability

Even though, as shown above, the diffusive behavior of water in C-S-H has been the subject of multiple investigations, less information is available regarding the structural characteristics of the adsorbed water. Youssef et al. (Youssef, Pellenq and Yildiz, 2011), used molecular modeling based on the structural C-S-H model of Pellenq et al. (R. J. M. Pellenq *et al.*, 2009) to study water in confinement (interfacial/interlayer water). The authors showed with partial pair correlations of the water oxygen and hydrogen atoms that the local order of the confined water differed from that reported experimentally for bulk water (Soper, 2007). The hydrophilic nature of C-S-H is explained by these authors as coming from the defective silicate chains, which act as hydrogen-bond (H-bond) acceptor sites, and from interlayer calcium ions, which coordinate water molecules (Youssef, Pellenq and Yildiz, 2011). This mechanism of surface hydrophilicity has been confirmed by studies on similar systems; Bonnaud et al. (Bonnaud *et al.*, 2012) showed using GCMC and MD methods that the hydrophilicity of Ca^{2+} ions physisorbed in silica nanopores (a simplified model of C-S-H) decelerates the water dynamics as compared to the hydroxylated silica surfaces without calcium ions. These authors also observed that the tetrahedral arrangement of bulk water is disturbed near the hydrophilic surface, and perturbed much more in the presence of calcium ions at the surface, due to water molecules being coordinated to Ca^{2+} (Bonnaud *et al.*, 2012). As discussed by Bourg and Steefel (2012) water within silica nanopores can be split into two types depending on the pore size of the porous adsorbent: 2-20 nm wide pores contain significant amounts of surface water (located in the ~3 first monolayers from the hydrophilic surface), which is highly structured and different from the bulk-like water found in the center of the pores, while pores narrower than ~2 nm contain only confined water that is influenced by the two hydrophilic surfaces (Bourg and Steefel, 2012). This simplified model is representative of water in the C-S-H phase: the first type would correspond to gel-pore water, with interfacial water (closest to the surface of C-S-H) having different structural characteristics than the bulk-liquid-like water. The second type corresponds to interlayer water confined between two C-S-H surfaces (Pinson *et al.*, 2015). As a general trend, water near the surface of a hydrophilic mineral is highly structured, both in terms of translational and orientational dynamics, and its properties depend strongly on the nature of the substrate (Wang *et al.*, 2005; Marry and Turq, 2008; Bourg and Steefel, 2012; Johnston, 2018; Schoonheydt, Johnston and Bergaya, 2018).

In this paper, the structural properties of interfacial and interlayer water in C-S-H are probed using a combination of experimental and molecular modeling techniques. The technique of neutron diffraction with isotopic substitution (NDIS) is used to probe the short-range order of water adsorbed on C-S-H surfaces (H E Fischer, Barnes and Salmon, 2006; Cuello, 2008). This method has previously been applied to systems showing structural similarities to C-S-H, such as clay minerals (Skipper, Soper and McConnell, 1991; Powell, Fischer and Skipper, 1998; Pitteloud *et al.*, 2000). To perform the molecular modeling simulations, a simple model of C-S-H has been developed using a modified version of the CLAYFF force-field. Comparisons of the calculated and experimental

X-ray PDFs of C-S-H in the literature demonstrate the challenges associated with creating an atomistic model that captures the complexity and disorder of the C-S-H phase. One particular challenge in comparing these models with experimental results is that most atomistic models developed for C-S-H (with very few exceptions) (Masoumi *et al.*, 2019) share the similarity of being bulk models (i.e., they are based on C-S-H structures that are infinite in at least two directions), whereas experimental studies suggest that C-S-H is composed of nanocrystals with dimensions of only a few nanometers (Meral, Benmore and Monteiro, 2011). The C-S-H model that we present in this work consists of a single particle with dimensions of a few nanometers in every direction.

The paper is organized as following: First, the stoichiometry of our experimental C-S-H samples and the distribution of water as a function of RH are discussed. Then, the development of the C-S-H model is described, including its validation by comparison to experimental scattering data. Finally, based on our simulation and experimental results, we examine the structure and hydrogen-bonding (H-bonding) behavior of interfacial and interlayer water in C-S-H and calcium-aluminum-silicate-hydrate (C-A-S-H) samples conditioned at 55% and 98% of RH.

2 Materials and Methods

2.1 Sample preparation

C-S-H samples with Ca/Si = 1 and 1.27 were synthesized by reacting calcium oxide and fumed silica in water inside a N_2 wet glove-box. Calcium oxide was obtained by calcination of $CaCO_3$ (Sigma-Aldrich, Fluka, Bioultra) at 1000 °C for 18 h and stored in a vacuum desiccator until usage. Fumed silica SiO_2 (Sigma-Aldrich, Aerosil 200) was placed in an oven at 40°C for ~24 h to remove physisorbed water prior to each experiment. Deionized water was boiled and degassed with N_2 gas to remove all dissolved CO_2. The quantities of calcium oxide and fumed silica required to prepare C-S-H of predetermined stoichiometry were calculated using the method reported by Haas and Nonat(Haas and Nonat, 2015) (see Supplementary Information Table S3). Samples were reacted under stirring conditions for ~1 month in High Density Polyethylene (HDPE) bottles inside a wet N_2 glove-box, then filtered using Millipore® filter paper (0.22 µm, GSW1 UM), and wet C-S-H residue was left to dry inside the glove-box for 12 h. A part of these C-S-H samples was set aside for characterization of a fully-hydrated C-S-H. The remaining C-S-H was oven-dried at 40 °C in a vacuum oven for 24 h. After drying, samples were conditioned at controlled RH of 55 or 98 % using saturated salt solutions of $Mg(NO_3)_2{\cdot}6H_2O$ or K_2SO_4, respectively, in duplicate with normal and deuterated water for 1 week. As samples are sensitive to atmospheric CO_2, all synthesis and conditioning processes were performed under an inert gas atmosphere of N_2. The C-A-S-H samples with Ca/Si = 1 and 1.2 and Al/Si = 0.1 were synthesized following a protocol that can be found elsewhere.(Roosz *et al.*, 2018)

Following these protocols, we obtained C-S-H samples labeled CSH_Ca/Si_%RH_h/d, where Ca/Si is the Ca/Si ratio of a sample, %RH is the relative humidity at which is was conditioned, and *h* or *d* signify conditioning with normal or deuterated water (Table 1). The C-A-S-H samples were labeled CASH_Ca/Si_%RH_h/d. In the discussion of the results of neutron diffraction with isotopic substitution experiment (explained later), we refer to the difference between deuterated and hydrogenated samples as CSH_Ca/Si_%RH_d-h, for example CSH_1_55RH_d-h. If the properties of the C-S-H samples with a specific Ca/Si ratio are discussed in general, we refer to these as CSH_Ca/Si.

2.2 Sample characterisation

Inductively coupled plasma - atomic emission spectrometer (ICP-AES)

Ca/Si ratios were determined using ICP-AES (Varian 720ES Agilent). The C-S-H particles (5-10 mg) were dissolved by adding concentrated 14M HNO_3 (distilled) and 28M HF (47-51%, Trace Metal™, for Trace Metal Analysis, Fisher Chemical) acids, followed by heating the solution for ~24h at 80°C. The final step involved diluting with boric acid and ultrapure water prior to the measurement.

Water adsorption volumetry

Water adsorption isotherms were obtained at 25 °C using a Belsorp-Max instrument by BEL JAPAN Inc.III. A long acquisition time of at least 2 weeks was required due to the slow equilibrium kinetics. Prior to the measurements, all samples were outgassed at 40 °C for 24 h under a residual pressure of 4.652×10^{-5} Pa. The classical Brunauer−Emmett−Teller (BET) theory and a generalized t-plot method were used to analyze the isotherms.(Brunauer, Emmett and Teller, 1938) The BET theory was employed to obtain energetic C constants, which were used to plot t-curves based on the method discussed by Hagymassy (Hagymassy, Brunauer and Mikhail, 1969) (Table 1).

Thermogravimetric analysis

Thermogravimetric analysis (TGA, Mettler-Toledo TGA-DSC3+) was used to examine the thermal decomposition and the water content of the C-S-H and C-A-S-H samples. The samples were analyzed at a heating rate of 10°C/min up to 600°C in a N_2 environment with a flow rate of 20 mL/min. The samples were loaded in aluminum crucibles and were hermetically sealed with aluminum caps inside a glove-box or a glove-bag filled with N_2 equilibrated at the same RH used to condition the sample. The sample mass used for TGA analyses varied between 8 and 30 mg.

Attenuated Total Reflection Fourier-transform infrared (ATR-FTIR) spectrometry

FTIR spectra were acquired on an IS10 ThermoFischer spectrometer with high-performance diamond ATR Smart iTX™ Accessory (IRSTEA, Grenoble). The different vibrational bands were assigned using the OMNIC software.

Synchrotron X-Ray diffraction

Synchrotron XRD measurements for the C-S-H samples were performed at the ID31 and ID22 beamlines of the European Synchrotron Radiation Facility (ESRF) in Grenoble, France. Prior to analysis, C-(A)-S-H samples were loaded into 1.5 mm (ID31) or 2 mm (ID22) polyimide capillaries in glove-bags or a wet glove-box at the same RH values. The capillaries were closed on both ends using a two-parts epoxy adhesive.

At the ID31 beamline, a monochromatic X-ray beam of 78 keV (λ = 0.159 Å) was used to obtain scattering patterns of C-S-H with Ca/Si = 1. The data sets were collected using a PilatusX 2M CdTe detector placed at a sample-to-detector distance of d_1 = 1.226 m to obtain scattering patterns with a Q range of 0.1-6.2 $Å^{-1}$, allowing the measurement of the Bragg peak corresponding to the interlayer distance of C-S-H. A second set of experiments was performed with a shorter sample-to-detector distance of d_2 = 0.224 m, yielding a Q range 0.6-27.6 $Å^{-1}$, for PDF analyses of the short- and medium-range order. C-S-H samples with Ca/Si = 1.27 were measured

at the ID22 beamline with a monochromatic X-ray beam of 31 keV (λ = 0.4 Å). An angular range of 0.001-16° 2Θ was used with a sample-to-detector distance of d = 1.4 m, corresponding to a Q range of 0.00027-4.37 $Å^{-1}$.

Data were automatically corrected for internal dark current. Two-dimensional images of the scattered intensity were azimuthally integrated using the pyFAI software package (Kieffer and Wright, 2013). The pattern from the empty capillary was subtracted as a background. PDFs were obtained using the PDFGetX3 software (Juhás *et al.*, 2013).

The C-A-S-H samples were measured at the 11-ID-B beamline at the Advanced Photon Source, Argonne National Laboratory. The samples were analysed with a monochromatic X-ray beam of 58.6 keV (λ = 0.2115 Å). The data were collected with a Perkin Elmer XRD 1621 N ES detector and sample-to-detector distance of d = 0.799 m to access a Q range of 0.2-10.4 $Å^{-1}$. Data were automatically corrected for internal dark current. Two-dimensional images of the scattered intensity were azimuthally integrated using the GSAS II software package (Toby and Dreele, 2013).

2.3 Neutron diffraction with isotopic substitution

Neutron diffraction with isotopic substitution (NDIS) experiments (doi:10.5291/ILL-DATA.6-07-37, doi:10.5291/ILL-DATA.6-07-32) of C-S-H samples were performed at the D4 diffractometer (Fischer *et al.*, 2002) of the Institut Laue-Langevin (ILL), France. The incident wavelength of incoming neutrons was 0.4963 Å, which was determined using a Ni powder reference. The samples were loaded in cylindrical (6.05 mm inner diameter, 6.35 mm outer diameter) vanadium containers sealed with a metallic O-ring under controlled atmospheres, using the same RH values as the one used to condition the samples. The sample containers were weighed before and after each measurement to verify that no dehydration had occurred. Measurements were performed at ambient temperature (298 K). Results were corrected for inelasticity, multiple scattering, absorption, instrumental resolution, and background using the CORRECT program (Howe, McGreevy and Zetterstrom, 1998) and a custom-built Python code. Scattering and absorption cross sections were calculated using values from Sears' tables (Sears, 1992). Scattering cross sections values for H and D were modified to account for 0.4963 Å neutrons and for the adsorbed and bulk pore water, which lie outside of neutron's coherence volume. After the above-mentioned experimental corrections, the neutron structure factor S(Q) is obtained, which contains information about the structural organization of the material at the atomic level. Subsequent Fourier transformation of the S(Q) yields the density function G(r), which is equivalent to the more commonly reported X-ray pair distribution function (PDF) (Cuello, 2008), except for the difference in scattering lengths between neutrons and X-rays. Prior to calculation of the G(r), the total S(Q) was multiplied by a window function selected to reduce the effects of the limited momentum transfer range (Lorch, 1969).

NDIS experiments for the C-A-S-H samples were performed at the SANDALS diffractometer, at the ISIS pulsed neutron source, United Kingdom. Experiments were performed at ambient temperature (298 K). The C-A-S-H samples were loaded in flat plate containers made of a "null scattering" alloy of Ti and Zr (35 mm x 35 mm x 2 mm) under controlled atmospheres, at the same RH values as the ones used to condition the samples. The sample containers were weighed before and after each measurement to verify that no dehydration had

occurred. The measurements used neutron beam with wavelengths ranging from 0.05 to 4.95 Å, with a resulting Q range of 0.13 to 50 $Å^{-1}$. Results were corrected for inelasticity, multiple scattering, absorption, instrumental resolution, and background using the Gudrun package (Soper, 2012).

Scattering patterns were obtained by using samples conditioned with two different isotopes of H (^{1}H and D). Results were analysed using the so-called first order difference method, by which all partial structure factors not involving H are cancelled out to obtain a partial structure factor centred on H (i.e. reflecting only contributions of interatomic pairs involving at least one H atom). After Fourier transformation, the resulting G(r) is a partial pair distribution function centred on the H atom (H E Fischer, Barnes and Salmon, 2006; Cuello, 2008). Prior to G(r) calculation, the total S(Q) was multiplied by a window function selected to reduce the effects of the limited momentum transfer range (Lorch, 1969). Additional information on the NDIS method is provided in the Supplementary Information.

2.4 Molecular dynamics simulation

Atomistic simulations were performed at the Cori supercomputer at the National Energy Research Scientific Computing Center (NERSC, USA) using the MD simulation code LAMMPS (Plimpton, 1997), which solves Newton's equations of motion for many-particle systems interacting through pairwise potentials. Interatomic interactions were described using the SPC/E water model (Berendsen, Grigera and Straatsma, 1987), and the CLAYFF model of mineral-water interactions (Cygan, Liang and Kalinichev, 2004). The CLAYFF force field was chosen because of its versatility and successful descriptions of various systems including clay minerals (Wang *et al.*, 2005; Kalinichev, Wang and Kirkpatrick, 2007; Ferrage *et al.*, 2010; Bourg and Sposito, 2011; Bourg and Steefel, 2012), zeolites (Ockwig *et al.*, 2008), and other phases (Skelton *et al.*, 2011; Roscioni, Muccioli and Zannoni, 2017; Fernandez-Martinez *et al.*, 2020) validated against the results of X-ray and neutron scattering experiments (Kalinichev, Wang and Kirkpatrick, 2007; Ferrage *et al.*, 2011) and a variety of other experimental techniques (Wander and Clark, 2008; Underwood and Bourg, 2020).

A variety of force fields has been applied to simulate C-S-H and its crystalline analogues. These include the CLAYFF model, successfully applied to simulate a periodic C-S-H structure by Kalinichev and co-workers (Kalinichev and Kirkpatrick, 2002; Androniuk, 2017), as well as a number of specialised force fields for cementitious systems, such as CSH-FF (Shahsavari, Pellenq and Ulm, 2011), as summarized by Mishra et al. (Mishra *et al.*, 2017) One versatile option is the reactive force field ReaxFF (Van Duin *et al.*, 2001), applied to C-S-H by several authors (Manzano *et al.*, 2012; Abdolhosseini Qomi *et al.*, 2014; Bauchy *et al.*, 2014; Kovačević *et al.*, 2015), which can predict covalent bond dissociation and formation reactions. Unfortunately, comparison of ReaxFF simulation predictions with experimental microstructural data is complicated by its tendency to overestimate unit cell sizes, dissociation of the silica chains (Kovačević *et al.*, 2015), and the formation of silanol groups (Manzano *et al.*, 2012; Abdolhosseini Qomi *et al.*, 2014). Finally, various studies have complemented the force field based approaches outlined above using DFT methods, an approach that provides powerful fundamental insight but remains computationally costly for disordered systems such as C-S-H (Manzano *et al.*, 2012; Kunhi Mohamed *et al.*, 2020).

In the present study, we have applied the CLAYFF force field to model, for the first time, a nanoparticle of C-S-H, including non-satisfied bonds at the edges in *x* and *y* directions. The modifications to the CLAYFF force field required to model the edge surfaces of C-S-H nanoparticles were performed based on the algorithms described in Lammers et al. (Lammers *et al.*, 2017).

Newton's equations of motion were solved using the Verlet algorithm with a 1 fs step. Electrostatic and dispersion interactions beyond a cut-off length of 15 Å were computed by Ewald summation. Water molecules were kept rigid using the SHAKE algorithm. The silica chains were kept semi-rigid by applying equilibrium bond angles Θ_0 taken from the X-ray crystal structure of tobermorite (Bonaccorsi, Merlino and Kampf, 2005), with angle bending force constant K adapted from the INTERFACE force field of Heinz et al.(Heinz *et al.*, 2005). The C-S-H nanoparticle was fixed for the first 15 ps, during which only water molecules were allowed to move, after which all atoms were allowed to move. The system was equilibrated for ~1.5 ns and, then, simulated for ~3.5 ns production runs in the NVT ensemble at T = 298 K. Analyses of the MD trajectories were performed using custom-made Python codes. Atomic structures were converted to PDFs using the DiffPy-CMI package (Kieffer and Wright, 2013) and averaged over multiple frames using a custom-made Python code. For the analysis of H-bonding structure, for simplicity, an H-bond was considered to exist if the intermolecular O-H distance was less than < 2.375 Å (Machesky *et al.*, 2008).

2.5 C-S-H nanoparticle model construction

As a starting structure to build a C-S-H nanoparticle model we used the unit cell parameters and the atomic coordinates of the 14 Å tobermorite model by Bonaccorsi et al. (Bonaccorsi, Merlino and Kampf, 2005). A supercell model was obtained by multiplication of the tobermorite unit cell in the x, y, and z directions. The bulk tobermorite supercell was then cleaved in the z direction along the plane of interlayer Ca ions (removing half of the exposed surface Ca ions), which created an uncharged basal surface identical to that examined in previous studies (Androniuk, 2017). To construct a nanoparticle, the tobermorite structure was then cleaved in the x and y directions, which created surfaces referred to hereafter as the x and y edge surfaces (Figure 1).

To construct these x and y edge surfaces, Ca-O bonds were broken in the x direction and Si-O bonds were ruptured in the y direction. In order to make sure that the edges carried no under coordinated metals (Si or Ca), in agreement with Pauling's bond-valence theory and with the original CLAYFF model, we used the algorithm developed by Lammers et al. (Lammers *et al.*, 2017) (The full list of parameters is reported in Table S2 in the Supplementary Information.) This approach resulted in the definition of two oxygens types not listed in the CLAYFF model. The first is a *deprotonated* silanol (>SiO^-) oxygen (Od, with charge q = -1.525 e), which has been previously used by authors to simulate clay edge surfaces (Tournassat *et al.*, 2016; Collin *et al.*, 2018). The second is a *bridging edge* oxygen (Obe, with q=-1.2875 e), which is coordinated to one structural Si and one structural Ca atom. This bridging edge oxygen is found on the y edges and is under-coordinated by one structural Ca atom compared to CLAYFF bridging oxygen (Ob with q = -1.05 e).

A structure with a ratio of Ca/Si = 1 was then obtained by randomly removing bridging silica tetrahedra from our model tobermorite nanoparticle (Richardson, 2014). To maintain a charge-balanced structure, one of the

bridging oxygens previously coordinated to the removed Si atom was replaced by a hydroxyl group, while the other was converted to a deprotonated silanol oxygen (See Supplementary Information Figure S5). The resulting structure consists of silicate dimers and pentamers, which were shown to give energetically the most stable structures (Kovačević *et al.*, 2015, 2016).The lengths of these chains can be calculated using the Q^n definition describing different silicon environments identified by NMR: Q^1 are the species with one Si neighbour, and Q^2 have two Si neighbours. For this model, the ratio $Q^1/(Q^1+Q^2)$ is higher than generally reported for C-S-H with Ca/Si = 1 and closer to the value expected if Ca/Si = 1.2 (Cong and Kirkpatrick, 1995; Brunet *et al.*, 2004). The reason for this too high number of Q^1 species may be the limited size of the nanoparticle, in which to achieve the Ca/Si = 1 the majority of bridging silicate tetrahedra had to be removed. Overall, we note that the precise structure of C-S-H remains unknown, therefore we have tried to use the simplest C-S-H structure that was consistent with available information.

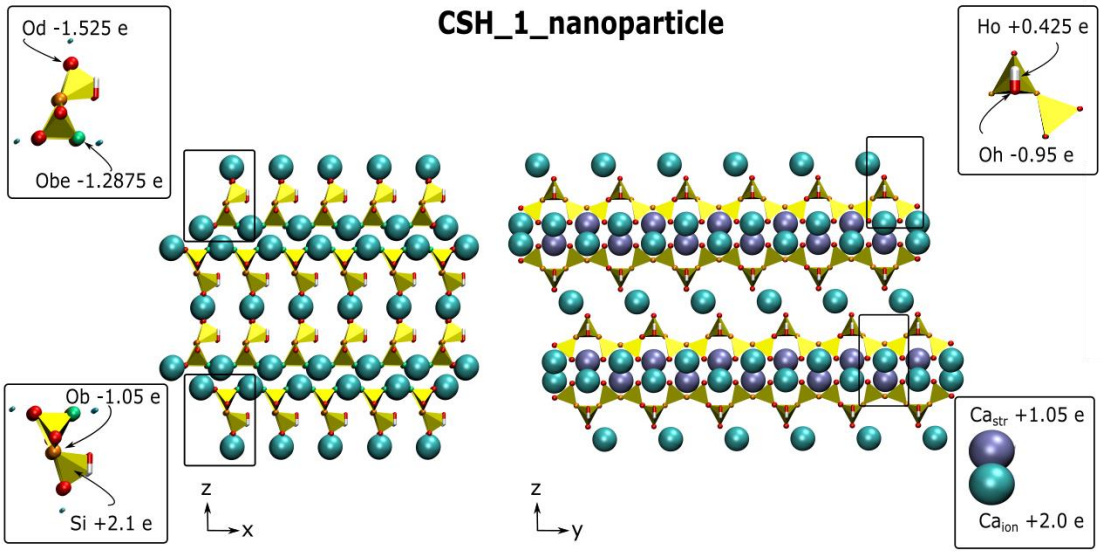

Figure 1. Idealized C-S-H nanoparticle structure in x direction (left) and y direction (right) showing all the atom types: ionic calcium Ca_{ion} (turquoise spheres), structural calcium Ca_{str} (violet spheres), tetrahedral silica Si (yellow polyhedra), bridging oxygens Ob (orange dots), hydroxyl oxygens and hydrogens Oh and Ho (red and white licorice), bridging edge oxygens Obe (green dots), and deprotonated oxygens Od (red dots).

In this work, we simulated two models with two different hydration states. A high hydration state in which the 1892-atom C-S-H nanoparticle is suspended in a water droplet containing 12705 water molecules, which we named CSH_1_98RH, and a low hydration state where the particle is hydrated with only 448 water molecules, CSH_1_55RH. Thus, CSH_1_55RH model contains one monolayer of water, i.e. water within 3 Å from the C-S-H surface. In order to understand better the properties of the adsorbed interfacial water, we compared the first monolayer of water in CSH_1_98RH (referred later to as CSH_1_98RH_monolayer), with the water in CSH_1_55RH. The CSH_1_98RH_monolayer compises about 1000 water molecules, which is roughly 2.2 times more than in CSH_1_55RH. These hydration states were selected to mimic the CSH_1_98RH_h (presence of bulk-

liquid-like water, water to solid ratio 0.32 g/g) and CSH_1_55RH_h experimental systems (presence of only interfacial and interlayer water, water to solid ratio of 0.24 g/g).

2.6 Stoichiometry of water in C-S-H

A precise determination of the stoichiometry and the types of water within the experimental samples is needed to analyze the NDIS data. Both bound water (i.e., water chemically incorporated into the structure of C-S-H) and so-called free water (i.e., water adsorbed on the surfaces and found in the capillary pores of C-S-H) are present in the samples and scatter neutrons differently. Therefore, a precise quantification of the amounts of structural hydroxyls, interlayer water, adsorbed interfacial, and bulk-like water in the capillary pores is paramount.

The C-S-H has a highly variable stoichiometry, which mainly depends on the Ca/Si ratio and hydration state of the sample and is directly related to the abundance of defects in the C-S-H structure (Feldman and Sereda, 1970; Richardson, 2008; Rodriguez *et al.*, 2015; Roosz *et al.*, 2016). In our case, a key challenge was the estimation of the relative amounts of hydroxyls, interlayer water, interfacial water, and bulk pore water at varying RH values. Moreover, for a subset of our samples an additional complication arose from the incomplete deuteration of the deuterated C-S-H samples. To overcome this problem we applied the method described by Roosz et al. (Roosz *et al.*, 2016) and adapted it to the various RH values and deuteration levels of our samples (Roosz *et al.*, 2016). The degrees of deuteration were obtained from ATR-FTIR spectra by comparing the relative areas under the O-H and O-D stretching frequencies at 3500 cm^{-1} and 2600 cm^{-1}, respectively (see Figure S3 in the Supplementary Information).

The total mass of water was obtained from the TGA measurements by assuming that at 300°C all the water in C-S-H had evaporated. Roosz et al. (Roosz *et al.*, 2016) used 150°C as a threshold value judging from the complete collapse of the interlayer spacing at this temperature by XRD. However, careful inspection of our data for C-S-H with various Ca/Si ratios and RH values revealed that 300°C is a more appropriate threshold value to ensure that all bound water has evaporated. This value is lies in the range of temperatures (260-600°C) in which a phase transition between tobermorite 14 Å and tobermorite 9.6 Å is observed, indicating the loss of highly bound water (Yu and Kirkpatrick, 1999). The remaining weight loss from 300°C-600°C was assumed to be due to the loss of hydroxyl groups, as portlandite dehydroxylation occurs around 450°C (Jansen *et al.*, 2018). The maximum temperature was 600°C due to melting temperature of aluminum crucibles used. Roosz et al. noted that the temperature ranges used here are approximate and are sensitive to drying method and temperature (Roosz *et al.*, 2016).

Adsorbed interfacial water content was quantified using the t-plot method, i.e. by plotting the volume of water adsorbed vs. the number of monolayers adsorbed at a certain value of RH. The specific surface area (SSA) and the volume of the monolayer $V_{monolayer}$ were derived from the BET equation. Then the volume of water at a corresponding RH level was calculated by multiplying the statistical number of layers by $V_{monolayer}$. Interlayer water content was estimated by combining the values of the basal spacing (i.e., the d_{001} reflection) from the XRD data and the hysteresis observed by WSI (Table 1). Capillary bulk pore water content was calculated by

subtracting the interlayer and adsorbed water masses from the total water mass. The same procedure was applied to the deuterated samples, taking into account the corresponding degrees of deuteration. The results of the above-described experiments and the stoichiometry for the C-(A)-S-H nanoparticles and the corresponding distribution of water are shown in Tables 1-2.

3 Results and discussion

3.1 Types of water and water content in C-S-H

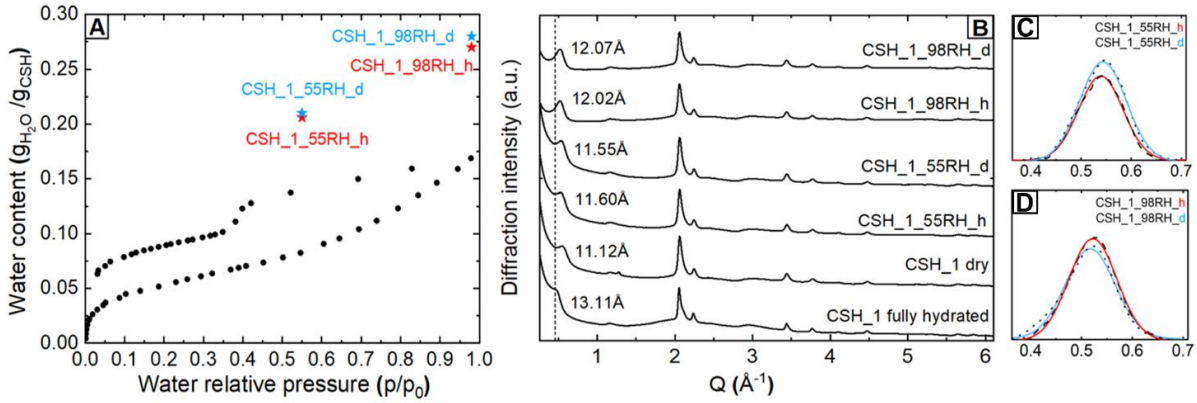

Figure 2. (A) Water adsorption/desorption isotherm of CSH_1. Black circles show WSI results. Red and blue stars indicate the water content deduced from the TGA data for hydrogenated and deuterated samples at 55 and 98% RH. (B) XRD patterns of CSH_1 fully hydrated (dried overnight in the glove-box), CSH_1 dry (oven dried at 40°C in vacuum), and hydrogenated and deuterated CSH_1 at 55 and 98% RH (conditioned for ~1 week). The vertical dashed line shows the Q value associated with the d_{001} reflection of CSH_1 fully hydrated. (C,D) Examples of Pseudo-Voigt fits to the d_{001} reflection.

Adsorption/desorption isotherm for CSH_1 are shown in Figure 2 (other isotherms for C-(A)-S-H are shown in Figure S4 in the Supplementary Information). In accordance with findings of Roosz et al. (Roosz *et al.*, 2016) and the IUPAC classification of Sing et al. (Sing, 1985) the isotherms belong to the type-II with H3 hysteresis loop behavior, signaling the presence of mesopores. The calculated BET SSA decreases with increasing Ca/Si ratios, from 187 m^2/g for CSH_1 to 132 m^2/g for CSH_1p27 (data for other Ca/Si ratios not shown here). The C-A-S-H samples follow a similar trend, with SSA values generally higher for C-A-S-H than for C-S-H (Table 1). The total amount of water derived from the TGA curves for CSH_1 samples is shown in Figure 2. Both deuterated and hydrogenated C-S-H samples hold larger amounts of water as quantified by TGA than by WSI at the same RH values. One possible explanation is the limited equilibration time. The TGA samples were equilibrated in specific RH atmospheres by storing the C-S-H samples in dessicators over the saturated salt solutions for ~1 week. The C-S-H samples measured with WSI were equilibrated for a few hours at each corresponding value of RH (done automatically by the instrument). Therefore, consistent with conclusions of Odler (Odler, 2003), the amount of adsorbed water in the samples equilibrated for longer times (TGA experiment) is larger than in samples with shorter equilibration times (WSI experiment). Another potential difference is the normalization of the WSI points: Roosz et al. (Roosz *et al.*, 2016) normalized adsorbed water amounts by the mass of C-S-H dried at 150°C, estimated to correspond to fully dehydrated C-S-H, whereas we used the mass of C-S-H dried at 50°C, which is a an optimal pre-measurement sample degassing temperature.

As expected, the total mass of water is higher for the 98% RH samples than for the 55% RH samples, as the former contain capillary bulk water as well as interfacial and interlayer water. At 55% RH, samples contain 0.22 to 0.26 g water per g of dry C-S-H, as determined upon heating to 300°C, with the total mass of water decreasing slightly with increasing Ca/Si ratio. The abundance of hydroxyls is similar for all samples of same Ca/Si ratio (Table 2), and the difference in water content is due to varying RH levels. Therefore, at similar RH values and Ca/Si ratios, C-A-S-H samples contain larger amounts of adsorbed water than C-S-H samples due to their higher SSA and monolayer volume.

Table 1. Results of ICP, XRD, TGA, WSI, and ATR FT-IR experiments used to determine the stoichiometry of C-(A)-S-H samples used in NDIS experiment.

	ICP	XRD	Thermogravimetric analysis			Water sorption isotherms (BET method)			ATR FT-IR
Sample name	Ca/Si ratio	d_{001} (Å)	Mass loss (25-300 °C) (g/g_{dryCSH})	Mass loss (300-600°C) (g/g_{dryCSH})	Total mass loss (25-600°C) (g/g_{dryCSH})	BET c-value (-)	$V_{monolayer}$ (cm^3/g)	SSA_{BET} (m^2/g)	D/H ratio
CSH_1_55RH_h	1.04	11.6(1)	0.206	0.039	0.245	69	55	187	0.44
CSH_1_55RH_d		11.5(1)	0.21	0.047	0.257				
CSH_1_98RH_h		12.0(2)	0.27	0.05	0.32				21.4
CSH_1_98RH_d		12.1(2)	0.28	0.062	0.342				
CSH_1.27_55RH_h	1.27	10.3(1)	0.169	0.059	0.225	87	40	132	~0.5
CSH_1.27_55RH_d		10.3(1)	0.175	0.064	0.238				
CASH_1_55RH_h	0.9	12.4(2)	0.22	0.04	0.261	55	108	353	0.52
CASH_1_55RH_d		12.3(2)	0.24	0.045	0.285				
CASH_1.2_55RH_h	1.1	12.4(2)	0.207	0.039	0.246	67	90	291	~0.5
CASH_1.2_55RH_d		12.2(2)	0.216	0.05	0.266				

XRD patterns of C-S-H with varying water content are shown in Figure 2. Results indicate that the d_{001} spacing varies with Ca/Si ratio and RH level. The fully hydrated C-S-H has a full interlayer space with d_{001} around 13.1(1) Å. Upon drying at 40°C in vacuum, the interlayer water evaporates and the d_{001} value decreases to 11.1(1) Å. When these oven-dried samples were subjected to humid atmospheres, interlayer water was partially reincorporated as reflected in the d_{001} values shown in Table 1. The d_{001} reflection value and the total water contents derived from the TGA data were similar for hydrogenated and deuterated samples at the same RH values, with slight differences possibly due to the fitting errors of the XRD data and to the choice of temperature range (25 to 300 °C) used to quantify water content from TGA results. Moreover, the d_{001} reflection does not always uniquely reflect the interlayer spacing, as d_{001} can be modulated by variations in scattering domain

size(Grangeon, Claret, Linard, *et al.*, 2013) and interstratification phenomena (Grangeon, Claret, Linard, *et al.*, 2013; Gaboreau *et al.*, 2020). Nonetheless, previous studies have evidenced a trend towards decreasing d-spacing with increasing Ca/Si ratio (Grangeon, Claret, Linard, *et al.*, 2013; Richardson, 2014), with significant scatter hypothesized to result from differences in drying conditions, hydration levels, and sample handling (Roosz *et al.*, 2016; Gaboreau *et al.*, 2020).

We note, in passing hat the assigned stoichiometry of water in our samples may be, at least to some extent, unique to our dataset as the stoichiometry of water in C-(A)-S-H samples is sensitive to defect density (i.e., Ca/Si and Al/Si ratios) (Feldman and Sereda, 1970; Richardson, 2004; Lothenbach and Nonat, 2015), drying method (Roosz *et al.*, 2016; Gaboreau *et al.*, 2020), hydration level (Richardson, 2008; Roosz *et al.*, 2016) and sample handling (notably exposure to CO_2) in manners that remain incompletely understood.

Table 2. Water stoichiometry in hydrogenated and deuterated C-(A)-S-H samples conditioned at 55% RH and 98% RH (more detailed stoichiometry in Supplementary Information Table S1)

Stoichiometry	**Name**	**H_2O**	**D_2O**
$Ca_1Si_1O_{2.8}$ $(OH)_{0.4}$	CSH_1_55RH_h	1.32	
	CSH_1_55RH_d	0.99	0.42
	CSH_1_98RH_h	3.2	
	CSH_1_98RH_d		3.43
$Ca_1Si_{0.8}O_{2.43}$ $(OH)_{0.59}$	CSH_1.27_55RH_h	0.93	
	CSH_1.27_55RH_d	0.58	0.47
$Ca_1Si_{1.1}Al_{0.11}O_{2.8}$ $(OH)_{0.4}$	CASH_1_55RH_h	1.39	
	CASH_1_55RH_d	0.85	0.81
$Ca_1Si_{0.9}Al_{0.09}O_{2.63}$ $(OH)_{0.45}$	CASH_1.2_55RH_h	1.45	
	CASH_1.2_55RH_d	0.55	0.71

3.2 C-S-H structure

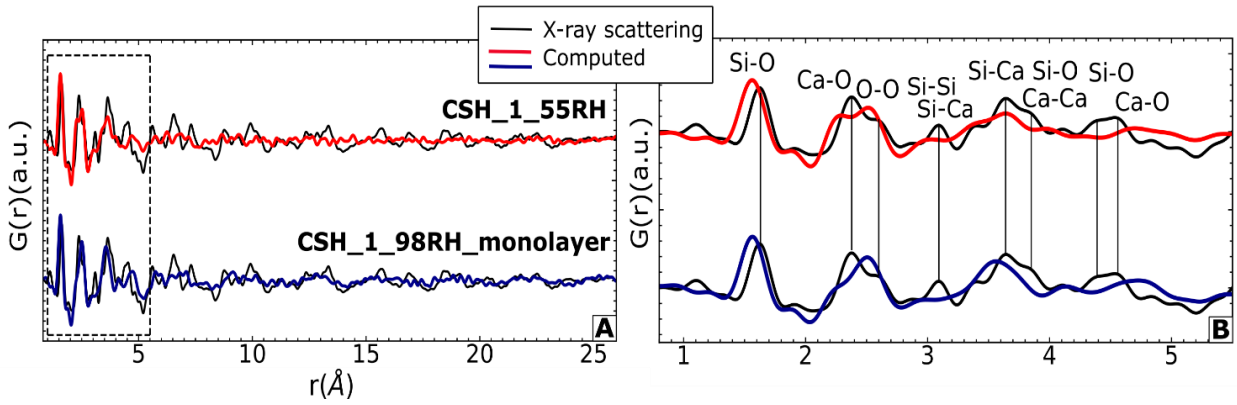

Figure 3. (A) Experimental X-ray PDF of CSH_1_55RH (black lines) compared to the computed X-ray PDF for CSH_1_55RH (red line, top) and CSH_1_98RH_monolayer (darkblue line, bottom); (B) An enlarged region between 1-5.5 Å.

In this section we present the C-S-H models and compare the results of the structural analysis with the experimental X-ray and neutron scattering data. The starting point of our model validation was to compare the experimental X-ray PDF data with the calculated PDFs derived from our MD simulation results (Figure 3). The first observation after comparing the two calculated PDFs is that the CSH_1_98RH_monolayer is less disordered than the CSH_1_55RH structure. The calculated CSH_1_98RH_monolayer PDF broadly reproduces the overall shape of the peaks up to 30 Å, though the intensities of the predicted correlations are generally lower than those observed in the experimental data. The level of discrepancy with the experimental PDFs remains at an acceptable level, with the main peak distances reproduced (though with some shifts) as also reported by previous authors (Abdolhosseini Qomi *et al.*, 2014; Bauchy *et al.*, 2015; Cuesta *et al.*, 2021).

A significantly lower degree of long-range structure is observed in the predicted PDF of the CSH_1_55RH sample, with no obvious correlations beyond 5.5-6 Å. This difference can be explained by the presence of an ordered interlayer space in CSH_1_98RH containing a full monolayer of water, which stabilizes the structure and prevents the C-S-H layers from collapsing into each other. This effect is clearly demonstrated by the difference between the atomic density profiles of structural calcium atoms of the two structures in the direction normal to the basal surface (Figure 4), where the results for CSH_1_55RH show that the layers are highly distorted. A possible explanation of this distortion may reside in the simplifications of the CLAYFF force field (Cygan, Liang and Kalinichev, 2004), notably its reliance on fixed partial charges and its non-bonded representation of interatomic interactions within minerals. Our results suggest that reactive force fields, such as ReaxFF, where atomic charges are calculated at each simulation timestep, may enable a more realistic description of the transition from hydrated to dehydrated C-S-H interlayers (Van Duin *et al.*, 2001; Senftle *et al.*, 2016).

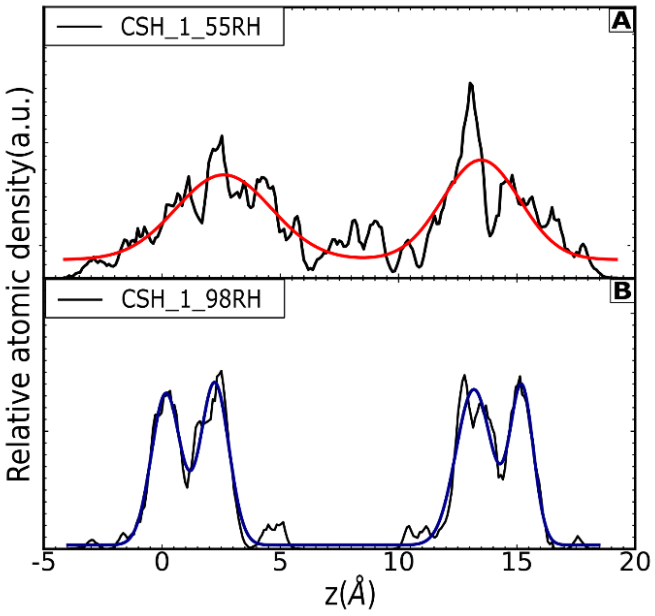

Figure 4. Computed atomic density profiles of structural calcium atoms along the z direction for CSH_1_55RH (A) and CSH_1_98RH (B), with corresponding Gaussian fits in red and blue.

Beyond the unexpectedly high structural distortion in the CSH_1_55RH system highlighted in Figure 4, the interlayer distance calculated by fitting a Gaussian function through the structural calcium density profile yields a predicted basal spacing $d_{001\text{-MD}}$ = 11.0(2) Å, relatively close to the measured value of $d_{001\text{-XRD}}$ = 11.6(1) Å derived from the XRD measurements. In CSH_1_98RH, the higher degree of interlayer hydration yields a larger basal spacing with excellent agreement between simulations and experiments ($d_{001\text{-MD}}$ = 13.0(2) Å vs. $d_{001\text{-XRD}}$ = 13.1(2), as reported in Table 1).

Comparison of X-ray PDF results over shorter distances (Figure 3B) shows that the two structures display similar short-range order. Experimentally, clear peaks are observed at ~1.6 Å and ~2.4 Å corresponding to Si-O and Ca-O correlations, respectively, followed by peaks at ~3.1 Å (Si-Si and Si-Ca), ~3.6 Å (Si-O and Si-Ca), ~3.8 Å (Ca-Ca), and ~4.3 Å (Si-O) (Soyer-Uzun *et al.*, 2012; White *et al.*, 2015). The calculated X-ray PDF data reproduce these correlations, with a slight shift for some of the peaks in both CSH_1_55RH and CSH_1_98RH_monolayer. The shifts in the first two peaks, corresponding to Si-O and Ca-O distances, can be directly attributed to a limitation of the CLAYFF potentials, as these distances derive directly from the force-field parameters. Another explanation for the Si-O distances differing from the experimental values could be the Si-O and Si-O-Si bond and angle parameters, which were adapted from the INTERFACE force field (Heinz *et al.*, 2005).

The shifts in other peaks are likely due to the limitations of the C-S-H model: the size of the modeled nanoparticle is 44 Å at its longest side and the model clearly lacks crystallinity due to the high concentration of defects. Nonetheless, the main correlations up to 5 Å and their corresponding intensities are reasonably reproduced by the model.

The next step in the model validation was to calculate the neutron scattering patterns, i.e. the total and partial S(Q) and G(r) functions (Figure 5). The calculated total structure factor of CSH_1_55RH reproduces the overall shape of the experimental S(Q), but the experimental C-S-H sample presents sharper Bragg peaks, a feature not

captured by the calculated S(Q). As stated above, this is probably due to the limited size of the coherent domain of our nanoparticle, which does not capture the long-range order that is present in some parts of the C-S-H samples. Still, the model reproduces satisfactorily the background oscillations from the diffuse scattering arising from the presence of water and the inherent disorder of the structure (Figure 5A).

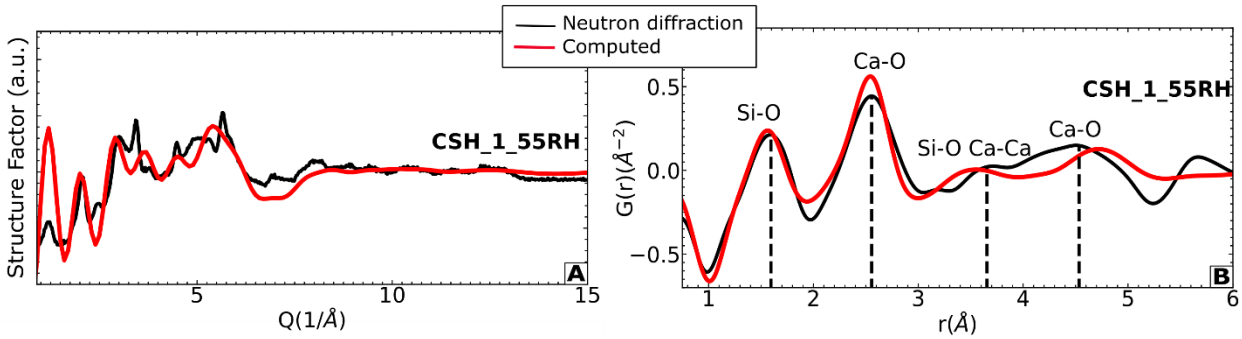

Figure 5. (A) Total neutron structure factor and (B) total neutron G(r) of CSH_1_55RH_h showing the peaks corresponding to the atom pair correlations. Experimental data in black, computed data in red.

Consideration of the total neutron G(r) confirms the broad consistency between experimental and computational results (Figure 5B). We note in passing that the experimental G(r), derived by a Fourier transformation of the structure factor, becomes unreliable at real-space correlation distances below ~0.7 Å, as the scattered intensity was measured only up to a Q-range of 23.5 Å^{-1}.

3.3 Water structure

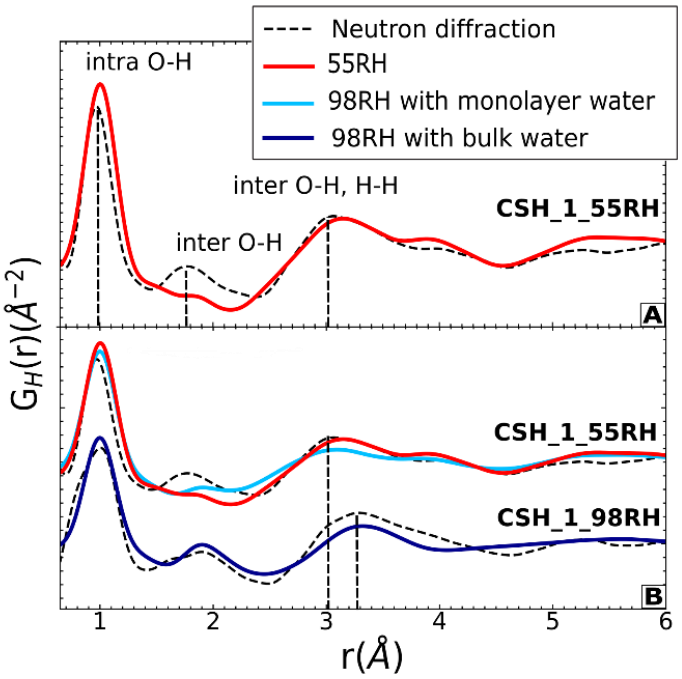

Figure 6. (A) Partial neutron PDF of CSH_1_55RH_d-h and computed PDF CSH_1_55RH, showing the most significant atom correlations. (B) Partial neutron PDF of experimental (dashed black line) vs calculated CSH_1_55RH (red line) and CSH_1_98RH with a monolayer of water (light blue line); experimental (dashed black line) vs calculated CSH_1_98RH with bulk water (dark blue line)

The Fourier transform of the first order difference S(Q) functions results in a partial $G_H(r)$, or partial PDF (Figure 6). The difference function represents the weighted sum of all the correlations functions involving hydrogen atoms. It is, therefore, significantly more sensitive to the structure of water than the results presented in the previous section. The neutron PDF functions in Figure 6 show overall similarities in the peak intensities and positions of the bulk capillary water in experimental CSH_1_98RH_d-h and in the calculated PDF of CSH_1_98RH containing bulk water, shown in dark blue.

The first peak at ~1 Å corresponds to the intra-molecular O-H distance. The second peak at ~1.8 Å corresponds to the intermolecular H-bonding. It is clear from Figure 6B that the position and intensity of the intermolecular H-bonding peak is reproduced by CSH_1_98RH model containing bulk water. The red and light blue curves compare the short-range order of interfacial/interlayer water calculated for the CSH_1_55RH system and for the CSH_1_98RH_monolayer (i.e. system containing only ~1 monolayer of water) against experimental results obtained for CSH_1_55RH (dashed black line).

The main difference between these curves is that the intensity of the measured H-bonding peak of the CSH_1_55RH_d-h sample is underestimated by the CSH_1_55RH model. Possible explanations for this discrepancy include model limitations as well as potential differences in water content (i.e., the real 55RH sample may contain more water) and NDIS data treatment artefacts associated with the Fourier transformation of the S(Q) to derive $G_H(r)$. A key point of agreement of these curves, however, is in the peak at ~3 Å.

This peak results from intermolecular correlations of the O-H and H-H atoms beyond the second nearest neighbor; therefore, it reflects the structure of the H-bonded water network, rather than that of individual H-bonds recorded by the peak at ~1.8 Å. At this ~3 Å peak, our results evidence a significant difference between interfacial/interlayer and bulk-like water, with a shift in peak position from ~3.3 Å (for bulk-liquid-like water) to ~3 Å (for interfacial/interlayer water) captured by both experimental and computational results. In particular, the computed PDF of CSH_1_55RH captures both the intensity and the peak position at ~3 Å of experimental CSH_1_55RH_d-h, thus confirming that the 55% RH results probe interfacial/interlayer water. Further comparison with computed PDF of CSH_1_98RH_monolayer reveals that although the position and broadening of the H-bonding peak deviate somewhat from the CSH_1_55RH data, the position of the intermolecular O-H/H-H peak is within the 3 Å value. A comparison with the bulk-liquid-like water in CSH_1_98RH reveals a shift of this peak position to a value ~0.2 Å longer than for CSH_1_55RH. From this we can conclude that the local environment of the first monolayer of water on the surface of C-S-H is very similar to C-S-H containing only interfacial water. Likewise, the structure of water further than ~1 monolayer from the surface strongly resembles that of bulk liquid water.

Comparison with NDIS results obtained for other samples reveals that the same features of the short-range order of water are found for the CSH_1.27 sample (Figure 7A) as well as for the C-A-S-H samples with Ca/Si = 1 and 1.2. The experimental C-A-S-H PDFs have lower peak intensities and broader peaks than the corresponding C-S-H PDFs (Figure 7B), likely because a smoothing window was required to compensate for the higher signal-to-noise ratio of the C-A-S-H data (particularly when extracting the difference signal between the deuterated and hydrogenated samples).

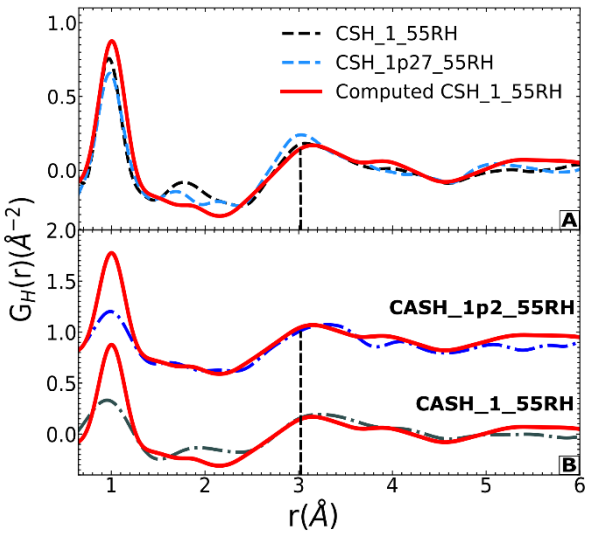

Figure 7. (A) Partial neutron PDFs of the experimental CSH_1p27_55RH_d-h (dashed blue line) compared to experimental and computed CSH_1_55RH (red line). (B) Partial neutron PDFs of experimental CASH_1_55RH_d-h (dash dotted gray line) and CASH_1p2_55RH_d-h (dash dotted blue line) compared to the computed CSH_1_55RH.

The similar local structure of interfacial/interlayer water in our C-A-S-H and C-S-H samples is consistent with a first-order approximation according to which the structure of C-A-S-H is similar to that obtained by substituting bridging Si by Al in C-S-H (Richardson, 2014). In our samples, one tenth of Si atoms were substituted by Al, apparently with only limited effect on the structure of interfacial/interlayer water. At higher Al/Si ratios, however, the structure of water in C-A-S-H may be different due to the increased density of surface Ca ions required to charge balance structural Al.

Grangeon et al. (2017) showed that the maximum Ca/Si ratio achievable by removing bridging silica tetrahedra without precipitating portlandite is ~1.25 (Grangeon *et al.*, 2017). Therefore, we suggest that the local environment of water is dictated by the manner in which defects are introduced. Considering that in CSH_1_55RH and CSH_1.27_55RH defects can be created by removing the bridging silica tetrahedra, we presume that the structure of interfacial/interlayer water is similar for samples with these two Ca/Si values. To achieve higher Ca/Si ratios it would be necessary to introduce calcium ions in the interlayer or in the larger pores, leading to portlandite precipitation and, thus, probably creating a different water environment.

3.4 Distribution of interfacial and interlayer water on a C-S-H nanoparticle

Predicted water distribution within our two C-S-H nanoparticulate systems, CSH_1_55RH and CSH_1_98RH_monolayer, is shown in Figure 8. As mentioned above, a first qualitative assessment reveals that the structure of the CSH_1_98RH model is less distorted than that of CSH_1_55RH. This difference in crystallinity is observed at distances greater than ~6 Å in the experimental PDFs (see Figure 3). This is likely due to the fact that the interlayer space of CSH_1_98RH is filled with water molecules, which have a stabilizing influence on the interlayer, affecting the crystallinity of the particle (Jiménez-Ruiz *et al.*, 2017). Although the structural distortion of our CSH_1_55RH model may reflect a limitation of the force field used here, another potential explanation is the small size and isolated nature of our model C-S-H nanoparticle. In real C-S-H samples, nanoparticles are

agglomerated together within a larger solid matrix, which may help mitigate the stresses associated with sample drying. Indeed, whereas the diffuse scattering is well represented (see Figure 5A) in the calculated diffraction patterns for our CSH nanoparticle, these calculated patterns lack the Bragg peaks observed in the experimental patterns. This implies that the nanoparticle is probably too small to possess a coherent domain size able to reproduce the periodicity of the real sample. In small nanoparticles, the comparatively high importance of surface energy (vs. bulk energy) can result in significant structural relaxation (Banfield and Zhang, 2001), as observed in our 55RH model. In this context, the greater distortion of the 55RH than the 98RH model suggests more unfavorable interfacial energy at the lower hydration level, in agreement with almost twice lower coordination number of Ca^{2+} with water molecules, $N_{Ca\text{-}H2O}$, predicted for CSH_1_55RH than for CSH_1_98RH_monolayer (H_2O per Ca^{2+} ~1.78 vs. ~3.44, respectively).

Bearing in mind the above-mentioned differences in crystallinity between the two models, we now characterise the water distribution and H-bonding characteristics of interfacial and interlayer water. Due to the presence of highly negatively charged deprotonated surface oxygens (Od) and bridging edge oxygens (Obe), the surface of C-S-H is negatively charged. This controls the distribution of Ca^{2+} ions on the surfaces and in the interstitial cavities created by defects. In turn, these adsorbed Ca^{2+} ions are strong centers of charge that generate hydrophilic centers at the surface (Ohtaki and Radnai, 1993; Bonnaud, Coasne and Pellenq, 2012; Loganathan *et al.*, 2016). According to our simulations, most calcium ions are bonded to the deprotonated oxygen atoms at the surface, forming inner-sphere complexes (Charlet, 1994), and they complete their coordination shell using water molecules. Therefore, for both CSH_1_55RH and CSH_1_98RH_monolayer, we discriminate between two types of water molecules on the C-S-H surface: (i) type I water molecules are those that coordinate surface Ca ions, while (ii) type II water includes all other interfacial/interlayer water molecules. Importantly, type I water molecules hardly accept any H-bonds, since the O atom of these molecules points towards the Ca^{2+} ion as shown by the results of neutron diffraction(Marcus, 1988) and molecular orbital calculations (Ohtaki and Radnai, 1993).

According to our simulations, in CSH_1_55RH, type I water represents ~61% of the water in the sample, which is roughly 1.78 H_2O per Ca ion. The distribution of locations sampled by type I and type II water molecules during a 5 ns trajectory is highlighted in Figure 8 as red and grey dots, respectively. Both types of water predominantly form thin films on the basal and edge surfaces, representing ~89.3% of the total water, with the remainder observed in the distorted interlayer. Type I water molecules donate the majority of H-bonds to deprotonated silanol oxygens (Od) and to water oxygens (Ow). The deprotonated oxygens receive about 0.54 H-bonds per Od with an average bond length (d) of 1.73 Å, and water oxygens receive roughly 0.3 H-bonds per Ow with d = 1.99 Å. Type II water molecules interact more strongly with deprotonated silanol oxygens (~0.71 H-bonds accepted per Od with d = 1.66 Å) and less strongly with water oxygens (~0.12 H-bonds received per Ow with d = 2.06 Å). Both types of water donate fewer H-bonds to the hydroxyl groups of surface silanols (~0.2 H-bonds in total per Oh with d = 1.97 Å).

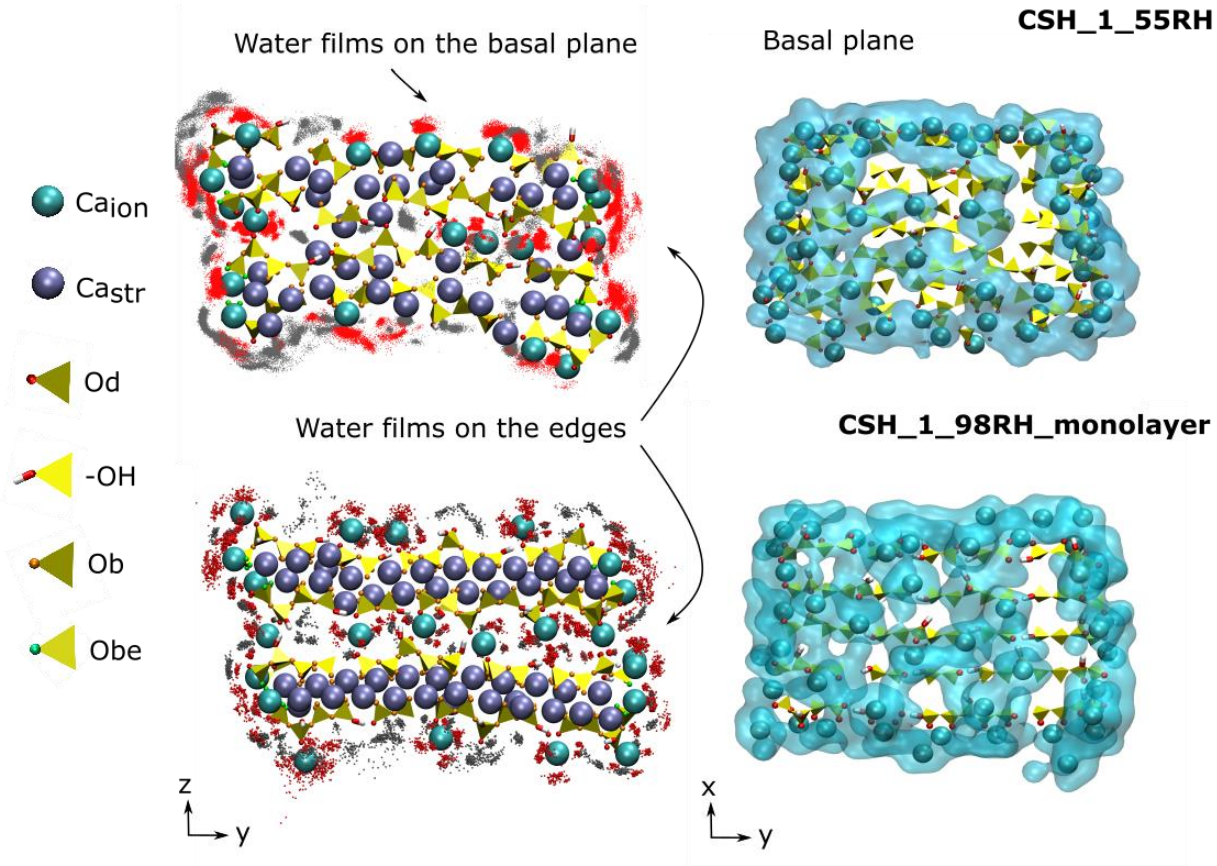

Figure 8. (top left) Cross-section of CSH_1_55RH after ~5 ns. Type I and type II water oxygens (red and grey dots, respectively) are shown as a cloud of coordinates sampled over a ~5 ns trajectory. (bottom left) Same as the previous panel for CSH_1_98RH_monolayer sampled over ~0.1 ns. Water forms thin films on the external surfaces and in the interlayer nanopore. (top and bottom right) Distribution of water on the upper external basal surface of the CSH_1_55RH and CSH_1_98RH nanoparticles. Water molecules (transparent blue surfaces) surround Ca^{2+} ions (turquoise spheres), signaling that these cations correspond to the most hydrophilic areas on the C-S-H surface.

The cross-section of CSH_1_98RH_monolayer reveals that the structure is much less distorted than that of CSH_1_55RH (Figure 8). The relative abundance of water in CSH_1_98RH allows the interlayer to be filled with water as seen by the interlayer spacing of about 13 Å (XRD value 13.1(2) Å for a fully hydrated C-S-H, Supplementary Information Figure S1C). The water molecules coordinated around calcium ions in the interlayer prevent the C-S-H layers from collapsing into each other (Figure 4).

In this simulation, the amount of water present in the interlayer is ~26% of the total. Hence, the ratio of interlayer water to the interfacial water is roughly 2.5 times that of CSH_1_55RH. Not surprisingly, the larger share of the interlayer water affects the overall distribution and H-bonding behaviour of water molecules in CSH_1_98RH. More precisely, in our CSH_1_98RH_monolayer, type I water comprises ~53% of the total (i.e. about 530 out of 1000 water molecules found in the first monolayer from the C-S-H surface), so approximately 3.44 H_2O per Ca^{2+}. (Figure 8). As in CSH_1_55RH, type I water donates the majority of H-bonds to the surface of C-S-H and to other water molecules. However, it donates not only to Od (~0.8 H-bonds received per Od with d = 1.68 Å), but also to the surface bridging

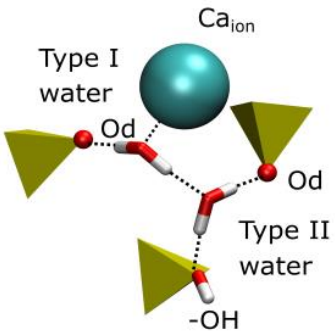

Figure 9. Examples of some of the typical connections formed at the surfaces of the C-S-H nanoparticle. Ca ions (turquoise) coordinate type I water oxygens (red and white licorice), which donate H-bonds to deprotonated oxygens (red sphere) of surface silanols (yellow polyhedra) and to type II water molecules. The type II water molecules accept H-bonds from type I water molecules and donate H-bonds to deprotonated oxygens (red sphere) of surface silanols (yellow polyhedra) and to the oxygen (red and white licorice) of surface silanols (yellow polyhedra).

oxygens Ob (~0.21 H-bonds per Ob, d = 1.85 Å), and bridging edge oxygens Obe (~0.24 H-bonds accepted per Obe, d = 1.91 Å). Type II water molecules donate a significant majority of H-bonds to the surface deprotonated oxygens Od, about 1.34 H-bonds per Od with d = 1.66 Å.

The rest of H-bonds is shared between other water molecules (~0.25 H-bonds received per Ow, d = 1.96 Å), and surface bridging oxygens (~0.19 H-bonds per Ob, d = 1.86 Å) and hydroxyl oxygens (~0.42 H-bonds per Oh atom, d = 1.95 Å). The latter is contrary to CSH_1_55RH, where silanol hydroxyl groups are quite hydrophobic. The reason is likely due to the abundance of water molecules in CSH_1_98RH, therefore the availability of H-bonding opportunities, and the possibility of creating an H-bonding network.

Overall, the interfacial water properties and structure are mostly similar in the partially hydrated system (CSH_1_55RH) and in the first monolayer of the fully hydrated system (CSF_1_98RH_monolayer). Observed differences in interfacial water structure in the two systems are ascribed to the greater degree of Ca hydration, fully hydrated interlayer, and the presence of bulk water in the fully hydrated system.

4 Conclusion

We have established an *in silico* nanoparticle model for C-S-H and validated it using experimental data. This combined approach enabled us to study the properties of the different types of water present in C-S-H conditioned at varying relative humidities. We also compared our results to a low-CO_2 substitute for C-S-H, C-A-S-H. The results show the same structural characteristics of water for the C-S-H samples with the two Ca/Si ratios studied (1 and 1.27) as well as for the C-A-S-H samples. The main mechanism for water adsorption is the coordination of water by hydrophilic Ca^{2+} ions, which induces a strong H-bond network with other water molecules and with surface oxygen atoms. The silanol groups play a minor role in this wettability mechanism: the C-S-H surface is characterized by a combination of wet and dry regions, where wet areas are dominated by the presence of hydrophilic calcium ions with strong hydration shells (Figure 8), whereas dry areas expose only silica chains and silanol hydroxyls.

The results of the simulations show that the presence of water in C-S-H can have a strong influence on the atomistic-level integrity of the layered structure. As shown in Figures 3 and 8, the more hydrated structure shows a larger degree of mesoscale ordering, with a larger domain coherent size. This effect could be due to the fact that the modelled C-S-H nanoparticle contained only two silicate layers, such that the interactions of water molecules with the surface played a large role in the total intermolecular interactions within the whole system. Similar results, where the water molecules exert a strong influence on the bulk properties of inorganic nanoparticles, have been presented previously for other systems (Gilbert *et al.*, 2006).

The wettability mechanism depicted here is susceptible to change at higher Ca/Si ratios, with the formation of secondary portlandite. Whereas the exact location of the (nano)portlandite phase is still a matter of discussion (Grangeon *et al.*, 2017), its presence and different surface structure could modify the overall structural characteristics of the adsorbed water. Future experiments with samples containing higher Ca/Si ratios should be performed to verify this hypothesis.

5 Acknowledgements

Use of the Geochemistry-Mineralogy platform at ISTerre is acknowledged. A.F.-M. and A.E.S.V.-D. acknowledge funding from the ANR-JCJC 'NUANCE' project (grant ANR-17-CE08-0057). We thank the IDEX mobility scholarship program of the University of Grenoble-Alpes for supporting a research stay at Princeton University. We thank the Institut Laue-Langevin, ISIS Neutron and Muon Source, European Synchrotron Radiation Facility, and Advanced Proton Source for allocated beamtimes. I.C.B. was supported by the U.S. Department of Energy, Office of Science, Office of Basic Energy Sciences, Geosciences Program under Award DE-SC0018419. Molecular dynamics simulations were performed using resources of the National Energy Research Scientific Computing Center (NERSC), which is supported by the U.S. Department of Energy, Office of Science, under Award DE-AC02-05CH11231. This research used resources of the Advanced Photon Source, a U.S. DOE Office of Science User Facility operated for the DOE Office of Science by Argonne National Laboratory under Contract No. DE-AC02-06CH11357. Leighanne C. Gallington is thanked for her help during data acquisition at 11-ID-B (APS, ANL). Z.Z. thanks BRGM for cofounding her PhD.

Chapter 5 Dynamics of water in calcium silicate hydrates

5.1. Introduction

The dynamics of water in cement and particularly within the C-S-H phase have been a subject of years of research. The importance of understanding diffusional behavior of water lies in its importance to influence the mechanical properties of cement, the durability of concrete structures, and ionic transportation processes that are relevant, for example, for nuclear waste disposal systems (Bordallo, Aldridge and Desmedt, 2006).

Different methods have been used to study the dynamics of water in cementitious systems, such as infra-red and Raman spectroscopies, Nuclear Magnetic Resonance (NMR), Broadband Dielectric Spectroscopy, Inelastic (INS) and Quasielastic Neutron Scattering (QENS), ab-initio and Molecular Dynamics (MD) simulations (Fischer *et al.*, 2014). Each of these techniques provides a different view of the water dynamics, probing different time domains.

^{1}H NMR relaxation has been applied extensively to study cement pore structure, water distribution and dynamics within the pores from the late 70's (Blinc *et al.*, 1978). The popularity of the technique is explained by its non-destructive and non-invasive nature, though it is not exempt from drawbacks, which include a complexity of spectra interpretation and possible paramagnetic impurities in the cementitious materials hindering experimental results (Valori, McDonald and Scrivener, 2013). In a ^{1}H NMR relaxation experiment the ^{1}H nuclei are imposed a coherent precession, i.e. all nuclei rotate together in phase. This initial coherent precession of the nuclei can be stimulated by a short radio frequency pulse sent to a nuclei that shifts the magnetization away from the applied field direction, and disturbs the equilibrium Boltzmann population.

Two important magnitudes in ^{1}H NMR relaxation studies are the T_1 and T_2 relaxation times. The T_2 is a spin-spin relaxation time, which shows the loss of rotational phase coherence of nuclei that are precessing initially together. The T_1 is known as the spin-lattice relaxation time, which is the time at which the nuclei return to being aligned with the magnetic field, and recover thermal equilibrium by exchanging energy with the lattice (the sample to which the nuclei belong). The T_1 and T_2 time measurements give information about the rotations and translations of water within the sample over wide range of timescales, thus allowing to get insight into pore size distribution and microstructure. Generally, the dynamics of water measured by ^{1}H NMR relaxation experiments probe three different timescales: (i) The hopping time of ~1.3 ns for adsorbed water diffusing on the pore surface; (ii) The residency time of ~13 μs for water molecules adsorbed on the pore surface; (iii) The water exchanged between interlayer and gel pores in about 5 ms (Valori, McDonald and Scrivener, 2013).

Barberon, Korb et al. (2003) performed nuclear magnetic relaxation dispersion (NMRD) measurements to probe the water dynamics during hydration of a cement sample. The authors found that at the hopping time of water in the cement surface was about 0.7 ns for the first 7h, and progressively became roughly 1.3 ns after 12 h (Barberon *et al.*, 2003). Previously, Korb et al. (Korb, Whaley Hodges and

Bryant, 1998) had showed that a ~1.3 ns value for hopping time of water on the cement surface was also applicable for other cementitious systems. Similar values for the hopping times were found using MD simulations of water on tobermorite surfaces by Kalinichev et al (Kalinichev, Wang and Kirkpatrick, 2007) and on C-S-H by Qomi et al.(Qomi *et al.*, 2014).

Looking at longer time-scales, McDonald et al. (McDonald *et al.*, 2005) performed two-dimensional T_1-T_2 correlation experiments of hydrating cement pastes, and derived a relationship of $T_1=4T_2$ (related exponentially). From these experiments, a residency time of about 13 μs for the water molecules adsorbed on the cement pore surface was derived (Valori, McDonald and Scrivener, 2013). Monteilhet, Korb and co-workers (2006) measured the exchange of water between interlayer and gel pores, obtaining a value of about 5 ms for 3-5 day old samples. This relatively long exchange time was explained by steric conditions hindering migration of water from Ca ions in the interlayer. These values were subsequently used to calculate self-diffusion coefficient of water $D_{H2O}=5x10^{-10}$ m^2/s, which is in agreement with the value $D_{H2O}=6x10^{-10}$ m^2/s obtained by Kalinichev et al. for pore water above the interface (Kalinichev, Wang and Kirkpatrick, 2007). The absence of signal for older samples was suggested to be due to increased confinement and gel tortuosity as sample ages (Monteilhet *et al.*, 2006; Valori, McDonald and Scrivener, 2013).

Neutron scattering techniques are particularly well adapted to the study of water adsorbed on cement pores. They cover time domains from the ms (neutron spin-echo) to the ps (neutron spectroscopy), thus allowing the study of interfacial processes of water diffusion and exchange. The focus here will be given to incoherent neutron scattering techniques, which give information about the correlations of 'single particles'. This includes Brownian diffusion, vibrational and rotational motions of molecules in liquids and in solids (Eckert, 1992). The study of these motions makes the INS method very similar to IR and Raman spectroscopies.

The water molecule can perform different types of motion simultaneously: translational and rotational diffusion motions, while having internal vibrational modes. The translational diffusion is probed by QENS, which measures the autocorrelation function of hydrogen atoms' movements. QENS spectra are centered on zero energy transfer, and have the form of a Lorentzian function, where the width in energy tells about the timescale of the diffusive motion (Eckert, 1992). In QENS experiments, neutrons interact with the large incoherent cross-section of the hydrogen atom, probing the molecular motions from the nanosecond to picosecond scale (Amann-Winkel *et al.*, 2016). Vibrational neutron spectroscopy has some advantages over optical spectroscopies: i) Since neutrons interact with the nuclei, there are no selections rules; ii) neutron scattering methods are non-destructive; iii) Experimental neutron spectroscopy data can be easily complemented and/or interpreted by computer simulated data, using molecular simulation techniques such as Density Functional Theory of Force-Field based MD (Mitchell *et al.*, 2005). Drawbacks of these methods include the complexity of data treatment, difficult experiments which require rigorous planning and the need of large specimens, expensive experiments, and in many cases the need of complementary calculated data.

Livingston et al. in 1994 were one of the first to use QENS to classify evaporable and non-evaporable water from cement pores. Specifically, the authors noted that non-evaporable water consists of

structural OH groups, as well as bound hydration water (interlayer water). From the point of view of the dynamics, the difference between the two resided in the fact that OH groups do not have translational or rotational mode of motion, but only vibrational, and that bound water has a rotational freedom of movement, but not translational. The adsorbed water was classified as having rotational, vibrational, and translational modes of motion, with the latter being described as confined, jump diffusion. On the opposite, capillary free water showed all modes of motion, the translational mode being characterized as unconfined, free diffusion (Livingston *et al.*, 1994). As it will be shown in this chapter, these conclusions, which were obtained from QENS data, are in accordance with the results of our MD simulations: we found that interlayer water is nearly immobile, whilst interfacial adsorbed water shows quite restrained jump-like diffusion.

Inelastic neutron scattering studies of water confined in different systems, ranging from Vycor glass (Bellissent-Funel, Chen and Zanotti, 1995), chalk (Berg *et al.*, 2017), sol-gel silica glass (Crupi *et al.*, 2003) to clay minerals (Hunvik *et al.*, 2020) etc., have revealed a particular signature of the confinement, with a flattening and attenuation of the translational modes present in ice Ih at 8 and 20 meV (experiments are typically performed at low temperatures to limit the thermal effects on the vibrations) (Bellissent-Funel and Teixeira, 1991; Faraone *et al.*, 2004; Larsen *et al.*, 2020). This signature can be used as a proxy for water 'structured' by the presence of an interface.

Bordallo et al. (2006) studied water dynamics in hardened cement paste using QENS and INS techniques. The authors observed three characteristic maxima at about 10, 40, and 80 meV (Bordallo, Aldridge and Desmedt, 2006). The peak at about 10 meV had been assigned earlier to the translations of water molecules inside the cage by Bellisent-Funnel et al. and by Faraone et al. (Faraone *et al.*, 2004). These last authors had investigated the dynamics of water in cement paste by means of QENS and INS using the so-called relaxing cage models for supercooled water, the reasoning being that confined water has the properties comparable to supercooled water (Bellissent-Funel, Chen and Zanotti, 1995). The low energy peaks at ~10 and 30 meV were attributed to the translations of water inside the cage. The peak at 331 cm^{-1} (40 meV) is well-known as a signal of lattice modes involving the translational oscillations of the hydroxyl group attached to Ca in Ca-OH (FitzGerald *et al.*, 1999). As it was shown in a study by Thomas using INS, at Ca/Si=1 there is no portlandite signal (Thomas *et al.*, 2003). Nemes et al. (2006) performed QENS and INS studies of hydrated cement paste under varying RH levels. The INS data showed a peak at 6 meV attributed to water translations which exhibited a RH dependence, thus identified as coming from interfacial/interlayer water. (Nemes, Neumann and Livingston, 2006).

Bordallo et al.(Bordallo, Aldridge and Desmedt, 2006) performed QENS experiments on cement pastes obtaining diffusion coefficients of ~10^{-9} m^2/s for unbound water (bulk-like capillary pore water), slower for the gel pore water ~10^{-10} m^2/s (physically bound water in pores less than 100 Å in diameter), and in a time scale longer than the ns (and therefore inaccessible in these experiments) for chemically bound water. Fratini et al. using QENS identified both 'glassy' water and 'immobile' (or chemically bound) water components in a curing cement paste. The authors showed that the diffusion of chemically bound water was also on time scales beyond the ones of the experiment, while glassy water continuously converts to immobile water as cement paste aged (Fratini *et al.*, 2002).

Molecular Dynamics simulations can probe the dynamics of water in confined systems from the ps to the ns range. This allows direct comparisons with experimental results from ^{1}H NMR, INS, QENS, and other experimental techniques, allowing therefore to get insights into dynamical behavior of confined water at the nanoscale. The major drawback of applying MD simulations to study the dynamics of water is the necessity of long simulations with small timesteps, which are computationally costly. Long simulation times (up to 10 ns) for large systems (10^3 atoms) with fine time-steps (~1 fs) are necessary to probe interfacial phenomena and fast vibrational dynamics near interfaces, resulting in long (~weeks/months) simulation times (Abdolhosseini Qomi *et al.*, 2021).

Kalinichev and co-workers performed one of the earliest successful applications of MD simulations to understand the dynamics of confined water in tobermorite (a crystalline counterpart to C-S-H). The authors made use of the CLAYFF force field and SPC water model to study the diffusion of water at the external faces and the interlayer of tobermorite. They reported diffusion coefficients of $5.0x10^{-11}$ m^2/s for water in the channels of tobermorite and of $6.0x10^{-10}$ m^2/s for water on the external interface. These values were significantly lower than the one of bulk water $2.3x10^{-9}$ m^2/s (Kalinichev, Wang and Kirkpatrick, 2007), showing the strong control of the dynamics by the interface. Their calculation was supported by ^{1}H NMRD measurements performed by Korb, Barberon and co-workers (Korb, Whaley Hodges and Bryant, 1998; Barberon *et al.*, 2003).

Youssef et al. (2011)(Youssef, Pellenq and Yildiz, 2011) performed molecular simulations of water in C-S-H, showing a 'glassy' behavior of water in the interlayer, similarly to the report by Faraone et al.(Faraone *et al.*, 2004) and Fratini et al. (Fratini *et al.*, 2002) using the QENS method. This 'glassy' behavior is reflected in the mean-square displacement of water molecues, which consisted of three stages: a ballistic motion at short timescales ($t < 0.4$ ps), cage behavior at intermediate timescales (0.4 ps $< t < 400$ ps), and diffusive motion at longer times. The 'glassy' behavior was explained to be due to heterogeneous hydrogen bond strengths between the water molecules and the highly hydrophilic C-S-H walls.

Qomi et al. further developed the structural model of C-S-H by Pellenq et al. to create a set of more than 150 samples of C-S-H of varying Ca/Si ratios. In line with findings of Youssef et al. (Youssef, Pellenq and Yildiz, 2011) they found that the interlayer spacing is quasi two-dimensional and the diffusion proceeds in the direction of layers. The authors reported the self-diffusion of water in the interlayer 10 times smaller than observed by QENS, and 1000 smaller than in bulk water, so to be in the order of 10^{-12} m^2/s (Qomi *et al.*, 2014).

As this brief review shows, the dynamics of confined water have been studied by various techniques, which are extensively summarized in a recent review by Qomi et al. (Abdolhosseini Qomi *et al.*, 2021).

This compilation of experimental studies converges towards a classification of water components in cement pastes as a function of the dynamical properties, with three compartments: (i) capillary (bulk-like) water; (ii) gel water (water confined in pores); (iii) chemically bound water (hydroxyls and water molecules with restricted motion. A characteristic of these studies is that they have been performed on cement pastes, and sometimes on concrete samples. This has, on one hand, the advantage of capturing

the complexity of the systems, which contain many different phases and different water contents (which can vary much from one study to another). On the other hand, this 'macroscopic' approach in the sample preparation prevents the understanding of the control that particular structural elements such as the pores or surfaces within C-S-H can have over the total dynamics of the system. Our study is limited to C-S-H precisely for this reason: to provide a mechanistic understanding of the water dynamics on the most abundant phase of Portland cement, C-S-H. Our approach includes a combination of Inelasic Incoherent Neutrons Scattering Experiment, complemented by MD simulations, WSI and TGA data, for varying Ca/Si and RH levels. First, we discuss the influence of Ca/Si ratios and varying RH levels in our experimental IINS data. Then we use the calculated GDOS data to deepen the understanding of experimental data. Finally, we calculate the diffusion constant for interfacial and interlayer water, and compare them to that of bulk water.

5.2. Materials and methods

5.2.1. Sample preparation

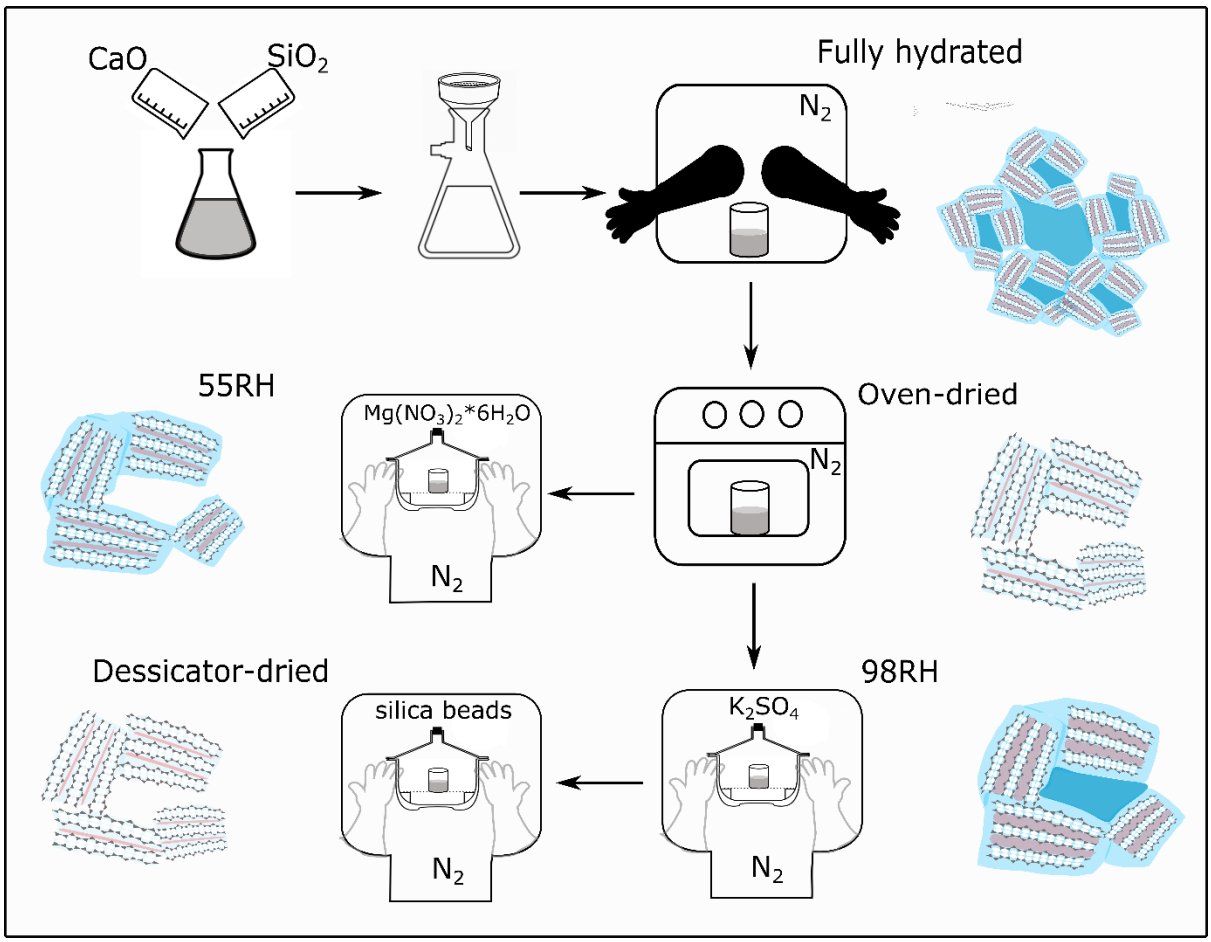

Figure 5.2.1.1. Schematic drawing of a synthesis protocol and a schematic representation of C-(A)-S-H samples of varying water content.

C-S-H samples of Ca/Si=1, 1.2, and 1.33 were synthesized by reacting calcium oxide and fumed silica in water inside a N_2 wet glove-box. Calcium oxide was obtained by calcination of $CaCO_3$ (Sigma-Aldrich, Fluka, Bioultra) at 1000 °C for 18 h and stored in a vacuum desiccator until usage. Fumed silica SiO_2 (Sigma-Aldrich, Aerosil 200) was placed in an oven at 40°C for ~24 h to remove physisorbed water prior to each experiment. Deionized water was boiled and degassed with N_2 gas to remove all dissolved CO_2. The quantities of calcium oxide and fumed silica required to prepare C-S-H of predetermined stoichiometry were calculated using the method reported by Haas and Nonat (Haas and Nonat, 2015) (Table 5.2.1.1).

Table 5.2.1.1. Amounts of reagents used for the synthesis of C-S-H samples.

Ca/Si ratio	Sample	CaO (mmol)	CaO (mmol/mL)	CaO (grams)	SiO_2 (mmol)	SiO_2 (mmol/mL)	SiO_2 (grams)	Total V(H_2O) (mL)
1	CSH_1	163.02	0.1716	9.11	152	0.16	9.12	1900
1.2	CSH_1.2	73.18	0.1825	4.1	58.72	0.1468	3.53	800
1.33	CSH_1.33	79.4	0.197	4.45	59.5	0.146	3.57	800

Samples were reacted under stirring conditions for ~1 month in High Density Polyethylene (HDPE) bottles inside a wet N_2 glove-box, then filtered using Millipore® filter paper (0.22 μm, GSW1 UM), and wet C-S-H residue was left to dry inside the glove-box for ~12 h. A part of these C-S-H samples was put aside to have a 'fully-hydrated' C-S-H. The remaining C-S-H was oven-dried at 40 °C in a vacuum oven for ~24 h. A part of these samples was put aside to have 'oven-dried' C-S-H. After drying, samples were conditioned at controlled RH of 55%RH and 98%RH using saturated salt solutions of $Mg(NO_3)_2{\cdot}6H_2O$ or K_2SO_4, respectively for ~1 week (Figure 5.2.1.1). Then samples conditioned at 98%RH were stored inside the vacuum desiccators containing silica beads, to remove any adsorbed and bulk water.

We refer to these samples as 'desiccator-dried' samples. As samples are sensitive to atmospheric CO_2, all synthesis and conditioning processes were performed under an inert gas atmosphere of N_2. The C-A-S-H samples with Ca/Si=0.9, and Al/Si=0.1, were synthesized following the protocol that can be found elsewhere (Roosz *et al.*, 2018). C-A-S-H samples were conditioned under 55% and 98%RH for ~1 month. Such different equilibration times were due to the availability of the neutron beamtime. We note that any future experiments involving water adsorption in C-(A)-S-H should be done in the same timeframe to eliminate the equilibration time effect.

Following these conditioning protocols, we obtained C-S-H samples labeled CSH_Ca/Si_%RH, where %RH is the relative humidity value at which they were conditioned (Table 5.2.1.2). The C-A-S-H samples were labeled CASH_Ca/Si_%RH. In the text we refer to 'wet' and 'dry' C-(A)-S-H samples. The 'wet' include fully-hydrated and 98% RH samples; 'dry' refer to 55% RH, desiccator-dried, and oven-dried samples.

Table 5.2.1.2. The summary of the TGA, WSI, and XRD results for 'wet' and 'dry' C-(A)-S-H samples.

	'wet'				**'dry'**			
Name	**TGA (w.%)**	**$WSI_{ads.}$ (mol/g CSH)**	**d_{001} (Å)**	**Name**	**TGA (w.%)**	**$WSI_{ads.}$ (mol/g CSH)**	**SSA (m^2/g)**	**d_{001} (Å)**
CASH_0.9_98RH	37	0.02225	13.74	CASH_0.9_55RH	20	0.00835	353	12.4
CASH_0.9_fully hydrated	29		14.45	CASH_0.9_desiccator-dried	16			12.51
				CASH_0.9_oven-dried	19			12.02
CSH_1_98RH	27	0.02031	12.31	CSH_1_55RH	22	0.00443	180	12
CSH_1_fully hydrated	28		13.11	CSH_1_desiccator-dried	17			11.57
				CSH_1_oven-dried	18			10.58
				CSH_1.2_desiccator-dried	17		177	10.6
CSH_1.33_98RH	26	0.01411	11.9	CSH_1.33_55RH	19	0.00438	135	
CSH_1.33_fully hydrated	27		11.5	CSH_1.33_desiccator-dried	16			10.40
				CSH_1.33_oven-dried	17			9.8

5.2.2. Inductively coupled plasma - atomic emission spectrometer (ICP-AES).

Ca/Si ratios were determined using ICP-AES (Varian 720ES Agilent). The C-S-H particles (5-10 mg) were dissolved by adding concentrated 14M HNO_3 (distilled) and 28M HF (47-51%, Trace Metal™, for Trace Metal Analysis, Fisher Chemical) acids, followed by heating the solution for ~24h at ~80°C. The final step involved diluting with boric acid and ultrapure water prior to the measurement.

5.2.3. Water adsorption volumetry

Water adsorption isotherms were obtained at 25 °C using a Belsorp-Max instrument by BEL JAPAN Inc.III. A long acquisition time of at least 2 weeks was required due to the slow equilibrium kinetics. Prior to the measurements, all samples were outgassed at 50 °C for 24 h under a residual pressure of 4.652×10^{-5} Pa. The classical Brunauer–Emmett–Teller (BET) theory was used to analyze the isotherms and derive the specific surface area (SSA).(Brunauer, Emmett and Teller, 1938) (Table 5.2.1.2).

5.2.4. Thermogravimetric analysis

Thermogravimetric analysis (TGA, Mettler-Toledo TGA-DSC3+) was used to examine the thermal decomposition and the water content of the C-S-H and C-A-S-H samples. The samples were analyzed at a heating rate of 10°C/min up to 600°C in a N_2 environment with a flow rate of 20 mL/min. The samples were loaded in aluminum crucibles and were hermetically sealed with aluminum caps inside a glove-box or a glove-bag, filled with N_2 equilibrated at the same RH used to condition the sample. The sample mass used for TGA analyses varied between 8 and 30 mg.

5.2.5. Synchrotron X-Ray diffraction

Synchrotron XRD measurements for the C-S-H samples were performed at the ID31 beamline of the European Synchrotron Radiation Facility (ESRF) in Grenoble, France. Prior to analysis, C-(A)-S-H samples were loaded into 1.5 mm (ID31) polyimide capillaries, inside the glove-bags or wet glove-box at the same RH values. The capillaries were closed on both ends using a two-parts epoxy adhesive.

At the ID31 beamline, a monochromatic X-ray beam of 78 keV (λ = 0.159 Å) was used to obtain scattering patterns of C-S-H samples. The data sets were collected by using a PilatusX 2M CdTe detector placed at a sample-to-detector distance of d_1 = 1.226 m to obtain scattering patterns with a Q range of 0.1-6.2 $Å^{-1}$, allowing the measurement of the Bragg peak corresponding to the interlayer distance of C-S-H. Data were automatically corrected for internal dark current. Two-dimensional images of the scattered intensity were azimuthally integrated using the pyFAI software package (Kieffer and Wright, 2013). The pattern from the empty capillary was subtracted as a background.

The C-A-S-H samples were measured at the 11-ID-B beamline at the Advanced Photon Source, Argonne National Laboratory. The samples were analyzed with a monochromatic X-ray beam of 58.6 keV (λ = 0.2115 Å). The data were collected with a Perkin Elmer XRD 1621 N ES detector and sample-to-detector distance of d = 0.799 m to access a Q range of 0.2-10.4 $Å^{-1}$. Data were automatically corrected for

internal dark current. Two-dimensional images of the scattered intensity were azimuthally integrated using the GSAS II software package (Toby and Dreele, 2013).

5.2.6. Inelastic Incoherent Neutron Scattering

INS spectra of C-S-H samples with Ca/Si=1.2 and 1.33 were collected in the energy range from 133.3 to 1940 cm^{-1} (16.5 to 240 meV) with an energy resolution of $\Delta E/E \sim$ 2-3% using the Lagrange (LArge GRaphite ANalyser for Genuine Excitations) secondary spectrometer at the hot source of high-flux reactor of the Institut Laue-Langevin (ILL), France (Ivanov, Jimenéz-Ruiz and Kulda, 2014; Jiménez-Ruiz, Ivanov and Fuard, 2014). A combination of two double focusing monochromators was used to access the energy range: Cu(220) to access the intermediate energies, and Si(311) for lower energies.

The energy transfer range was obtained by subtracting the final energy of 4.5 meV of PolyGraphite (PG) analyzers from the experimentally obtained one. The samples were loaded into the hollow aluminium cells, which were sealed under the RH conditions corresponding to the C-S-H samples. The INS spectra were collected at 10 K (to lower the Debye-Waller factor) for the samples, the empty holders, and the cryostat. The background spectrum from the latter were subtracted from the raw INS spectra of the C-S-H samples. The obtained intensity was normalized by the monitor counts using LAMP (Large Array Manipulation Program) software (Richard, Ferrand and Kearley, 1996).

The final $S(\boldsymbol{Q}, \omega)$ from Cu(220) and Si(311) reflecting planes were manually merged to obtain the final $S(\boldsymbol{Q}, \omega)$ in the range 133.3 to 1940 cm^{-1}. Providing that the final wavevector, k_f , is much smaller than the incident wavevector k_i , the observed intensity is directly proportional to the generalized density of states (GDOS), which in the case of hydrogenated samples is the hydrogen partial density of states.

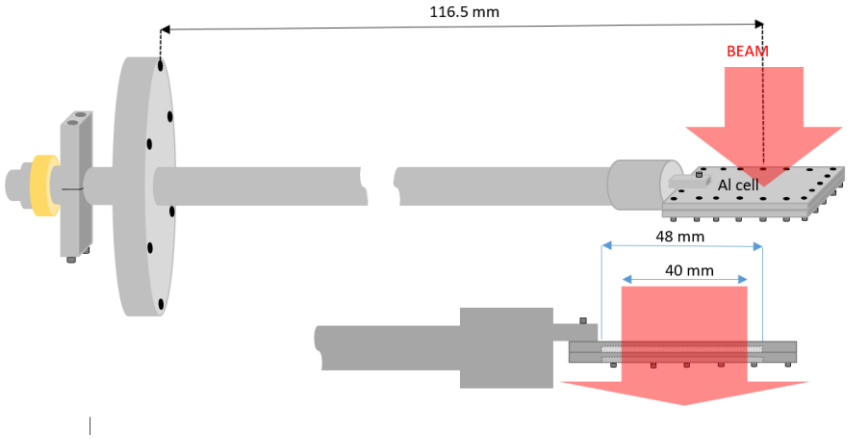

Figure 5.2.6.1. Schematic of sample mounting at TOSCA, ISIS. (Image is a courtesy of by Campillo Sylvain).

The INS spectra of C-S-H samples with Ca/Si=1, and C-A-S-H samples with Ca/Si=0.9, were measured at 10 K using TOSCA spectrometer at the ISIS spallation Neutron and Muon Source (Rutherford Appleton Laboratory, UK) (Parker *et al.*, 2014; Pinna *et al.*, 2018). TOSCA is an indirect geometry time-of-flight spectrometer operating in the energy transfer ranges up to 8000 cm^{-1} with a $\Delta E/E$ resolution of ~1.25%. The samples were loaded in Al cells and sealed with In-wire under the RH conditions

corresponding to the C-S-H samples. All manipulations were performed inside a wet glove-box or glove-bags to prevent contamination by carbon dioxide. The Al cells were then mounted on a center stick connected to a gas handling system (Figure 5.2.6.1). The INS signals from sample scattered neutrons and empty Al cells were recorded by detectors both in forward and in backward directions for about 4 hours per sample. The neutron beam size was about 40 mm x 40 mm. The resulting data were combined using Mantid software (STFC, 2017). The inelastic signal coming from the empty Al cells were subtracted and the spectra were scaled by the sample mass. The data were normalized by initial sample mass, i.e. the mass of the oven-dried C-S-H samples before conditioning at varying RH levels.

5.2.7. Molecular Dynamics Simulations

Atomistic simulations were performed at the Cori supercomputer at the National Energy Research Scientific Computing Center (NERSC, USA) using the MD simulation code LAMMPS (Plimpton, 1997), which solves Newton's equations of motion for many-particle systems interacting through pairwise potentials. Interatomic interactions were described using the SPC/E water model (Berendsen, Grigera and Straatsma, 1987) and the CLAYFF model of mineral-water interactions (Cygan, Liang and Kalinichev, 2004). The CLAYFF force field was chosen because of its versatility and successful descriptions of various systems including clay minerals (Wang *et al.*, 2005; Kalinichev, Wang and Kirkpatrick, 2007; Ferrage *et al.*, 2010; Bourg and Sposito, 2011; Bourg and Steefel, 2012), zeolites (Ockwig *et al.*, 2008), and other phases (Skelton *et al.*, 2011; Roscioni, Muccioli and Zannoni, 2017; Fernandez-Martinez *et al.*, 2020) validated against the results of X-ray and neutron scattering experiments (Kalinichev, Wang and Kirkpatrick, 2007; Ferrage *et al.*, 2011) and a variety of other experimental techniques (Wander and Clark, 2008; Underwood and Bourg, 2020).

A hydrated C-S-H nanoparticle model described elsewhere (Zhakiyeva *et al.*, 2021) was used. The C-S-H nanoparticle was fixed for the first 15 ps, during which only water molecules were allowed to move. Water molecules were kept rigid using the SHAKE algorithm. The silica chains were kept semi-rigid by applying fixed angles taken from the X-ray crystal structure of tobermorite. After 15 ps the C-S-H nanoparticle was allowed to move without any constraints. The system was equilibrated for ~1.5 ns, followed by the production runs performed for ~3.5 ns in a NVT-ensemble (T=298K). Newton's equations of motion were solved using the Verlet algorithm with a 1 fs step. Electrostatic and dispersion interactions beyond a cut-off length of 15 Å were computed by Ewald summation. Analyses of the MD trajectories were performed using custom-made Python codes, over the frames from the production runs. GDOS of the resulting structures from the production run were calculated using the Molecular Dynamics Analysis for Neutron Scattering Experiments (MDANSE) python application (Goret, Aoun and Pellegrini, 2017).

5.3. Results and discussion

5.3.1. Experimental IINS data

Varying RH levels in CSH_1

The IINS spectra for C-S-H with Ca/Si=1 of varying hydration levels are shown in Figure 5.3.1.1. A first comparison between the C-S-H and ice Ih (light grey) spectra allows distinguishing between the 'drier' C-S-H samples as the three spectra in the bottom of Figure 5.3.1.1, and 'wet' C-S-H samples as the two upper spectra. The former contain interlayer and interfacial water, showing a lower water content than the 'wet' samples (as deduced also from WSI, TGA and XRD data, see Chapter 3). The latter spectra resulted from the C-S-H samples containing bulk capillary pore water in addition to the interlayer and interfacial water.

Lower energy modes (0-320 cm^{-1})

The power spectra of ice Ih (grey curve in Figure 5.3.1.1) can be broken down into lower energy regions representing translational modes 0-323 cm^{-1} (0-40 meV), the librational region, which are hindered rotations of H-bonded water molecules, at 444-968 cm^{-1} (55-120 meV), and high frequency intramolecular vibrations, such as bending modes at 1613 cm^{-1} (200 meV) and O-H stretching modes at 3307 cm^{-1} (410 meV) (Levchenko *et al.*, 2007).

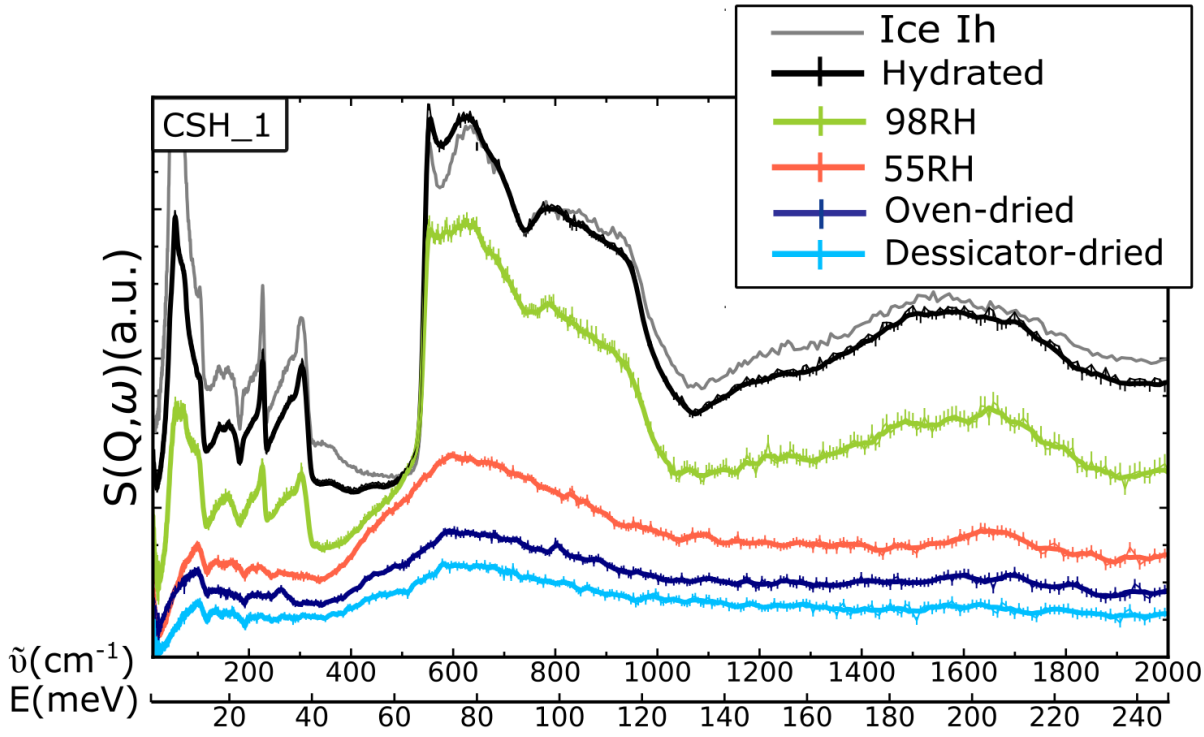

Figure 5.3.1.1. The evolution of the CSH_1 samples by increasing hydration state For the sake of clarity, all the spectra have been arbitrarily shifted along the S(Q, ω) axis. All the spectra have been normalized to the mass of sample in the beam.

The lower energy translational modes in ice Ih are characterized by the triangular features at 57 cm^{-1} (~7 meV) known as acoustic modes, and at 226 and 298 cm^{-1} (28 and 37 meV) known as optic modes. These modes involve the O-H stretch for a tetrahedral bonding motif in the ice lattice (Mitchell *et al.*, 2005). The same translational modes are evident in the 'wet' C-S-H samples, with slightly lower relative intensities than in ice Ih if compared to the intensities of the librational modes. On the other hand, the 'dry' C-(A)-S-H samples demonstrate a dramatic change in the region of lower energies, with translational and acoustic modes attenuated and shifted to higher frequencies. This signifies that the ordered structure coming from the H-bonding network is not present, meaning that the water is strongly bound to the C-(A)-S-H surfaces and that water molecules have a different local order than in ice Ih.

This behavior has been observed by other authors for water adsorbed at the solid-water interfaces of other nanosystems (Bordallo, Aldridge and Desmedt, 2006; Levchenko *et al.*, 2007; Russo *et al.*, 2011; Berg *et al.*, 2017; Sheka *et al.*, 2019; Larsen *et al.*, 2020; Monet *et al.*, 2020). In the case of cementitious materials, and following previous INS studies, the peaks at around 80 and 242 cm^{-1} (10 and 30 meV) can be used as 'fingerprints' of confined water. According both to computer simulations (Chen *et al.*, 1999) and experimental studies on Vycor glasses (Bellissent-Funel, Chen and Zanotti, 1995; Faraone *et al.*, 2004), these peaks were attributed to the translational motions of water molecules inside the confining cage. In our case, the peaks that we observe are at about 97 and 249 cm^{-1} (12 meV and 30.9 meV).

The differences in the values with respect to other studies could be due to the improved resolution of the instruments, as the INS studies were performed on cement systems nearly 25 years ago. Another possible explanation is that these peaks tend to shift and vary in spectral intensity depending on the ions present in the system and the hydration state, respectively. Indeed, Larsen et al. (2020) showed that the confined water peak in fluorohectorites shifted from about 64.5 cm^{-1} (8 meV) to more than 80 cm^{-1} (10 meV) depending on the nature of the interlayer cation and different water content (Larsen *et al.*, 2020). The calculated power spectra by Cygan et al. (2015) for the monolayer hydrate of Ba – montmorillonite resulted in a small peak at about 89.5 cm^{-1} (11.1 meV) and was attributed to the bending and stretching modes of the strongly bound water molecules (Cygan *et al.*, 2015). Finally, the temperature of the experiment affects the intensities of these peaks, with a significant sharpening of the signals as temperature goes below 0°C (Bellissent-Funel, Chen and Zanotti, 1995). In our case, we have assigned these peaks to the dangling hydrogens of strongly bound interfacial water molecules, based on the calculated partial GDOS as will be explained later.

Librational modes (300-1000 cm^{-1})

The librational modes found between roughly 300-1000 cm^{-1} (37-124 meV) are very sensitive to the strength of the hydrogen-bonds. The librational modes include the rocking, twisting, and wagging modes with their corresponding energies increasing accordingly. These modes tend to merge with each other (Cygan *et al.*, 2015). The librational edge represents the start of the librational modes energies, with a sharper edge at the low frequency side signaling the presence of a highly ordered structure with

degeneration of some of these modes into a sharp peak, meaning that the water in ice forms an extensive H-bonding network.

The evolution of the shift of the librational edge as a function of the water content can be followed by the changes observed from about 350 cm^{-1} (~43.3 meV) for 'dry' to nearly 520 cm^{-1} (~204 meV) for 'wet' C-S-H samples. The absence of a clear librational edge (a broken degeneracy of the librational modes) similar to ice confirms the absence of bulk-like water in the 'dry' C-S-H samples. Among the 'dry' C-S-H samples the librational modes of the oven-dried and desiccator dried samples show shoulders at about 500 cm^{-1} (a convolution of the rocking, twisting and wagging modes), and 55RH C-S-H sample showing a smoother and sharper edge. This is in good agreement with the results of TGA, XRD and WSI, which show that the C-S-H samples conditioned at 55% RH contain 17% and 31% more water than the oven- and desiccator-dried samples, respectively (Chapter 3). As it was reported by Roosz et al. using experimental methods (Roosz *et al.*, 2016) and by Zhou et al. (Zhou *et al.*, 2019) using a the combination of DFT and MD calculations, the C-S-H contains both interlayer and multilayer adsorbed water at this RH.

The 'wet' C-S-H samples on the other hand reveal a close resemblance to ice, as they contain bulk liquid-like capillary pore water in addition to the interlayer and interfacial water. The CSH_1_98RH incorporates less bulk water than the fully hydrated C-S-H sample as shown by the results of the TGA and XRD experiments. Indeed, the start of the librational edge of CSH_1_98RH coincides with that of CSH_1_55RH, followed by a sharp vertical rise coinciding with the librational edge of ice Ih at around 500 cm^{-1} (62 meV) shown in Figure 5.3.1.1 (red and green lines). The 'combined' edge of CSH_1_98RH shows that the sample contains multilayer water, together with bulk capillary pore water. The amount of the bulk water is however not sufficient to completely hide the signals coming from the multilayer and interlayer water.

Intermolecular modes (1500-4000 cm^{-1})

At higher energies we find intermolecular modes, such as so-called scissoring or H-O-H bending modes at around 1650 cm^{-1} (205 meV) and O-H stretching modes at around 3600 cm^{-1} (446 meV). The values of both modes tend to shift to higher frequencies when increasing the water content. In our case, both bending and stretching modes are difficult to distinguish from the background signals. There are several explanations: first, there is a $\boldsymbol{Q}$ dependence in IN1-Lagrange and TOSCA instruments where the data have been collected. The limited $\boldsymbol{Q}$ range of these instruments means that at higher energy transfers the resolution is dampened significantly. Secondly, the Debye-Waller effect, i.e. the thermal fluctuations, at higher $\boldsymbol{Q}$ values substantially attenuates the intensity in the spectra. The experiment is performed at 10 K to avoid the maximum of thermal fluctuations. Finally, at higher $\boldsymbol{Q}$ ranges there is an increase in multiphonon intensity, which gives a rising background with increasing $\boldsymbol{Q}$ values.

Varying RH levels in CASH_0.9

IINS spectra of CASH_0.9 with different water contents are shown on Figure 5.3.1.2. A detailed qualitative examination reveals a significant similarity to the CSH_1. This behavior is expected, as in our samples the ratio of Al ions per Si is 0.1, so the effect of the Al seems to be limited. Nonetheless, there are some differences that should be addressed.

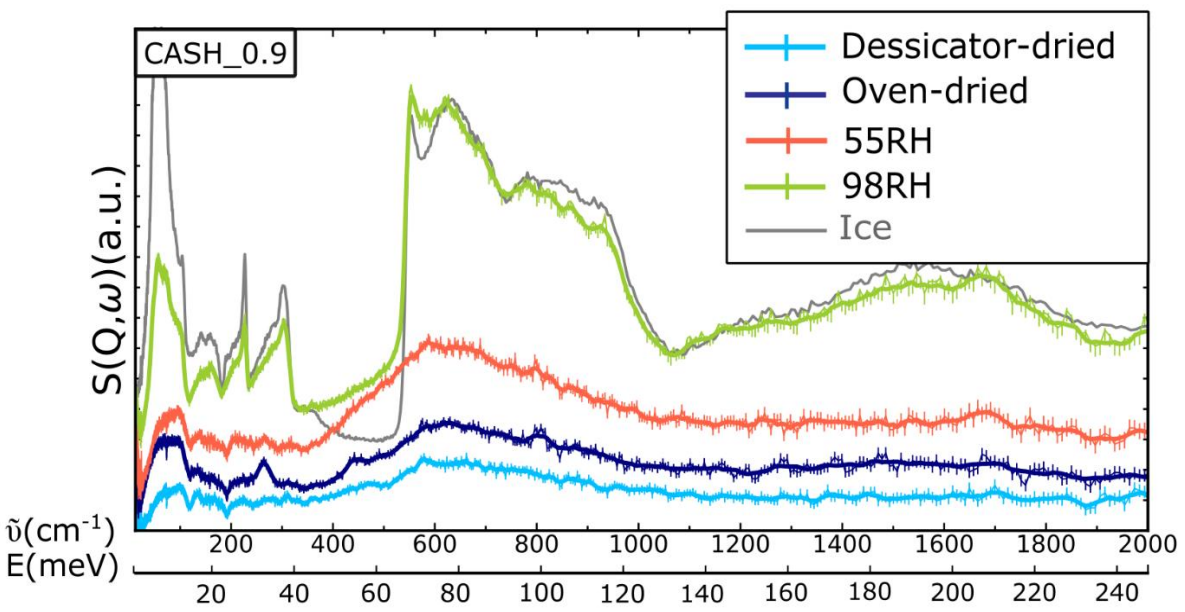

Figure 5.3.1.2. The evolution of the CASH_0.9 samples by increasing hydration state. For the sake of clarity, all the spectra have been arbitrarily shifted along the S(Q, ω) axis.

First, similar to the CSH_1_98RH, the CASH_0.9_98RH contains multilayer water and some bulk pore water, as deduced from the librational edge, which could be decomposed as a linear combination of the signals from CASH_0.9_55H, and ice Ih edges. However, the relative intensities of the lower energy range translational modes (100-250 cm^{-1}, 15-40 meV) to the intensities of the librational modes correspond much more to ice Ih, than in CSH_1. This can be explained by the greater amount of water adsorbed at a given RH for CASH_0.9 than for the CSH_1 samples as shown by the results of WSI, TGA and XRD (Table 5.2.1.2).

It is quite striking that the shape of CASH_0.9_98RH (green) coincides with the shape of Ice Ih (grey on Figure 5.3.1.2), except for the absence of the characteristic dip in intensity at 350-550 cm^{-1} (43.4-68 meV) and the lower intensities of the acoustic mode at 56.5 cm^{-1} (7 meV). This demonstrates nicely how the multilayer water adsorption leads to a capillary condensation of water in the larger gel pores and capillary pores when increasing RH. Another difference is in the acoustic mode peak which was damped and shifted in CSH_1, and is wider in case of CASH_0.9 in line with our discussion about the changing value, shape and intensity of this band.

Varying RH levels in CSH_1.33

The evolution of spectra for C-S-H with Ca/Si=1.33 (CSH_1.33) as a function of RH is shown in Figure 5.3.1.3. The same tendency towards the formation of an ice-like structure is observed at increasing RH values. However, there are few significant differences stemming from the changing nature of C-S-H depending on the Ca/Si ratio.

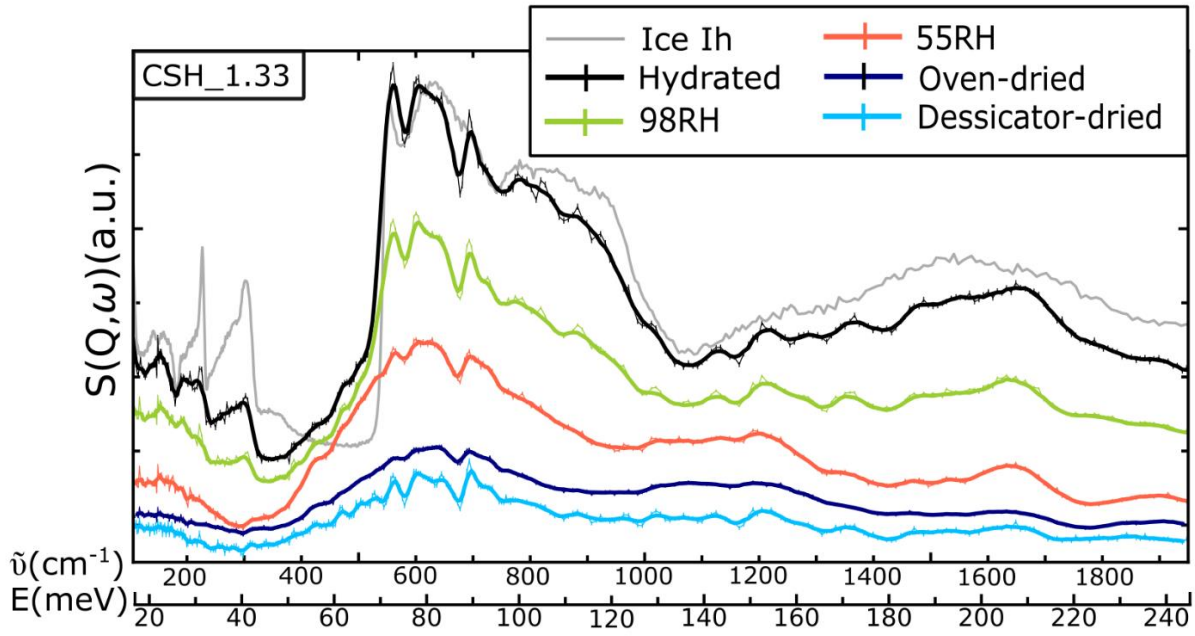

Figure 5.3.1.3. The evolution of the CSH_1.33 samples by increasing hydration state For the sake of clarity, all the spectra have been arbitrarily shifted along the S(Q, ω) axis.

First, differences are observed in the range of low energies for CSH_1.33 as compared to CSH_1 and CASH_0.9. A very different shape of spectra at lower energies come from the peculiarities of the IN1-Lagrange instrument where the data has been collected. The ***Q*** range for CSH_1.33 samples spans from 100-2000 cm^{-1} (~15-250 meV), which is obtained by stitching the IN1-Lagrange data from the two monochromators manually (see Methods section 5.2.6. for more details). The acoustic signals at 226 and 298 cm^{-1} (28 and 37 meV) present in ice Ih exist also in CSH_1.33_fully_hydrated, and with lesser intensities in CSH_1.33_98RH samples.

Second, the 'wet' CSH_1.33 samples show less ice-like features than C-S-H_1 samples for a given RH. The librational bands of both the CSH_1.33_fully_hydrated (black) and CSH_1.33_98RH (green) samples can be composed by linear combinations of the CSH_1.33_55RH (red in Figure 5.3.1.3) and ice Ih edges. This can be explained by three factors: (i) the tendency of the C-S-H samples to adsorb less water at a given RH with increasing Ca/Si ratios. This observation is supported by the results of WSI, which show that the amount of adsorbed water at 98% RH is 1.1 times more for CASH_0.9 than for CSH_1, and 1.6 times more than for CSH_1.33 (Table 5.2.1.2). (ii) A high number of Ca^{2+} sites in the sample implies a higher proportion of Ca-hydration water, which is highly structured (i.e., non-bulk water).

The results of our MD simulations, as well as by other authors (Bonnaud, Coasne and Pellenq, 2012), showed that Ca^{2+} ions act as hydrophilic centers, thus creating hydration shells around, and inducing H-bonding network (see more details in Chapter 4). Therefore, the bigger number of calcium ions results in larger part of bulk water bound, thus decreasing the proportion of bulk-like water (iii) We note that in case of adsorbed water the equilibration time is a major factor for the amount of water adsorbed on the C-(A)-S-H surfaces (Odler, 2003; Beaudoin and Odler, 2019). In our case, the

CASH_0.9 sample was equilibrated under 98% RH conditions 4 times longer than the C-S-H samples (1 month *vs.* 1 week). Therefore, a larger amount of adsorbed water can be explained partially by lengthy exposure to high humidity atmosphere.

Overall, for all C-(A)-S-H samples at higher RH levels we observed a very close resemblance to ice Ih due to the presence of bulk-like pore water, whereas at lower RH levels the typical confined water signals at lower energies were present in CSH_1 and CASH_0.9 samples. The shapes of the librational modes are distinct for adsorbed interfacial water and bulk pore ice-like water in all C-(A)-S-H samples.

The amount and distribution of water as a function of Ca/Si

Let's now focus on the differences in IINS spectra arising from changing Ca/Si ratios represented in Figure 5.3.1.4 for 'wet and 'dry' C-(A)-S-H samples.

Here we should note that we are discussing simultaneously the *amount* and *distribution* of adsorbed water. The IINS is a powerful technique in that sense because it allows observing directly both of these characteristics. Certainly, there is a direct dependence between an increased amount of water and an enhanced spectral intensity. At the same time the type of water affects the overall shape (and to some extent the intensity) of the spectra. The two types of water that IINS allows us to distinguish definitely are the interfacial and interlayer water vs bulk-like water. Bearing this in mind, we can focus on each hydration level closely.

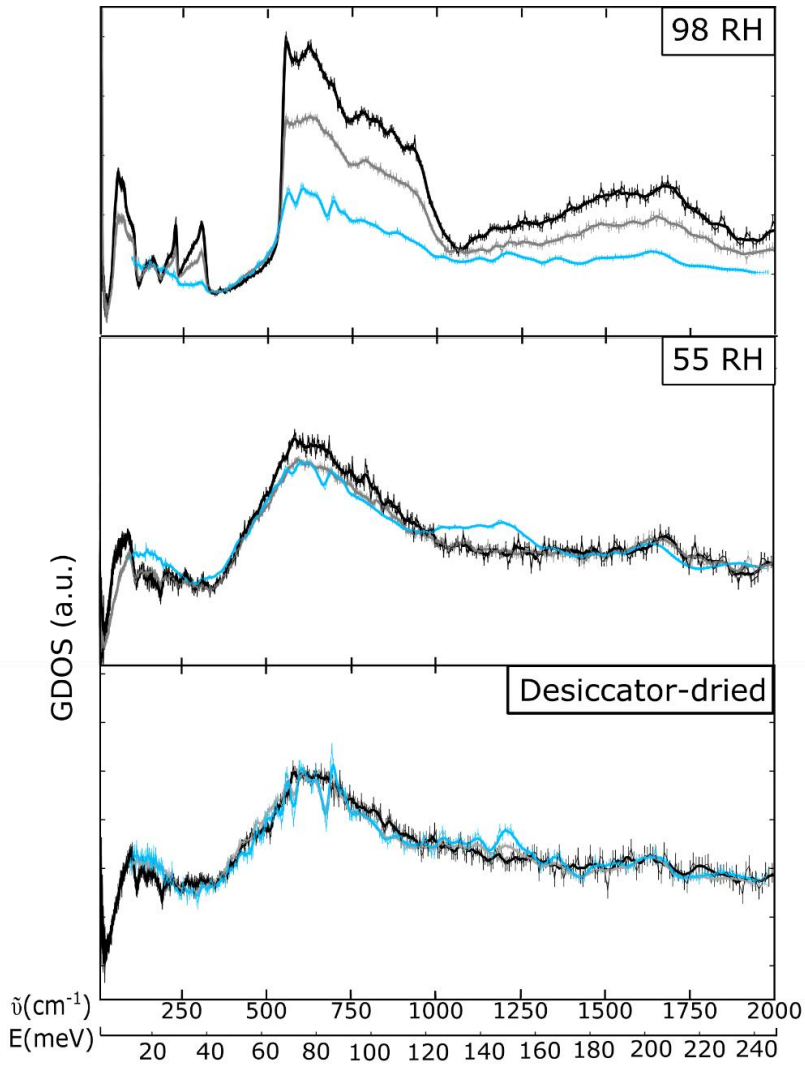

Figure 5.3.1.4. Density of states for C-(A)-S-H samples varying with RH levels and Ca/Si ratios. CASH_0.9 samples are in black, CSH_1 are in dark grey, and CSH_1.33 in blue colors on all spectra.

The conditioning protocol (shown schematically in Figure 5.2.1.1) has an effect on the total amount of adsorbed water as a function of Ca/Si (Table 5.2.1.2). The 'wet' or fully hydrated C-S-H samples show a steep decrease in the amount of adsorbed water at increasing Ca/Si ratios. The 'dry' C-S-H samples show lesser difference in the amount of adsorbed water at rising Ca/Si ratios as seen by the amount of water in 55% RH samples (Table 5.2.1.2). The least change can be seen for very dry samples, which were dried in a desiccator over N_2 for about a month or longer. These trends correlate well with the IINS data, where in case of 98RH samples we can follow the increasing amounts of adsorbed water with decreasing Ca/Si ratios (top Figure 5.3.1.4). The ratios of the areas calculated from the IINS spectra over the range of 340 to 1914 cm^{-1} (42.2 to 237.3 meV) compare well with WSI adsorbed amounts shown in Table 5.2.1.2. However, as noted earlier in this section 5.3.1 the equilibration time is an important factor when adsorption of water in C-(A)-S-H is discussed (Odler, 2003). As Badmann et al. (1981) noted in their work, at the RH levels > 95% RH the adsorption is superimposed by capillary condensation, therefore the adsorbed volume is more a function of time than humidity (Badmann, Stockhausen and Setzer,

1981). The longer exposure to higher RH atmosphere of CASH_0.9 could have affected the higher amount of water adsorbed as compared to CSH_1, and CSH_1.33.

The same logic can be applied for the 55RH samples (middle in Figure 5.3.1.4), where the relative decrease in areas is less apparent than for 98 RH samples. The CASH_0.9_55RH contains about 1.9 times more adsorbed water than CSH_1, and CSH_1.33 samples due to a significantly higher surface area of CASH_0.9 sample. However, at the same time the amount of total interlayer water increases for these samples as we go to higher Ca/Si ratios (Chapter 3 Figure 3.3.1.5), thus giving roughly similar GDOS areas.

This property of C-(A)-S-H of adsorbing less water at higher Ca/Si ratios can be explained by the decreasing surface area shown in Table 5.2.1.2. The SSA decreases from 353 m^2/g for CASH_0.9, to about 180 m^2/g for CSH_1, slightly less for CSH_1.2 with 177 m^2/g, and down to 135 m^2/g for CSH_1.33. An interesting analysis of XRD data was performed by (Grangeon, Claret, Linard, *et al.*, 2013). The authors showed that the narrowing of the full width half-maximum (FWHM) and decrease of the d_{001} reflection in XRD data with increasing Ca/Si ratios could be due to an increased stacking of C-S-H layers. However, Grangeon and co-workers warn that it is not the only explanation of the observed phenomenon, that effects such as interstratification (stacking of structurally different layers along **c*** axis), turbostratism (random rotations of layers), merging of the layer upon drying, and the limitations of the XRD experiment can take place as well. Nonetheless, later Gaboreau et al. (2020) applied the same XRD analysis, and together with TGA, WSI, FT-IR data showed that the stacking of the layers increases from 3-6 to about 8 as the ratio of Ca/Si increases from 1 to 1.2 (Gaboreau *et al.*, 2020). The authors also observed the decreasing SSA calculated from WSI data with rising Ca/Si (Roosz *et al.*, 2016; Gaboreau *et al.*, 2020).

Therefore, we conclude that the amount of adsorbed water is a delicate balance between the equilibration time and available surface area. On the other hand, the distribution of the adsorbed water is most probably affected by an increased number of Ca^{2+} ions, not only in the interlayer, but also on the surfaces of C-(A)-S-H. These calcium ions form hydrophilic sites for water that is highly structured.

Finally, this comparison for desiccator dried samples (bottom spectra in Figure 5.3.1.4), shows that they have matching intensities, except for the region around 1100 cm^{-1} (136.4 meV). This intensity is characteristic of the hydrogen bonding, specifically is represents the in-plane deformation γ(O-H---O), that occurs between 600 cm^{-1} (for weak H-bonding) to 1200 cm^{-1} (for strong H-bonding) (Mitchell *et al.*, 2005). This is in line with our conclusion from Chapter 4 about Ca^{2+} ions inducing H-bonding network, thus higher number of Ca^{2+} ions would increase the number of H-bonds the C-(A)-S-H of higher Ca/Si ratios.

At this point the limit of interpretation of experimental data without computed complementary data is reached. In order to confirm or disprove our conclusions on experimental data we turn to section 5.3.2.

5.3.2. Computed IINS data

Bulk water vs interfacial and interlayer water

The GDOS can be calculated from the MD trajectories and can be compared directly to the vibrational spectra obtained from the IINS experiment. A time step of 1-4 fs needs to be used to capture the high energy intramolecular vibrations.

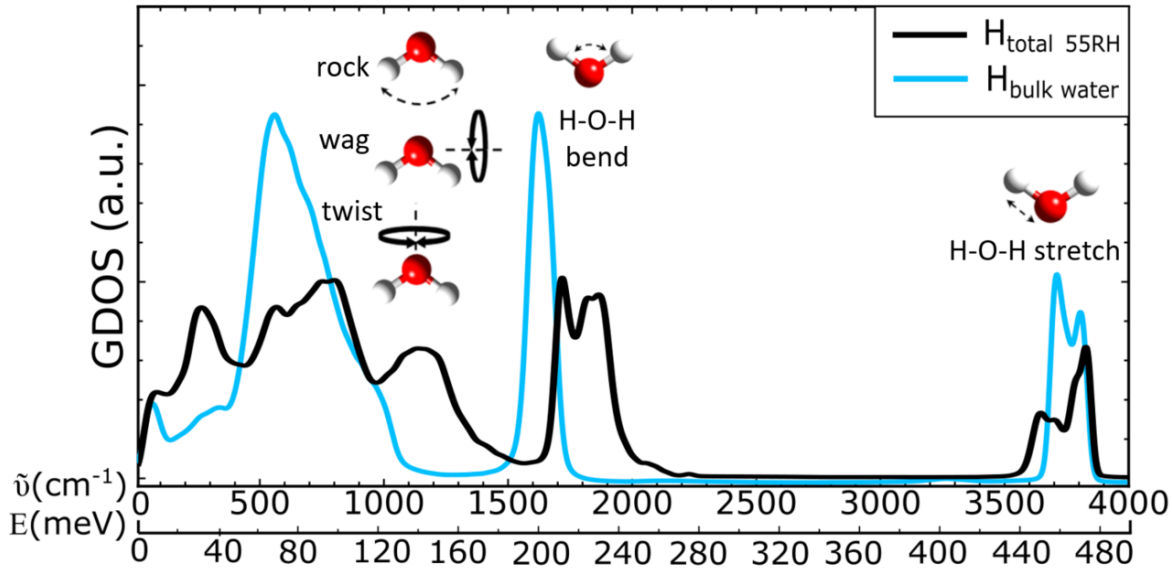

Figure 5.3.2.1. Calculated GDOS for hydrogen atoms for CSH_1_55RH model and a simulated box of bulk water. The water librational modes (rocking, wagging, twisting) occur from about 300 to 1000 cm^{-1}, bending modes about 1600 cm^{-1}, and stretching modes about 3600 cm^{-1}. The drawings of water vibrations were taken from Cygan et al. (Cygan *et al.*, 2015)

GDOS were calculated for all hydrogens in the 55RH model and for the bulk water, parametrized using an SPC/E model (Figure 5.3.2.1). The shapes and intensities of the vibrational modes of water in CSH_1_55RH model are very different from the ones of bulk water. Differences are present in all regions of the spectra, from the lower frequencies, where we observe a peak at 260 cm^{-1} (~32.2 meV) which is not present in bulk water, followed by the librational modes having half the intensity of bulk water, and an additional broad peak centered around 1100 cm^{-1} (136.4 meV). The origins of these signals will be addressed later. Intramolecular vibrations are observed at higher frequencies, such as H-O-H bending peak generally expected at around 1600 cm^{-1} (198.4 meV) and O-H stretching signal at around 3600 cm^{-1} (446.3 meV).

The bending peak for calculated bulk water is centered at the expected value, whilst the bending in CSH_1_55RH is split into two, occurring at about 1725 and 1830 cm^{-1} (213.5 meV and 226.5 meV), thus signifying a clear deviation from the bulk water. The stretching modes for bulk water are centered at 3730 cm^{-1} (462.4 meV) and 3810 cm^{-1}(472.4 meV), and for CSH_1_55RH at 3677 and 3830 cm^{-1} (455.9 and 474.8 meV). The blue shift from expected stretching values are most probably due to the limitations of the SPC/E water model, in addition to the interlayer and interfacial water properties in CSH_1_55RH.

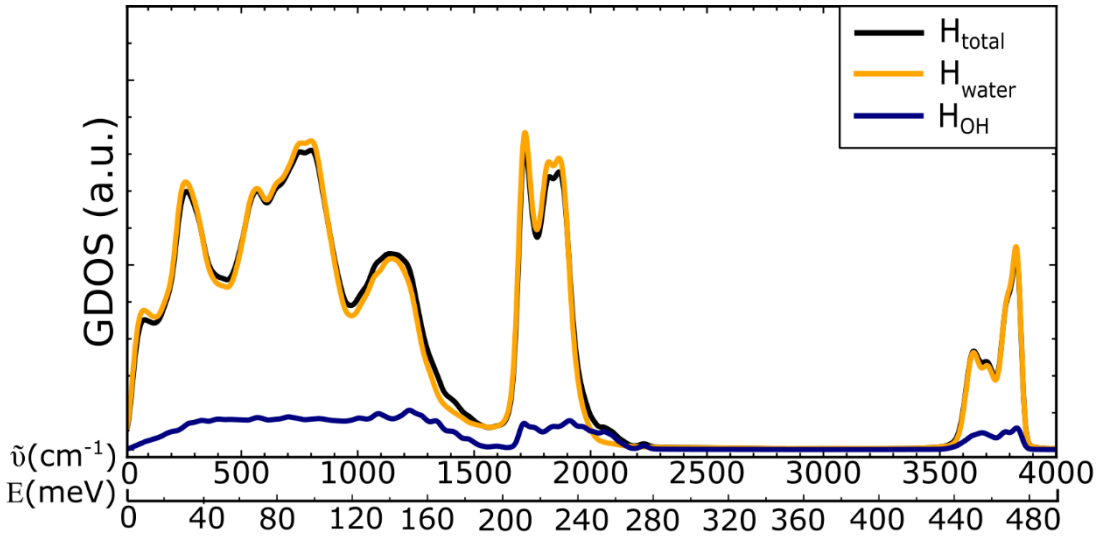

Figure 5.3.2.2. The calculated GDOS for CSH_1_55RH. The GDOS of all hydrogens in the system in black, of all hydrogens of water in yellow accounting for nearly all the intensity in the total GDOS, and all hydroxyl hydrogens in blue showing roughly 6 times less intensity than the GDOS of water hydrogens.

The results of the calculated total GDOS of all the hydrogens in the CSH_1_55RH system consist from the contributions from hydrogens of water and hydrogens of hydroxyls. There are 132 hydrogens of hydroxyls and 896 hydrogens of water, so ~6.7 times less of the former. Therefore, the total GDOS signal is dominated by the hydrogens of molecular water (Figure 5.3.2.2).

Partial GDOS: contributions from different hydrogens

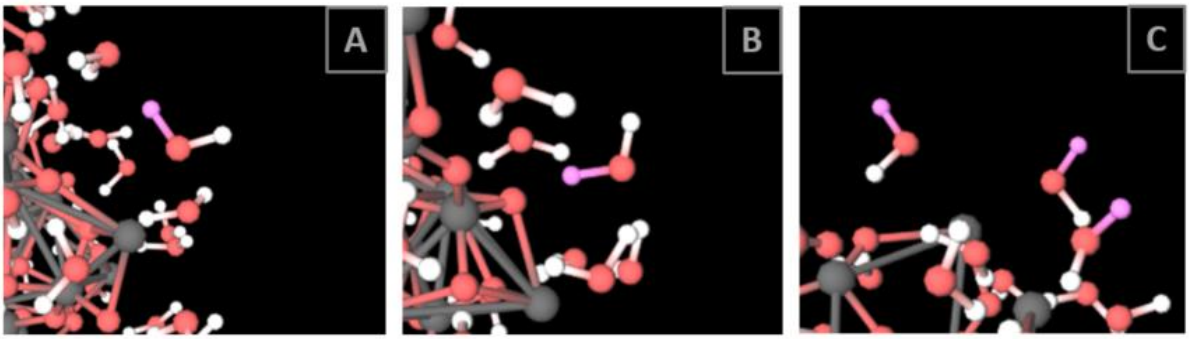

Figure 5.3.2.3. Snapshots from MDANSE used to calculate GDOS. (A) The water hydrogens forming H-bonds with other water molecules; (B) Water hydrogens donating H-bond to surface oxygens; (C) Dangling water hydrogens pointing out of C-S-H surface.

The GDOS of water hydrogens can be separated depending on the local environment of the H atoms: (A) Water hydrogens in the first hydration shell of calcium ions, and/or forming H-bonds with the C-S-H surfaces; (B) hydrogens forming hydrogen-bonds with other water molecules (A), hydrogens not being involved in any kind of bonding (C, all in Figure 5.3.2.3). All these different types of hydrogens result in IINS signals at different energies as shown in Figure 5.3.2.4.

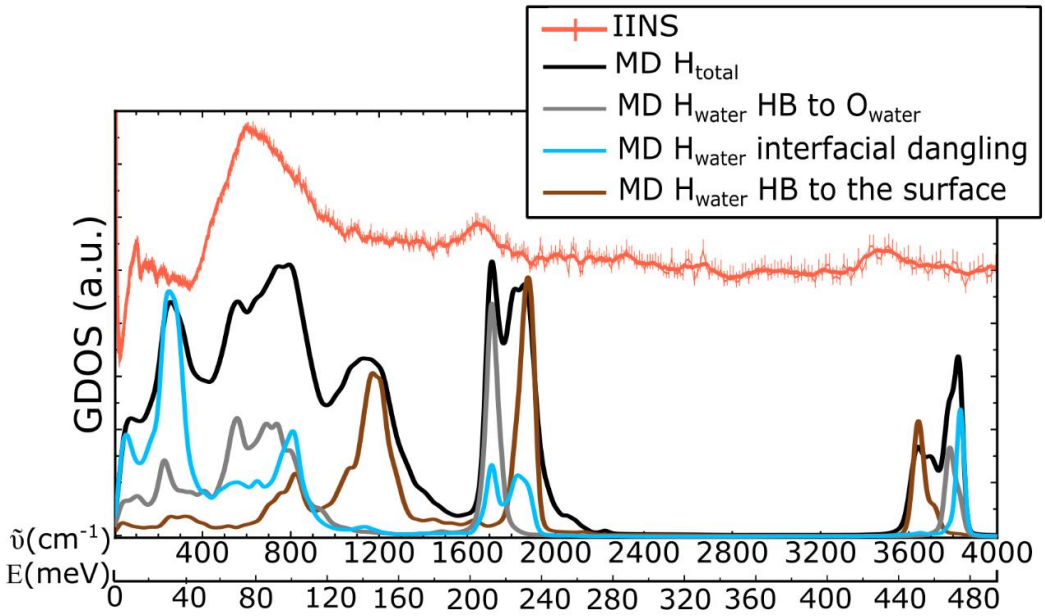

Figure 5.3.2.4. (Top) Experimental IINS spectrum for CSH_1_55RH; (Bottom) Calculated GDOS showing contributions from different hydrogen types.

The lower frequency (<300 cm^{-1}) contributions come mainly from the dangling water hydrogens and from the water molecules H-bonded to other water molecules, as demonstrated in light blue in Figure 5.3.2.4. It was shown in Figure 5.3.1.1 of the experimental GDOS of decreasing RH levels that the signal at about 55 cm^{-1} (7 meV) in ice decreases in intensity and broadens for samples containing interfacial and interlayer water. Now we complement this conclusion with our calculated GDOS, where these peaks at 80 cm^{-1} (9.9 meV) and 260 cm^{-1} (32.2 meV) come from the dangling interfacial water hydrogens and H-bonded interfacial water molecules. Moreover, when only an interlayer region is selected in CSH_1_55RH and CSH_1_98RH models, these lower energy signals disappear as shown in Figure 5.3.2.5, meaning that there are no dangling water hydrogens in the interlayer region.

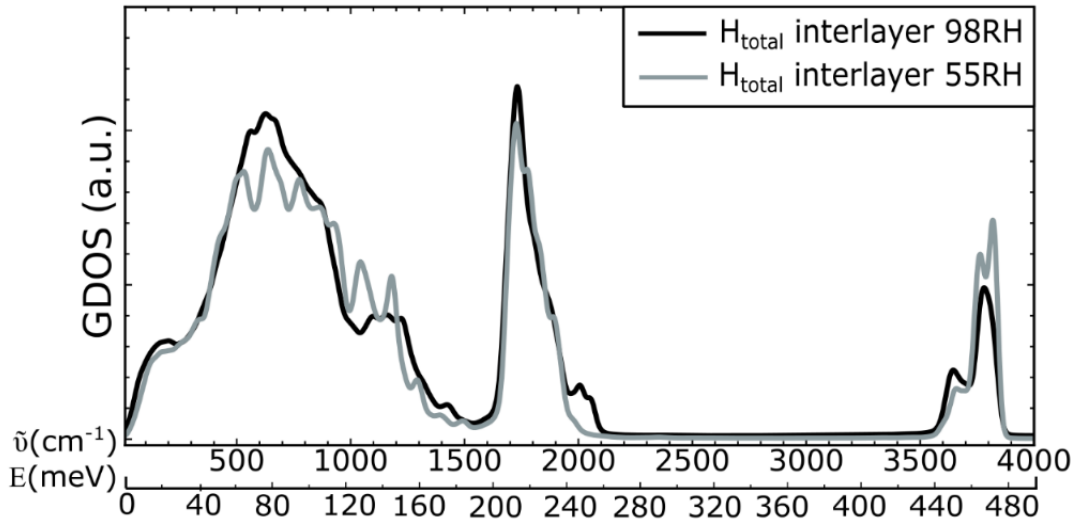

Figure 5.3.2.5. Calculated GDOS of total hydrogens in selected interlayer regions in CSH_1_98RH and CSH_1_55RH models.

Experimental vs calculated GDOS

Here, we compare the experimental data to our calculated GDOS, and further link the conclusions made in the experimental section 5.3.1. We have chosen the CSH_1_oven-dried (relevant also for CASH_0.9) as an example of a dry sample that contains signals that can be explained only by the calculated GDOS.

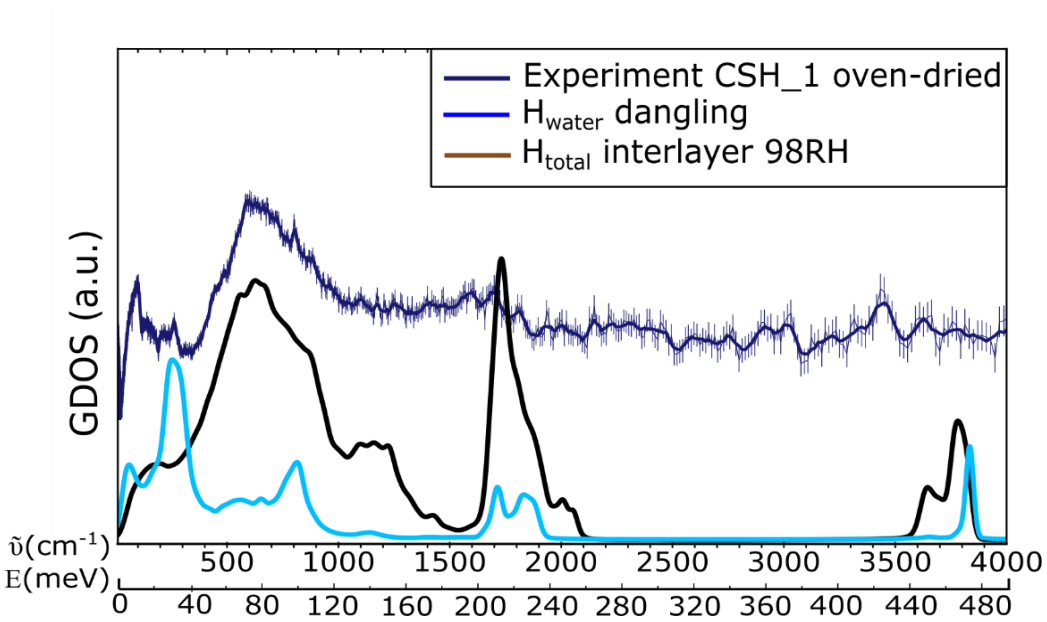

Figure 5.3.2.6. (Top) Experimental IINS spectra for CSH_1 oven-dried; (Bottom) Calculated GDOS showing contributions from different hydrogen types.

GDOS have been calculated using only the motions from atoms within the interlayer and the first adsorbed layer in CSH_1_55RH and CSH_1_98RH. As it was shown in Chapter 4, the 98RH model contains ~26% of total water in the interlayer, 2.5 times more than 55RH model. As we discussed earlier (Zhakiyeva *et al.*, 2021), water has a structuring effect on the C-S-H interlayer, resulting in a larger coherent scattering domain. Therefore, the calculated GDOS of the interlayer of 98RH reproduce more accurately the sharp librational edge and the librational modes in 55RH samples.

At low energies, we observe the two peaks at 80 cm^{-1} and 260 cm^{-1} (9.9 and 32.2 meV) assigned to dangling interfacial hydrogens Figure 5.3.2.4. The peak at 260 cm^{-1} (32.2 meV) is present only in the oven dried samples for CSH_1 and CASH_0.9, leading to a conclusion that probably these samples possess a thin layer of interfacial water, a monolayer, whilst in more hydrated samples there are multilayers of interfacial water, and in the desiccator dried samples the monolayer is patchy.

The signals at around 1100 cm^{-1} (136.4 meV) come from the strongly H-bonded water molecules, which donate H-bonds to the deprotonated surface oxygens. As shown in Figure 5.3.2.7, the intensity of the signal at 1100 cm^{-1} increases proportionally to the Ca/Si. Our MD models reveal that the surface (both at the external interface and at the interlayer) H-bonded water molecules also contribute to the intensity in this region (Figure 5.3.2.7). Thus, we suggest that the increased number of H-bonds at higher Ca/Si ratios result in enhanced intensity at 1100 cm^{-1} (136.4 meV) region.

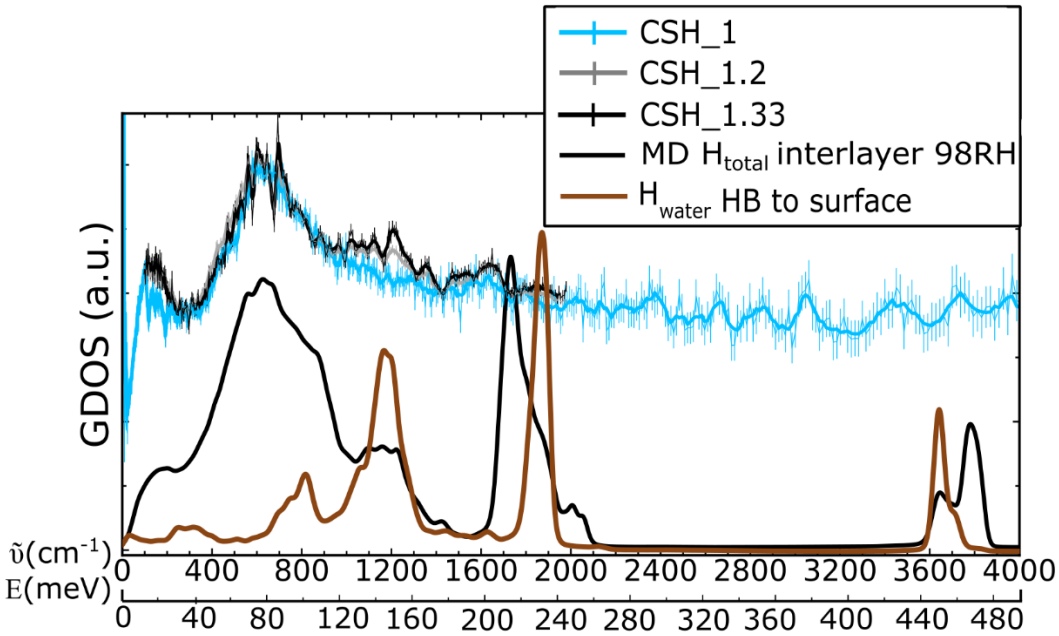

Figure 5.3.2.7. (Top) Experimental IINS spectra for CSH_1, CSH_1.2, and CSH_1.33 which were desiccator-dried; (Bottom) Calculated GDOS showing contributions from different water hydrogens H-bonded to the C-S-H surface.

Diffusion of water in CSH_1_55RH

The trajectories of oxygen atoms of water were followed over 5 ns, revealing a very restricted motion over the course of the production run (Figure 5.3.2.8, left). The MSD of water molecules in C-S-H and bulk water shown in Figure 5.3.2.8 (right) were used to calculate self-diffusion constants for water at the basal planes of the C-S-H model, obtaining a value of 6.8×10^{-11} m²/s. This value can be compared with other values from the literature: Kalinichev et al. showed that water in the channels of tobermorite has a self-diffusion coefficient of 5×10^{-11} m²/s, which is much lower than 2.3×10^{-9} m²/s for bulk water (Kalinichev, Wang and Kirkpatrick, 2007). In a recent review Qomi et al. (2021) reported several values for interfacial water from 2.6 to 5×10^{-11} m²/s (Abdolhosseini Qomi *et al.*, 2021), these values are in agreement with the one provided here.

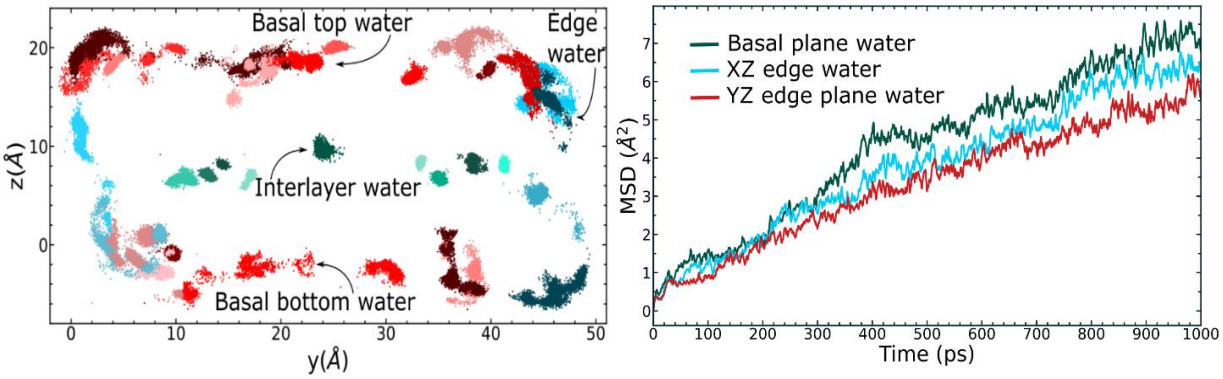

Figure 5.3.2.8. (left) The trajectories of water oxygens followed for 5 ns shown in the YZ plane for CSH_1_55RH; (right) The MSD of water molecules on the C-S-H surfaces measured for 1 ns.

5.4. Conclusions

Data from Inelastic Incoherent Neutrons Scattering experiments, complemented by MD simulations, WSI and TGA data, is revealed as an excellent tool to probe the vibrational dynamics of water in confined systems such as C-(A)-S-H surfaces and pores. The spectra exhibit a range of features that allow attributing different properties to the water in the different regions of the samples. Our combined approach showed that at the lower energies (<300 cm^{-1} or 37.2 meV) the so-called 'fingerprint' signal of the confined water at around 80 cm^{-1} (9.9 meV) was present in the drier C-(A)-S-H samples, with the oven-dried samples showing a peak at 260 cm^{-1} (32.2 meV) possibly belonging to a thin monolayer of interfacial water.

At intermediate energies, the shape of the librational region is different for water confined at interfaces, showing a broad band that starts at ~300 cm^{-1} (37.2 meV), as opposed to 550 cm^{-1} (68.2 meV) for bulk-like water. The librational edges for samples containing both multilayer adsorbed and bulk water were a linear combination of the edges of these two types of water, signifying the presence of both. The high energy (>1000 cm^{-1} or 124 meV) intermolecular bending and stretching modes were present in the experimental data, but with significantly dampened intensities. The calculated GDOS reproduced these intermolecular vibrations, albeit blue shifted due to the nature of confined water in our dry samples, and peculiarities of the SPC/E potential.

Differences in both the amount and the distribution of adsorbed water were found when increasing the Ca/Si ratio. At 98% RH, CSH_1.33 samples adsorbed less water than CSH_1, which in turn adsorbed less water than CASH_0.9. The water at higher Ca/Si ratios also was also more structured, i.e. less bulk-like. This observation can be rationalized by considering the number of adsorption sites for water present in the different samples. At high Ca/Si, more Ca^{2+} is present in the samples. This cation acts as a strong center of charge, very hydrophilic, thus creating more adsorption sites for the water. This water is not only bonded to the Ca^{2+} cation, but it also forms hydrogen bonds with oxygen atoms from the structure, resulting in a vibrational mode that is visible at ~1100 cm^{-1} (136.4 meV) whose intensity increases with the Ca/Si value.

Confined, strongly bound water from the first coordination sphere of Ca^{2+} has been observed to have limited diffusivity and to form strong hydrogen bonds with surface oxygen atoms, in particular in the interlayer region. Previous authors have observed an increase of the stacking along the **c*** direction upon increase of the Ca/Si ratio in the samples. This increased stacking could lead to an eventual higher crystallinity, with better defined sites for water adsorption (water from the Ca^{2+} hydration shell). The increase in the crystallinity would therefore be concomitant to an increase of the intensity of the feature at ~1100 cm^{-1} (136.4 meV).

These results converge towards a picture where the evolution from thin layers of adsorbed water to bulk capillary water is dampened by the structure of C-(A)-S-H, in particular by the availability of Ca^{2+} sites that tend to keep the water in the form of structured surface layers.

Conclusions

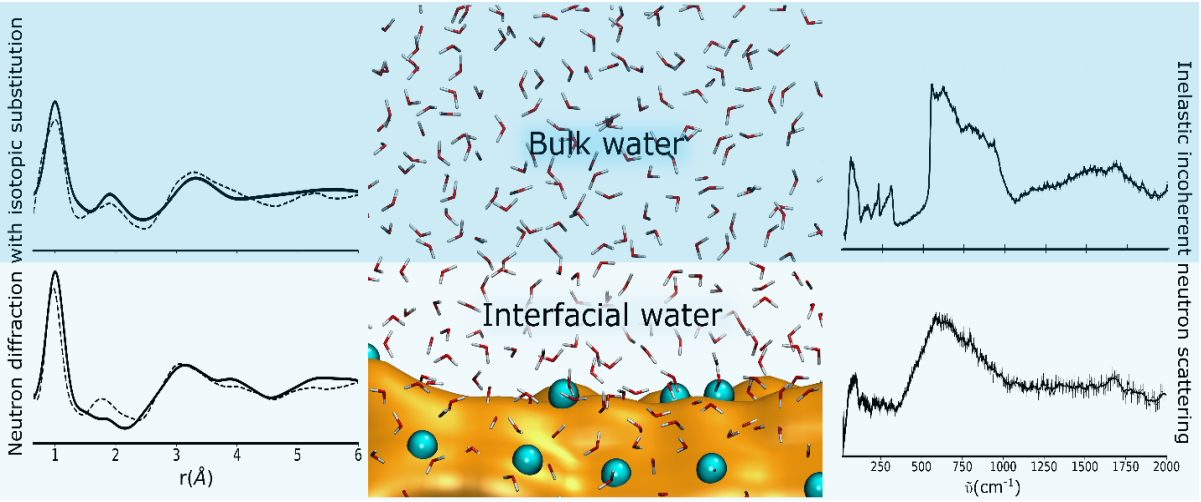

In this Ph.D. project, the structure and dynamics of water in the different pores of C-(A)-S-H were studied using a combination of neutron and X-ray scattering techniques with laboratory-based methods such as water sorption isotherms (WSI), infrared spectroscopy and thermogravimetric analyses. In particular, for the first time the neutron diffraction with an isotopic substitution and inelastic incoherent neutron scattering experiments were used to investigate the structure and dynamics of water in the C-(A)-S-H phase. The experimental data were complemented with molecular simulations of the first *in silico* nanoparticle model of C-(A)-S-H. This multitechnique approach was used to shed new light onto the following questions:

What is the effect of Ca/Si ratios on the overall stoichiometry and water distribution in C-(A)-S-H?

The increase of the total H_2O/Si with increasing Ca/Si is a well known trend, where the wide scattering of existing data in the H_2O/Si values was suggested to be due to different experimental conditions causing different water content in the samples from different studies (Richardson, 2014; Lothenbach and Nonat, 2015; L'Hôpital *et al.*, 2016; Roosz *et al.*, 2016; Abdolhosseini Qomi *et al.*, 2021). However, up to our knowledge, a direct correlation between the dependence of H_2O/Si with increasing Ca/Si ratios and different hydration levels has not been previously reported. Therefore, in this work, C-(A)-S-H samples with 5 different water contents and 12 different Ca/Si ratios were analyzed. The 5 hydration levels included: fully-hydrated, oven-dried (40°C, vacuum), conditioned at 55% and 98% RH, and desiccator-dried C-(A)-S-H samples after being conditioned at 98% RH. We referred to fully-hydrated and 98RH samples as to 'wet' samples, and to the rest as to 'dry' samples.

The amount of total H_2O per Si showed an upward trend with increased Ca/Si ratios. The 'dry' C-(A)-S-H samples contained roughly the same weight fraction of water irrespective of the Ca/Si. On the contrary, 'wet' samples showed a variation in the weight percent of total water due to varying capillary condensation in the pores. WSI data pointed at a decrease in the amount of adsorbed water with increasing Ca/Si ratios. However, the capillary condensation interfering with the adsorption of water at RH levels exceeding 95% resulted in the dependence of the total water content on the equilibration time. Therefore, for 98RH samples the equilibration time was a more important factor than the effect of

increased amount of calcium ions in high Ca/Si ratio samples, which resulted in varying H_2O/Si amounts.

The XRD data showed a decrease of d_{001} reflection value with increased Ca/Si ratios until the Ca/Si of about 1.27, after which it is relatively constant. The data reported in the literature (Renaudin *et al.*, 2009; Soyer-Uzun *et al.*, 2012; Richardson, 2014; Grangeon *et al.*, 2016; Gaboreau *et al.*, 2020) show large scatter (around 3 Å) of the d_{001} value, which is often attributed to different water contents in the C-(A)-S-H samples. Hence, a direct relationship exists between the d_{001} value and an increased amount of total water in the interlayer induced by the swelling of the interlayer. In addition, we propose that the decrease in the d_{001} value with increasing Ca/Si ratios can be explained by the C-(A)-S-H layers becoming more highly charged due to an increased number of calcium ions, reducing the effective repulsion between layers and leading to a decrease of the interlayer distance while accommodating more water molecules in the defects and around calcium ions.

How does the structure of water on the C-(A)-S-H interfaces and interlayers differ from the one of bulk water? Is the structure of water for C-(A)-S-H dependent on Ca/Si ratios?
The local ordering of water molecules adsorbed at C-(A)-S-H / water interfaces was studied using neutron diffraction with isotopic substitution (NDIS). The nanoparticle model of C-S-H built to interpret the neutron scattering data was based on the 14 Å tobermorite structure (Bonaccorsi, Merlino and Kampf, 2005) to which defects were introduced to reach Ca/Si=1 (Richardson, 2014). The difference between numerous earlier atomic models of C-S-H (R. J.-M. Pellenq *et al.*, 2009; Abdolhosseini Qomi *et al.*, 2014; Kovačević *et al.*, 2015; Androniuk, 2017; Kunhi Mohamed *et al.*, 2018) and this C-S-H model, is that previous structures were in majority bulk models, whereas our model was finite in all three dimensions, i.e., a nanoparticle. The obtained model structure was populated with water molecules mimicking 55% and 98% RH samples. The average intermolecular bond length between the hydrogen and oxygen atoms' intermolecular correlations beyond the second nearest neighbor was found to be about 0.2 Å shorter for interfacial and interlayer water than for bulk water. This distance is indicative of the H-bonding network, thus emphasizing the distinction between interfacial and interlayer water, and the bulk water.

Moreover, the same structural characteristics of water for the C-S-H samples were found for the C-A-S-H samples.

What is the effect of increased hydration level both on the local structure and long-range structure?
The local structure of water in 55RH model and the first monolayer of interfacial water in 98RH model showed that structurally water was very similar. The difference was observed in the number of H-bonds, with a more hydrated model showing (unsurprisingly) an increased number of H-bonds. The relevance of the two models was confirmed by X-ray Pair Distribution Function (PDF) analysis. Interestingly, the more hydrated structure showed a larger degree of mesoscale ordering, with a larger domain coherent size. This effect could be due to the fact that the modelled C-S-H nanoparticle contained only two silicate layers, such that the interactions of water molecules with the surface played a large role in the total intermolecular interactions within the whole system. Similar results, where the water molecules exert a

strong influence on the bulk properties of inorganic nanoparticles, have been presented previously for other nanoparticle systems (Gilbert *et al.*, 2006).

What is the wetting mechanism of the C-(A)-S-H surfaces?

The main mechanism for water adsorption was found to be the coordination of water by hydrophilic calcium ions, which induce a strong H-bond network with other water molecules and with surface oxygen atoms. The silanol groups play a minor role in this wettability mechanism: the C-S-H surface was characterized by a combination of wet and dry regions, where wet areas were dominated by the presence of hydrophilic calcium ions with strong hydration shells, whereas dry areas exposed only silica chains and silanol hydroxyls.

What is the influence of different hydration states on the dynamics of water in C-(A)-S-H?

The dynamics of water were studied using inelastic incoherent neutron scattering (IINS) and yielding for the first time the vibrational density of states of water in C-(A)-S-H samples function of Ca/Si (0.9, 1, 1.2, and 1.33) and RH levels.

The IINS spectra exhibited a range of features that allowed attributing different properties to the water in the different regions of the samples. Spectra from the 'wet' samples had strong similarities to that of ice Ih (measurements were performed at T = 10 K), showing translational lattice modes that pointed to the presence of a bulk water-like component. On the other hand, 'dry' samples showed 'fingerprint' signals of confined water. The generalized density of states (GDOS) was calculated based on our atomistic simulation C-S-H models with 55% and 98% RH levels. The calculated GDOS reproduced most of the experimental results, and confirmed that our 'drier' samples contained thin layers of interfacial water, with water hydrogens having dangling non-bonded hydroxyls at the water – air interface. The 'wet' samples, on the other hand, contained parts of multilayer adsorbed and bulk pore water, as evidenced from characteristic librational edges. The calculated GDOS reproduced also the intermolecular vibrations (bending and stretching), albeit blue shifted due to the nature of confined water in our dry samples, and peculiarities of the SPC/E potential.

What is the effect of different Ca/Si ratios on the dynamics of water in C-(A)-S-H?

Differences in both the amount and the distribution of adsorbed water were found when increasing the Ca/Si ratio. At 98% RH the higher Ca/Si ratio samples adsorbed less water than C-(A)-S-H samples with lower Ca/Si ratios. The water at higher Ca/Si ratios was also more structured, i.e. less bulk-like. This observation can be rationalized by considering the number of adsorption sites for water present in the different samples. At high Ca/Si, more Ca^{2+} is present in the samples. This cation acts as a strong center of charge, very hydrophilic, thus creating more adsorption sites for water. This water was not only bonded to the Ca^{2+} cation, but it also formed hydrogen bonds with oxygen atoms from the structure, resulting in a vibrational mode that is visible at ~1100 cm^{-1} whose intensity increases with the Ca/Si value. Confined, strongly bound water from the first coordination sphere of Ca^{2+} has been observed to possess limited diffusivity and to form strong hydrogen bonds with surface oxygen atoms, in particular in the interlayer region. Previous authors have noted an increase of the stacking along the **c*** direction upon increase of the Ca/Si ratio in the samples (Grangeon, Claret, Linard, *et al.*, 2013;

Gaboreau *et al.*, 2020). This increased stacking could lead to a higher crystallinity, with better-defined sites for water adsorption (water from the Ca^{2+} hydration shell). The increase in the crystallinity would therefore be concomitant to an increase of the intensity of the feature at ~1100 cm^{-1}.

These results converge towards a picture where the evolution from thin layers of adsorbed water to bulk capillary water is dampened by the structure of C-(A)-S-H, in particular by the availability of Ca^{2+} sites that tend to keep the water in the form of structured surface layers.

Future perspectives

To fully grasp the complexity of the C-(A)-S-H phase further studies are paramount. Some of the remaining issues could be addresses as following:

- Perform NDIS and IINS experiments on C-(A)-S-H samples of higher Ca/Si ratios, similar to the real hydrated cement. Potentially, the water structure and dynamics should be different for the high Ca/Si ratios C-(A)-S-H due to an increased number of calcium ions. The C-S-H structure is known to evolve in a 'monotonous' way from low Ca/Si to a Ca/Si ~ 1.4, where the precipitation of portlandite (or portlandite nanosheets) is observed (Grangeon *et al.*, 2017). Studying this transition to a multi-phase systems would be of high interest for the community of cement chemistry.
- The CSH_1 nanoparticle MD model should be modified to higher Ca/Si ratios by adding Ca^{2+} ions and balancing them with $2OH^-$ to reach the Ca/Si of about 1.7-2. The reactive force field (for example, ReaxFF) could be employed to observe chemical reactions of water with C-(A)-S-H. Another possibility would be to use GCMC (or GCMC syntax in LAMMPS) by setting the value of the chemical potential describing the wanted RH level.
- A different prospect with the CSH_1 nanoparticle model would be to study aggregation effects in a meso-scale model populated by many of the C-S-H nanoparticles generated here (as it was done for smectites (Underwood and Bourg, 2020)). The generated data could be compared to neutron or X-ray small angle scattering data. These kind of models would allow inferring the relative control that surface chemistry and steric conditions during drying or re-wetting.
- Certainly, all of these manipulations should also be done for the C-A-S-H. The atomistic model of C-S-H could be converted to C-A-S-H by replacing some bridging Si atoms with Al.

To sum up, there are a lot of possible directions in which the results of this thesis could be used. The complexity of the C-(A)-S-H is a challenge, but it is also an asset.

Annex 1 Drying tests

A.1.1. Drying conditions testing

Zhang and Scherer performed extensive tests to identify the best method to stop the hydration process of cement and to make samples suitable for experimentation (Zhang and Scherer, 2011). In brief, the studied methods were:

- *Freeze-drying:* a method of reducing very rapidly the temperature of the sample to that of liquid nitrogen (-196°C), so that the water in cement becomes solid. The drawbacks of the method are the potential damaging stresses can result from volume expansion, hydraulic pressure, and crystallization pressure.
- *Solvent exchange:* the method works by replacing the free water in the sample by an organic solvent, which is later removed via volatilization. The solvents used should be miscible with water and have small molecular size. Generally used solvents include: acetone, isopropanol, methanol, benzene, hexane, toluene, dimethyl sulfoxide etc. The drawback of the method is a possible chemical reaction between the solvent and cement species, especially in the case of methanol. Isopropanol was thought to be the best solvent for cement-based applications (Feldman, 1987).
- *Vacuum drying:* the sample is put in a chamber with p ≤0.1 Pa (similarly to D-drying, see below). The method is not very effective as it does not remove all water, while possibly causing microcracks and stresses similar to the ones caused by oven-drying at 60°C and 105°C.
- *D-drying:* in this method the sample is kept inside the desiccator, which is connected to a trap cooled by dry ice (solid CO_2) and ethanol to -79°C, and the partial pressure (p) of water vapor over the is 0.07 Pa. D-drying is generally assumed to remove all of the physically adsorbed (unbound) water in the cement paste pores and to be the best microstructure-preserving drying method. The drawbacks of the method include the removal of some bound water (i.e. structural water) and rather slow arresting of hydration.
- *P-drying:* is drying to the vapor pressure of magnesium perchlorate hydrates (dehydrate and tetrahydrate) at r.t., so that the partial p of water is ~ 1.1 Pa. The major drawback of the technique is that it contains residual pore water. D-drying, P-drying, and vacuum drying methods are similar because they cannot arrest the hydration effectively due to slow water removal.
- *Oven-drying:* the most widespread method, which however has a lot of disadvantages. The advantages of oven-drying are the effective removal of water and its easy execution. The drawbacks, however, include the damages to the microstructure, altering of the pore structure, and the removal of structural water (Scherer, 1990; Gallé, 2001). However, in this work the oven-drying was chosen as the method of removing the majority of water. The justification lies in the specific drying conditions that we have applied. Generally, the temperatures causing structural damage are above 60°C (105°C is another widespread value) at ambient p. Another major drawback in using a 'normal' oven is that the specimen is subjected to carbon dioxide

during the drying. Therefore, the vacuum oven with N_2 flushing in (before and after the evacuation) was used to perform drying tests at varying temperatures (Figure A.1.1). As it is clear from the XRD results, high temperatures (100°C, 150°C) coupled with evacuation, damage the structure significantly. At the same time the shrinkage of the interlayer is dramatic (2.3-2.5 Å), signifying the removal of the majority of interlayer water. The drying at 40°C in vacuum resulted in reduction of d_{001} reflection by about 2 Å. It was apparent that rather low temperature of 40°C does not allow to remove all water, evidenced by FT-IR results as well (Figure A.1.2). However, it was chosen as the fastest and the most reliable way of removing the majority of 'evaporable' water, while causing minimal damage to the microstructure.

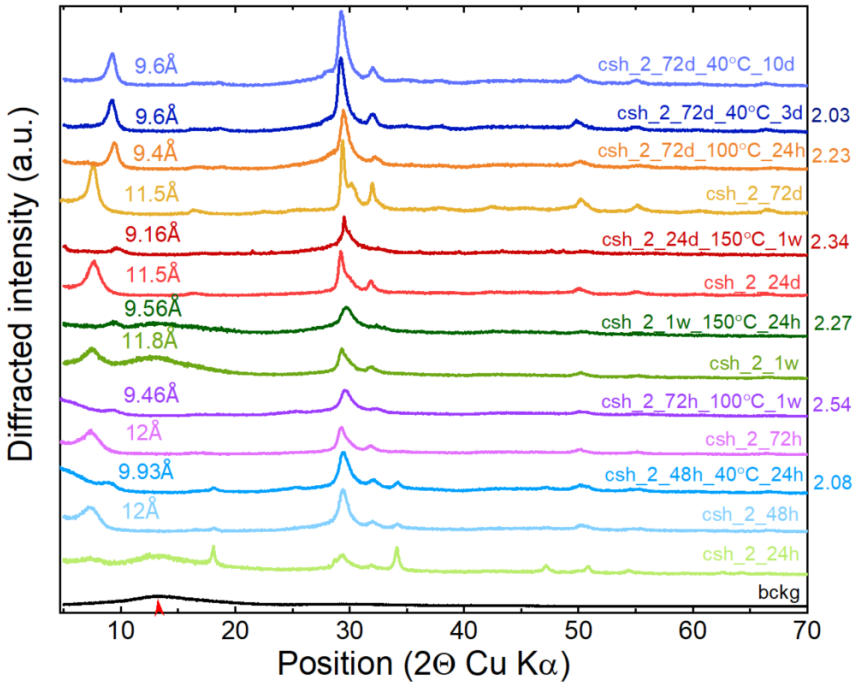

Figure A.1.1.The XRD data showing the drying tests by varying drying temperature for CSH with Ca/Si=1.26. The numbers on the right outside the figure signify the reduction in d_{001} reflection value (Å) from the fully hydrated state to after drying state. The data were recorded using laboratory XRD instrument with a special dome to protect the C-S-H samples from carbonation (more in Chapter 3), which gave a characteristic background (black line) shown with red arrow at 13° 2Θ.

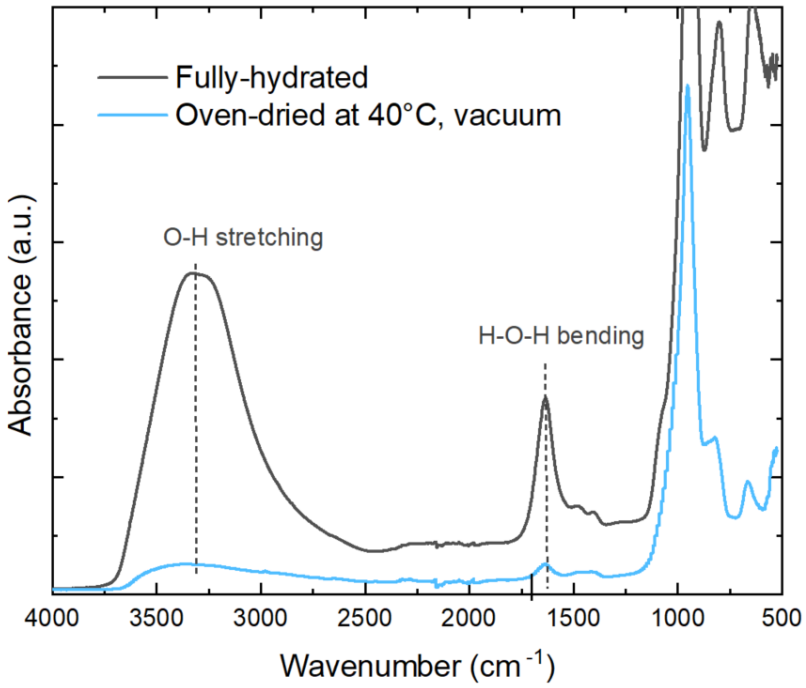

Figure A.1.2. The FT-IR spectra of fully hydrated and oven-dried C-S-H. The spectra show the presence of water O-H stretching (3350 cm^{-1}) and H-O-H bending (1650 cm^{-1}) signals after drying as well.

Annex 2 Aging of synthetic C-(A)-S-H

A.2.1. IINS results

The continuous evolution over time of the amount and distribution of the porosity and water in hydrated cement is referred to as 'aging'. Even though this phenomenon has been widely reported for hydrated cement pastes (H. Taylor, 1997), there are no major conclusions/evidences of the 'aging' of the synthetic C-(A)-S-H phase. Here, we report a set of observations based on the results of TGA and IINS experiments that show the presence of aging phenomena in C-(A)-S-H.

The nature of the changes depends on the conditions under which the samples are stored. In particular, changes were observed for samples conditioned at 55% RH (also because they were priority samples for neutron scattering experiments, so there was more data concerning 55RH samples). Measurements performed on C-(A)-S-H 55RH samples 6 to 11 months after the initial IINS experiment show a shift of the librational edge to lower energies, and a broadening of the librational bands. In particular, the CSH_1_55RH sample (Figure A.2.1.1) recorded 11 months later showed a slight shift of the librational edge to lower energies, and slight dampening of the librational modes intensity (500-1000 cm^{-1}). An increase in the intensity of the modes at 1100 cm^{-1} is observed for C-A-S-H samples.

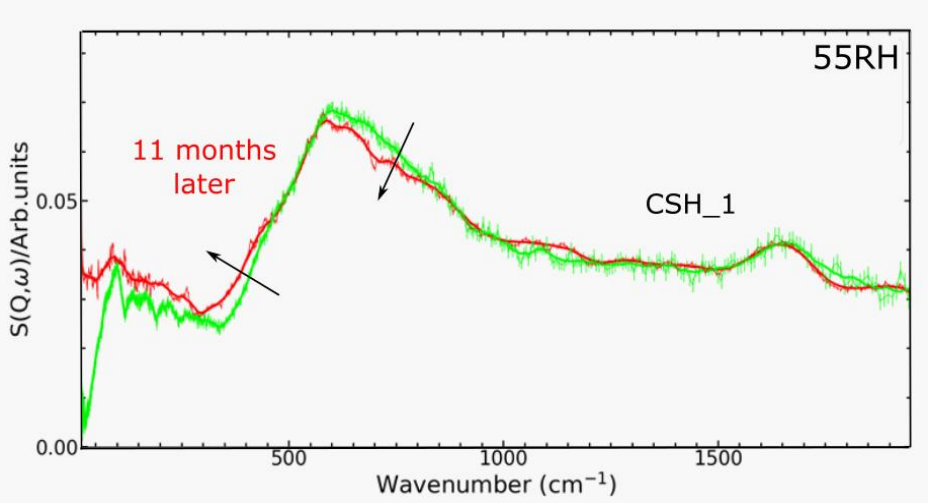

Figure A.2.1.1. The IINS data for CSH_1_55RH collected with 11 months difference. The earlier (in bright green) spectrum was collected at TOSCA, ISIS, and later (in red) spectrum at IN1-Lagrange, ILL.

Results from CASH_55RH samples with Ca/Si=0.9 and 1.1 (Figure A.2.1.2) showed a shift towards lower energies of the librational edge and a slight increase in the intensity of 1100 cm^{-1} region. The latter was identified as coming from strongly H-bonded water hydrogens donating H-bonds to the C-(A)-S-H surfaces, based on our calculated GDOS (Chapter 5).

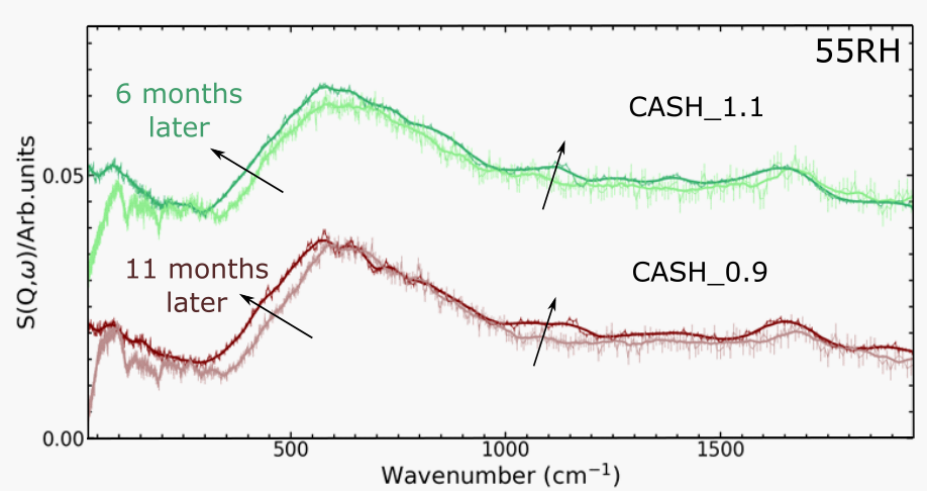

Figure A.2.1.2. The IINS data for CASH_0.9 and 1.1, collected with 6 and 11 months difference. The earlier (in light green and light brown) spectra were collected at TOSCA, ISIS, and later (in dark green and dark brown) spectra at IN1-Lagrange, ILL.

A similar shift to lower energies and damping of the librational modes intensity was observed for CSH_1 desiccator-dried samples (Figure A.2.1.3). Generally, the shift of the librational edge towards lower energies and broadening of the librational modes implies a less ordered H-bond network, whereas an increase in the intensity at 1100 cm^{-1} stems from an increased number of H-bonds. It is possible that water in these relatively dry samples redistributes over time, forming H-bonds with the C-(A)-S-H surface and other water molecules, i.e., finding more lower enegy sites of adsorption at the surface.

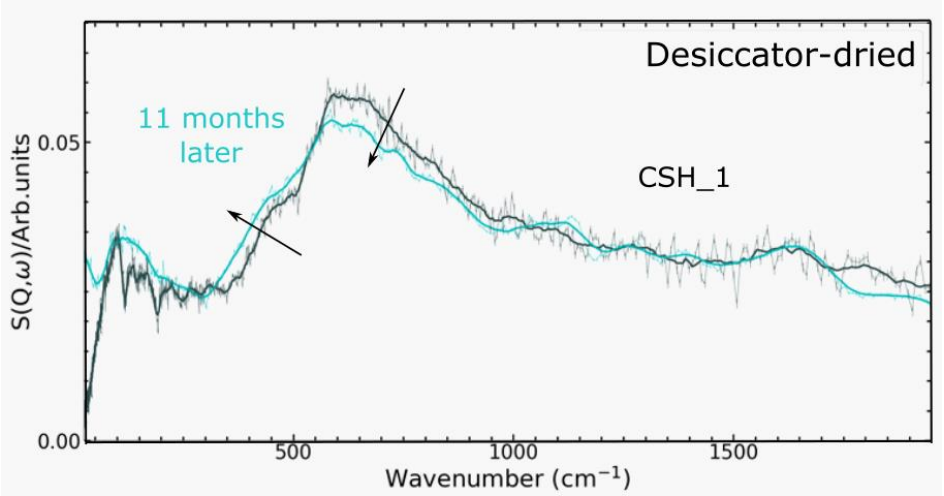

Figure A.2.1.3. The IINS data for CSH_1_desiccator-dried collected with 11 months difference. The earlier (in grey) spectrum was collected at TOSCA, ISIS, and later (in blue) spectrum at IN1-Lagrange, ILL.

The main issue with the IINS data is that they were collected using different instruments: TOSCA at ISIS, and IN1-Lagrange. The resolution of these instruments is different, with TOSCA having about 1.25% $\Delta E/E$, and IN1-Lagrange varying depending on the face of the monochromators used, but in general showing less resolution than TOSCA (more in Chapter 2 and 5). Thus, a part of the differences between the spectra could be caused by experimental resolution of the instruments.

A.2.2. Thermogravimetric analysis results

TGA results also point to changes in the amount and distribution of water over time. The TGA data were collected for a C-S-H sample with 3 months of difference. The data presented in Figure A.2.2.1. belong to C-S-H with Ca/Si=1.27 at three different hydration levels: desiccator-dried, 55RH and 98RH.

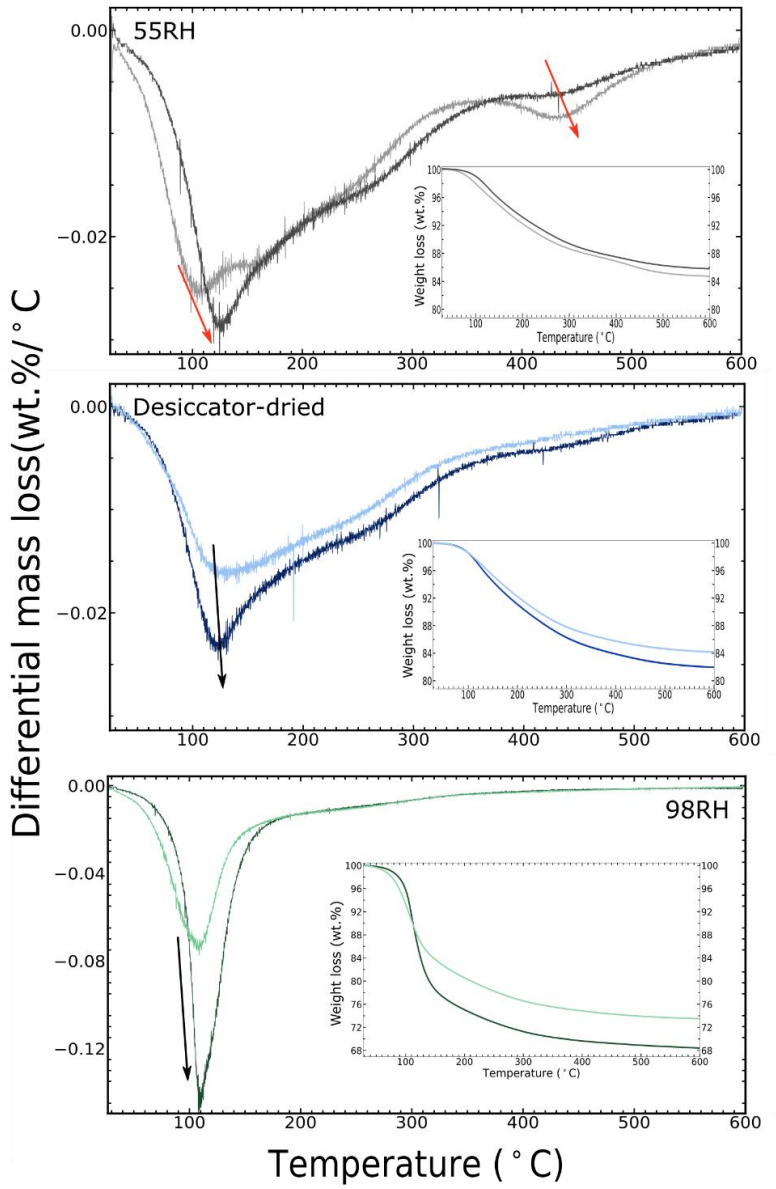

Figure A.2.2.1. The TGA and dTG curves for CSH_1.27 collected with 3 months difference. Lighter colored curves were collected earlier, and darker colored ones 3 month later.

The 55RH and desiccator-dried samples showed slight variations of 2 to 3 weight percent in the total water amount over time. The slight change in the amount of total water is unsurprising as samples at these RH levels possess only some interlayer and interfacial water. However, the differential mass loss (dTG) curves (Figure A.2.2.1. top and middle) show a slight shift to higher temperatures, meaning that probably water became stronger bound over time. The same trend is observed for the dTG curves of the 98RH sample (Figure A.2.2.1. bottom). The 98RH sample showed an increase in the amount of total

water over time of ~5 %, meaning that indeed the longer equilibration time leads to larger amount of adsorbed water for samples conditioned at RH levels > 95% (see Chapter 3).

Conclusion

Overall, the 'aging' data presented here point toward constant evolution of water in the synthetic C-(A)-S-H, just like in a hydrated cement. The changes may not be significant for 'drier' samples, but for samples conditioned at high RH levels (>95%), the equilibration time is an important factor. However, careful tests with equal conditioning times and using the same instrument are needed to confirm and to quantify the aging phenomenon in synthetic C-(A)-S-H.

Supplementary Information for Chapter 4

Structure of water adsorbed on nanocrystalline calcium silicate hydrate determined from neutron scattering and molecular dynamics simulations

Zhanar Zhakiyeva[1,2,*], Gabriel J. Cuello[2,*], Henry E. Fischer[2], Daniel T. Bowron[3], Catherine Dejoie[4], Valerie Magnin[1], Sylvain Campillo[1], Sarah Bureau[1], Agnieszka Poulain[1], Rogier Besselink[1], Stephane Gaboreau[5], Sylvain Grangeon[5], Francis Claret[5], Ian C. Bourg[6,*], Alexander E. S. Van Driessche[1], Alejandro Fernandez-Martinez[1,*]

[1] *University of Grenoble Alpes, University of Savoie Mont Blanc, CNRS, IRD, IFSTTAR, ISTerre, 38000 Grenoble, France.*

[2] *Institut Laue–Langevin, 71 Avenue des Martyrs, CS 20 156, 38042 Grenoble Cedex 9, France.*

[3] *ISIS, Science and Technology Facilities Council Rutherford Appleton Laboratory, Harwell Oxford, Didcot, UK.*

[4] *ESRF, The European Synchrotron, 71 Avenue des Martyrs, CS40220, 38043 Grenoble Cedex 9, France*

[5] *BRGM, 3 Avenue Guillemin, Orléans Cedex 2 45060, France.*

[6] *Department of Civil and Environmental Engineering and High Meadows Environmental Institute, Princeton University, Princeton, New Jersey 08544, United States.*

*Corresponding Authors: Zhanar Zhakiyeva (zhanar.zhakiyeva@univ-grenoble-alpes.fr), Gabriel J. Cuello (cuello@ill.eu), Ian C. Bourg (bourg@princeton.edu), Alejandro Fernandez (Alex.Fernandez-Martinez@univ-grenoble-alpes.fr)

S.1. Neutron Diffraction with Isotopic Substitution

The result of a diffraction experiment on a liquid or an amorphous system (water in a disordered nanocrystalline C-S-H phase in our case) is a diffraction pattern or diffractogram, which is a sum of all scattered intensity from all coherence volumes in the sample. The measured intensity (I) is a function of the scattering vector (Q), which is related to the incident wavelength λ and scattering angle 2θ:

$$Q = \frac{4\pi sin\theta}{\lambda} \qquad eq.(S1)$$

Therefore, a diffractogram can be obtained by varying λ or 2θ, or both. In the case of a reactor source of neutrons (D4c, ILL) a monochromatic beam is used and 2θ is varied, whereas in time-of-flight pulsed sources (SANDALS, ISIS) both λ and 2θ are varied (Henry E. Fischer, Barnes and Salmon, 2006).

To obtain the sample intensity, the intensities contributed by the empty container and the instrument background are measured and subtracted. The data are corrected for attenuation (from absorption and scattering) and multiple scattering (from within the sample and sample environment). A vanadium standard is measured as well to normalize the sample scattering data to absolute units of scattering cross section. The effect relies on a property of vanadium to scatter neutrons completely incoherently, therefore resulting in a structureless flat background.

The data are presented in units of barn per steradian per atom (where barn is a neutron scattering unit equal to 1 barn = 100 fm^2) as a function of the scattering vector. The corrected intensity is given within the so-called static approximation (in which the energy exchanged between the incident neutron and the sample is minimal compared to the incident neutron energy) as:

$$I(Q) = \sum_{\alpha} c_\alpha \overline{b_\alpha^2} + F(Q) \qquad eq.(S2)$$

where c_α is the atomic fraction of species α and $\overline{b_\alpha^2}$ is its mean square scattering length (an intrinsic measure of the tendency of nuclei to scatter neutrons, in units of fm). The first component in equation 2 is known as the self-scattering term and gives a downward slope to $I(Q)$ with increasing Q due to the recoil effect by the light nuclei (H and D). The second component $F(Q)$ contains the structural information as:

$$F(Q) = \sum_{\alpha}\sum_{\beta} c_\alpha c_\beta \; b_\alpha b_\beta \left[S_{\alpha\beta}(Q) - 1\right] \qquad eq.(S3)$$

where b_α and b_β are the mean coherent scattering lengths of species α and β and $S_{\alpha\beta}(Q)$ are their partial structure factors. The Fourier transformation of the partial structure factors yields the real space partial pair distribution function (PDF) $g_{\alpha\beta}(r)$. This last function defines the probability of finding an atom β at a distance r from an atom α (and equally β from α) as:

$$g_{\alpha\beta}(r) = 1 + \frac{1}{2\pi^2\rho_n}\int_0^\infty \left[S_{\alpha\beta}(Q) - 1\right]Q^2 \frac{\sin Qr}{Qr} dQ \qquad eq.(S4)$$

where ρ_n is the atomic number density (number of atoms per volume of the unit cell, Å^{-3}). In equation 4 an integral is taken over the whole Q-space, from zero to infinity. In a real diffraction experiment the Q-range is finite, and the integral is taken from zero to Q_{max} leading to broader peaks and non-physical oscillations in $g(r)$. To reduce this problem, the $S(Q)$ can be convoluted with a window function, $M(Q)$, which has the property of going to zero as Q_{max} is approached, thus modifying equation 4 to:

$$g_{\alpha\beta}(r) = 1 + \frac{1}{2\pi^2\rho_n}\int_0^\infty \left[S_{\alpha\beta}(Q) - 1\right]Q^2 \frac{\sin Qr}{Qr} M(Q)dQ \qquad eq.(S5)$$

In our case, we used the Lorch function defined as:

$$L(Q, \Delta_0) = \frac{sinQ\Delta_0}{Q\Delta_0} \qquad eq.(S6)$$

where $\Delta_0 = \frac{2\pi}{Q_{max}}$ defines the resolution of the radial distribution function (Lorch, 1969).

In a diffraction experiment, all partial structure factors and their corresponding PDFs are summed up in a single diffractogram. In order to obtain information about the partials separately, it is necessary to modulate either c_α or b_α without modifying the system structure. Modulating c_α requires a change in sample composition, which is not possible without modifying the structure. Modulating b_α, on the other hand, is possible because of the tendency of different isotopes of the same element to scatter neutrons differently. However, not all isotopes are suitable for the implementation of this neutron diffraction with isotopic substitution (NDIS) method, as the method requires a sufficient contrast between the scattering lengths of the two isotopes of the same element. In our case, we use the high contrast between the b_α values of different isotopes of hydrogen, ^{1}H and ^{2}H (D), to perform NDIS experiments (Pitteloud *et al.*, 2003).

The *first-order difference* of the total structure factor of samples with ^{1}H and samples with D leads to a partial structure factor where all contributions not involving H are cancelled out, given as:

$$\Delta_H(Q) = c_H\left(\overline{b}_H^2 - \overline{b}_D^2\right) + c_H^2\left(\overline{b}_H^2 - \overline{b}_D^2\right)[S_{HH}(Q) - 1] + \sum_{\alpha\neq H} 2c_H c_\alpha (b_H - b_D) b_\alpha [S_{H\alpha}(Q) - 1]$$

eq. (S7)

Finally, the real-space pair correlation function $G_H(r)$ is then a weighted sum of the partial PDFs centered on H atom:

$$G_H(r) = \frac{1}{2\pi^2\rho_n}\int_0^\infty \left[\Delta_H(Q) - c_H^2(b_H^2 - b_D^2)\right] Q^2 \frac{\sin Qr}{Qr} dQ$$

$$= c_H^2(b_H^2 - b_D^2)[g_{HH}(r) - 1] + \sum_{\alpha\neq H}^{n} 2c_H c_\alpha (b_H - b_D) b_\alpha [g_{H\alpha}(r) - 1] \qquad \text{eq. (S8)}$$

S.2. X-ray diffraction results for C-(A)-S-H samples

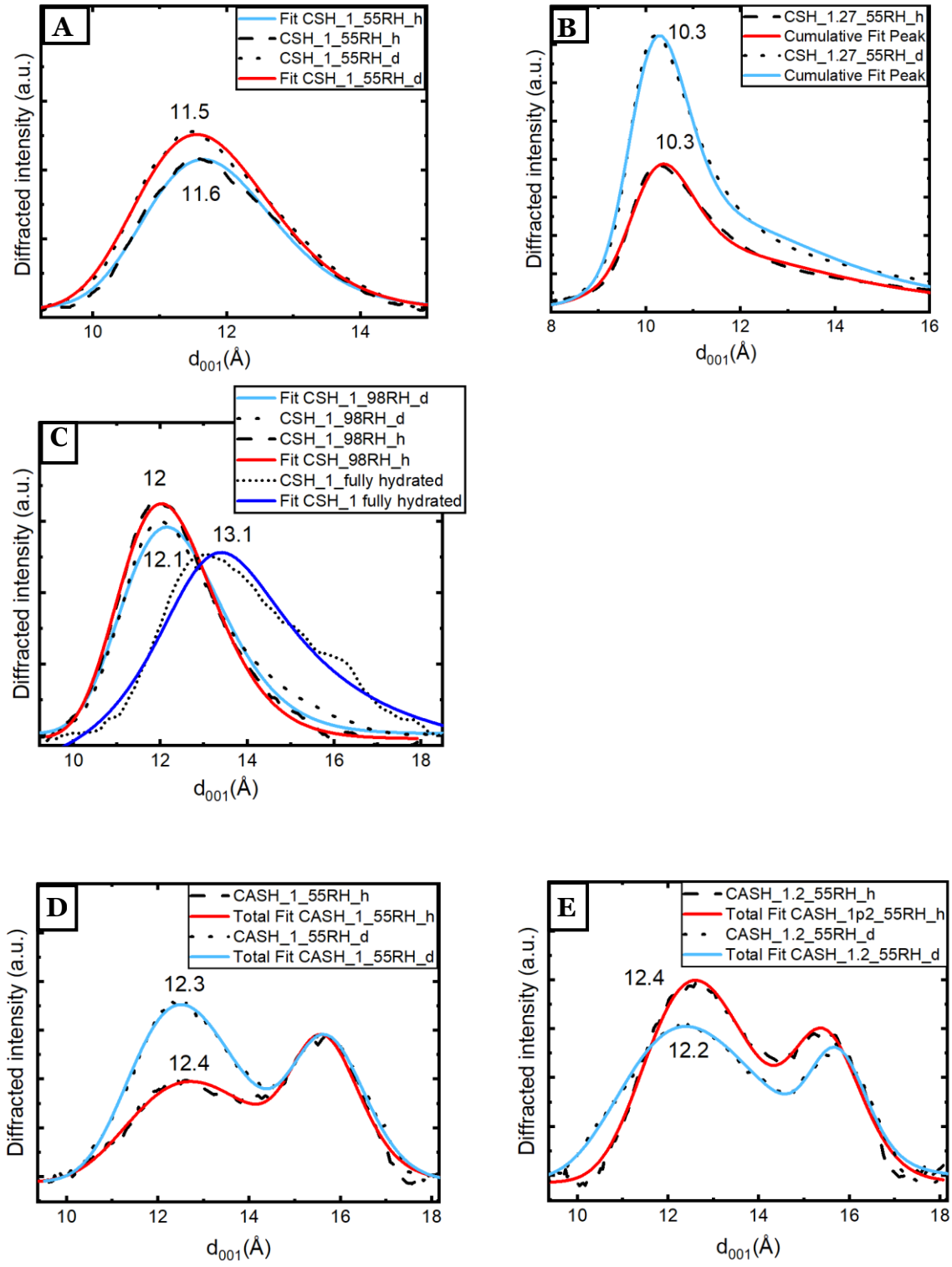

Figure S1. Experimental XRD patterns (dashed lines) focused on the d_{001} reflection for (A) CSH_1_55RH samples; (B) CSH_1.27_55RH samples; (C) CSH_1_98RH samples; (D) CASH_1_55RH samples; and (E) CASH_1.2_55RH samples, with corresponding Gaussian and Pseudo-Voigt fits (bold lines). The basal spacings in tobermorites(Biagioni, Merlino and Bonaccorsi, 2015)*, mineral analogs of C-S-H, vary as follows: ~14 Å*

tobermorite (plombierite(Bonaccorsi, Merlino and Kampf, 2005)*) with a full interlayer and chemical composition* $Ca_5Si_6O_{16}(OH)_2 \cdot 7H_2O$*; ~11 Å tobermorite*(Merlino, Bonaccorsi and Armbruster, 2001) $Ca_5Si_6O_{17} \cdot 5H_2O$ *(as well as clinotobermorite, a dimorph of tobermorite) with a partially filled interlayer; and ~9.6 Å tobermorite (obtained through partial dehydration of 11Å clinotobermorite at 225°C, the natural analog being riversideite) with a chemical composition* $Ca_5Si_6O_{16}(OH)_2$ *with no interlayer water*(Merlino, Bonaccorsi and Armbruster, 2000)*. Similar transitions in basal spacing are observed upon heating 14 Å tobermorite as the* $8H_2O$ *per formula unit decreases to* $4H_2O$ *at 90°C,* $2H_2O$ *at 200°C, and finally* $0H_2O$ *at 260-600°C.*(Yu and Kirkpatrick, 1999)

S.3.Thermogravimetric analysis of the C-(A)-S-H samples

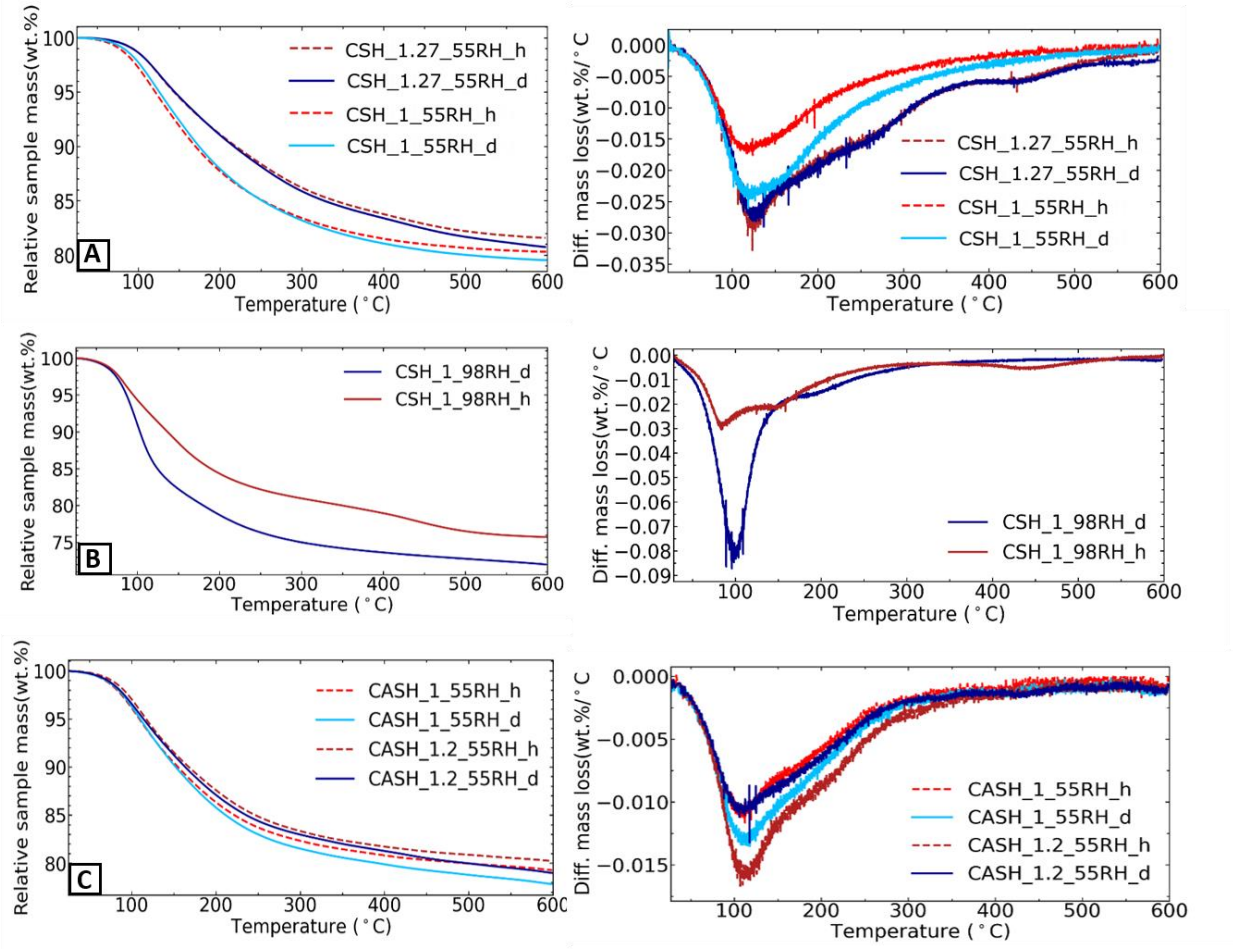

Figure S2.Thermogravimetric (TG, left) and differential TG (dTG, right) curves of (A) CSH_1 and CSH_1.27 conditioned at 55% RH; (B) CSH_1 at 98% RH; and(C) CASH_1 and CASH_1.2 conditioned at 55% RH. As stated in the text, we assign the mass loss from 25°C to 300°C to water removal, and from 300°C to 600°C to dehydroxylation.

S.4. Attenuated Total Reflectance-Fourier Transform Infrared (ATR FT-IR) spectra of the C-(A)-S-H samples

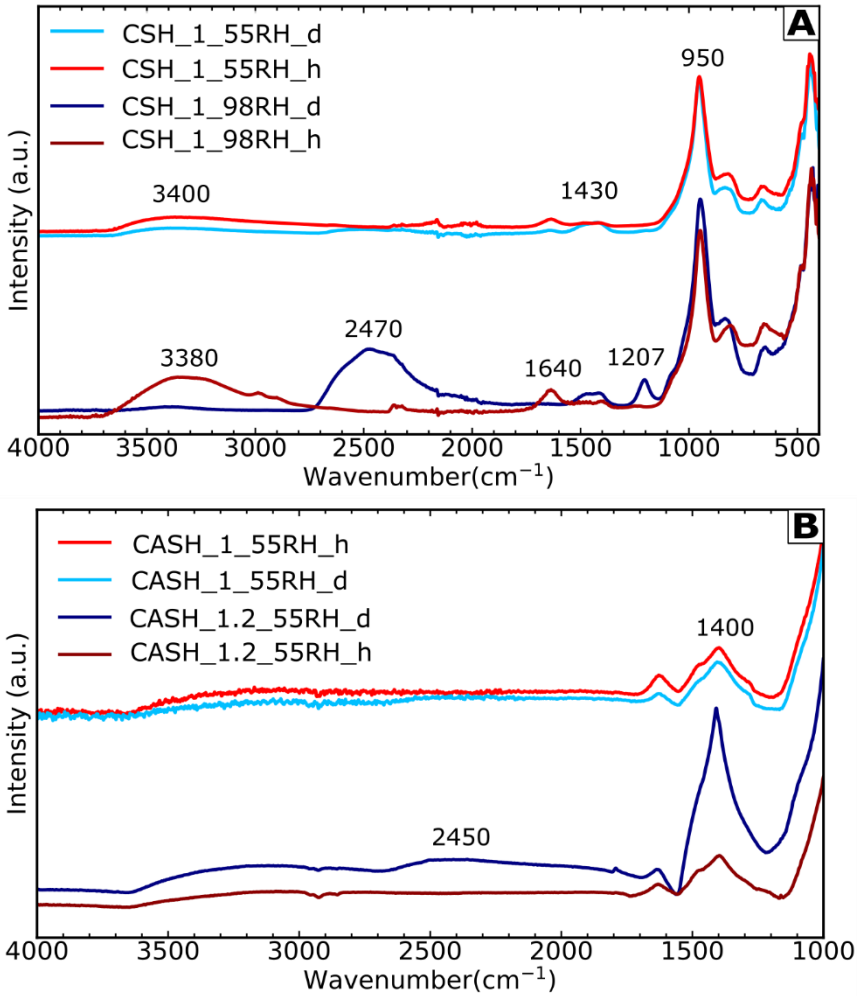

Figure S3. ATR FT-IR spectra of (A) CSH_1 at 55%RH and 98%RH and (B) CASH_1 and CASH_1.2 samples at 55% RH. Asymmetric and symmetric stretching vibrations of Si-O bonds are found at 800-1200cm-1; carbonate bands at ~1400cm-1, H-O-H bending at ~1640cm-1; O-D stretching at ~2450cm-1; O-H stretching at ~3400cm-1.

S.5. Water sorption isotherms of the C-(A)-S-H samples

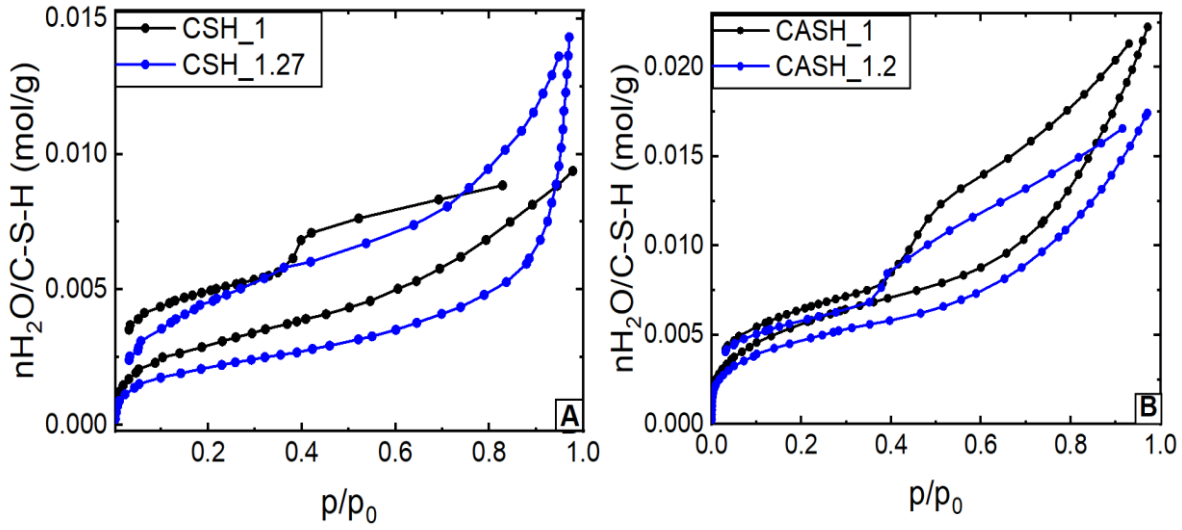

Figure S4. Water sorption Isotherms of (A) CSH_1 and CSH_1.27, and (B) CASH_1 and CASH_1.2 samples.

S.6. Water stoichiometry of the C-(A)-S-H samples

Stoichiometry	Name	H_2O total	D_2O total	H_2O inter-layer	H_2O adsor-bed	H_2O pore	D_2O inter-layer	D_2O adsor-bed	D_2O pore
$Ca_1Si_1O_{2.8}(OH)_{0.4}$	CSH_1_55RH_h	1.32		0.65	0.67				
	CSH_1_55RH_d	0.99	0.42	0.55	0.44		0.23	0.19	
	CSH_1_98RH_h	3.2		0.95	1.04	1.21			
	CSH_1_98RH_d		3.43				1.05	1.12	1.26
$Ca_1Si_{0.8}O_{2.43}(OH)_{0.59}$	CSH_1.27_55RH_h	0.93		0.45	0.48				
	CSH_1.27_55RH_d	0.58	0.47	0.3	0.28		0.23	0.24	
$Ca_1Si_{1.1}Al_{0.1}O_{2.8}(OH)_{0.4}$	CASH_1_55RH_h	1.39		0.64	0.75				
	CASH_1_55RH_d	0.85	0.81	0.43	0.42		0.39	0.42	
$Ca_1Si_{0.9}Al_{0.09}O_{2.63}(OH)_{0.45}$	CASH_1.2_55RH_h	1.45		0.57	0.88				
	CASH_1.2_55RH_d	0.55	0.71	0.23	0.32		0.25	0.46	

Table S1. Water stoichiometry in hydrogenated and deuterated C-(A)-S-H samples conditioned at 55% RH and 98% RH

S.7. Defects in CSH_1 models

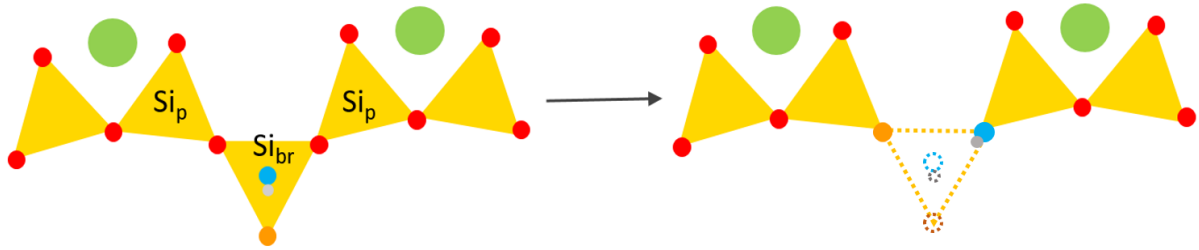

Figure S5. Schematic of defect creation by removing bridging silica tetrahedral. Yellow triangles represent SiO_4 tetrahedra; circles represent bridging oxygens (red), hydroxyl oxygens (blue), hydroxyl hydrogens (gray), deprotonated oxygens (orange), and structural calcium atoms (green). During defect creation, the bridging silicon atom is removed along with its deprotonated oxygen and hydroxyl group. Its two bridging oxygens are replaced by a deprotonated oxygen and a hydroxyl group. This maintains the charge neutrality of the system.

S.8. Parameters of the CSH_1_55RH and CSH_1_98RH model systems

Atom parameters						
Species	**Symbol**	**σ (Å)**	**Ɛ (eV)**	**q (e^-)**	**Number of atoms**	**Reference**
Ionic calcium	Ca	2.36084	1.95028e-02	2.0	154	
Structural calcium	Cao	5.56170	2.18109e-07	1.05	198	Cygan et al. (2004)(Cygan, Liang and Kalinichev, 2004)
Tetrahedral silicon	Si	3.302027	7.98102e-08	2.1	339	
Bridging oxygens	Ob	3.16556	6.73853e-03	-1.05	602	
Hydroxyl oxygen	Oh	3.16556	6.73853e-03	-0.95	132	
Hydroxyl hydrogen	Ho	0.0	0.0	0.425	132	
Deprotonated oxygen	Od	3.16556	6.73853e-03	-1.525	272	
Bridging edge oxygen	Obe	3.16556	6.73853e-03	-1.2875	72	
CSH_98RH model (40016 atoms)						
Water oxygen	Ow	3.16556	6.73853e-03	-0.82	12705	Cygan et al. (2004)(Cygan, Liang and Kalinichev, 2004)
Water hydrogen	Hw	0.0	0.0	0.41	25410	
CSH_55RH model (3236 atoms)						
Water oxygen	Ow	3.16556	6.73853e-03	-0.82	448	Cygan et al. (2004)(Cygan, Liang and Kalinichev, 2004)
Water hydrogen	Hw	0.0	0.0	0.41	896	
Bond parameters						
Species	**K (eV/ Å²)**		**R_0 (Å)**		**Reference**	
O-H	24.0291		1.0		Cygan et al. (2004)(Cygan, Liang and Kalinichev, 2004)	
Angle parameters						
Species	**K (eV/ rad²)**		**Θ_0 (°)**		**Reference**	
H-O-H	1.98472		109.47		Cygan et al. (2004)(Cygan, Liang and Kalinichev, 2004)	
Si-O-Si	4.3363		137.5, 134.95		K adapted from Heinz et al.(2005)(Heinz *et al.*, 2005)	
O-Si-O	4.3363		97.2, 103.3		Θ_0 from Bonaccorsi et al.(2005)(Bonaccorsi, Merlino and Kampf, 2005)	

Table S2. Potential parameters used for MD simulations of CSH_1_55RH and CSH_1_98RH. The σ and Ɛ correspond to the size and the energetic parameters for interactions between two atoms of identical type according to the Lennard-Jones 6-12 model of Van der Waals interactions. For interaction between two atoms of non-identical types, σ and Ɛ were determined using the Lorentz-Berthelot combining rule. All parameters were taken from the CLAYFF mineral model and SPC/E water model, except the partial charges of Od and Obe atoms.

S.9. An example of partial charges calculations following the algorithm by Lammers et al.(Lammers *et al.*, 2017)

CLAYFF-compatible partial charges for undercoordinated bridging edge oxygens (formal charge -2.0), coordinated to one structural Si atom (formal charge +4.0; CLAYFF partial charge +2.1; four-coordinated) and one structural Ca atom (formal charge +2.0; CLAYFF partial charge +1.05; four-coordinated) were calculated using the following relation. More details on the formula are provided in Lammers et al.(Lammers *et al.*, 2017)

$$Z_{Obe}^{p} = -2.00 + \frac{1 * (4.0 - 2.1)}{4} + \frac{1 * (2.0 - 1.05)}{4} = -1.2875$$

S.10. Synthesis amounts

Ca/Si ratio	**Sample**	**CaO (mmol)**	**CaO (mmol/mL)**	**CaO (grams)**	**SiO_2 (mmol)**	**SiO_2 (mmol/mL)**	**SiO_2 (grams)**	**Total V(H_2O) (mL)**
1.27	CSH_1.27	78.88	0.197	4.42	58.72	0.146	3.54	800
1	CSH_1	163.02	0.1716	9.141	152	0.16	9.132	1900

Table S3. Amounts of reagents used for the synthesis of CSH_1 and CSH_1.27.

References:

Abdolhosseini Qomi, M. *et al.* (2014) 'Combinatorial molecular optimization of cement hydrates', *Nature Communications*, 5(1), p. 4960. doi: 10.1038/ncomms5960.

Abdolhosseini Qomi, M. J. *et al.* (2021) 'Advances in atomistic modeling and understanding of drying shrinkage in cementitious materials', *Cement and Concrete Research*. Elsevier Ltd, 148(January), p. 106536. doi: 10.1016/j.cemconres.2021.106536.

Allen, A. J., Thomas, J. J. and Jennings, H. M. (2007) 'Composition and density of nanoscale calcium-silicate-hydrate in cement', *Nature Materials*, 6(4), pp. 311–316. doi: 10.1038/nmat1871.

Allen, M. P. (2004) 'Introduction to molecular dynamics', in *Computational Soft Matter: From Synthetic Polymers to Proteins, Lecture Notes*, pp. 1–28. doi: 10.1016/B978-0-12-816954-4.00001-2.

Allen, M. P. and Tildesley, D. J. (1991) *Computer Simulation of Liquids: Second Edition*. 1st edn. Oxford: Oxford University Press. doi: 10.1093/oso/9780198803195.001.0001.

Amann-Winkel, K. *et al.* (2016) 'X-ray and Neutron Scattering of Water', *Chemical Reviews*, 116(13), pp. 7570–7589. doi: 10.1021/acs.chemrev.5b00663.

Androniuk, I. *et al.* (2017) 'Adsorption of gluconate and uranyl on C-S-H phases: Combination of wet chemistry experiments and molecular dynamics simulations for the binary systems', *Physics and Chemistry of the Earth*. Elsevier Ltd, 99, pp. 194–203. doi: 10.1016/j.pce.2017.05.005.

Androniuk, I. (2017) *Effects of cement organic additives on the adsorption of uranyl ions on calcium silicate hydrate phases : experimental determination and computational molecular modelling*. Ecole nationale supérieure Mines-Télécom Atlantique. Available at: https://tel.archives-ouvertes.fr/tel-01591443.

Androniuk, I. and Kalinichev, A. G. (2020) 'Molecular dynamics simulation of the interaction of uranium (VI) with the C–S–H phase of cement in the presence of gluconate', *Applied Geochemistry*. Elsevier Ltd, 113, p. 104496. doi: 10.1016/j.apgeochem.2019.104496.

Aranda, M. A. G. (2016) 'Recent studies of cements and concretes by synchrotron radiation crystallographic and cognate methods', *Crystallography Reviews*. Taylor & Francis, 22(3), pp. 150–196. doi: 10.1080/0889311X.2015.1070260.

Badmann, R., Stockhausen, N. and Setzer, M. J. (1981) 'The statistical thickness and the chemical potential of adsorbed water films', *Journal of Colloid And Interface Science*, 82(2), pp. 534–542. doi: 10.1016/0021-9797(81)90395-7.

Banfield, J. F. and Zhang, H. (2001) 'Nanoparticles in the environment', *Reviews in Mineralogy and Geochemistry*, 44, pp. 1–58. doi: 10.2138/rmg.2001.44.01.

Barberon, F. *et al.* (2003) 'Probing the Surface Area of a Cement-Based Material by Nuclear Magnetic Relaxation Dispersion', *Physical Review Letters*, 90(11), p. 4. doi: 10.1103/PhysRevLett.90.116103.

Bauchy, M. *et al.* (2014) 'Order and disorder in calcium-silicate-hydrate', *Journal of Chemical Physics*, 140(21). doi: 10.1063/1.4878656.

Bauchy, M. *et al.* (2015) 'Fracture toughness of calcium-silicate-hydrate from molecular dynamics simulations', *Journal of Non-Crystalline Solids*. Elsevier B.V., 419, pp. 58–64. doi: 10.1016/j.jnoncrysol.2015.03.031.

Beaudoin, J. J., Ramachandran, V. S. and Feldman, R. F. (1990) 'Interaction of chloride and C-S-H', *Cement and Concrete Research*, 20(6), pp. 875–883. doi: https://doi.org/10.1016/0008-8846(90)90049-4.

Beaudoin, J. and Odler, I. (2019) *Hydration, Setting and Hardening of Portland Cement*. 5th edn, *Lea's Chemistry of Cement and Concrete*. 5th edn. Elsevier Ltd. doi: 10.1016/B978-0-08-100773-0.00005-8.

Bellissent-Funel, M.-C., Chen, S. H. and Zanotti, J.-M. (1995) 'Single-particle dynamics of water

molecules in confined space', *Physical Review E*. American Physical Society, 51(5), pp. 4558–4569. doi: 10.1103/PhysRevE.51.4558.

Bellissent-Funel, M. C. and Teixeira, J. (1991) 'Dynamics of water studied by coherent and incoherent inelastic neutron scattering', *Journal of Molecular Structure*, 250(2–4), pp. 213–230. doi: 10.1016/0022-2860(91)85029-3.

Berendsen, H. J. C., Grigera, J. R. and Straatsma, T. P. (1987) 'The Missing Term in Effective Pair Potentials', (6), pp. 6269–6271. doi: 10.1021/j100308a038.

Berg, M. C. *et al.* (2017) 'Water Mobility in Chalk: A Quasielastic Neutron Scattering Study', *Journal of Physical Chemistry C*, 121(26), pp. 14088–14095. doi: 10.1021/acs.jpcc.7b01998.

Biagioni, C., Merlino, S. and Bonaccorsi, E. (2015) 'The tobermorite supergroup: a new nomenclature', *Mineralogical Magazine*, 79(2), pp. 485–495. doi: 10.1180/minmag.2015.079.2.22.

Blinc, R. *et al.* (1978) 'NMR Relaxation Study of Adsorbed Water in Cement and C3S Pastes', *Journal of the American Ceramic Society*. John Wiley & Sons, Ltd, 61(1–2), pp. 35–37. doi: https://doi.org/10.1111/j.1151-2916.1978.tb09224.x.

Bonaccorsi, E., Merlino, S. and Kampf, A. R. (2005) 'The crystal structure of tobermorite 14 Å (plombierite), a C-S-H phase', *Journal of the American Ceramic Society*, 88(3), pp. 505–512. doi: 10.1111/j.1551-2916.2005.00116.x.

Bonnaud, P. A. *et al.* (2012) 'Thermodynamics of water confined in porous calcium-silicate-hydrates', *Langmuir*, 28(31), pp. 11422–11432. doi: 10.1021/la301738p.

Bonnaud, P. A., Coasne, B. and Pellenq, R. J. M. (2012) 'Solvated calcium ions in charged silica nanopores', *Journal of Chemical Physics*, 137(6). doi: 10.1063/1.4742854.

Bordallo, H. N., Aldridge, L. P. and Desmedt, A. (2006) 'Water dynamics in hardened ordinary portland cement paste or concrete: From quasielastic neutron scattering', *Journal of Physical Chemistry B*, 110(36), pp. 17966–17976. doi: 10.1021/jp062922f.

Bourg, I. C. and Sposito, G. (2011) 'Molecular dynamics simulations of the electrical double layer on smectite surfaces contacting concentrated mixed electrolyte (NaCl-CaCl(2)) solutions', *Journal of Colloid and Interface Science*. Elsevier Inc., 360(2), pp. 701–715. doi: 10.1016/j.jcis.2011.04.063.

Bourg, I. C. and Steefel, C. I. (2012) 'Molecular dynamics simulations of water structure and diffusion in silica nanopores', *Journal of Physical Chemistry C*, 116(21), pp. 11556–11564. doi: 10.1021/jp301299a.

Brunauer, S., Emmett, P. H. and Teller, E. (1938) 'Adsorption of Gases in Multimolecular Layers', *Journal of the American Chemical Society*. American Chemical Society, 60(2), pp. 309–319. doi: 10.1021/ja01269a023.

Brunet, F. *et al.* (2004) 'Application of 29 Si Homonuclear and 1 H-29 Si Heteronuclear NMR Correlation to Structural Studies of Calcium Silicate Hydrates', *J. Phys. Chem. B* , 108, pp. 15494–15502. doi: 10.1021/jp031174g.

CEMBUREAU (2020) *Cementing the European Green Deal, Reaching climate neutrality along the cement and concrete value chain by 2050*, *The European Cement Association, Brussels*. Available at: https://cembureau.eu/media/kuxd32gi/cembureau-2050-roadmap_final-version_web.pdf.

Charlet, L. (1994) 'Reactions at the Mineral-Water Interface BT - Chemistry of Aquatic Systems: Local and Global Perspectives', in Bidoglio, G. and Stumm, W. (eds). Dordrecht: Springer Netherlands, pp. 273–305. doi: 10.1007/978-94-017-1024-4_11.

Chen, J. J. *et al.* (2004) 'Solubility and structure of calcium silicate hydrate', *Cement and Concrete Research*, 34(9), pp. 1499–1519. doi: 10.1016/j.cemconres.2004.04.034.

Chen, S. H. *et al.* (1999) 'Model for single-particle dynamics in supercooled water', *Physical Review E*. American Physical Society, 59(6), pp. 6708–6714. doi: 10.1103/PhysRevE.59.6708.

Claret, F. *et al.* (2004) 'Clay minerals in the Meuse-Haute Marne underground laboratory (France): Possible influence of organic matter on clay mineral evolution', *Clays and Clay Minerals*, 52(5), pp.

515–532. doi: 10.1346/CCMN.2004.0520501.

Collin, M. *et al.* (2018) 'Molecular Dynamics Simulations of Water Structure and Diffusion in a 1 nm Diameter Silica Nanopore as a Function of Surface Charge and Alkali Metal Counterion Identity', *Journal of Physical Chemistry C*, 122(31), pp. 17764–17776. doi: 10.1021/acs.jpcc.8b03902.

Cong, X. and Kirkpatrick, R. J. (1995) '1H — 29Si CPMAS NMR study of the structure of calcium silicate hydrate', *Advances in Cement Research*, 7(27), pp. 103–111. doi: 10.1680/adcr.1995.7.27.103.

Crupi, V. *et al.* (2003) 'Structure and dynamics of water confined in a nanoporous sol-gel silica glass: A neutron scattering study', *Molecular Physics*, 101(22), pp. 3323–3333. doi: 10.1080/0026897031000163879O.

Cuello, G. J. (2008) 'Structure factor determination of amorphous materials by neutron diffraction', *Journal of Physics: Condensed Matter*. Ustron, POLAND: Iop Publishing Ltd, 20(24). doi: 244109 10.1088/0953-8984/20/24/244109.

Cuesta, A. *et al.* (2021) 'Local structure and Ca/Si ratio in C-S-H gels from hydration of blends of tricalcium silicate and silica fume', *Cement and Concrete Research*, 143, p. 106405. doi: https://doi.org/10.1016/j.cemconres.2021.106405.

Cygan, R. T. *et al.* (2015) 'Inelastic Neutron Scattering and Molecular Simulation of the Dynamics of Interlayer Water in Smectite Clay Minerals', *Journal of Physical Chemistry C*, 119(50), pp. 28005–28019. doi: 10.1021/acs.jpcc.5b08838.

Cygan, R. T., Liang, J. J. and Kalinichev, A. G. (2004) 'Molecular models of hydroxide, oxyhydroxide, and clay phases and the development of a general force field', *Journal of Physical Chemistry B*, 108(4), pp. 1255–1266. doi: 10.1021/jp0363287.

Van Damme, H. (2018) 'Concrete material science: Past, present, and future innovations', *Cement and Concrete Research*. Elsevier, 112, pp. 5–24. doi: 10.1016/j.cemconres.2018.05.002.

van Deventer, J. S. J., White, C. E. and Myers, R. J. (2021) 'A Roadmap for Production of Cement and Concrete with Low-CO2 Emissions', *Waste and Biomass Valorization*, 12(9), pp. 4745–4775. doi: 10.1007/s12649-020-01180-5.

Van Duin, A. C. T. *et al.* (2001) 'ReaxFF: A reactive force field for hydrocarbons', *Journal of Physical Chemistry A*, 105(41), pp. 9396–9409. doi: 10.1021/jp004368u.

Eckert, J. (1992) 'Theoretical introduction to neutron scattering spectroscopy', *Spectrochimica Acta Part A: Molecular Spectroscopy*, 48(3), pp. 271–283. doi: 10.1016/0584-8539(92)80058-5.

Everett, D. H. (1972) 'Manual of Symbols and Terminology for Physicochemical Quantities and Units, Appendix II: Definitions, Terminology and Symbols in Colloid and Surface Chemistry: ', *Pure and Applied Chemistry*, 31(4), pp. 577–638. doi: doi:10.1351/pac197231040577.

Faraone, A. *et al.* (2004) 'Quasielastic and inelastic neutron scattering on hydrated calcium silicate pastes', *Journal of Chemical Physics*, 121(7), pp. 3212–3220. doi: 10.1063/1.1772755.

Faucon, P. *et al.* (1997) 'Study of the structural properties of the C-S-H(I) by molecular dynamics simulation', *Cement and Concrete Research*, 27(10), pp. 1581–1590. doi: https://doi.org/10.1016/S0008-8846(97)00161-0.

Feldman, R. F. (1987) 'Diffusion measurements in cement paste by water replacement using Propan-2-OL', *Cement and Concrete Research*, 17(4), pp. 602–612. doi: https://doi.org/10.1016/0008-8846(87)90133-5.

Feldman, R. F. and Sereda, P. J. (1970) 'A new model for hydrated Portland cement and its practical implications.', *Engineering Journal (Canada)*, 53(8/9), pp. 53–59.

Fernandez-Martinez, A. *et al.* (2020) 'Curvature-induced hydrophobicity at imogolite-water interfaces', *Environmental Science: Nano*. Royal Society of Chemistry, 7(9), pp. 2759–2772. doi: 10.1039/d0en00304b.

Ferrage, E. *et al.* (2010) 'Hydration properties and interlayer organization of water and ions in synthetic na-smectite with tetrahedral layer charge. Part 1. Results from X-ray diffraction profile modeling',

Journal of Physical Chemistry C, 114(10), pp. 4515–4526. doi: 10.1021/jp909860p.

Ferrage, E. *et al.* (2011) 'Hydration properties and interlayer organization of water and ions in synthetic na-smectite with tetrahedral layer charge. Part 2. Toward a precise coupling between molecular simulations and diffraction data', *Journal of Physical Chemistry C*, 115(5), pp. 1867–1881. doi: 10.1021/jp105128r.

Ferraris, C. F. and Wittmann, F. H. (1987) 'Shrinkage mechanisms of hardened cement paste', *Cement and Concrete Research*, 17(3), pp. 453–464. doi: https://doi.org/10.1016/0008-8846(87)90009-3.

Fischedick, M. *et al.* (2014) 'Industry', in *Climate Change 2014: Mitigation of Climate Change. Contribution of Working Group III to the Fifth Assessment Report of the Intergovernmental Panel on Climate Change*. Cambridge University Press, pp. 743–810. Available at: https://www.ipcc.ch/site/assets/uploads/2018/02/ipcc_wg3_ar5_chapter10.pdf.

Fischer, H. E. *et al.* (2002) 'D4c: A very high precision diffractometer for disordered materials', *Applied Physics A*, 74(1), pp. s160–s162. doi: 10.1007/s003390101087.

Fischer, Henry E., Barnes, A. C. and Salmon, P. S. (2006) 'Neutron and x-ray diffraction studies of liquids and glasses', *Reports on Progress in Physics*, 69(1), pp. 233–299. doi: 10.1088/0034-4885/69/1/R05.

Fischer, H E, Barnes, A. C. and Salmon, P. S. (2006) 'Neutron and x-ray diffraction studies of liquids and glasses', *Reports on Progress in Physics*, 69(1), pp. 233–299. doi: 10.1088/0034-4885/69/1/r05.

Fischer, J. *et al.* (2014) 'Looking at hydrogen motions in confinement: The uniqueness of Quasi-Elastic Neutron Scattering', *European Physical Journal: Special Topics*, 223(9), pp. 1831–1847. doi: 10.1140/epjst/e2014-02229-4.

FitzGerald, S. A. *et al.* (1999) 'Inelastic neutron scattering study of the hydration of tricalcium silicate', *Journal of Materials Research*. 2011/01/31. Cambridge University Press, 14(3), pp. 1160–1165. doi: DOI: 10.1557/JMR.1999.0154.

Fratini, E. *et al.* (2002) 'Quasi-Elastic Neutron Scattering Study of Translational Dynamics of Hydration Water in Tricalcium Silicate', *The Journal of Physical Chemistry B*, 106(1), pp. 158–166. doi: 10.1021/jp010536m.

Frenkel, Daan, B. S. (2001) 'Understanding molecular simulation: from algorithms to applications. Vol. 1. Elsevier'.

Fujii, K. and Kondo, W. (1981) 'Heterogeneous equilibrium of calcium silicate hydrate in water at 30 °C', *Journal of the Chemical Society, Dalton Transactions*. The Royal Society of Chemistry, (2), pp. 645–651. doi: 10.1039/DT9810000645.

Gaboreau, S. *et al.* (2020) 'Hydration Properties and Interlayer Organization in Synthetic C-S-H', *Langmuir*. American Chemical Society, 36(32), pp. 9449–9464. doi: 10.1021/acs.langmuir.0c01335.

Gallé, C. (2001) 'Effect of drying on cement-based materials pore structure as identified by mercury intrusion porosimetry: A comparative study between oven-, vacuum-, and freeze-drying', *Cement and Concrete Research*, 31(10), pp. 1467–1477. doi: https://doi.org/10.1016/S0008-8846(01)00594-4.

Gilbert, B. *et al.* (2006) 'Surface Chemistry Controls Crystallinity of ZnS Nanoparticles', *Nano letters*, 6, pp. 605–610. doi: 10.1021/nl052201c.

Goret, G., Aoun, B. and Pellegrini, E. (2017) 'MDANSE: An Interactive Analysis Environment for Molecular Dynamics Simulations', *Journal of Chemical Information and Modeling*. American Chemical Society, 57(1), pp. 1–5. doi: 10.1021/acs.jcim.6b00571.

Grangeon, S., Claret, F., Lerouge, C., *et al.* (2013) 'On the nature of structural disorder in calcium silicate hydrates with a calcium/silicon ratio similar to tobermorite', *Cement and Concrete Research*, 52, pp. 31–37. doi: https://doi.org/10.1016/j.cemconres.2013.05.007.

Grangeon, S., Claret, F., Linard, Y., *et al.* (2013) 'X-ray diffraction: A powerful tool to probe and understand the structure of nanocrystalline calcium silicate hydrates', *Acta Crystallographica Section B: Structural Science, Crystal Engineering and Materials*, 69(5), pp. 465–473. doi: 10.1107/S2052519213021155.

Grangeon, S. *et al.* (2016) 'Structure of nanocrystalline calcium silicate hydrates: Insights from X-ray diffraction, synchrotron X-ray absorption and nuclear magnetic resonance', *Journal of Applied Crystallography*, 49, pp. 771–783. doi: 10.1107/S1600576716003885.

Grangeon, S. *et al.* (2017) 'Quantitative X-ray pair distribution function analysis of nanocrystalline calcium silicate hydrates: A contribution to the understanding of cement chemistry', *Journal of Applied Crystallography*, 50(1), pp. 14–21. doi: 10.1107/S1600576716017404.

Gregg, S. J., Sing, K. S. W. and Salzberg, H. W. (1967) 'Adsorption Surface Area and Porosity', *Journal of The Electrochemical Society*. The Electrochemical Society, 114(11), p. 279C. doi: 10.1149/1.2426447.

Haas, J. and Nonat, A. (2015) 'From C-S-H to C-A-S-H: Experimental study and thermodynamic modelling', *Cement and Concrete Research*. Elsevier Ltd, 68, pp. 124–138. doi: 10.1016/j.cemconres.2014.10.020.

Hagymassy, J., Brunauer, S. and Mikhail, R. S. (1969) 'Pore structure analysis by water vapor adsorption: I. t-Curves for water vapor', *Journal of Colloid and Interface Science*, 29(3), pp. 485–491. doi: https://doi.org/10.1016/0021-9797(69)90132-5.

Heinz, H. *et al.* (2005) 'Force field for mica-type silicates and dynamics of octadecylammonium chains grafted to montmorillonite', *Chemistry of Materials*, 17(23), pp. 5658–5669. doi: 10.1021/cm0509328.

Hou, D. (2020) *Molecular Simulation on Cement-Based Materials*, *Molecular Simulation on Cement-Based Materials*. doi: 10.1007/978-981-13-8711-1.

Howe, M. A., McGreevy, R. L. and Zetterstrom, P. (1998) 'CORRECT: A correction programme for neutron diffraction data', *NFL Studsvik internal report*.

Hunvik, K. W. B. *et al.* (2020) 'CO2 Capture by Nickel Hydroxide Interstratified in the Nanolayered Space of a Synthetic Clay Mineral', *The Journal of Physical Chemistry C*. American Chemical Society, 124(48), pp. 26222–26231. doi: 10.1021/acs.jpcc.0c07206.

Ivanov, A., Jimenéz-Ruiz, M. and Kulda, J. (2014) 'IN1-Lagrange-the new ILL instrument to explore vibration dynamics of complex materials', *Journal of Physics: Conference Series*, 554(1), pp. 1–7. doi: 10.1088/1742-6596/554/1/012001.

Jansen, D. *et al.* (2018) 'The early hydration of OPC investigated by in-situ XRD, heat flow calorimetry, pore water analysis and 1H NMR: Learning about adsorbed ions from a complete mass balance approach', *Cement and Concrete Research*, 109, pp. 230–242. doi: https://doi.org/10.1016/j.cemconres.2018.04.017.

Jennings, H. M. (2008) 'Refinements to colloid model of C-S-H in cement : CM-II', 38, pp. 275–289. doi: 10.1016/j.cemconres.2007.10.006.

Jiménez-Ruiz, M. *et al.* (2017) 'Combination of Inelastic Neutron Scattering Experiments and ab Initio Quantum Calculations for the Study of the Hydration Properties of Oriented Saponites', *The Journal of Physical Chemistry C*, 121(9), pp. 5029–5040. doi: 10.1021/acs.jpcc.6b11836.

Jiménez-Ruiz, M., Ivanov, A. and Fuard, S. (2014) 'LAGRANGE - The new neutron vibrational spectrometer at the ILL', *Journal of Physics: Conference Series*, 549(1). doi: 10.1088/1742-6596/549/1/012004.

Johnston, C. T. (2018) *Clay mineral–water interactions*, *Surface and Interface Chemistry of Clay Minerals*. Edited by F. Schoonheydt, R; Johnston, C T; Bergaya. Elsevier. doi: https://doi.org/10.1016/B978-0-08-102432-4.00004-4.

Jönsson, B. *et al.* (2005) 'Controlling the cohesion of cement paste', *Langmuir*, 21(20), pp. 9211–9221. doi: 10.1021/la051048z.

Juhás, P. *et al.* (2013) 'PDFgetX3 : a rapid and highly automatable program for processing powder diffraction data into total scattering pair distribution functions', *Journal of Applied Crystallography*. International Union of Crystallography, 46(2), pp. 560–566. doi: 10.1107/S0021889813005190.

Kalinichev, A. G. and Kirkpatrick, R. J. (2002) 'Molecular dynamics modeling of chloride binding to the surfaces of calcium hydroxide, hydrated calcium aluminate, and calcium silicate phases', *Chemistry of Materials*, 14(8), pp. 3539–3549. doi: 10.1021/cm0107070.

Kalinichev, A. G., Wang, J. and Kirkpatrick, R. J. (2007) 'Molecular dynamics modeling of the structure, dynamics and energetics of mineral-water interfaces: Application to cement materials', *Cement and Concrete Research*, 37(3), pp. 337–347. doi: 10.1016/j.cemconres.2006.07.004.

Kieffer, J. and Wright, J. P. (2013) 'PyFAI: a Python library for high performance azimuthal integration on GPU', *Powder Diffraction*. 2013/11/14. Cambridge University Press, 28(S2), pp. S339–S350. doi: DOI: 10.1017/S0885715613000924.

Korb, J.-P., Whaley Hodges, M. and Bryant, R. (1998) 'Translational diffusion of liquids at surface of microporous materials: new theoretical analysis of field cycling magnetic relaxation measurements', *Magnetic Resonance Imaging*, 16(5), pp. 575–578. doi: https://doi.org/10.1016/S0730-725X(98)00051-4.

Kovačević, G. *et al.* (2015) 'Atomistic modeling of crystal structure of Ca1.67SiHx', *Cement and Concrete Research*, 67, pp. 197–203. doi: 10.1016/j.cemconres.2014.09.003.

Kovačević, G. *et al.* (2016) 'Revised Atomistic Models of the Crystal Structure of C-S-H with high C/S Ratio', *Zeitschrift für Physikalische Chemie*, 230, pp. 1411–1424. doi: 10.1515/zpch-2015-0718.

Kunhi Mohamed, A. *et al.* (2018) 'An atomistic building block description of C-S-H - Towards a realistic C-S-H model', *Cement and Concrete Research*. Elsevier, 107, pp. 221–235. doi: 10.1016/j.cemconres.2018.01.007.

Kunhi Mohamed, A. *et al.* (2020) 'The Atomic-Level Structure of Cementitious Calcium Aluminate Silicate Hydrate', *Journal of the American Chemical Society*, 142(25), pp. 11060–11071. doi: 10.1021/jacs.0c02988.

L'Hôpital, E. *et al.* (2016) 'Influence of calcium to silica ratio on aluminium uptake in calcium silicate hydrate', *Cement and Concrete Research*. Elsevier Ltd, 85, pp. 111–121. doi: 10.1016/j.cemconres.2016.01.014.

Lammers, L. N. *et al.* (2017) 'Molecular dynamics simulations of cesium adsorption on illite nanoparticles', *Journal of Colloid and Interface Science*. Elsevier Inc., 490, pp. 608–620. doi: 10.1016/j.jcis.2016.11.084.

Larsen, S. R. *et al.* (2020) 'Physicochemical characterisation of fluorohectorite: Water dynamics and nanocarrier properties', *Microporous and Mesoporous Materials*. Elsevier Inc., 306(June), p. 110512. doi: 10.1016/j.micromeso.2020.110512.

Lefmann, K. (2019) 'Neutron Scattering: Theory, Instrumentation, and Simulation'.

Lehne, J. and Preston, F. (2018) *Making Concrete Change Innovation in Low-carbon Cement and Concrete The Royal Institute of International Affairs, Chatham House Report Series,*. Available at: https://www.chathamhouse.org/sites/default/files/publications/2018-06-13-making-concrete-change-cement-lehne-preston-final.pdf.

Levchenko, A. A. *et al.* (2007) 'Dynamics of water confined on a TiO2 (anatase) surface', *Journal of Physical Chemistry A*, 111(49), pp. 12584–12588. doi: 10.1021/jp076033j.

Livingston, R. *et al.* (1994) 'Application of Neutron Scattering Methods to Cementitious Materials.', *MRS Proceedings*, 376, p. 459. doi: doi:10.1557/PROC-376-459.

Loganathan, N. *et al.* (2016) 'Cation and Water Structure, Dynamics, and Energetics in Smectite Clays: A Molecular Dynamics Study of Ca-Hectorite', *Journal of Physical Chemistry C*, 120(23), pp. 12429–12439. doi: 10.1021/acs.jpcc.6b00230.

Lorch, E. (1969) 'Neutron diffraction by germania, silica and radiation-damaged silica glasses', *Journal of Physics C: Solid State Physics*, 2(2), pp. 229–237. doi: 10.1088/0022-3719/2/2/305.

Lothenbach, B. and Nonat, A. (2015) 'Calcium silicate hydrates: Solid and liquid phase composition', *Cement and Concrete Research*. Elsevier Ltd, 78, pp. 57–70. doi: 10.1016/j.cemconres.2015.03.019.

Machesky, M. L. *et al.* (2008) 'Surface Protonation at the Rutile (110) Interface: Explicit Incorporation of Solvation Structure within the Refined MUSIC Model Framework', *Langmuir*, 24(21), pp. 12331–12339. doi: 10.1021/la801356m.

Manzano, H. *et al.* (2012) 'Confined Water Dissociation in Microporous Defective Silicates: Mechanism, Dipole Distribution, and Impact on Substrate Properties', *Journal of the American Chemical Society*. American Chemical Society, 134(4), pp. 2208–2215. doi: 10.1021/ja209152n.

Marcus, Y. (1988) 'Ionic Radii in Aqueous Solutions', *Chemical Reviews*, 88(8), pp. 1475–1498. doi: 10.1021/cr00090a003.

Marry, V. and Turq, P. (2008) 'Structure and dynamics of water at a clay surface from molecular dynamics simulation', pp. 4802–4813. doi: 10.1039/b807288d.

Maruyama, I. *et al.* (2018) 'Cavitation of water in hardened cement paste under short-term desorption measurements', *Materials and Structures/Materiaux et Constructions*, 51(6). doi: 10.1617/s11527-018-1285-x.

Maruyama, I. *et al.* (2019) 'Dynamic microstructural evolution of hardened cement paste during first drying monitored by 1H NMR relaxometry', *Cement and Concrete Research*. Elsevier, 122, pp. 107–117. doi: 10.1016/j.cemconres.2019.04.017.

Masoumi, S. *et al.* (2019) 'Effective Interactions between Calcium-Silicate-Hydrate Nanolayers', *The Journal of Physical Chemistry C*. American Chemical Society, 123(8), pp. 4755–4766. doi: 10.1021/acs.jpcc.8b08146.

McDonald, P. J. *et al.* (2005) 'Surface relaxation and chemical exchange in hydrating cement pastes: A two-dimensional NMR relaxation study', *Physical Review E*. American Physical Society, 72(1), p. 11409. doi: 10.1103/PhysRevE.72.011409.

McDonald, P. J., Rodin, V. and Valori, A. (2010) 'Characterisation of intra- and inter-C–S–H gel pore water in white cement based on an analysis of NMR signal amplitudes as a function of water content', *Cement and Concrete Research*, 40, pp. 1656–1663. doi: 10.1016/j.cemconres.2010.08.003.

Meral, C., Benmore, C. J. and Monteiro, P. J. M. (2011) 'The study of disorder and nanocrystallinity in C-S-H, supplementary cementitious materials and geopolymers using pair distribution function analysis', *Cement and Concrete Research*. Elsevier Ltd., 41(7), pp. 696–710. doi: 10.1016/j.cemconres.2011.03.027.

Merlino, S., Bonaccorsi, E. and Armbruster, T. (2000) 'The real structures of clinotobermorite and tobermorite 9 Å: OD character, polytypes, and structural relationships', *European Journal of Mineralogy*, 12(2), pp. 411–429. doi: 10.1127/0935-1221/2000/0012-0411.

Merlino, S., Bonaccorsi, E. and Armbruster, T. (2001) 'The real structure of tobermorite 11A: normal and anomalous forms, OD character and polytypic modifications', *European Journal of Mineralogy*, 13(3), pp. 577–590. doi: 10.1127/0935-1221/2001/0013-0577.

Mikhail, R. S., Kamel, A. M. and Abo-El-Enein, S. A. (1969) 'Surface properties of cement hydration products. I. Pore structure of calcium silicate hydrates prepared in a suspension form', *Journal of Applied Chemistry*, 19(11), pp. 324–328. doi: 10.1002/jctb.5010191105.

Mishra, R. K. *et al.* (2017) 'cemff: A force field database for cementitious materials including validations, applications and opportunities', *Cement and Concrete Research*, 102, pp. 68–89. doi: https://doi.org/10.1016/j.cemconres.2017.09.003.

Mitchell, P. C. H. *et al.* (2005) *Vibrational Spectroscopy with Neutrons*, *Series on Neutron Techniques and Applications*. WORLD SCIENTIFIC. doi: doi:10.1142/5628.

Monet, G. *et al.* (2020) 'Solid wetting-layers in inorganic nano-reactors: The water in imogolite nanotube case', *Nanoscale Advances*, 2(5), pp. 1869–1877. doi: 10.1039/d0na00128g.

Monteilhet, L. *et al.* (2006) 'Observation of exchange of micropore water in cement pastes by two-dimensional T(2)-T(2) nuclear magnetic resonance relaxometry.', *Physical review. E, Statistical, nonlinear, and soft matter physics*. United States, 74(6 Pt 1), p. 61404. doi: 10.1103/PhysRevE.74.061404.

Muller, A. C. A. *et al.* (2013) 'Use of bench-top NMR to measure the density , composition and desorption isotherm of C-S-H in cement paste', *Microporous and Mesoporous Materials*. Elsevier Inc., 178, pp. 99–103. doi: 10.1016/j.micromeso.2013.01.032.

Nemes, N. M., Neumann, D. A. and Livingston, R. A. (2006) 'States of water in hydrated C3S (tricalcium silicate) as a function of relative humidity', *Journal of Materials Research*, 21(10), pp. 2516–2523. doi: 10.1557/jmr.2006.0332.

Ockwig, N. W. *et al.* (2008) 'Molecular dynamics studies of nanoconfined water in clinoptilolite and heulandite zeolites', *Physical Chemistry Chemical Physics*, 10(6), pp. 800–807. doi: 10.1039/b711949f.

Odler, I. (2003) 'The BET-specific surface area of hydrated Portland cement and related materials', 33, pp. 2049–2056. doi: 10.1016/S0008-8846(03)00225-4.

Ohtaki, H. and Radnai, T. (1993) 'Structure and Dynamics of Hydrated Ions', *Chemical Reviews*, 93(3), pp. 1157–1204. doi: 10.1021/cr00019a014.

Papatzani, S., Paine, K. and Calabria-Holley, J. (2015) 'A comprehensive review of the models on the nanostructure of calcium silicate hydrates', *Construction and Building Materials*. Elsevier Ltd, 74, pp. 219–234. doi: 10.1016/j.conbuildmat.2014.10.029.

Parker, S. F. *et al.* (2014) 'Recent and future developments on TOSCA at ISIS', *Journal of Physics: Conference Series*, 554(1). doi: 10.1088/1742-6596/554/1/012003.

Pellenq, R. J.-M. *et al.* (2009) 'A realistic molecular model of cement hydrates', *Proceedings of the National Academy of Sciences*, 106(38), pp. 16102–16107. doi: 10.1073/pnas.0902180106.

Pellenq, R. J. M. *et al.* (2009) 'A realistic molecular model of cement hydrates', *Proceedings of the National Academy of Sciences of the United States of America*, 106(38), pp. 16102–16107. doi: 10.1073/pnas.0902180106.

Pinna, R. S. *et al.* (2018) 'The neutron guide upgrade of the TOSCA spectrometer', *Nuclear Instruments and Methods in Physics Research, Section A: Accelerators, Spectrometers, Detectors and Associated Equipment*, 896(March), pp. 68–74. doi: 10.1016/j.nima.2018.04.009.

Pinson, M. B. *et al.* (2015) 'Hysteresis from Multiscale Porosity : Modeling Water Sorption and Shrinkage in Cement Paste', 064009, pp. 1–17. doi: 10.1103/PhysRevApplied.3.064009.

Pitteloud, C. *et al.* (2000) 'Structure of interlayer water in Wyoming montmorillonite studied by neutron diffraction with isotopic substitution', *Physica B: Condensed Matter*, 276–278. doi: 10.1016/S0921-4526(99)01422-2.

Pitteloud, C. *et al.* (2003) 'Neutron diffraction studies of ion coordination and interlayer water structure in smectite clays: Lanthanide(III)-exchanged Wyoming montmorillonite', *Colloids and Surfaces A: Physicochemical and Engineering Aspects*, 217(1–3), pp. 129–136. doi: 10.1016/S0927-7757(02)00567-8.

Placzek, G. (1952) 'The Scattering of Neutrons by Systems of Heavy Nuclei', *Physical Review*. American Physical Society, 86(3), pp. 377–388. doi: 10.1103/PhysRev.86.377.

Plimpton, S. (1997) 'Short-Range Molecular Dynamics', *Journal of Computational Physics*, 117(6), pp. 1–42. Available at: http://www.cs.sandia.gov/~sjplimp/main.html.

Powell, D. H., Fischer, H. E. and Skipper, N. T. (1998) 'The structure of interlayer water in Li-montmorillonite studied by neutron diffraction with isotopic substitution', *Journal of Physical Chemistry B*, 102(52). doi: 10.1021/jp982966r.

Powers, T. C.; Brownyard, T. L. (1946) 'Studies of the Physical Properties of Hardened Portland Cement Paste', *ACI Journal Proceedings*, 43(9), pp. 249–336. doi: 10.14359/15301.

Powles, J. G. (1973) 'The structure of molecular liquids by neutron scattering', *Advances in Physics*. Taylor & Francis, 22(1), pp. 1–56. doi: 10.1080/00018737300101259.

Qomi, M. J. A. *et al.* (2014) 'Anomalous composition-dependent dynamics of nanoconfined water in the interlayer of disordered calcium-silicates', *Journal of Chemical Physics*, 140(5). doi: 10.1063/1.4864118.

Ramirez-Cuesta, T., Parker, S. F. and Tomkinson, J. (no date) 'TOSCA User Guide Manual ', pp. 1–66. Available at: http://www.isis.rl.ac.uk/molecularspectroscopy/tosca/.

Rapaport, D. C. (2004) *The Art of Molecular Dynamics Simulation*. 2nd edn. Cambridge: Cambridge University Press. doi: DOI: 10.1017/CBO9780511816581.

Renaudin, G. *et al.* (2009) 'Structural characterization of C-S-H and C-A-S-H samples-Part I: Long-range order investigated by Rietveld analyses', *Journal of Solid State Chemistry*, 182(12), pp. 3312–3319. doi: 10.1016/j.jssc.2009.09.026.

Richard, D., Ferrand, M. and Kearley, G. J. (1996) 'Analysis and Visualisation of Neutron-Scattering Data', *Journal of Neutron Research*. IOS Press, 4, pp. 33–39. doi: 10.1080/10238169608200065.

Richardson, I. G. (2004) 'Tobermorite/jennite- and tobermorite/calcium hydroxide-based models for the structure of C-S-H: Applicability to hardened pastes of tricalcium silicate, β-dicalcium silicate, Portland cement, and blends of Portland cement with blast-furnace slag, metakaol', *Cement and Concrete Research*, 34(9), pp. 1733–1777. doi: 10.1016/j.cemconres.2004.05.034.

Richardson, I. G. (2008) 'The calcium silicate hydrates', *Cement and Concrete Research*, 38(2), pp. 137–158. doi: 10.1016/j.cemconres.2007.11.005.

Richardson, I. G. (2013) 'The importance of proper crystal-chemical and geometrical reasoning demonstrated using layered single and double hydroxides research papers'. International Union of Crystallography, pp. 150–162. doi: 10.1107/S205251921300376X.

Richardson, I. G. (2014) 'Model structures for C-(A)-S-H(I)', *Acta Crystallographica Section B: Structural Science, Crystal Engineering and Materials*. International Union of Crystallography, 70(6), pp. 903–923. doi: 10.1107/S2052520614021982.

Richardson, I. G. and Groves, G. W. (1992) 'Microstructure and microanalysis of hardened cement pastes involving ground granulated blast-furnace slag', *Journal of Materials Science*, 27(22), pp. 6204–6212. doi: 10.1007/BF01133772.

Rodriguez, E. T. *et al.* (2015) 'Composition, silicate anion structure and morphology of calcium silicate hydrates (C-S-H) synthesised by silica-lime reaction and by controlled hydration of tricalcium silicate (C3S)', *Advances in Applied Ceramics*, 114(7), pp. 362–371. doi: 10.1179/1743676115Y.0000000038.

Roosz, C. *et al.* (2016) 'Distribution of Water in Synthetic Calcium Silicate Hydrates', *Langmuir*. American Chemical Society, 32(27), pp. 6794–6805. doi: 10.1021/acs.langmuir.6b00878.

Roosz, C. *et al.* (2018) 'Thermodynamic properties of C-S-H, C-A-S-H and M-S-H phases: Results from direct measurements and predictive modelling', *Applied Geochemistry*, 92, pp. 140–156. doi: https://doi.org/10.1016/j.apgeochem.2018.03.004.

Roscioni, O. M., Muccioli, L. and Zannoni, C. (2017) 'Predicting the Conditions for Homeotropic Anchoring of Liquid Crystals at a Soft Surface. 4-n-Pentyl-4′-cyanobiphenyl on Alkylsilane Self-Assembled Monolayers', *ACS Applied Materials and Interfaces*, 9(13), pp. 11993–12002. doi: 10.1021/acsami.6b16438.

Rougelot, T., Skoczylas, F. and Burlion, N. (2009) 'Water desorption and shrinkage in mortars and cement pastes: Experimental study and poromechanical model', *Cement and Concrete Research*. Elsevier Ltd, 39(1), pp. 36–44. doi: 10.1016/j.cemconres.2008.10.005.

Rovira-Esteva, M. (2014) *Short-range order in disordered phases*. Computational and Applied Physics of the Department of Physics and Nuclear Engineering of the Technical University of Catalonia.

Van Ruijven, B. J. *et al.* (2016) 'Long-term model-based projections of energy use and CO2 emissions from the global steel and cement industries', *Resources, Conservation and Recycling*. Elsevier B.V., 112, pp. 15–36. doi: 10.1016/j.resconrec.2016.04.016.

Russo, D. *et al.* (2011) 'Vibrational density of states of hydration water at biomolecular sites: Hydrophobicity promotes low density amorphous ice behavior', *Journal of the American Chemical Society*, 133(13), pp. 4882–4888. doi: 10.1021/ja109610f.

Scherer, G. W. (1990) 'Theory of Drying', *Journal of the American Ceramic Society*. John Wiley & Sons, Ltd, 73(1), pp. 3–14. doi: https://doi.org/10.1111/j.1151-2916.1990.tb05082.x.

Schneider, M. *et al.* (2017) 'Suppressing Crack Formation in Particulate Systems by Utilizing Capillary Forces', *ACS Applied Materials and Interfaces*, 9(12), pp. 11095–11105. doi: 10.1021/acsami.6b13624.

Schoonheydt, R. A., Johnston, C. T. and Bergaya, F. (2018) *Clay minerals and their surfaces*, *Surface and Interface Chemistry of Clay Minerals*. Edited by F. Schoonheydt, R; Johnston, C T; Bergaya. Elsevier. doi: https://doi.org/10.1016/B978-0-08-102432-4.00001-9.

Scrivener, K. (2017) *Cement Chemistry and Sustainable Cementitious Materials*, *EDX online course*. Available at: https://www.edx.org/course/cement-chemistry-and-sustainable-cementitious-mate.

Scrivener, K. L. and Kirkpatrick, R. J. (2008) 'Innovation in use and research on cementitious material', *Cement and Concrete Research*, 38(2), pp. 128–136. doi: 10.1016/j.cemconres.2007.09.025.

Sears, V. F. (1992) 'Neutron scattering lengths and cross sections', *Neutron News*, 3, pp. 26–37.

Senftle, T. P. *et al.* (2016) 'The ReaxFF reactive force-field: development, applications and future directions', *npj Computational Materials*, 2(1), p. 15011. doi: 10.1038/npjcompumats.2015.11.

Shahsavari, R., Pellenq, R. J. M. and Ulm, F. J. (2011) 'Empirical force fields for complex hydrated calcio-silicate layered materials', *Physical Chemistry Chemical Physics*, 13(3), pp. 1002–1011. doi: 10.1039/c0cp00516a.

Sheka, E. F. *et al.* (2019) 'Computationally Supported Neutron Scattering Study of Natural and Synthetic Amorphous Carbons', *Journal of Physical Chemistry C*, 123(25), pp. 15841–15850. doi: 10.1021/acs.jpcc.9b03675.

Sing, K. S. W. (1985) 'Reporting physisorption data for gas/solid systems with special reference to the determination of surface area and porosity (Recommendations 1984)', *Pure and Applied Chemistry*, 57(4), pp. 603–619. doi: doi:10.1351/pac198557040603.

Sinko, R., Bažant, Z. P. and Keten, S. (2018) 'A nanoscale perspective on the effects of transverse microprestress on drying creep of nanoporous solids', *Proceedings of the Royal Society A: Mathematical, Physical and Engineering Sciences*, 474(2209). doi: 10.1098/rspa.2017.0570.

Sivia, D. S. (2011) *Elementary Scattering Theory: For X-ray and Neutron Users*. Oxford University Press.

Skalny, J. and Odler, I. (1972) 'Pore structure of calcium silicate hydrates', *Cement and Concrete Research*, 2(4), pp. 387–400. doi: 10.1016/0008-8846(72)90055-5.

Skelton, A. A. *et al.* (2011) 'Simulations of the quartz(10$\bar{1}$1)/water interface: A comparison of classical force fields, Ab initio molecular dynamics, and X-ray reflectivity experiments', *Journal of Physical Chemistry C*, 115(5), pp. 2076–2088. doi: 10.1021/jp109446d.

Skipper, N. T., Soper, A. K. and McConnell, J. D. C. (1991) 'The structure of interlayer water in vermiculite', *The Journal of Chemical Physics*, 94(8), pp. 5751–5760. doi: 10.1063/1.460457.

Soper, A. K. (2007) 'Joint structure refinement of x-ray and neutron diffraction data on disordered materials: Application to liquid water', *Journal of Physics Condensed Matter*, 19(33). doi: 10.1088/0953-8984/19/33/335206.

Soper, A. K. (2009) 'Inelasticity corrections for time-of-flight and fixed wavelength neutron diffraction experiments', *Molecular Physics*, 107(16), pp. 1667–1684. doi: 10.1080/00268970903025667.

Soper, A. K. (2012) 'GudrunN and GudrunX Programs for correcting raw neutron and x-ray total scattering data to differential cross section'.

Soyer-Uzun, S. *et al.* (2012) 'Compositional evolution of calcium silicate hydrate (C-S-H) structures by total X-ray scattering', *Journal of the American Ceramic Society*, 95(2), pp. 793–798. doi: 10.1111/j.1551-2916.2011.04989.x.

STFC (2017) *Mantid*. Available at: https://ww.mantidproject.org/.

Sun, E. W. H. and Bourg, I. C. (2020) 'Molecular dynamics simulations of mineral surface wettability by water versus CO2: Thin films, contact angles, and capillary pressure in a silica nanopore', *Journal of Physical Chemistry C*, 124(46), pp. 25382–25395. doi: 10.1021/acs.jpcc.0c07948.

Taylor, H. (1997) 'Hydration of the calcium silicate phases', *Cement chemistry*, pp. 113–156. doi: 10.1146/annurev.pc.10.100159.002325.

Taylor, H. F. W. (1950) 'Hydrated calcium silicates. Part I. Compound formation at ordinary temperatures', *Journal of the Chemical Society (Resumed)*. The Royal Society of Chemistry, (0), pp. 3682–3690. doi: 10.1039/JR9500003682.

Taylor, H. F. W. (1986a) 'Bound Water in Cement Pastes and its Significance for Pore Solution Compositions', *MRS Proceedings*. 2011/02/25. Cambridge University Press, 85, p. 47. doi: DOI: 10.1557/PROC-85-47.

Taylor, H. F. W. (1986b) 'Proposed Structure for Calcium Silicate Hydrate Gel', *Journal of the American Ceramic Society*, 69(6), pp. 464–467. doi: 10.1111/j.1151-2916.1986.tb07446.x.

Taylor, H. F. W. (1997) *Cement chemistry*. Thomas Telford Publishing. doi: doi:10.1680/cc.25929.

Taylor, H. F. W. and Howison, J. W. (1956) 'Relationships between calcium silicates and clay minerals', *Clay Minerals Bulletin*. 2018/03/14. Cambridge University Press, 3(16), pp. 98–111. doi: DOI: 10.1180/claymin.1956.003.16.06.

Thomas, J. J. *et al.* (2003) 'Ca-OH bonding in the C-S-H gel phase of tricalcium silicate and white portland cement pastes measured by inelastic neutron scattering', *Chemistry of Materials*, 15(20), pp. 3813–3817. doi: 10.1021/cm034227f.

Thomas, J. J. and Jennings, H. M. (2006) 'A colloidal interpretation of chemical aging of the C-S-H gel and its effects on the properties of cement paste', *Cement and Concrete Research*, 36(1), pp. 30–38. doi: 10.1016/j.cemconres.2004.10.022.

Thomas, J., Jennings, H. and Allen, A. (1999) 'The Surface Area of Hardened Cement Paste as Measured by Various Techniques', *Concr. Sci. Eng.*, 1.

Thommes, M. *et al.* (2015) 'Physisorption of gases, with special reference to the evaluation of surface area and pore size distribution (IUPAC Technical Report)', *Pure and Applied Chemistry*, 87(9–10), pp. 1051–1069. doi: 10.1515/pac-2014-1117.

Toby, B. H. and Dreele, R. B. Von (2013) 'GSAS-II : the genesis of a modern open-source all purpose crystallography software package'. International Union of Crystallography, pp. 544–549. doi: 10.1107/S0021889813003531.

Tournassat, C. *et al.* (2016) 'Molecular dynamics simulations of anion exclusion in clay interlayer Nanopores', *Clays and Clay Minerals*, 64(4), pp. 374–388. doi: 10.1346/CCMN.2016.0640403.

Underwood, T. R. and Bourg, I. C. (2020) 'Large-scale molecular dynamics simulation of the dehydration of a suspension of smectite clay nanoparticles', *Journal of Physical Chemistry C*, 124(6), pp. 3702–3714. doi: 10.1021/acs.jpcc.9b11197.

Valori, A., McDonald, P. J. and Scrivener, K. L. (2013) 'The morphology of C-S-H: Lessons from 1H nuclear magnetic resonance relaxometry', *Cement and Concrete Research*. Elsevier Ltd, 49, pp. 65–81. doi: 10.1016/j.cemconres.2013.03.011.

Vandamme, M. and Ulm, F.-J. (2009) 'Nanogranular origin of concrete creep', *Proceedings of the National Academy of Sciences*, 106(26), pp. 10552–10557. doi: 10.1073/pnas.0901033106.

Wander, M. C. F. and Clark, A. E. (2008) 'Structural and dielectric properties of quartz - Water interfaces', *Journal of Physical Chemistry C*, 112(50), pp. 19986–19994. doi: 10.1021/jp803642c.

Wang, J. *et al.* (2005) 'Structure , Energetics , and Dynamics of Water Adsorbed on the Muscovite (001) Surface : A Molecular Dynamics Simulation', (001), pp. 15893–15905.

Wenzel, O. *et al.* (2017) 'Investigating the pore structure of the calcium silicate hydrate phase', *Materials Characterization*. Elsevier, 133, pp. 133–137. doi: 10.1016/j.matchar.2017.09.035.

White, C. E. *et al.* (2015) 'Intrinsic differences in atomic ordering of calcium (alumino)silicate hydrates in conventional and alkali-activated cements', *Cement and Concrete Research*. Elsevier Ltd, 67, pp. 66–73. doi: 10.1016/j.cemconres.2014.08.006.

Wittmann, F. H. (1973) 'Interaction of Hardened Cement Paste and Water', *Journal of the American Ceramic Society*, 56(8), pp. 409–415. doi: 10.1111/j.1151-2916.1973.tb12711.x.

Wyrzykowski, M. *et al.* (2017) 'Water Redistribution within the Microstructure of Cementitious

Materials due to Temperature Changes Studied with 1H NMR', *Journal of Physical Chemistry C*, 121(50), pp. 27950–27962. doi: 10.1021/acs.jpcc.7b08141.

Youssef, M., Pellenq, R. J.-M. and Yildiz, B. (2011) 'Glassy Nature of Water in an Ultraconfining Disordered Material: The Case of Calcium–Silicate–Hydrate', *Journal of the American Chemical Society*. American Chemical Society, 133(8), pp. 2499–2510. doi: 10.1021/ja107003a.

Yu, P. and Kirkpatrick, R. (1999) 'Thermal dehydration of tobermorite and jennite', *Concrete Science and Engineering*, 1(3), pp. 185–191.

Zhakiyeva, Z. *et al.* (2021) 'Structure of water adsorbed on nanocrystalline calcium silicate hydrate determined from neutron scattering and molecular dynamics simulations', *Journal of Physical Chemistry C*, under revi.

Zhang, D., Ghouleh, Z. and Shao, Y. (2017) 'Review on carbonation curing of cement-based materials', *Journal of CO2 Utilization*. Elsevier, 21, pp. 119–131. doi: 10.1016/j.jcou.2017.07.003.

Zhang, J. and Scherer, G. W. (2011) 'Comparison of methods for arresting hydration of cement', *Cement and Concrete Research*. Elsevier Ltd, 41(10), pp. 1024–1036. doi: 10.1016/j.cemconres.2011.06.003.

Zhou, T. *et al.* (2019) 'Multiscale poromechanics of wet cement paste', *Proceedings of the National Academy of Sciences*, 116(22), pp. 10652 LP – 10657. doi: 10.1073/pnas.1901160116.